



ISBN

© 2016, Ian Sebastiaan Eliëns

Drukker:

The research described in this thesis is part of the research programme *The Singular Physics of One-Dimensional Electrons of the Foundation for Fundamental Research on Matter (FOM)*, which is part of the *Netherlands Organisation for Scientific Research (NWO)* and was carried out at the *Institute of Physics, University of Amsterdam in The Netherlands*.

# ON QUANTUM SEAS

## ACADEMISCH PROEFSCHRIFT

ter verkrijging van de graad van doctor

aan de Universiteit van Amsterdam

op gezag van de Rector Magnificus

Prof. dr. ir. K.I.J. Maex

ten overstaan van een door het College voor Promoties

ingestelde commissie,

in het openbaar te verdedigen in de Agnietenkapel

op woensdag 15 maart 2017, te 10:00 uur

door

## IAN SEBASTIAAN ELIËNS

geboren te Amsterdam

PROMOTIECOMMISSIE

Promotor:	Prof. dr. J.-S. Caux	Universiteit van Amsterdam
Copromotor:	Dr. R.G Pereira	IIP Natal, Brazil
Overige leden:	Prof. dr. T. Giamarchi	Université de Genève
	Dr. A. Lamacraft	University of Cambridge
	Prof. dr. ir. H.J.W. Zandvliet	Universiteit van Twente
	Prof. dr. F.E. Schreck	Universiteit van Amsterdam
	Prof. dr. K. Schoutens	Universiteit van Amsterdam
	Dr. V. Gritsev	Universiteit van Amsterdam
	Dr. J. van Wezel	Universiteit van Amsterdam

Faculteit der Natuurwetenschappen, Wiskunde en Informatica

# List of publications

This thesis is based on the following publications:

- [1] *Boundary versus bulk behavior of time-dependent correlations in one-dimensional quantum systems*  
I.S. Eliëns, F.B. Ramos, J.C. Xavier, R.G. Pereira  
*Phys. Rev. B* **93** 195129 (2016)
  
- [2] *Gold-induced nanowires on the Ge(100) surface yield a 2D and not a 1D electronic structure*  
N. de Jong, R. Heimbuch, I.S. Eliëns, S. Smit, E. Frantzeskakis, J.-S. Caux, H.J.W. Zandvliet, and M.S. Golden  
*Phys. Rev. B* **93** 235444 (2016)
  
- [3] *Separation of Timescales in a Quantum Newton's Cradle*  
R. van den Berg, B. Wouters, I.S. Eliëns, J. De Nardis, R.M. Konik, J.-S. Caux  
*Phys. Rev. Lett.* 225302 (2016)
  
- [4] *Split Fermi seas in one-dimensional Bose fluids*  
T. Fokkema, I.S. Eliëns, J.-S. Caux  
*Phys. Rev. A* **89** 033637 (2014)
  
- [5] *Correlations of zero-entropy critical states in the XXZ model: integrability and Luttinger theory far from the ground state*  
R. Vlijm, I.S. Eliëns, J.-S. Caux  
*SciPost Physics* **1** 1 (2016)
  
- [6] *General finite-size effects for zero-entropy states in quantum integrable models*  
I.S. Eliëns, J.-S. Caux  
*J. Phys. A: Math. Theor.* **49** 49 (2016)

Other publications by the author:

- [7] *Atomic spin chain realization of a model for quantum criticality*  
R. Toskovic, R. van den Berg, A. Spinelli, I.S. Eliëns, B. van den Toorn, B. Bryant, J.-S. Caux, A.F. Otte  
*Nature Physics* **12** 656-660 (2016)
  
- [8] *Diagrammatics for Bose condensation in anyon theories*  
I.S. Eliëns, J.C. Romers, F.A. Bais  
*Phys. Rev. B* **90** 195130 (2014)



*There is no value in anything until it is finished.*

— Genghis Khan



# Contents

<b>1</b>	<b>Introduction</b>	<b>11</b>
1.1	This thesis . . . . .	14
<b>2</b>	<b>One-dimensional quantum fluids</b>	<b>17</b>
2.1	Microscopic models and observables . . . . .	17
2.2	Luttinger liquid theory . . . . .	20
2.2.1	The Tomonaga-Luttinger Hamiltonian . . . . .	20
2.2.2	Bosonization . . . . .	22
2.3	Nonlinear Luttinger liquid theory . . . . .	25
2.3.1	Dynamic response functions . . . . .	26
2.3.2	The impurity model . . . . .	30
2.4	Conclusion . . . . .	32
<b>3</b>	<b>Boundary correlations in 1D</b>	<b>33</b>
3.1	Introduction . . . . .	33
3.2	Green's function for spinless fermions . . . . .	35
3.3	Mobile impurity model with open boundary . . . . .	40
3.4	Other correlation functions . . . . .	44
3.4.1	Density-density correlation . . . . .	44
3.4.2	Spin autocorrelations . . . . .	46
3.4.3	Green's function for spinful fermions . . . . .	48
3.5	Role of integrability . . . . .	51
3.6	Numerical results for spin chains . . . . .	56
3.6.1	Integrable spin-1/2 model . . . . .	57
3.6.2	Effects of bound states and nearly flat bands . . . . .	60
3.6.3	Higher- $S$ spin chains . . . . .	61
3.7	Boundary-bulk spin correlation . . . . .	65
3.8	Conclusion . . . . .	69
<b>4</b>	<b>Absence of Luttinger physics in golden chains on germanium</b>	<b>71</b>
4.1	Introduction . . . . .	71
4.2	The Au/Ge(001) system . . . . .	73
4.3	Experiments, data and discussion . . . . .	75
4.3.1	The direction of electron dispersion . . . . .	77
4.3.2	Real-space structure of the electronic states . . . . .	83

## 0. CONTENTS

---

4.4	Disorder in interacting electron systems . . . . .	87
4.4.1	Mechanisms for suppression of the DOS . . . . .	87
4.4.2	The anomalous LDOS suppression in Au/Ge(001) . . . . .	90
4.5	Stability of the Luttinger liquid state . . . . .	92
4.5.1	Renormalization Group arguments . . . . .	93
4.6	Conclusions . . . . .	94
<b>5</b>	<b>Bragg pulses and Newton's cradles</b>	<b>97</b>
5.1	Introduction . . . . .	97
5.2	Theoretical setup . . . . .	98
5.3	Results . . . . .	101
5.3.1	Steady state . . . . .	101
5.3.2	Density profile . . . . .	101
5.3.3	Momentum distribution function . . . . .	105
5.4	Conclusion . . . . .	108
<b>6</b>	<b>On the Moses sea</b>	<b>109</b>
6.1	Introduction . . . . .	109
6.2	Definitions . . . . .	111
6.3	Models . . . . .	111
6.3.1	Moses sea . . . . .	113
6.4	Correlations from integrability . . . . .	114
6.5	Effective field theory for static correlations . . . . .	118
6.5.1	Multi-component Tomonaga-Luttinger model . . . . .	119
6.5.2	Parity symmetric case . . . . .	123
6.5.3	Asymptotes of correlations . . . . .	124
6.5.4	Momentum distribution function . . . . .	126
6.6	Effective field theory for dynamic correlations . . . . .	129
6.6.1	Perturbative expressions for parameters in XXZ . . . . .	134
6.7	Conclusion . . . . .	136
<b>7</b>	<b>General finite-size effects</b>	<b>139</b>
7.1	Introduction . . . . .	139
7.2	Bethe ansatz and finite-size corrections . . . . .	141
7.3	The energy of zero-entropy states . . . . .	143
7.4	The shift function . . . . .	144
7.5	Energy and momentum of excitations . . . . .	146
7.6	Finite-size spectrum and critical exponents . . . . .	147
7.7	The symmetric case . . . . .	150
7.8	Impurity configurations . . . . .	151
7.9	Conclusion . . . . .	152
<b>8</b>	<b>Conclusion</b>	<b>155</b>

**Bibliography**

**157**



# Introduction

The one physical system, the brain, contains an accurate working model of the other [...]. Not just a superficial image of it, though it contains that as well, but an explanatory model, embodying the same mathematical relationships and the same causal structure. Now, that is knowledge. [...] So, the laws of physics have this special property, that physical objects as unlike each other as they could possibly be, can nevertheless embody the same mathematical and causal structure and to do it more and more so over time. So we are a chemical scum that is different.

---

David Deutch

Although the rules of quantum mechanics are well understood, the emergent behavior of large collections of quantum components continues to reveal surprises. One-dimensional systems are particularly fruitful in this respect.

Intuitively, there is at least one reason why many-particle physics in one space dimension should be qualitatively different from two or more dimensions: particles have no room to pass each other. This, combined with simplifying constraints due to the reduced dimensionality, seems to lie at the heart of many of the quirks of one-dimensional physics which are now rooted in deep and elaborate mathematical theory. Let us try to give an overview of some of the important features without diving too deep.

## 1. Introduction

---

The strong effects of interactions become apparent when one considers a gas of almost free particles. In fact, the somewhat artificial limit of truly free particles does not care much whether we are in one, two or three dimensions. But in gradually introducing interactions the low-energy physics will change in a dramatically different way for dimension  $d = 1$  compared to higher dimensional counterparts.

Let us start by imagining a gas of bosons. Whereas in higher dimensions the Bose-Einstein condensate persists in the ground state upon introducing repulsive interactions, in one dimension the condensate is immediately destroyed leading (there is no longer a macroscopic occupation of a single one-particle state). One often states that order is melted due to quantum fluctuations, and this is an instance of the Mermin-Wagner theorem at play which states that this effect is general in preventing one-dimensional systems to attain long-range order.

Considering fermions on the other hand, the free system is characterized by a Fermi-sea ground state and the low-energy physics is understood in terms of particle and hole excitations. Turning on interactions, the spectral properties—as measured by absorption and emission experiments—in higher dimensions are still very similar but with sharp  $\delta$  functions for the allowed energy versus momentum values of excitations replaced by broadened Lorentzians. On the contrary, in one dimension some regions of the energy-momentum plane are still strictly forbidden by the restrictions of one-dimensional kinematics (two-body elastic scattering cannot change the momenta) while on the non-forbidden side of the thresholds characteristic power-law singularities emerge. Power-laws also characterize the real space correlations, differently from  $d > 1$ .

Another effect of the lack of room in 1d appears when we consider particle statistics. While in three dimensions particles are either bosons or fermions, which has to do with the many-body wave function being symmetric or anti-symmetric when exchanging particles, in 2d and 1d the situation drastically changes. Intuitively one can explain this as follows: in order to test what happens to the wave function of a many-body system upon interchanging the constituent particles there should be a physical process responsible for this interchange without otherwise disturbing the system. This means that the particles should be kept far apart so that there is no influence of interaction effects. In two dimensions this is possible, but performing the exchange clockwise or counter clockwise is not equivalent leading to a plethora of exotic braid statistics and the corresponding particles are named anyons. In one dimension the situation is even more severe as no process is imaginable in which the particles are interchanged without interacting. This arguably removes all meaning from the concept of particle statistics and hence the names ‘fermion’ or ‘boson’, or at least makes particle statistics and interaction effects inseparably intertwined. While at first sight this may seem like a rather esoteric observation, it turns out that in the theory of one-dimensional systems this is of tremendous practical use as will be seen in the numerous times that we can freely map a problem formulated in terms of bosons to one in terms of fermions or *vice versa* (or even somewhere in

between) resulting in the necessary simplification to come to a solution.

Finally, let us mention the effect of spin-charge separation. This entails that, for example, adding an electron to a quantum wire its spin and charge quantum numbers can be carried separately by the system and may propagate with different velocities. While this may seem counter-intuitive at first, it is easily illustrated by a toy model why this can happen in one dimension and not in two or three: Consider a half-filled anti-ferromagnetically ordered lattice of electrons. Let us remove an electron (this is slightly easier to visualize than adding an electron but the logic is the same). If we try to separate the resulting charge and spin excitation in 1d there is no additional energy cost, but in a 2d or 3d lattice there will be a string or sheet excitation in the magnetic order of which the energy increases with size, hence spin and charge excitation are confined to each other [9] (see Fig. 1.1).

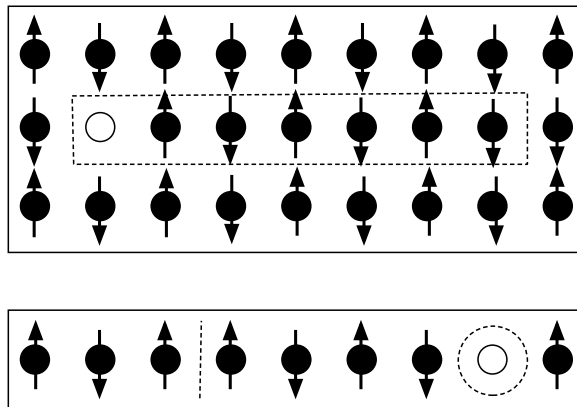


Figure 1.1: Illustration of the possibility of spin-charge separation in 1d in a toy model. Top: In a 2d system, trying to separate the spin and charge excitation leads to a domain wall in the anti-ferromagnetic spin order with an energy penalty proportional to its length. Bottom: In 1d the energy cost of a spin and charge excitation does not increase if we separate them from each other indicating the possibility that they are carried separately by the system.

These character traits of the one-dimensional quantum world will be pervasive in the theoretical considerations presented in this thesis. They are present in the rich collection of models and theoretical concepts that one-dimensional physics is exceptionally blessed with. Important will be so called quantum integrable models, the Bethe ansatz and conformal field theory. Just from a mathematical perspective, these are of outstanding beauty and deserve extensive investigation. They form the cornerstone of our understanding of one-dimensional physics, where the philosophy of John von Neumann should be kept in mind [10]:

The sciences do not try to explain, they hardly even try to interpret, they mainly make models. By a model is meant a mathematical construct which, with the addition of certain verbal interpretations, describes observed phenomena. The justification of such a mathematical construct is solely and precisely that it is expected to work.

Recent developments in experiments have put actual testing of the models of one-dimensional systems within reach (or sometimes even already in the published literature). Particularly the developments in ultra cold atomic gases in optical lattices [11] have put near-perfect realizations of textbook models in the hands of experimentalists in the lab. While the main chunk of this thesis is concerned with theoretical considerations sometimes supported by numerical evidence, the current convergence of theory and experiment is definitely one of the motivations behind this research.

### 1.1 This thesis

If this thesis was a Chinese syllable it would be in a superposition of the second (ˊ) and third (ˇ) tone. We start with low-energy equilibrium theory for one-dimensional (with one two-dimensional exception) quantum many-body systems while ending with high-energy out-of-equilibrium problems. Furthermore, we start with high level theory, progressing to down-to-earth experimental considerations and ending with more ivory-tower theory again. All in all it represents a collection of results mostly from the perspective of effective field theory and reasoning rooted in Bethe ansatz methods. While some questions are clearly related to experimental situations and sometimes we touch on fundamental questions in theoretical physics such as on the equilibration of closed quantum systems, other times this research is more of an exploration of the theoretical methods that together form the fabric of our understanding of the quantum world of many particles to see how they uphold in slightly non-standard situations. Bethe ansatz solvable (or quantum integrable) models are a perfect theoretical laboratory in this respect.

The thesis is written in such a way that all chapters can be read independently, which is part of the reason that it has become pretty lengthy. As a guide to the reader, let us outline the content of each chapter.

In chapter 2 we will start with a more elaborate introduction to one-dimensional quantum liquids and the techniques we will use to study them. This can be considered as a short review of the relevant literature. The most important concept is that of a nonlinear Luttinger liquid by which we mean a one-dimensional quantum liquid treated beyond the Luttinger liquid approximation, i.e. including dispersion curvature effects.

Chapter 3 deals with nonlinear Luttinger liquids with a boundary. Here, we combine the newly developed theory of nonlinear Luttinger liquids with the classic problem of having a boundary (i.e. a sudden potential barrier representing the end of, say, a quantum wire) in a one-dimensional system. It is shown that

adjusting the techniques used for Luttinger liquids with a boundary leads to predictions for time-dependent correlations which are different when measured in the bulk or at the boundary of the system. Similar to the properties described well within the Luttinger liquid approximation, the defining quantities for the band curvature effects show certain universal relations between bulk and boundary which can be used for experimental verification of nonlinear Luttinger liquid physics. We have tested these results in numerical simulations for integrable models. For non-integrable models with a boundary the predictions from nonlinear Luttinger liquid theory are considerably weaker for the boundary than for the bulk and we comment on the underlying mechanisms for this observation.

In chapter 4 we discuss an experimental system of self-organized atomic wires which form on a germanium surface after deposition of evaporated gold. Due to the highly anisotropic structure the hopes were high for finding effective one-dimensional conduction channels resulting in Luttinger liquid physics. Although certain experimental signatures seemed to point to hallmark Luttinger liquid predictions we show that exhaustive experimental investigations negate a one-dimensional scenario and put forward a two-dimensional scenario as most likely for the electron dynamics at the surface. By studying simple tight-binding models and reasoning based on the literature on disordered systems we argue that the observed characteristics are most likely caused by an interplay of disorder and interactions of the anisotropic 2d system rather than by one-dimensionality.

Changing gears a bit towards the study of out-of-equilibrium models, we discuss theoretical results pertaining Bragg pulse experiments and the quantum Newton's cradle setup of the group of David Weiss [12] in chapter 5. Apart from modeling the experimental situation relatively closely—be it for a limited parameter regime of strong interactions and very short single pulses—this study provides an interesting case to test different approximations and techniques. We combine results based on a local density approximation, integrability and nonlinear Luttinger liquid theory in obtaining measurable quantities.

Taking the quantum Newton's cradle as an inspiration, in chapter 6 we study a certain class of states in the Lieb-Liniger model for a one-dimensional gas of bosons and the XXZ model for a one-dimensional quantum magnet which share with the Bragg pulsed state that they consist of pockets of particles traveling with a certain mean momentum, but they have zero entropy density just like the ground state as if these pockets were completely cold. Their similarity with the ground state gives them a certain theoretical appeal and many of the techniques fit for the ground state can be generalized for this class of states. In the Bethe ansatz solution these states are represented by consecutive blocks of completely filled quantum numbers as if the ground-state Fermi sea configuration is split. For this reason we refer to such a state as a Moses sea. Dynamic response functions, static correlations and time-dependent correlations are computed using Bethe ansatz and a multi-component Luttinger liquid theory as well as a nonlinear Luttinger liquid theory developed for the appropriate correlations.

Fixing the parameters of an effective field theory for Bethe ansatz solvable

## 1. Introduction

---

models often proceeds by studying the finite-size corrections to the energy of low lying excitations. We extend this strategy in chapter 7 to Moses seas and show that general finite size corrections can be obtained for these states. This highlights the importance of the phase shifts at the effective Fermi points, a conclusion which has become clear in equilibrium systems by the recent developments in nonlinear Luttinger liquid theory. It gives the mathematical justification of certain results that were found in chapter 6 and fine-tunes our understanding the effects of the Hamiltonian time-evolution versus the reorganization of the state upon addition or removal of a particle or density fluctuation in correlations.

Finally, chapter 8 offers concluding remarks.

# One-dimensional quantum fluids

The career of a young theoretical physicist consists of treating the harmonic oscillator in ever-increasing levels of abstraction.

---

Sydney Coleman

In this chapter we embark on the study of one-dimensional quantum fluids. Typical applications one should have in mind are the description of electron liquids in quantum wires, Bose gases in elongated optical traps or spin chains as formed effectively in certain materials. We will touch upon certain microscopic models first—in particular those which are integrable—but we will quickly shift attention to effective-field-theory methods which are able to capture universal properties irrespective of the microscopic realization.

This chapter serves as an introduction to the ideas and techniques which will feature in the continuation of this thesis. We will not be able to do justice to all the facets nor to the interesting historical development of these ideas and the topic of quantum physics in one dimension. The marvelous book [9] serves as the basic reference for everything one-dimensional which predates the development of nonlinear Luttinger liquid theory. The review [13] takes over this role for the more recent developments. The pedagogical papers [14, 15] are also highly recommended. The reader is referred to these works for a much better discussion of the physical and historical background including all the relevant references.

## 2.1 Microscopic models and observables

Consider a gas of bosons confined to a one-dimensional tube. At low energies, when transverse fluctuations freeze out, one expects a model Hamiltonian of the general form

$$H = \frac{\hbar^2}{2m} \int dx \partial_x \Psi^\dagger(x) \partial_x \Psi(x) + \int dx dy \Psi^\dagger(x) \Psi^\dagger(y) V(|x-y|) \Psi(x) \Psi(y) \quad (2.1)$$

## 2. One-dimensional quantum fluids

---

to capture the physics well. Here  $x, y$  are coordinates along the tube,  $\Psi^{(\dagger)}(x)$  annihilates (creates) a boson at position  $x$  and  $V(|x-y|)$  is an effective interaction potential. For short range interactions and long length scales one moreover can imagine that a substitution  $V(|x-y|) \propto \delta(x-y)$  is allowed. Indeed, the resulting Lieb-Liniger model

$$H_{LL} = \frac{\hbar^2}{2m} \int dx [\partial_x \Psi^\dagger \partial_x \Psi + c \Psi^\dagger \Psi^\dagger \Psi \Psi], \quad (2.2)$$

is a good low-energy description of three-dimensional bosons confined to elongated traps. It has been shown that the coupling constant in that case can be expressed in terms of the one-dimensional scattering length,  $c = -2/a_{1D}$  [16–18], which is related as  $a_{1D} \approx -a_\perp(a_\perp/a_{3D} - 1.0326)$  to the oscillator length of the confining potential  $a_\perp$  and the three-dimensional scattering length  $a_{3D}$ . In cold atoms the three-dimensional scattering length is in fact variable by means of Feshbach resonance [11] leading to a versatile experimental platform to study properties and regimes of the Lieb-Liniger model.<sup>1</sup>

As Lieb and Liniger noted and exploit in their seminal paper [19] in which they formulated and solve the model that carries their names, the Hamiltonian  $H_{LL}$  in Eq. (2.2) can be diagonalized by Bethe ansatz. This technique, first employed by Hans Bethe [20] to solve the Heisenberg spin chain

$$H_{XXX} = \sum_j [S_j^x S_j^x + S_j^y S_j^y + S_j^z S_j^z - \hbar S_j^z] \quad (2.3)$$

constructs the eigenstates in terms of scattering states of suitably chosen ‘particles’.

The Lieb-Liniger model for a one-dimensional Bose gas and a slight generalization of Eq. (2.3) known as the XXZ model,

$$H_{XXZ} = \sum_j [S_j^x S_j^x + S_j^y S_j^y + \Delta S_j^z S_j^z - \hbar S_j^z], \quad (2.4)$$

will be our theoretical laboratory. As excellent ‘experimental’ setups beseeem, these models—thanks to there their exact solution—allow to extract a great deal of information with excellent control.

The  $N$ -body wave functions of Bethe ansatz solvable models are completely determined by the two-particle scattering phase shifts  $\theta(\lambda)$  due to the property of non-diffractive scattering, closely related to the notion of quantum integrability [21].<sup>2</sup> This leads to a classification of states in terms of rapidities  $\{\lambda_j\}$

---

<sup>1</sup>We will put  $\hbar = 1$  throughout this thesis and usually consider  $m = 1/2$  for the Lieb-Liniger model. The strength of interaction in this model is determined by the dimensionless parameter  $\gamma = c/\rho_0$ , but we usually put the mean density to be unity  $\rho_0 = 1$ .

<sup>2</sup>Quantum integrable systems are supposed to be the quantum counter part of classical integrable systems [21] but the discussion of what should be the precise definition of quantum integrability is still open [22].

(quasi-momenta). A quantization condition enforced by choosing (anti-)periodic boundary conditions in the finite system of length  $L$  leads to the so-called Bethe equations which can generically be written (in logarithmic form) as

$$p_0(\lambda_j)L + \sum_{k=1}^N \theta(\lambda_j - \lambda_k) = 2\pi I_j. \quad (2.5)$$

Here, the quantum numbers  $I_j$  can be chosen as integers or half-odd integers depending on the number of particles  $N$  and possibly subject to some constraints.

The origin of Eq. (2.5) can be easily understood: A particle  $j$  traversing the circle of circumference  $L$  on which we have placed our system, will acquire a phase determined by its momentum  $p_0(\lambda_j)$  as well as a scattering phase from the interaction with the  $N-1$  other particles on the ring. In the case of diffractionless scattering the latter is just the sum of the two-body phase shifts  $\theta(\lambda_j - \lambda_k)$ . The Bethe equations simply state that in order to satisfy the periodicity condition the phase associated to the momentum plus the total scattering phase should add up to  $2\pi$  times a (half-odd) integer.

In many considerations, the information of the specific model can be put into the momentum function  $p_0(\lambda)$  and scattering phase shift  $\theta(\lambda)$  while the form of Eq. (2.5) remains valid. This allows manipulation of the solution in a uniform fashion where specialization to the model at hand can be done in the final steps. This technique is particularly fruitful in discussing results in the thermodynamic limit ( $N, L \rightarrow \infty$  with  $N/L$  fixed) and in discussing thermodynamic quantities in which case the Bethe equations become integral equations and a powerful formalism to derive analytic and numeric results exists [23–25].

Note that while experimental realizations may no longer be validly described by the Lieb-Liniger or XXZ models at high energies, the accessibility of the full Hilbert space has many interesting theoretical consequences. High-energy properties can for example in principle be studied just as well as the physics of the ground state, opening up the way to the study of out-of-equilibrium and dynamic effects in an exact manner which are often out of reach for other theoretical methods. This will play an important role in this thesis.

Closer to the traditional questions of condensed matter physics is the use of a complete basis in the computation of correlation functions encoding observable quantities which can be probed by experiment. In experiments one often probes the system by an external source of for example photons, neutrons or electrons. The linear response is then governed by the Kubo formula and be expressed in terms of space and time dependent correlation function of the form  $C(x, t) = \langle \mathcal{O}^\dagger(x, t) \mathcal{O}(0, 0) \rangle$  or alternatively by its Fourier transform  $C(k, \epsilon)$  encoding the energy and momentum resolved signal. Here  $\mathcal{O}$  denotes some local operator which couples to the perturbing field, such as  $\mathcal{O} = \rho$  or  $\mathcal{O} = \Psi$ . Having access to the complete basis  $|\alpha\rangle$  allows in principle to compute such quantities, for example

by evaluating the Lehmann expansion

$$C(k, \epsilon) \propto \sum_{\alpha} |\langle \alpha | \mathcal{O} | 0 \rangle|^2 \delta(\epsilon - E_{\alpha} + E_0) \delta(k - P_{\alpha} + P_0). \quad (2.6)$$

Although formally an insightful way of representing correlations, practically the evaluation of Eq. (2.6) is highly nontrivial. In the case of XXZ and Lieb-Liniger, efficient determinant expressions for matrix elements combined with heuristics on the behavior of matrix elements of local operators are implemented in the ABACUS algorithm [26] in order to select a large but finite number of terms in the sum which nevertheless account for the correlation function to great accuracy. In this thesis, most of the time we will be concerned with effective field theory methods to compute correlations but these are often compared to results obtained with ABACUS or sometimes other numerical methods.

The depth and extent of Bethe ansatz related topics and techniques, and the theme of quantum integrability reach far beyond the limited scope of this thesis. The book [24] serves as a standard reference for what will be used here. Other textbooks for this material include [23, 27, 28].

## 2.2 Luttinger liquid theory

A common strategy in physics is to focus on the long wavelength and long time-scale properties of physical systems in order to capture the universal aspects which are often independent of more short-distance details. One-dimensional systems form a very interesting testing ground for this approach. On the one hand, such effective-field-theory methods are fantastically successful for one-dimensional systems. On the other hand, a naive implementation turns out to miss essential features when it comes to dynamics. Fortunately, the existing integrable models provide a platform that makes accurate tests of approximate techniques possible.

### 2.2.1 The Tomonaga-Luttinger Hamiltonian

In dimensions two and higher, an interacting Fermi gas can to first approximation be modelled as free fermions with renormalized parameters. This is roughly the content of Landau's Fermi liquid theory [29]. We understand now that the free fermion field theory is a fixed point of the renormalization group (RG) flow and repulsive interactions are an irrelevant perturbation.

For one-dimensional systems, it was Haldane [30, 31] who noted that it is rather the Tomonaga-Luttinger Hamiltonian [32, 33] than free fermions which plays the role of the appropriate fixed point model in this case. While interactions are inherent to this model it is still completely solvable by a mapping central to this thesis known as bosonization. In analogy with the higher dimensional case Haldane coined the term 'Luttinger liquid' and we will consider Luttinger liquid theory to mean describing the physics of some other physical system or model by using calculations and reasoning based on the Tomonaga-Luttinger model [see Eqs. (2.7), (2.11), (2.14)].

The Tomonaga-Luttinger (TL) model for spinless fermions is formulated in terms of two branches of chiral fermions

$$\begin{aligned}
 H_{TL} = v_F \int dx \{ & : \psi_R^\dagger (-i\partial_x) \psi_R : + : \psi_L^\dagger (i\partial_x) \psi_L : \} \\
 & + \int dx \{ (g_4/2) [\rho_R \rho_R + \rho_L \rho_L] + g_2 \rho_R \rho_L \} \quad (2.7)
 \end{aligned}$$

where the colons denote normal ordering with respect to a Dirac sea for the right and left moving fermions  $\psi_{R,L}$ , where  $\rho_{R,L} = : \psi_{R,L}^\dagger \psi_{R,L} :$  and  $v_F$  is the Fermi velocity.

The TL model is somewhat artificial. In the context of Luttinger liquid theory it should be considered an approximation to a more realistic model for which the fermion field  $\Psi_F$  is projected onto small sub-bands around the Fermi momenta  $\pm k_F$  according to

$$\Psi_F \sim e^{ik_F x} \psi_R + e^{-ik_F x} \psi_L. \quad (2.8)$$

The fields  $\psi_{R,L}$  thus capture the long wavelength properties corresponding to low-energy excitations on the ground state. The effective interaction parameters  $g_{2,4}$  can be perturbatively related to the Fourier components of an interaction potential  $V(|x-y|)$  as  $g_4 = V_0$ ,  $g_2 = V_{2k_F}$ , but beyond weak interactions these have no real physical meaning.

The crucial approximation made to arrive at Eq. (2.7) from a more general model is that of linear dispersion. This is expected to be a valid approximation as long as the physics is determined by excitations involving momenta very close to the Fermi points  $\pm k_F$ . In fact, only quantities determined by zero-momentum excitations in the thermodynamic limit are faithfully reproduced by the TL model. As we will see, this is true for static correlations and corresponds to certain terms of time-dependent correlations but not all. The identification of certain additional finite-momentum excitations contributing to time-dependent correlations will be part of nonlinear Luttinger liquid theory which will be discussed later on. We will discuss more on the relation of a microscopic model to the TL Hamiltonian in the next section.

Apart from assumptions on the dispersion, the TL model clearly also deals with a very specific ultra-local interaction. A momentum dependence of the interaction parameters  $g_{2,4} \rightarrow g_{2,4}(k)$  can be taken into account and still leads to a solvable model, but the long-distance behavior is the same when we identify  $g_{2,4} = g_{2,4}(k=0)$ .<sup>3</sup>

---

<sup>3</sup>One technical subtlety is that a suitable regularization procedure needs to be employed to take care of UV divergences which could also be taken care of by an appropriate momentum dependence. Studying out-of-equilibrium properties has been done for TL models with varying momentum dependence of the interaction [34,35] where it was used to argue in favor of universal behavior if a quantity did not depend on the specific choice of momentum dependence.

## 2. One-dimensional quantum fluids

---

In writing Eq. (2.7) we have left out the Umklapp interaction term

$$\delta H_\lambda = \lambda \int dx \left[ e^{-i4k_F x} : \psi_R^\dagger \psi_R^\dagger \psi_L \psi_L : + e^{i4k_F x} : \psi_L^\dagger \psi_L^\dagger \psi_R \psi_R : \right] \quad (2.9)$$

which may be generated for lattice systems but which is highly fluctuating unless we are at commensurate fillings  $4k_F = 4\pi\rho_0 = 0 \pmod{2\pi}$ . In case  $\delta H_\lambda$  becomes relevant (in the renormalization group sense) it is responsible for opening a gap. We will be mostly interested in the case where this does not happen and we can safely omit  $\delta H_\lambda$  from the effective Hamiltonian. We understand ‘one-dimensional quantum liquids’ as the collection of one-dimensional gapless systems, which can however consist of bosons, fermions or spins.

We have left out any spin degrees of freedom thus far. In case one wants to study physical electron systems or for example the Hubbard model

$$H_{Hu} = -\frac{t}{2} \sum_{j;\sigma} \left( c_{j\sigma}^\dagger c_{j+1\sigma} + c_{j+1\sigma}^\dagger c_{j\sigma} \right) + U \sum_j n_{j\uparrow} n_{j\downarrow} \quad (2.10)$$

by effective-field-theory methods, spin becomes obviously an important property. The spinful Tomonaga-Luttinger model is defined by the Hamiltonian

$$H_{TL}^{(s)} = \sum_{a;\sigma} s_a v_F : \psi_{a\sigma}^\dagger (-i\partial_x) \psi_{a\sigma} : + \frac{1}{2} \sum_{a\sigma; a'\sigma'} g_{a\sigma, a'\sigma'} \rho_{a\sigma} \rho_{a'\sigma'} \quad (2.11)$$

(with  $a = R, L$ ;  $s_{R,L} = \pm 1$ ;  $\sigma = \uparrow, \downarrow$ ) which is exactly solvable in terms of decoupled spin and charge models [under the assumption of spin symmetry ( $\uparrow \leftrightarrow \downarrow$ ) and the general inversion symmetry ( $R \leftrightarrow L, x \leftrightarrow -x$ )]. This property of spin-charge separation is expected to be general for the low-energy modes of generic models and persists at high energies for the Hubbard model [28]. The resulting spinon and holon Hamiltonians are of the Tomonaga-Luttinger form again, but the details of the interaction generically lead to different effective velocities of spinon and holon modes.

Most of our discussions will be based on the spinless model. As the spin and charge parts of the spinful model are separately described by a Tomonaga-Luttinger Hamiltonian as well, many results can easily be translated to the spinful case although care should be taken in details concerning the effective parameters.

### 2.2.2 Bosonization

Let us now outline the way to solve and derive consequences from the TL model (2.7). The crucial ingredient is the bosonization identities

$$\psi_{R,L} = \frac{\varkappa_{R,L}}{\sqrt{2\pi\eta}} e^{-i\sqrt{2\pi}\phi_{R,L}}, \quad \rho_{R,L} = \mp \frac{1}{\sqrt{2\pi}} \partial_x \phi_{R,L}. \quad (2.12)$$

Here,  $\varkappa_{R,L}$  are so-called Klein factors lowering the number of right/left movers leaving particle-hole excitations on the Dirac sea in tact,  $\eta$  is a small-distance

scale related to the regularization of the TL model and  $\phi_{R,L}$  are bosonic fields with the commutation relations

$$[\partial_x \phi_{R,L}(x), \phi_{R,L}(y)] = \pm i \delta(x-y), \quad [\phi_R(x), \phi_L(y)] = 0. \quad (2.13)$$

The equations in (2.12) can be derived in finite size as rigorous operator identities making use of the properties of the Dirac sea ground state of the free TL model  $g_{2,4} = 0$  but—importantly—not of the properties of the strictly linear dispersion [30, 36]. This is essential in justifying the inclusion of dispersion curvature in the bosonized model, which is important in going beyond the Luttinger liquid approximation. Bosonization dates back to the early days of quantum mechanics when Bloch [37] used that the similarity of the spectrum of one-dimensional fermions and a harmonic chain to study  $x$ -ray diffraction. See [38] for a nice historical introduction and additional references.

Solving for the eigenstates of Hamiltonian  $H_{TL}$  is straightforward making use of another consequence of bosonization,  $:\psi_{R,L}^\dagger(\mp i \partial_x) \psi_{R,L} := (1/2)(\partial_x \phi_{R,L})^2$ , which reveals that the interacting fermionic Hamiltonian  $H_{TL}$  is quadratic in terms of the bosonic fields and can be written as

$$H_{TL} = \frac{v}{2} \int dx \left[ \frac{1}{K} (\partial_x \phi)^2 + K (\partial_x \theta)^2 \right], \quad (2.14)$$

where we defined  $\theta, \phi = (\phi_L \pm \phi_R)/\sqrt{2}$  and

$$v = v_F \sqrt{(1 + g_4/(2\pi v_F))^2 - (g_2/(2\pi v_F))^2}, \quad K = \sqrt{\frac{2\pi v_F + g_4 - g_2}{2\pi v_F + g_4 + g_2}}. \quad (2.15)$$

Here  $v$  is the effective velocity of propagating density modes and  $K$  is related to the compressibility and is the single effective interaction parameter. For weak interactions  $K \approx 1 - (V_0 - V_{2k_F})/2\pi v_F$ .

It is useful to define the rescaled fields  $\vartheta, \varphi$  by  $\phi = \sqrt{K} \varphi$  and  $\theta = \vartheta/\sqrt{K}$  and correspondingly

$$\phi_{R,L} = \left( \frac{K^{-1/2} + K^{1/2}}{2} \right) \varphi_{R,L} + \left( \frac{K^{-1/2} - K^{1/2}}{2} \right) \varphi_{L,R}, \quad (2.16)$$

in terms of which the Hamiltonian  $H_{TL}$  in Eq. (2.14) is brought back to the form at the non-interacting point  $K = 1$ .

Correlation functions are then straightforward to compute using that

$$\left\langle e^{i\alpha\sqrt{2\pi}\phi_{R,L}(x,t)} e^{-i\alpha\sqrt{2\pi}\phi_{R,L}(0,0)} \right\rangle = \left[ \frac{\eta}{i(vt \pm x - i0)} \right]^{\alpha^2}. \quad (2.17)$$

The strategy in using the TL model to compute physical quantities is now to write the required correlation functions in terms of the chiral fermions  $\psi_{R,L}$  using a projection of the form in Eq. (2.8), applying the bosonization identities to write

## 2. One-dimensional quantum fluids

---

it in terms of the bosonic fields and then use Eqs. (2.16) and (2.17) to compute the result. The expectation is that this reproduces correct asymptotics  $x \rightarrow \infty$  of correlations, which are determined by the states close to the Fermi momentum. As an example, we state the results for density-density correlations function

$$\frac{\langle \rho(x)\rho(0) \rangle}{\rho_0^2} \sim 1 - \frac{K}{2(\pi\rho_0x)^2} + \frac{A_1 \cos(2k_F x)}{(\rho_0x)^{2K}} \quad (2.18)$$

based on the projection  $\rho(x) \sim \rho_0 - \partial_x \phi(x)/\sqrt{\pi} + \sqrt{A_1} \cos(2k_F x - \sqrt{\pi}\phi(x))$  and identifying  $\eta = \rho_0^{-1}$  as a natural short distance scale. Here,  $A_1$  is a non-universal prefactor dependent on the short-distance physics which does not follow from the bosonization identity but has to be fixed independently, for example from the finite-size scaling of certain matrix elements [39–41]. The similar result for the one-body density matrix is

$$\frac{\langle \Psi_F^\dagger(x)\Psi_F(0) \rangle}{\rho_0} \sim \frac{C_0 \sin(k_F x)}{(\rho_0x)^{K/2+1/(2K)}} \quad (2.19)$$

following from the projection in Eq. (2.8).

In principle, all ingredients for the calculation of physical correlations using the Luttinger liquid approach are outlined above, but let us make a few concluding remarks.

Consider again the projection of the fermionic operator in Eq. (2.8). In words this equation states that, in projecting a physical annihilation operator onto the low-energy subspace, we need only to keep the modes near  $\pm k_F$ . While these are indeed expected to lie in the low-energy subspace, some other low-energy configurations are not well-captured by retaining only the modes around  $\pm k_F$ , namely configurations obtained by adding so called ‘Umklapp excitations’ which correspond to taking particles from left to right Fermi point or *vice versa*. While in a free theory such states are never created by a single particle tunneling out of the system (which is how we interpret the application of the operator  $\Psi_F$ ), in an interacting theory such configurations can be important and one needs to do a more general projection of the Fermi operator which can be roughly thought of as  $\Psi_F|_{k \approx (2n+1)k_F} \sim e^{i(2n+1)k_F x} [\psi_L^\dagger \psi_R]^n \psi_R$  (for positive  $n$ ) or in bosonized form

$$\Psi_F|_{k \approx (2n+1)k_F} \sim e^{i(2n+1)k_F x} e^{i\sqrt{2\pi}[n\phi_L - (n+1)\phi_R]}. \quad (2.20)$$

The higher  $n$  components usually lead to subdominant contributions, but not always. See [31] and [9, 13] for further details.

Next, suppose we are interested in calculating correlations for a bosonic model rather than a fermionic model, such as for Lieb-Liniger. Then one uses a Jordan-Wigner string to map between bosonic and fermionic operators

$$\Psi_B(x) = \exp\left(-i\pi \int^x dy \rho(y)\right) \Psi_F(x) \quad (2.21)$$

and bosonization of the density operator  $\rho(x) = k_F/\pi + \partial_x \phi/\sqrt{\pi}$  in the exponent leading to  $\Psi_B \sim e^{-i\sqrt{\pi}\theta}$  (neglecting terms corresponding to momenta close to  $2nk_F$  similar to the additional Umklapp terms for fermions). This way, one bosonizes the bosonic operator after which the computation of correlations can proceed as in the fermionic case. The bosonization formula can equivalently be derived following Haldane's seminal harmonic fluid approach [31], expressing the bosonic field in a phase-density representation  $\Psi_B = \sqrt{\rho} \exp(-i\sqrt{\pi}\theta)$ .

Note that the Jordan-Wigner string leads to a vertex operator similar to the ones appearing in the bosonization. In general, string operators of the form

$$\exp\left(-i2\pi\alpha \int^x dy \rho_{R,L}(y)\right) = \exp\left(\pm i\alpha\sqrt{2\pi}\phi_{R,L}(x)\right). \quad (2.22)$$

will play an important role in dealing with the effective low-energy theory beyond the TL approximation.

Using above two remarks, one may compute the full scope of Luttinger liquid predictions for single-component bosons or fermions, like

$$\frac{\langle \Psi_F^\dagger(x) \Psi_F(0) \rangle}{\rho_0} \approx \sum_{m \geq 0} \frac{C_m \sin[(2m+1)k_F x]}{(\rho_0 x)^{(2m+1)^2 K/2 + 1/(2K)}}, \quad (2.23)$$

$$\frac{\langle \Psi_B^\dagger(x) \Psi_B(0) \rangle}{\rho_0} \approx \sum_{m \geq 0} \frac{B_m \cos[2mk_F x]}{(\rho_0 x)^{2m^2 K + 1/(2K)}}, \quad (2.24)$$

$$\frac{\langle \rho(x) \rho(0) \rangle}{\rho_0^2} \approx 1 - \frac{K}{2(\pi\rho_0)^2} + \sum_{k \geq 1} \frac{A_k \cos(2mk_F x)}{(\rho_0 x)^{2m^2 K}}. \quad (2.25)$$

One is of course not restricted to consider static correlations in the Tomonaga-Luttinger model. Inclusion of time dependence amounts to substituting  $x \rightarrow x \mp vt$  in the correlations for the free bosonic fields  $\varphi_{R,L}$  as is clear from Eq. (2.17). We note however that, while static correlations of physical models are accurately represented by Luttinger liquid theory, the situation for time-dependent correlations is more subtle (see Sec. 2.3).

## 2.3 Nonlinear Luttinger liquid theory

The past decade has seen some dramatic advances in understanding band curvature effects in one-dimensional quantum liquids. This section deals with a few of the techniques and insights that have evolved in treating this problem, which we will collectively call nonlinear Luttinger liquid theory. One of the key observations is that many physically interesting quantities are determined by the modes close to the Fermi points, adequately described by the Tomonaga-Luttinger Hamiltonian, interacting with a single high-energy particle or hole, with physics analogues to the X-ray edge singularity. This pertains to the late time and long distance asymptotes of correlations, which are directly related to the singular features in the momentum and energy domain of the corresponding

Fourier transform. The latter have most often been the focus of recent developments, in particular dynamic response functions such as the spectral function and dynamic structure factor. We will adopt this perspective in this section and consider the problem of computing features of these functions. The behavior of space and time dependent correlations can then be viewed as a corollary of these by taking the appropriate Fourier transforms in a saddle-point approximation.

### 2.3.1 Dynamic response functions

The probability of a particle to tunnel into or out of the system in a momentum and energy conserving tunneling event is encoded in the spectral function  $A(k, \epsilon)$ . It can be defined as

$$A(k, \epsilon) = -\frac{1}{\pi} \text{Im} G(k, \epsilon) \text{sgn } \epsilon \quad (2.26)$$

where  $G(k, \epsilon)$  is the time-ordered Green's function

$$G(k, \epsilon) = -i \int dt dx e^{i(\epsilon t - kx)} \langle T \Psi(x, t) \Psi^\dagger(0, 0) \rangle. \quad (2.27)$$

We will focus exclusively on the case of zero temperature for which the average  $\langle \dots \rangle$  is performed in the ground state (for finite temperatures one should average over the Gibbs ensemble). It is insightful to write down the Lehmann expansion in terms of a complete basis  $|\alpha\rangle$  with energies  $E_\alpha$ ,

$$A(k, \epsilon > 0) = \frac{1}{2\pi} \sum_{\alpha} |\langle \alpha | \Psi_k^\dagger | 0 \rangle|^2 \delta(\epsilon - E_\alpha + E_0), \quad (2.28)$$

$$A(k, \epsilon < 0) = \frac{1}{2\pi} \sum_{\alpha} |\langle \alpha | \Psi_k | 0 \rangle|^2 \delta(\epsilon + E_\alpha - E_0), \quad (2.29)$$

where  $|0\rangle$  denotes the ground state. For a free system, the ground state consists of a filled Fermi sea and only final states  $|\alpha\rangle$  of the form  $\Psi_k^\dagger|0\rangle$  for  $\epsilon > 0$  and  $\Psi_k|0\rangle$  for  $\epsilon < 0$  contribute leading to  $A(k, \epsilon) \propto \delta(\epsilon - \xi_k)$ . Hence the spectral function simply represents a  $\delta$  function peak corresponding to the dispersion of the model. This holds irrespective of dimension.

Let us now turn on interactions. In dimensions  $d > 1$ , interactions generically renormalize the mass shell  $\xi_k$  and broaden the  $\delta$  function. Close to the Fermi level the result is a Lorentzian of which the width (corresponding to the inverse lifetime  $\tau_k^{-1}$  of the quasiparticle excitation with momentum  $k$ ) vanishes as one approaches the Fermi level such that the lowest energy quasiparticles are infinitely long lived and a sharply peaked spectral function is recovered. This is one of the main features of Fermi liquid theory.

Calculations based on the Tomonaga-Luttinger model show that the 1d case is dramatically different. In the TL model, the spectral function in the vicinity of  $k_F$  is [42–46]

$$A(k, \epsilon) \propto \text{sgn } \epsilon \frac{\theta[\epsilon^2 - v(k - k_F)^2]}{\epsilon - v(k - k_F)} [\epsilon^2 - v^2(k - k_F)^2]^{(K+K^{-1}-2)/4}. \quad (2.30)$$

One finds sharp thresholds with one-sided power-law singularities at  $\epsilon = \pm v(k - k_F)$  related to the strictly linear dispersion.

The non-zero value of the spectral function outside of the line  $\epsilon = v(k - k_F)$  can be understood in perturbation theory by interpreting the spectral function as the tunneling probability and considering the processes which may be at play. In the presence of interactions a particle with energy  $\epsilon > v|k - k_F|$  may tunnel into the system by exciting an additional particle-hole pair in the branch of left movers in order to land on the right moving mass shell  $\epsilon = v(k - k_F)$ . Similarly, a particle with energy  $\epsilon < -v|k - k_F|$  can tunnel out of the system by creating a right moving hole and a left moving particle-hole pair. Hence, the tunneling of a single particle into or out of the system creates three excitations, a particle or hole on one branch and a particle-hole pair on the opposite branch.

This picture is easily extended to the case of non-linear dispersion for which the bare mass shell of right movers is given by  $\xi_k = v_F(k - k_F) + (k - k_F)^2/(2m)$ . The hole mass shell still determines the threshold of the spectral function as even in the presence of band curvature there is no way a single hole can give up energy by exciting additional particle-hole excitations. The properties of the  $\epsilon > 0$  domain on the other hand of the spectral function change drastically: the threshold is no longer given by the particle mass shell but rather by the inverted and transposed hole mass shell. The reason is that due to the dispersion non-linearity a particle with energy below the mass shell can give up both excess momentum and energy to an additional particle-hole pair landing on the mass shell but closer to the Fermi point. The lowest energy configuration for  $\epsilon > 0$  and  $k_F < k < 3k_F$  for example, consists of a single hole at momentum  $k_F - k$  and two particles at  $k_F$ . Similar reasoning allows to sketch the full domain of support of  $A(k, \epsilon)$  by tracing the lowest energy net particle or hole configuration as a function of momentum. It turns out that this always correspond to a single high-energy particle or hole accompanied by additional particles and holes residing at the Fermi points. One insight of nonlinear Luttinger liquid theory is that the identification of such configurations extends beyond weak interactions and this forms the basis of the new phenomenological theory based on the impurity model.

Next, let us consider the dynamic structure factor (DSF)  $S(q, \omega)$ , measuring the probability of exciting a density fluctuation with momentum  $q$  and energy  $\omega$ . The definition reads

$$S(q, \omega) = \int dx dt e^{i(\omega t - qx)} \langle \rho(x, t) \rho(0, 0) \rangle \quad (2.31)$$

or in terms of the Lehmann expansion

$$S(q, \omega) = \frac{1}{2\pi} \sum_{\alpha} |\langle \alpha | \rho_q^{\dagger} | 0 \rangle|^2 \delta(\omega - E_{\alpha} + E_0) \quad (2.32)$$

where  $\rho_q^{\dagger} = \sum_k \Psi_{k+q}^{\dagger} \Psi_k$ . For a free model, the support of  $S(q, \omega)$  for fixed  $q$  can easily be determined by considering the particle-hole excitations on the

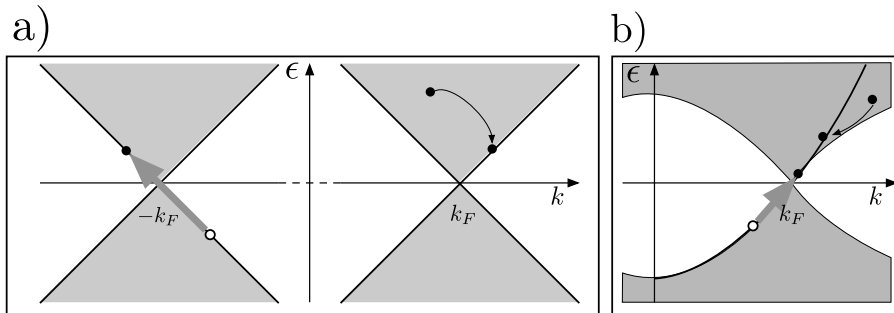


Figure 2.1: Illustration of the spectral function and the tunneling processes defining the domain of support. a) In the Tomonaga-Luttinger liquid the edges of support are determined by the strictly linear dispersion and coincide with the mass shell for both particles and holes. A particle with energy  $\epsilon$  and momentum  $k$  within the cone  $\epsilon > v|k - k_F|$  can tunnel into the system by exciting a particle-hole pair on the left moving branch. b) Nonlinear dispersion allows a particle with energy below the mass shell to tunnel onto the mass shell by exciting an additional particle-hole pair on the same branch. The domain of support for particles with momentum  $k_F < k < 3k_F$  corresponds to the transposed and inverted hole mass shell.

Fermi sea ground state. For  $0 < q < k_F$  the excitations that can be created by  $\rho_q^\dagger$  correspond to taking a single particle with momentum between  $k_F - q$  and  $k_F$  from the Fermi sea and putting it outside with momentum between  $k_F$  and  $k_F + q$ . The minimum and maximum of the domain of support  $\omega_\mp$  correspond to the extrema of the excitation energy. For a dispersion  $\xi_k$  without inflection points, such as for fermions in the continuum with quadratic dispersion relation

$$\xi_k = (k^2 - k_F^2)/2m, \quad (2.33)$$

the thresholds correspond to a deep hole with momentum  $k_F - q$  or a high-energy particle with momentum  $k_F + q$ . (Note that for example for lattice fermions, the situation can be slightly more complicated, and there is a type of folding back of the DSF.) In the case of free fermions with dispersion quadratic  $\xi_k$ , the DSF can be exactly computed as

$$S^{(0)}(q, \omega) = \frac{m}{q} \theta(q^2/2m - |\omega - v_F q|). \quad (2.34)$$

The width of the DSF,  $\delta\omega = q^2/m$ , can be interpreted as the inverse lifetime of density fluctuations. In the limit  $m \rightarrow \infty$  the width of the box shrinks while its height increases and one recovers the Luttinger liquid result,  $S(q, \omega) \propto q\delta(\omega - vq)$ , in line with the bosonization solution for which the eigenstates essentially

correspond to quantized density modes. Note that similarly in the  $q \rightarrow 0$  limit the box-shape reproduces the  $\delta$  function suggesting that the ‘collective’ density modes correspond to the ‘correct’ quasiparticle excitations in 1d similar to the ‘single-particle’ quasiparticles measured by the spectral function in Fermi liquid theory.

For the DSF, the edges of the domain of support are easily identified with certain configurations of particle-hole excitations, even in the noninteracting case. The upper threshold  $\omega_+$  corresponding to a high energy particle and a hole residing at the Fermi point, while the lower threshold  $\omega_-$  corresponds to a hole deep in the Fermi sea while the particle resides at the Fermi point. This suggests again to treat this problem in terms of a high-energy impurity interacting with the low-energy Luttinger liquid modes. We will see that this indeed transforms the step edges into power-law singularities and that for repulsive interactions the effective attraction between created particle and hole lead to a divergent singularity at the lower threshold  $\omega_-$  (see Fig. 2.2).

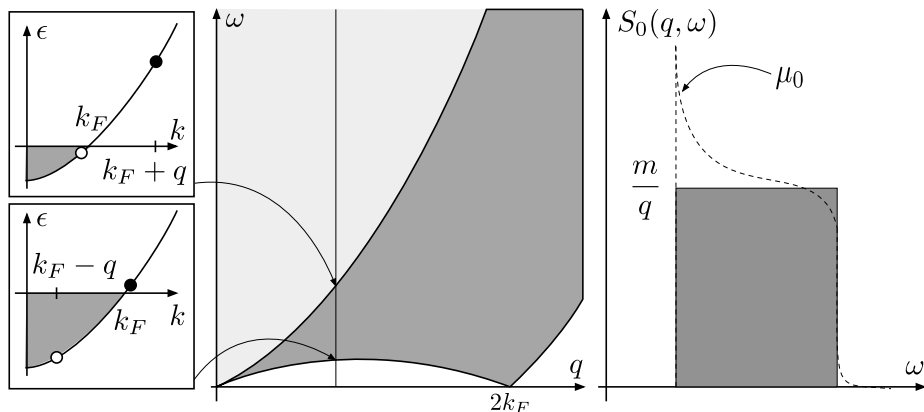


Figure 2.2: The DSF for free fermions. The nonzero value corresponds to the possibility to excite a particle-hole excitation with momentum  $q$ . The threshold configurations corresponding to the edges of the domain of support are a hole of momentum  $k_F - q$  and a particle with momentum  $k_F$  for the lower threshold  $\omega_-$  and a particle at  $k_F + k$  with a hole at  $k_F$  for the upper threshold  $\omega_+$ . Interactions will change the step edges into threshold singularities. The upper edge corresponds to the transition to the multi-particle hole continuum for which the DSF no longer needs to be zero. The lower threshold still represents a true edge of the domain of support.

### 2.3.2 The impurity model

We will now outline computations concerning threshold singularities of dynamic response functions using an effective impurity model. The model

$$H_{MIM} = H_{TL} + H_d + H_{\text{int}} \quad (2.35)$$

with

$$H_{TL} = \int dx \frac{v}{2} [(\partial_x \varphi_L)^2 + (\partial_x \varphi_R)^2] \quad (2.36)$$

$$H_d = \int dx d^\dagger (\varepsilon - iu\partial_x) d \quad (2.37)$$

$$H_{\text{int}} = \int dx \frac{1}{\sqrt{2\pi}} [\kappa_L \partial_x \varphi_L - \kappa_R \varphi_R] d^\dagger d \quad (2.38)$$

takes into account all marginal operators for a mobile impurity interacting with a Luttinger liquid for states with at most one impurity. One can argue in perturbation theory [13, 47] that

$$\kappa_{R,L} \approx V_{k \mp k_F} - V_0 \quad (2.39)$$

to first order in the interaction potential. Beyond weak interactions we should find other means to fix the parameters but the mobile impurity model can be promoted to a phenomenological theory for the thresholds of dynamic response functions.

The unitary operator

$$U = \exp \left\{ -i \int dx \frac{1}{\sqrt{2\pi}} [\gamma_L \varphi_L - \gamma_R \varphi_R] \right\} \quad (2.40)$$

decouples the low-energy modes from the impurity up to irrelevant operators [48, 49] if we identify

$$\frac{\gamma_{R,L}}{2\pi} = \frac{\kappa_{R,L}}{u \mp v}. \quad (2.41)$$

One way of seeing this is by computing rotated fields  $\bar{d}$ ,  $\bar{\varphi}_{R,L}$  with

$$\bar{d} = U^\dagger d U = e^{i\sqrt{1/2\pi}[\gamma_L \varphi_L - \gamma_R \varphi_R]} d \quad (2.42)$$

$$\partial_x \bar{\varphi}_{R,L} = U^\dagger \partial_x \varphi_{R,L} U = \partial_x \varphi_{R,L} - \sqrt{2\pi} \gamma_{R,L} d^\dagger d \quad (2.43)$$

and observing that

$$H_{MIM} = \frac{v}{2} \int dx [(\partial_x \bar{\varphi}_L)^2 + (\partial_x \bar{\varphi}_R)^2] + \int dx \bar{d}^\dagger (\varepsilon - iu\partial_x) \bar{d}. \quad (2.44)$$

Physically, the parameters  $\gamma_{R,L}$  correspond to the scattering phase shift between the high-energy impurity and the modes at the right and left Fermi momentum.

With the help of Eq. (2.44) the expression of correlations written in terms of the  $\bar{d}$  and  $\bar{\varphi}_{R,L}$  fields becomes straightforward. The computation of dynamic response functions in the vicinity of threshold singularities proceeds as follows:

1. Identify the threshold configuration of impurity and low-energy modes.
2. Project the physical operators, say  $\Psi$  or  $\rho$  accordingly onto low-energy and impurity sub-bands in terms of the operators  $\psi_{R,L}$  and  $d$ .
3. Use bosonization and the rotation by the unitary operator  $U$  to express the correlation in terms of  $\bar{d}$  and  $\bar{\varphi}_{R,L}$  and evaluate the expression.

As a concrete example, let us consider the DSF in the domain  $0 < q < 2k_F$  for fermions in the continuum. The lower threshold corresponds to a deep hole with momentum  $k = k_F - q$  and a particle at the right Fermi point  $k_F$ . In order to compute the DSF we project the density operator therefore as

$$\rho(x, t) \rightarrow e^{iqx} \psi_R(x, t) d^\dagger(x, t) + \text{h.c.} \quad (2.45)$$

where  $d^\dagger$  is the *annihilation* operator for the hole (note that with these conventions we have to identify  $\varepsilon = -\omega_-$ ). This leads us to express the DSF according to

$$S(q, \omega) \sim \int dx dt e^{i\omega t} \langle \psi_R(x, t) d^\dagger(x, t) d(0, 0) \psi_R^\dagger(0, 0) \rangle. \quad (2.46)$$

The correlator is then written in terms of free bosonic and impurity fields as a product, which after plugging in the Tomonaga-Luttinger correlator reads

$$\langle \bar{d}^\dagger(x, t) \bar{d}(0, 0) \rangle \left( \frac{i}{2\pi[x - vt]} \right)^{\left( \frac{\sqrt{K}}{2} + \frac{1}{\sqrt{K}} + \frac{\gamma_R}{2\pi} \right)^2} \left( \frac{-i}{2\pi[x + vt]} \right)^{\left( \frac{\sqrt{K}}{2} - \frac{1}{\sqrt{K}} + \frac{\gamma_R}{2\pi} \right)^2} \quad (2.47)$$

Using the impurity correlator  $\langle \bar{d}(x, t) d^\dagger(0, 0) \rangle = e^{i\epsilon t} \delta(x - ut)$  one finds result

$$S(q, \omega > \omega_-) \sim \left( \frac{\delta\omega}{\omega - \omega_-} \right)^{\mu_0} \quad (2.48)$$

with

$$\mu_0 = 1 - \left( \frac{\sqrt{K}}{2} + \frac{1}{\sqrt{K}} + \frac{\gamma_R}{2\pi} \right)^2 + \left( \frac{\sqrt{K}}{2} - \frac{1}{\sqrt{K}} + \frac{\gamma_R}{2\pi} \right)^2. \quad (2.49)$$

To first order in the interaction this gives  $\mu_0 = 1 - (1 + \gamma_R/2\pi)^2 - (\gamma_L/2\pi)^2 \approx \gamma_R/\pi \approx 2(V_q - V_0)m/|q|$ . In the general case the phase shifts  $\gamma_{R,L}$  should be considered phenomenological parameters to be fixed by independent means.

## 2. One-dimensional quantum fluids

---

As another example computation, consider the spectral function at the hole mass shell  $\xi_k$  for  $|k| < k_F$ . The corresponding impurity configuration consists of a single deep hole hence we project the fermionic operator as

$$\Psi(x, t) \rightarrow e^{ikx} d(x, t). \quad (2.50)$$

The resulting expression for the spectral function is

$$A(k, \epsilon) \sim \int dx dt e^{i\epsilon t} \langle d^\dagger(0, 0) d(x, t) \rangle \quad (2.51)$$

which evaluates to

$$A(k, \epsilon < \xi_k) \sim \left( \frac{\delta\epsilon}{\xi_k - \epsilon} \right)^{\mu_{0,-}}, \quad \mu_{0,-} = (\gamma_R/2\pi)^2 + (\gamma_L/2\pi)^2. \quad (2.52)$$

Note that the exponent is now quadratic in the phaseshifts and hence second order in the interaction.

The most tricky step in the calculation of the threshold exponents for other values of momenta is the correct identification of the corresponding impurity configuration and the projection of the physical operator,  $\rho(x, t)$  or  $\Psi(x, t)$ , accordingly. For lower threshold of the DSF at momentum  $q_n = 2nk_F + q$  for instance, the density operator should be projected as  $\rho \sim e^{-iq_n x} \psi_R^\dagger [\psi_R^\dagger \psi_L]^n d + \text{h.c.}$  for instance, while at the lower threshold for the spectral function at momentum  $k_n = 2nk_F + k$  one uses  $\Psi \rightarrow e^{ik_n x} [\psi_L^\dagger \psi_R] d$ .

## 2.4 Conclusion

We have given a short overview of some models and methods important for the theoretical study one-dimensional quantum liquids. Particular focus has been put on the existence of quantum integrable models characterized by non-diffractive scattering of excitations and effective-field-theory methods to compute static correlations (Luttinger liquid theory) as well as the singular properties of dynamic response functions (nonlinear Luttinger liquid theory). Even within these subjects, many important aspects have been left out. For example, fixing the parameters of the effective field theory models is an important step in comparing to experiment or numerics. We have also not discussed the representation of a low-energy effective field theory in terms of fermionic quasi-particles constructed by ‘reading the bosonization identity backwards’

$$\tilde{\psi}_{R,L} \sim e^{-i\sqrt{2\pi}\varphi_{R,L}}. \quad (2.53)$$

We hope however to have given a gist of the different approaches, knowing that excellent explanations exist in the literature, and to have provided enough of an introduction into the topic to frame the research described in continuation of this thesis.

# Boundary correlations in 1D

The end is nigh.

---

Man in Oxford Street

In this chapter we study the influence of reflective boundaries on time-dependent correlations of one-dimensional quantum fluids at zero temperature beyond the Luttinger liquid approximation. Our analysis is based on an extension of effective mobile impurity models for nonlinear Luttinger liquids to the case of open boundary conditions. This chapter is an edited version of Phys. Rev. B **93** 195129 (2016) [1].

## 3.1 Introduction

Striking properties in many-body quantum systems often emerge from the interplay between interactions and a constrained geometry. In a Fermi gas confined to a single spatial dimension, for example, interactions lead to dramatically different spectral properties as compared to its higher dimensional counterparts described by Fermi liquid theory [42–44, 50].

The low-energy limit of one-dimensional (1D) Fermi gases is conventionally treated within the Luttinger liquid (LL) framework [9]. Indispensable in this respect is the exactly solvable Tomonaga-Luttinger (TL) model [32, 51], which allows a nonperturbative treatment of interactions at the cost of an artificially linearized dispersion relation for the constituent fermions. Using the technique of bosonization, the model is solved in terms of bosonic collective modes corresponding to quantized waves of density.

Static correlations and many thermodynamic properties are captured remarkably well by the Luttinger liquid approach. For many dynamic effects, however, it is clear that band curvature needs to be taken into account. For example, the relaxation of the bosonic sound modes, or the related width of the dynamical structure factor (DSF), are not captured by Luttinger liquid theory, which predicts a delta function peak for the DSF. Attempts to treat the DSF broadening

### 3. Boundary correlations in 1D

---

in the bosonized theory, in which the dispersion curvature translates to interactions between the modes diagonalizing the TL model, are hindered by on-shell divergences in the perturbative expansion. Certain aspects of the DSF broadening can nevertheless be captured in the bosonic basis [52–56]. An alternative approach uses a reformulation of the TL model including a quadratic correction to the dispersion in terms of fermionic quasiparticles. In the low-energy limit, these turn out to be weakly interacting [47, 57, 58] restoring some of the elements of Fermi liquid theory in one dimension. At high energies, insight into dynamic response functions such as the DSF and the spectral function, and in particular into the characteristic threshold singularities, can be obtained by mapping the problem to a mobile impurity Hamiltonian. This approach hinges on the observation that the thresholds correspond to configurations of a high energy hole or particle which can effectively be considered as separated from the low energy subband, and that the threshold singularities emerge from the scattering of the modes at the Fermi level on this impurity mode. This identifies the anomalous correlation structure of 1D gases as an example of Anderson’s orthogonality catastrophe [59] and links it to the physics of the x-ray edge singularity [48]. Many new results on dynamic correlations, in general and for specific models, have been obtained this way [15, 47, 60–62, 62–70]. This bears relevance to e.g. Coulomb drag experiments [53, 71–75] as well as relaxation and transport [76–80]. Dispersion nonlinearity also greatly influences the propagation of a density bump or dip, which would retain its shape when time-evolved under the linear theory but relaxes by emitting shock waves in the nonlinear theory [81–83]. Closer to the present work is the late-time dependence of correlations [84–86] which are related to the singularities in the frequency domain. Collectively, the extensions of LL theory that include band curvature effects may be called nonlinear Luttinger liquid (nLL) theory, but we will mainly be concerned with the mobile impurity approach to correlations (see Ref. [13] for further details).

Motivated by these theoretical advances, we study the effect of reflective boundaries on a 1D gas beyond the low-energy regime. Our work is also inspired by studies of “boundary critical phenomena” [87–89] within the LL framework that have unveiled remarkable effects, e.g., in the conductance of quantum wires [90–92], screening of magnetic impurities [93], Friedel oscillations in charge and spin densities [94–96], and oscillations in the entanglement entropy [97, 98].

We focus on response functions which can be locally addressed—such as the local density of states (LDOS) and autocorrelation functions—as these are expected to show the clearest bulk versus boundary contrast. Many studies have addressed the LDOS for LLs with a boundary [99–108]. LL theory predicts a characteristic power-law suppression (for repulsive interactions) of the LDOS at the Fermi level with different bulk and boundary exponents which are nontrivially but universally related [109, 110]. This has been verified using different techniques [99, 100, 106, 111] and is used as a consistency check in the experimental identification of LL physics [112, 113].

Away from the Fermi level, no universal results are known. This pertains

both to general statements on the restricted energy range where the power-law scaling is valid [100,106] and to details of the line shape at higher energies. Here, we deal with the latter and argue that the nonanalyticities of, e.g., the LDOS away from zero energy can be understood in the framework of nLL theory for systems with open and periodic boundary conditions alike. The main application of our theory is in describing the power-law decay of autocorrelation functions in real time. We show that bulk and boundary exponents are governed by the same parameters in the mobile impurity model and obey relations that depend only on the Luttinger parameter. These relations provide a quantitative test of the nLL theory. We perform this test by analyzing time-dependent density matrix renormalization group (tDMRG) [114,115] results for spin autocorrelations of critical spin chains. The statement about boundary exponents applies to integrable models in which the nonanalytic behavior at finite energies is not susceptible to broadening due to three-body scattering processes [15,47]. The effects of integrability breaking are also investigated, both numerically and from the perspective of the mobile impurity model. We find that for nonintegrable models the finite-energy singularities in boundary autocorrelations are broadened by decay processes associated with boundary operators in the mobile impurity model. As a result, the boundary autocorrelation decays exponentially in time in the nonintegrable case.

The remainder of this chapter is organized as follows. In Section 3.2, we discuss the LDOS for spinless fermions as a first example of how dynamical correlations in the vicinity of an open boundary differ from the result in the bulk. In Section 3.3, we present the mobile impurity model used to calculate the exponents in the LDOS near the boundary. In Section 3.4, we generalize our approach to predict relations between bulk and boundary exponents of other dynamical correlation functions, including the case of spinful fermions. Section 3.5 addresses the question whether finite-energy singularities exist in nonintegrable models. Our numerical results for the time decay of spin autocorrelation functions are presented in Section 3.6. Finally, we offer some concluding remarks in Section 6.7.

## 3.2 Green's function for spinless fermions

We are interested in 1D systems on a half-line, where we impose the boundary condition that all physical operators vanish at  $x = 0$ . Let us first discuss the case of spinless fermions on a lattice. We define the (non-time-ordered) Green's function at position  $x$  as

$$G(t, x) = \langle \{\Psi(x, t), \Psi^\dagger(x, 0)\} \rangle, \quad (3.1)$$

where  $\Psi(x)$  annihilates a spinless fermion at position  $x$  and the time evolution  $\Psi(x, t) = e^{iHt}\Psi(x)e^{-iHt}$  is governed by a local Hamiltonian  $H$ . The brackets  $\langle \dots \rangle$  denote the expectation value in the ground state of  $H$ . The Fourier

### 3. Boundary correlations in 1D

---

transform to the frequency domain yields the LDOS

$$\rho(\omega, x) = \frac{1}{2\pi} \int_{-\infty}^{\infty} dt e^{i\omega t} G(t, x). \quad (3.2)$$

The boundary case corresponds to the result for  $x = a$ , where  $a$  is the lattice spacing for lattice models or the short-distance cutoff for continuum models. We refer to the bulk case of  $G(t, x)$  as the regime  $x \gg a$  and  $vt < x$ , where  $v$  is the velocity that sets the light cone for propagation of correlations in the many-body system [116]. The latter condition allows one to neglect the effects of reflection at the boundary, and is routinely employed in numerical simulations aimed at capturing the long-time behavior in the thermodynamic limit [15, 64, 86, 117].

As our point of departure, consider the free fermion model

$$\begin{aligned} H_0 &= -\frac{1}{2} \sum_{x \geq 1} [\Psi^\dagger(x) \Psi(x+1) + \text{h.c.}] \\ &= \sum_k \varepsilon_k \Psi_k^\dagger \Psi_k, \end{aligned} \quad (3.3)$$

where  $\varepsilon_k = -\cos k$ , with  $k \in (0, \pi)$ , is the free fermion dispersion and we set  $a = 1$ . The single-particle eigenstates of  $H_0$  are created by

$$\Psi_k^\dagger = \sqrt{\frac{2}{\pi}} \sum_{x \geq 1} \sin(kx) \Psi^\dagger(x). \quad (3.4)$$

We focus on the case of half filling, in which the ground state is constructed by occupying all states with  $0 < k < \pi/2$ . In this case particle-hole symmetry rules out Friedel oscillations [96] and the average density is homogeneous,  $\langle \Psi^\dagger(x) \Psi(x) \rangle = 1/2$ . The Green's function is given exactly by

$$G_0(t, x) = \frac{4}{\pi} \int_0^{\pi/2} dk \sin^2(kx) \cos(\varepsilon_k t), \quad (3.5)$$

and the LDOS is

$$\rho_0(\omega, x) = \frac{2 \sin^2[x \arccos(\omega/\epsilon_0)]}{\pi \sqrt{\epsilon_0^2 - \omega^2}} \theta(\epsilon_0 - |\omega|), \quad (3.6)$$

where  $\epsilon_0 \equiv |\varepsilon_{k=0}| = 1$ .

The result for  $G_0(t, x)$  is depicted in Fig. 3.1 (a). First we note that, for any fixed position  $x$ , there is a clear change of behavior at the time scale  $t \sim T_{\text{ref}}(x) = 2x/v$  (where  $v = 1$  for free fermions). This corresponds to the time for the light cone centered at  $x$  to reflect at the boundary and return to  $x$ . For  $t < T_{\text{ref}}(x)$ ,  $G_0(t, x)$  is independent of  $x$  (*i.e.* translationally invariant for fixed  $t$  and  $x > vt/2$ ) and the result is representative of the bulk autocorrelation. The

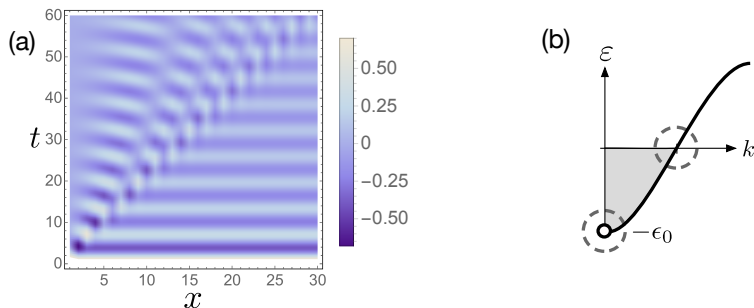


Figure 3.1: (a) Green's function  $G_0(t, x)$  for free fermions in a semi-infinite chain at half-filling [Eq. (3.5)], where  $x$  is the distance from the boundary. The dashed line represents the reflection time  $T_{\text{refl}}(x) = 2x/v$  with  $v = 1$ . (b) The deep hole configuration responsible for the oscillations at  $x = 0$  related to the singularities of the LDOS (Fig. 3.2). There is an equivalent high-energy particle configuration, not depicted. The dashed circles indicate the projection onto low-energy and impurity subbands important once interactions are taken into account.

arrival of the boundary-reflected correlations makes  $G_0(t, x)$  deviate from the bulk case and become  $x$ -dependent for  $t > T_{\text{refl}}(x)$ . After we take the Fourier transform to the frequency domain, the reflection time scale implies that the LDOS in Eq. (3.6) oscillates with period  $\Delta\omega(x) \sim 2\pi/T_{\text{refl}}(x) = \pi v/x$ . In the bulk case, the rapid oscillations in the frequency dependence of  $\rho_0(\omega, x \gg 1)$  are averaged out by any finite frequency resolution [108]. In numerical simulations of time evolution in the bulk, the usual procedure is to stop the simulation at  $t < x/v$  (or before in case the maximum time is limited by various sources of error [114, 115]). This avoids the reflection at the boundary but at the same time sets the finite frequency resolution.

Let us now discuss the time dependence of the Green's function at the boundary ( $x = 1$ ) versus in the bulk ( $x \gg 1, vt < x$ ). In both cases (see Fig. 3.2) the Green's function shows oscillations in the long-time decay which are not predicted by the usual low-energy approximation of linearizing the dispersion about  $k_F = \pi/2$  [9]. The explanation for the real-time oscillations is the same for open or periodic boundary conditions; for the case of periodic boundary conditions, see the reviews in Refs. [13, 84]. The oscillations stem from a saddle point contribution to the integral in Eq. (3.5) with  $k \approx 0$  [in the hole term of  $G_0(t, x)$ ] or  $k \approx \pi$  (in the particle term). This contribution is associated with an excitation with energy  $\epsilon_0$ , the maximum energy of a single-hole or single-particle excitation [see Fig. 3.1 (b)]. We call this energy the band edge of the free fermion dispersion. The propagator of the band edge mode decays more slowly in time due to its vanishing group velocity. The importance of this finite-energy

### 3. Boundary correlations in 1D

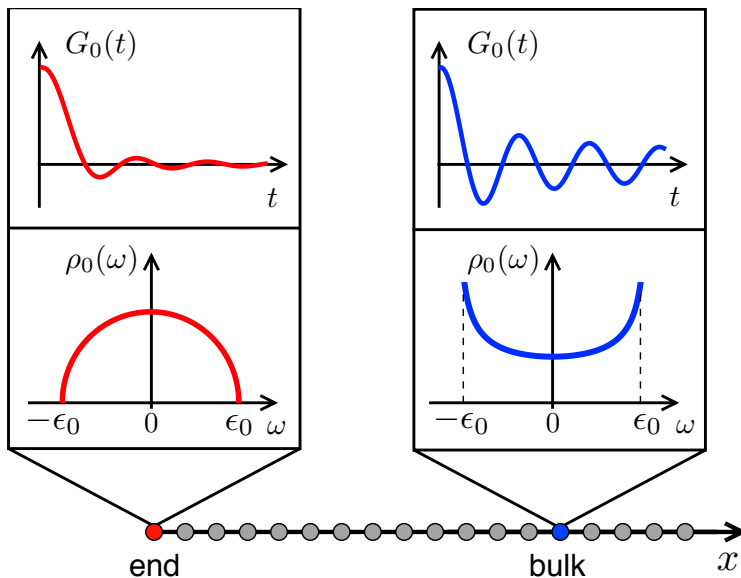


Figure 3.2: Noninteracting Green's function  $G_0(t, x)$  and LDOS  $\rho_0(\omega, x)$ . The curves on the left correspond to the chain end ( $x = 1$ ), and the curves on the right to a site in the bulk ( $x \gg 1$ ).

contribution is manifested in the LDOS as a power-law singularity at  $\omega = \pm\epsilon_0$  (see Fig. 3.2). Notice the clear difference between the bulk and the boundary case: while in the bulk the LDOS has a van Hove singularity at the band edge,  $\rho_0(\omega, x \gg 1) \sim |\omega \pm \epsilon_0|^{-1/2}$ , at the boundary one finds a square-root cusp  $\rho_0(\omega, x = 1) \sim |\omega \pm \epsilon_0|^{1/2}$ .

One of the main achievements of the nLL theory is to incorporate the contributions of finite-energy excitations in dynamical correlation functions for interacting 1D systems with band curvature [13, 84]. Our purpose here is to generalize this approach to describe the dynamics in the vicinity of a boundary. For concreteness, we consider the model

$$H = H_0 + V \sum_{x \geq 1} n(x)n(x+1), \quad (3.7)$$

where  $n(x) \equiv \Psi^\dagger(x)\Psi(x)$  in the density operator and we focus on the repulsive regime  $V > 0$ . Importantly, the model in Eq. (3.7) is integrable and exactly solvable by Bethe ansatz [24]. This guarantees that the band edge of elementary excitations is still well defined in the interacting case. We postpone a detailed discussion about integrability-breaking effects to Section 3.5.

Before outlining the derivation of the results for the interacting model (see Section 3.3), we summarize some known results together with our findings for

the Green's function and LDOS. The calculation within the LL framework leads to the well-known predictions [90, 109, 110]

$$G_{\text{LL}}(t, x) \sim 1/t^{\alpha+1}, \quad (3.8)$$

$$\rho(\omega \approx 0, x) \sim |\omega|^\alpha, \quad (3.9)$$

where the exponent  $\alpha$  is different for  $x$  in the bulk than at the boundary (subscript “end”):  $\alpha_{\text{bulk}} = (K + K^{-1})/2 - 1$  and  $\alpha_{\text{end}} = K^{-1} - 1$ , where  $K$  is the Luttinger parameter ( $K = 1$  for free fermions and  $K < 1$  for repulsive interactions). As mentioned above, the real-time oscillations are not predicted by LL theory. It is known that taking into account the finite-energy contributions within the nLL theory leads to the following contributions from the band-edge excitation in the bulk:

$$G_{\text{osc}}(t, x \gg 1) \sim e^{\pm i\epsilon t}/t^{\bar{\alpha}_{\text{bulk}}+1}, \quad (3.10)$$

$$\rho(\omega \approx \pm\epsilon, x \gg 1) \sim |\omega \mp \epsilon|^{\bar{\alpha}_{\text{bulk}}}, \quad (3.11)$$

where  $\epsilon$  is the renormalized band edge in the interacting system and the bulk exponent for the oscillating contribution is

$$\bar{\alpha}_{\text{bulk}} = -1/2 + \gamma^2/(2\pi^2 K), \quad (3.12)$$

with  $\gamma$  the phase shift of low-energy modes due to scattering off the high-energy hole [for free fermions,  $\gamma = 0$ ; the phase shift for the interacting model in Eq. (3.7) will be specified in Section 3.3].

Our new result is that the oscillating contribution at the boundary is given by

$$G_{\text{osc}}(t, x = 1) \sim e^{\pm i\epsilon t}/t^{\bar{\alpha}_{\text{end}}+1}, \quad (3.13)$$

$$\rho(\omega \approx \pm\epsilon, x = 1) \sim |\omega \mp \epsilon|^{\bar{\alpha}_{\text{end}}}, \quad (3.14)$$

with the same band-edge frequency  $\epsilon$  as in the bulk, but with a different exponent

$$\bar{\alpha}_{\text{end}} = 1/2 + \gamma^2/(\pi^2 K). \quad (3.15)$$

When the band-edge mode is the dominant finite-energy contribution to the Green's function, the asymptotic long-time decay of  $G(t, x)$  is well described by a linear combination of the Luttinger liquid term in Eq. (3.8) and the oscillating term in Eq. (3.10) or Eq. (3.13).

There are two noteworthy modifications in going from the bulk to the boundary: (i) an extra factor of  $1/t$  in the decay of  $G_{\text{osc}}(t, x)$ ; (ii) the doubling of the  $\mathcal{O}(\gamma^2)$  orthogonality catastrophe correction to the exponent [9, 59]. Both are recurrent in the exponents that will be discussed in Section 3.4. Furthermore, while both exponents vary with interactions, Eqs. (3.12) and (3.15) imply the relation

$$\bar{\alpha}_{\text{end}} - 2\bar{\alpha}_{\text{bulk}} = 3/2, \quad (3.16)$$

which is independent of the nonuniversal phase shift  $\gamma$ .

### 3.3 Mobile impurity model with open boundary

To derive the results above, we use the mode expansion that includes band-edge excitations

$$\Psi(x) \sim e^{ik_F x} \psi_R(x) + e^{-ik_F x} \psi_L(x) + d^\dagger(x), \quad (3.17)$$

where  $\psi_{R,L}$  denote the low-energy modes,  $d^\dagger$  creates a hole in the bottom of the band ( $k \approx 0$ ), and all fields on the right-hand side are slowly varying on the scale of the short-distance cutoff  $a$ .

A crucial assumption implicit in Eq. (3.17) is that we identify the excitations governing the long-time decay in the interacting model as being “adiabatically connected” with those in the noninteracting case, in the sense that they carry the same quantum numbers and their dispersion relations vary smoothly as a function of interaction strength. This condition can be verified explicitly for integrable models, where one computes exact dispersion relations for the elementary excitations. We should also note that for lattice models such as Eq. (3.7) the mode expansion must include a high-energy particle at the top of the band, with  $k \approx \pi$  [64]. In the particle-hole symmetric case the latter yields a contribution equivalent to that of the deep hole with  $k \approx 0$ , and we get the particle contribution in the LDOS simply by taking  $\omega \rightarrow -\omega$  in the result for the hole contribution. More generally, the high-energy spectrum of the interacting model may include other particles and bound states, which can also be incorporated in the mobile impurity model [15]; we shall address this question in Section 3.6.2.

In Eq. (3.17) we deliberately write the right and left movers separately, even though they are coupled by the boundary conditions [92, 93]. The condition  $\Psi(0) = 0$  is satisfied if we impose

$$\psi_L(0) = -\psi_R(0), \quad d(0) = 0. \quad (3.18)$$

These relations can be checked straightforwardly in the noninteracting case using the single-particle modes  $\Psi_k$ . The boundary condition on  $d(x)$  means that for any boundary operator that involves the high-energy mode we must take  $d(a) \sim a \partial_x d(0)$ .

We bosonize the low-energy modes with the conventions

$$\psi_{R,L} \sim e^{-i\sqrt{2\pi}\phi_{R,L}}, \quad (3.19)$$

$$\psi_{R,L}^\dagger \psi_{R,L} \sim \mp \frac{1}{\sqrt{2\pi}} \partial_x \phi_{R,L}, \quad (3.20)$$

where  $\phi_{R,L}(x)$  are chiral bosonic fields that obey

$$[\partial_x \phi_{R,L}(x), \phi_{R,L}(x')] = \pm i \delta(x - x'). \quad (3.21)$$

A convenient way to treat the boundary conditions for the low-energy modes is to use the folding trick [91, 92]: we include negative coordinates  $x < 0$  and

identify

$$\psi_L(x) \equiv -\psi_R(-x). \quad (3.22)$$

For the bosonic fields, we use

$$\phi_L(x) \equiv \phi_R(-x) + \sqrt{\pi/2}. \quad (3.23)$$

The effective Hamiltonian that describes the interaction between the band-edge mode and the low-energy modes is the mobile impurity model

$$\begin{aligned} H_{\text{MIM}} = & \int_{-\infty}^{\infty} dx \frac{v}{2} (\partial_x \varphi)^2 + \int_0^{\infty} dx d^\dagger \left( \epsilon + \frac{\partial_x^2}{2M} \right) d \\ & + \frac{v\gamma}{\sqrt{2\pi K}} \int_0^{\infty} dx d^\dagger d [\partial_x \varphi(x) + \partial_x \varphi(-x)]. \end{aligned} \quad (3.24)$$

Here  $\varphi(x)$  is the chiral boson that diagonalizes the Luttinger model on the unfolded line

$$\varphi(x) = \frac{K^{-\frac{1}{2}} + K^{\frac{1}{2}}}{2} \phi_R(x) + \frac{K^{-\frac{1}{2}} - K^{\frac{1}{2}}}{2} \phi_R(-x), \quad (3.25)$$

which obeys  $[\partial_x \varphi(x), \varphi(x')] = i \text{sgn}(x) \delta(x - x')$ . The parameters  $\epsilon$ ,  $-M$  and  $\gamma$  are nonuniversal properties of the hole with  $k = 0$  (which is treated as a mobile impurity): its finite energy cost, effective mass and dimensionless coupling to the low-energy modes, respectively. Note that the linear term in the dispersion vanishes for the band-edge mode, which is why we have to take into account the effective mass [see Fig. 3.1 (b)]. In models solvable by Bethe ansatz,  $\epsilon$  and  $\gamma$  are determined by the exact dispersion of single-hole excitations. The coupling  $\gamma$  can be obtained from the so-called shift function [65, 118] and the finite size spectrum [15] for periodic boundary conditions. In Galilean-invariant systems, we can relate  $\gamma$  to the exact spectrum by using phenomenological relations [66].

The Hamiltonian in Eq. (3.24) contains only marginal operators. It can be obtained from the mobile impurity model in the bulk [58] by applying the folding trick. Remarkably, all boundary operators that perturb this Hamiltonian and couple the  $d$  field to the bosonic modes are highly irrelevant, as they necessarily involve the derivative  $\partial_x d(0)$  (which by itself has scaling dimension  $3/2$ ). For the moment we neglect the effect of all formally irrelevant boundary operators, but return to this point in Section 3.5.

Like in the bulk case, we can decouple the impurity mode by the unitary transformation

$$U = \exp \left\{ i \frac{\gamma}{\sqrt{2\pi K}} \int_0^{\infty} dx [\varphi(x) + \varphi(-x)] d^\dagger d \right\}. \quad (3.26)$$

The fields transform as

$$\tilde{\varphi}(x) = U \varphi(x) U^\dagger = \varphi(x) + \frac{\gamma}{2\sqrt{2\pi K}} F_d(x), \quad (3.27)$$

$$\tilde{d}(x) = U d(x) U^\dagger = d(x) e^{-i \frac{\gamma}{\sqrt{2\pi K}} [\varphi(x) + \varphi(-x)]}, \quad (3.28)$$

### 3. Boundary correlations in 1D

---

where

$$F_d(x) = \int_0^\infty dy [\text{sgn}(x-y) + \text{sgn}(x+y)] d^\dagger(y) d(y). \quad (3.29)$$

Eq. (3.27) implies

$$\partial_x \tilde{\varphi}(x) = \partial_x \varphi(x) + \frac{\gamma}{\sqrt{2\pi K}} d^\dagger(x) d(x). \quad (3.30)$$

The Hamiltonian becomes noninteracting when written in terms of the transformed fields

$$H_{\text{MIM}} = \int_{-\infty}^{\infty} dx \frac{v}{2} (\partial_x \tilde{\varphi})^2 + \int_0^\infty dx \tilde{d}^\dagger \left( \epsilon + \frac{\partial_x^2}{2M} \right) \tilde{d}. \quad (3.31)$$

The crucial point is that the representation of the fermion field now contains a vertex operator:

$$\Psi(x) \sim d^\dagger(x) \sim \tilde{d}^\dagger(x) e^{-i\sqrt{2\pi\nu}\Theta(x)}, \quad (3.32)$$

where

$$\Theta(x) = \tilde{\varphi}(x) + \tilde{\varphi}(-x), \quad (3.33)$$

and

$$\nu = \gamma^2 / (4\pi^2 K). \quad (3.34)$$

After the unitary transformation, we can calculate correlations for the free fields using standard methods. The Green's function for the free  $\tilde{d}$  must be calculated with the proper mode expansion in terms of standing waves,  $\tilde{d}(x) = \sqrt{(2/\pi)} \int_0^{k_0} dk \sin(kx) \tilde{d}_k$ , where  $k_0 \ll a^{-1}$  is the momentum cutoff of the impurity sub-band. We obtain

$$\langle \tilde{d}(x, t) \tilde{d}^\dagger(x, 0) \rangle = e^{-i\epsilon t} \sqrt{\frac{-iM}{2\pi(t+i0)}} \left[ 1 - e^{i2Mx^2/(t+i0)} \right]. \quad (3.35)$$

In the bulk regime of Eq. (3.35), we neglect the rapidly oscillating factor  $\propto e^{i2Mx^2/t}$ ; in this case, the free impurity propagator decays as  $\sim t^{-1/2}$ . In the boundary case, we expand for  $x \sim a \ll \sqrt{t/M}$  and the free impurity propagator decays as  $\sim t^{-3/2}$ . This faster decay is due to the vanishing of the wave function at the boundary. It can also be understood by noting that at the boundary the impurity correlator can be calculated as

$$\langle \tilde{d}(a, t) \tilde{d}^\dagger(a, 0) \rangle \sim a^2 \langle \partial_x \tilde{d}(0, t) \partial_x \tilde{d}^\dagger(0, 0) \rangle, \quad (3.36)$$

### 3.3. Mobile impurity model with open boundary

and each spatial derivative amounts to an extra factor of  $t^{-1/2}$  due to the quadratic dispersion of the band-edge mode.

In addition to the free impurity propagator, we have to consider the correlator [92, 93, 109]

$$\langle e^{\pm i\sqrt{2\pi\nu}\Theta(x,t)} e^{\mp i\sqrt{2\pi\nu}\Theta(x,0)} \rangle \propto \left| \frac{x^2}{t^2(4x^2 - v^2t^2)} \right|^\nu. \quad (3.37)$$

Thus, in the bulk case ( $2x \gg vt$ ) the correlator for the the vertex operator adds a factor of  $\sim t^{-2\nu}$  to the decay of the Green's functions. In the boundary case, the factor is  $\sim t^{-4\nu}$ , a faster decay that stems from the correlation between  $\tilde{\varphi}(x)$  and  $\tilde{\varphi}(-x)$  for  $x \sim a$  (whereas these become uncorrelated right- and left-moving bosons in the bulk). Putting the effects together leads to

$$\begin{aligned} G_{\text{osc}}(t, a) &\sim \langle \tilde{d}(a, \pm t) \tilde{d}^\dagger(a, 0) \rangle \langle e^{i\sqrt{2\pi\nu}\Theta(a,t)} e^{-i\sqrt{2\pi\nu}\Theta(a,0)} \rangle \\ &\sim e^{\mp i\epsilon t} t^{-\frac{3}{2}-4\nu}, \end{aligned} \quad (3.38)$$

(where  $\pm$  corresponds to particle/hole impurity) which is the result in Eqs. (3.10) and (3.15).

The scaling dimension of the vertex operator  $e^{-i\sqrt{2\pi\nu}\Theta}$  can be related to a phase shift of the low-energy modes due to scattering with the  $d$  hole, establishing a connection with the orthogonality catastrophe [62]. For the integrable model in Eq. (3.7), the exact phase shift is a simple function of the Luttinger parameter [64]:

$$\gamma = \pi(1 - K), \quad (3.39)$$

where the exact Luttinger parameter is for  $0 \leq V \leq 1$

$$K = \frac{\pi}{2(\pi - \arccos V)}. \quad (3.40)$$

The renormalized band edge frequency is

$$\epsilon = \frac{\pi\sqrt{1 - V^2}}{2 \arccos V}. \quad (3.41)$$

The exact velocity of the low-energy modes and the effective mass of the impurity are also known:  $v = M^{-1} = \epsilon$  (in units where  $a = 1$ ).

In the free fermion limit, a particle tunneling into or out of the system is restricted to the free or occupied single-particle states. As is visible in Fig. 3.2 and Eq. (3.6) the LDOS is then identically zero outside of the bandwidth set by the dispersion relation. Turning on interactions allows for tunnelling processes in which the particle leaving or entering the system excites additional particle-hole pairs. This leads to a small but nonzero value for the LDOS beyond the threshold

### 3. Boundary correlations in 1D

---

energies. The effect can be included by carefully tracking the regulators in the Luttinger liquid correlator

$$\langle e^{i\sqrt{2\pi\nu}\varphi(x,t)} e^{-i\sqrt{2\pi\nu}\varphi(x,0)} \rangle \propto [i(vt - i0)]^{-\nu} \quad (3.42)$$

and the impurity correlator in Eq. (3.35). At the boundary and around the band-minimum, the LDOS can for instance be expressed as

$$\begin{aligned} \rho(\omega \approx -\epsilon, a) &\sim \int_{-\infty}^{\infty} dt \frac{e^{i(\omega+\epsilon)t}}{(vt + i0)^{4\nu}(t - i0)^{\frac{3}{2}}} \\ &\sim [\theta(\omega + \epsilon) - \sin(4\pi\nu)\theta(-\omega - \epsilon)]|\omega + \epsilon|^{\frac{1}{2}+4\nu}. \end{aligned} \quad (3.43)$$

We see that the shoulder ratio of the two-sided singularity is determined by an interplay of both the impurity and the low-energy propagators. This is similar, but slightly different than the two-sided singularities within the continuum of the spectral function and the dynamic structure factor [15] for which the shoulder ratio is determined by the exponents for right- and left-movers and the impurity propagator is just a delta function.

## 3.4 Other correlation functions

The mobile impurity model in Eq. (3.24) can be used to calculate the exponents in the long-time decay and finite-energy singularities of several dynamical correlation functions [13]. The general recipe for U(1)-symmetric models is to (i) identify the operator in the effective field theory that excites the band edge mode and carries the correct quantum numbers; (ii) write the operator in terms of free impurity and free bosons after the unitary transformation; and (iii) compute the correlator using the folding trick in the boundary case. In this section we apply this approach to calculate the exponents in the density autocorrelation of spinless fermions, spin autocorrelations of spin chains, and the single-particle Green's function of spinful fermions.

### 3.4.1 Density-density correlation

Let us now consider the density autocorrelation

$$C(t, x) \equiv \langle n(x, t)n(x, 0) \rangle. \quad (3.44)$$

Using the mode expansion in Eq. (3.17), we obtain the expression for the density operator including high-energy excitations

$$\begin{aligned} n(x) &= \Psi^\dagger(x)\Psi(x) \\ &\sim \psi_R^\dagger\psi_R + \psi_L^\dagger\psi_L + (e^{i2k_F x}\psi_L^\dagger\psi_R + \text{h.c.}) \\ &\quad + \left[ (e^{-ik_F x}\psi_R^\dagger + e^{ik_F x}\psi_L^\dagger)d^\dagger + \text{h.c.} \right], \end{aligned} \quad (3.45)$$

where  $k_F = \pi/(2a)$  for the half-filled chain in the model of Eq. (3.7) and we omitted operators that annihilate the ground state (a vacuum of  $d$  particles). In the boundary case,  $\psi_L$  and  $\psi_R$  are identified according to Eq. (3.22). The leading operator generated by the low-energy part of  $n(x)$  at the boundary is  $\sim \partial_x \varphi(0)$ , a dimension-one operator. As a result, the LL theory predicts the decay  $\langle n(a, t)n(a, 0) \rangle \sim 1/t^2$ . By contrast, in the bulk case the  $2k_F$  part of  $n(x)$  has dimension  $K$  and gives rise to  $\langle n(x \gg a, t)n(x \gg a, 0) \rangle \sim 1/t^{2K}$  as the leading contribution for repulsive interactions [9]. In summary, the low-energy term in the density autocorrelation is

$$C_{LL}(t, x) \sim t^{-\beta}, \quad (3.46)$$

with exponents

$$\beta_{\text{end}} = 2, \quad \beta_{\text{bulk}} = 2K. \quad (3.47)$$

On the other hand, the high-energy term in the mode expansion for the density at the boundary yields

$$\begin{aligned} n(a) &\sim d^\dagger(a) [e^{-ik_F a} \psi_R^\dagger(a) - e^{ik_F a} \psi_R^\dagger(-a)] + \text{h.c.} \\ &\sim \sin(k_F a) d^\dagger(a) \psi_R^\dagger(a) + \text{h.c.} \end{aligned} \quad (3.48)$$

After bosonizing and performing the unitary transformation, we find that the high-energy term is given by

$$\begin{aligned} n(a) &\sim \tilde{d}^\dagger(a) \exp \left[ i \sqrt{\frac{\pi}{2}} \left( \frac{1 - \gamma/\pi}{\sqrt{K}} + \sqrt{K} \right) \varphi(a) \right] \times \\ &\quad \times \exp \left[ i \sqrt{\frac{\pi}{2}} \left( \frac{1 - \gamma/\pi}{\sqrt{K}} - \sqrt{K} \right) \varphi(-a) \right] + \text{h.c.} \\ &\sim a \partial_x \tilde{d}^\dagger(0) \exp \left[ i \sqrt{2\pi} \left( \frac{1 - \gamma/\pi}{\sqrt{K}} \right) \varphi(0) \right] + \text{h.c.}, \end{aligned} \quad (3.49)$$

where we kept the leading operator in the expansion of the slowly-varying fields. From Eq. (3.49) it is straightforward to show that the autocorrelation function contains a term oscillating with the frequency of the high-energy hole:

$$C_{\text{osc}}(t, x) \sim e^{-i\epsilon t} t^{-\bar{\beta}}, \quad (3.50)$$

with the boundary exponent

$$\bar{\beta}_{\text{end}} = \frac{3}{2} + \frac{(1 - \gamma/\pi)^2}{K}. \quad (3.51)$$

This should be compared with the corresponding exponent in the bulk case [64]

$$\bar{\beta}_{\text{bulk}} = \frac{1 + K}{2} + \frac{(1 - \gamma/\pi)^2}{2K}. \quad (3.52)$$

### 3. Boundary correlations in 1D

---

Therefore, the exponents associated with the frequency- $\epsilon$  oscillating term in the density autocorrelation obey the relation

$$2\bar{\beta}_{\text{bulk}} - \bar{\beta}_{\text{end}} = K - \frac{1}{2}. \quad (3.53)$$

As mentioned in Section 3.3, in lattice models we also have to consider the band-edge mode corresponding to a particle at the top of the band. In this case the density operator contains an additional term that creates two high-energy modes, namely a hole at  $k = 0$  and a particle at  $k = \pi$ . In the noninteracting bulk case of Hamiltonian (3.3), this term yields a contribution that behaves as  $\sim e^{-i2\epsilon_0 t}/t$ , where the slow  $1/t$  decay stems from the propagators of the high-energy particle and hole. However, in the presence of a repulsive interaction  $V > 0$  the decay of this contribution changes to  $\sim e^{-i2\epsilon t}/t^2$  and decays faster than the frequency- $\epsilon$  term for  $t \gg 1/(Ma^2V^2)$  [64]. In the boundary case the equivalent contribution is subdominant even in the noninteracting case, where it becomes  $\sim e^{-i2\epsilon_0 t}/t^3$  due to the faster  $t^{-3/2}$  decay of the free impurity propagator at the boundary. Therefore, the long-time decay of the density autocorrelation  $C(t, x = a)$  is well described by a combination of the LL term in Eq. (3.46) and the frequency- $\epsilon$  term in Eq. (3.50).

For the integrable model in Eq. (3.7), we can calculate the exponents  $\bar{\beta}_{\text{bulk/end}}$  using Eqs. (3.39) and (3.40). We also note that the power-law decay of  $C_{\text{osc}}(t, x)$  implies a finite-energy nonanalyticity in the Fourier transform

$$C(\omega, x) \sim |\omega - \epsilon|^{\bar{\beta}-1}. \quad (3.54)$$

#### 3.4.2 Spin autocorrelations

As an application of our theory to spin chains, we consider the spin-1/2 XXZ model with an open boundary

$$H_{\text{XXZ}} = \sum_{j \geq 1} \left[ \frac{1}{2} (S_j^+ S_{j+1}^- + \text{h.c.}) + \Delta S_j^z S_{j+1}^z \right], \quad (3.55)$$

where  $\mathbf{S}_j$  is the spin operator on site  $j$  and  $\Delta$  is the anisotropy parameter. We are interested in the long-time decay of the longitudinal ( $\parallel$ ) and transverse ( $\perp$ ) spin autocorrelations

$$C^{\parallel}(t, j) \equiv \langle S_j^z(t) S_j^z(0) \rangle, \quad (3.56)$$

$$C^{\perp}(t, j) \equiv \langle S_j^+(t) S_j^-(0) \rangle. \quad (3.57)$$

We focus on the critical regime  $0 \leq \Delta \leq 1$ . Via a Jordan-Wigner transformation [9]

$$S_j^z = \Psi^\dagger(j) \Psi(j) - \frac{1}{2}, \quad (3.58)$$

$$S_j^- = (-1)^j \Psi(j) e^{i\pi \sum_{l < j} \Psi^\dagger(l) \Psi(l)}, \quad (3.59)$$

the XXZ model is equivalent to the spinless fermion model in Eq. (3.7) with interaction strength  $V = \Delta$ . Thus, for  $\Delta = 0$  (the XX chain) the model is equivalent to free fermions and some time-dependent correlations can be calculated exactly [119,120]. For  $0 < \Delta \leq 1$  the LL approach predicts the asymptotic decay of nonoscillating terms in the spin autocorrelations [93]:

$$C_{\text{LL}}^{\parallel}(t, j) \sim t^{-\beta^{\parallel}}, \quad C_{\text{LL}}^{\perp}(t, j) \sim t^{-\beta^{\perp}}, \quad (3.60)$$

with exponents

$$\beta_{\text{end}}^{\parallel} = 2, \quad \beta_{\text{bulk}}^{\parallel} = 2K, \quad (3.61)$$

$$\beta_{\text{end}}^{\perp} = \frac{1}{K}, \quad \beta_{\text{bulk}}^{\perp} = \frac{1}{2K}, \quad (3.62)$$

where the exact Luttinger parameter is given by Eq. (3.40) with  $V = \Delta$ . Notice that the exponents for transverse and longitudinal autocorrelations coincide at the SU(2) point  $\Delta = 1$ , where  $K = 1/2$ .

The high-energy contributions to the spin operator can be obtained starting from Eqs. (3.58) and (3.59) and employing the mode expansion for the fermionic field in Eq. (3.17) [13]. In the bulk case, we find

$$S_{j=x}^z \sim \tilde{d}^{\dagger}(x) \exp \left[ i\sqrt{\frac{\pi}{2}} \left( \frac{1+K-\gamma/\pi}{\sqrt{K}} \right) \varphi(x) \right] \quad (3.63)$$

$$\times \exp \left[ i\sqrt{\frac{\pi}{2}} \left( \frac{1-K-\gamma/\pi}{\sqrt{K}} \right) \varphi(-x) \right] + \text{h.c.},$$

$$S_{j=x}^- \sim \tilde{d}^{\dagger}(x) \exp \left[ -i\sqrt{\frac{\pi}{2}} \left( \frac{K+\gamma/\pi}{\sqrt{K}} \right) \varphi(x) \right]$$

$$\times \exp \left[ i\sqrt{\frac{\pi}{2}} \left( \frac{K-\gamma/\pi}{\sqrt{K}} \right) \varphi(-x) \right]. \quad (3.64)$$

At the boundary, we obtain

$$S_1^z \sim \partial_x \tilde{d}^{\dagger}(0) \exp \left[ -i\sqrt{2\pi} \left( \frac{1-\gamma/\pi}{\sqrt{K}} \right) \varphi(0) \right] + \text{h.c.}, \quad (3.65)$$

$$S_1^- \sim \partial_x \tilde{d}^{\dagger}(0) \exp \left[ -i\sqrt{2\pi} \left( \frac{\gamma}{\pi\sqrt{K}} \right) \varphi(0) \right]. \quad (3.66)$$

Calculating the correlators along the same lines as the previous examples, we obtain the oscillating terms in the autocorrelations

$$C_{\text{osc}}^{\parallel}(t, j) \sim e^{-i\epsilon t} t^{-\bar{\beta}^{\parallel}}, \quad (3.67)$$

$$C_{\text{osc}}^{\perp}(t, j) \sim e^{-i\epsilon t} t^{-\bar{\beta}^{\perp}}, \quad (3.68)$$

### 3. Boundary correlations in 1D

---

where

$$\bar{\beta}_{\text{end}}^{\parallel} = \frac{3}{2} + \frac{(1 - \gamma/\pi)^2}{K}, \quad (3.69)$$

$$\bar{\beta}_{\text{end}}^{\perp} = \frac{3}{2} + \frac{(\gamma/\pi)^2}{K}. \quad (3.70)$$

We also present, for comparison, the previously known exponents in the bulk [64, 121]:

$$\bar{\beta}_{\text{bulk}}^{\parallel} = \frac{1 + K}{2} + \frac{(1 - \gamma/\pi)^2}{2K}, \quad (3.71)$$

$$\bar{\beta}_{\text{bulk}}^{\perp} = \frac{1 + K}{2} + \frac{(\gamma/\pi)^2}{2K}. \quad (3.72)$$

The results for the longitudinal spin autocorrelation are the same as those for the density autocorrelation derived in Section 3.4.1, as expected from the mapping in Eq. (3.58). The bulk and boundary exponents for the spin autocorrelations obey a relation equivalent to Eq. (3.53)

$$2\bar{\beta}_{\text{bulk}}^{\perp/\parallel} - \bar{\beta}_{\text{end}}^{\perp/\parallel} = K - \frac{1}{2}, \quad (3.73)$$

which is independent of  $\gamma$ .

For the XXZ model we can simplify the result for the exponents using the exact phase shift in Eq. (3.39). The bulk exponents become

$$\bar{\beta}_{\text{bulk}}^{\parallel} = K + \frac{1}{2}, \quad (3.74)$$

$$\bar{\beta}_{\text{bulk}}^{\perp} = K + \frac{1}{2K} - \frac{1}{2}. \quad (3.75)$$

Our new results for the boundary exponents are

$$\bar{\beta}_{\text{end}}^{\parallel} = K + \frac{3}{2}, \quad (3.76)$$

$$\bar{\beta}_{\text{end}}^{\perp} = K + \frac{1}{K} - \frac{1}{2}. \quad (3.77)$$

#### 3.4.3 Green's function for spinful fermions

We now consider interacting spin-1/2 fermions, as described by the Hubbard model

$$H = - \sum_{x \geq 1} \sum_{\sigma = \uparrow, \downarrow} [\Psi_{\sigma}^{\dagger}(x) \Psi_{\sigma}(x+1) + \text{h.c.}] + U \sum_{x \geq 1} n_{\uparrow}(x) n_{\downarrow}(x), \quad (3.78)$$

where  $U > 0$  is the repulsive on-site interaction. Away from half-filling and in the absence of an external magnetic field, the low-energy spectrum is described by two bosonic fields corresponding to decoupled charge and spin collective modes. Our purpose here is to illustrate the effects of spin-charge separation on finite-energy contributions to time-dependent correlation functions. We focus on the single-particle Green's function

$$G_{\uparrow}(t, x) = \langle \{\Psi_{\uparrow}(x, t), \Psi_{\uparrow}^{\dagger}(x, 0)\} \rangle. \quad (3.79)$$

In the case of spinful fermions, singular features of dynamic correlations can in principle come from both spinon and holon impurities interacting with the low-energy modes [68, 69, 122]. For repulsive interactions, the spin velocity is smaller than the charge velocity [9], so the lower threshold of the spinon-holon continuum is expected to correspond to a finite-energy spinon impurity rather than a holon. Here we focus on the contribution from a single high-energy spinon to the Green's function and to the LDOS. It is implicitly assumed that the fermion-fermion interactions are strong enough that there is a sizeable separation between the spinon band edge and the holon band edge. Otherwise, weak interactions would imply a small energy scale for spin-charge separation, making it difficult to resolve the two contributions in real time or in the frequency domain.

We follow the construction in Ref. [122] to define the operators that create finite-energy spinons coupled to low-energy charge and spin bosons, maintaining the correct quantum numbers. Starting from bosonization expressions like

$$\psi_{R,\sigma} \sim e^{-i\sqrt{2\pi}\phi_{R\sigma}}, \quad (3.80)$$

we go to a spin and charge separated basis. The physical field is expanded in right and left movers and written in terms of charge and spin degrees of freedom. We will only need the right moving component for which the spinon part is projected onto the impurity operator. This leads to the projection

$$\Psi_{\uparrow} \sim d_s^{\dagger} e^{-i\sqrt{\pi}(\frac{1}{2}\Phi_s^* - \frac{1}{2}\Phi_c^* + \Theta_c^*)}. \quad (3.81)$$

Here  $\Phi_{\nu}^*$  and  $\Theta_{\nu}^*$ , with  $\nu = c, s$  for charge or spin, respectively, are the conjugate bosonic fields that diagonalize the Hamiltonian at the Luther-Emery point where spin and charge modes are exactly separated. The bosonic fields satisfy  $[\partial_x \Phi_{\nu}^*(x), \Theta_{\nu'}^*(x')] = i\delta_{\nu\nu'}\delta(x - x')$ .

The impurity model is

$$\begin{aligned} H_{\text{MIM}} = & \int_0^{\infty} dx \sum_{\nu=c,s} \frac{v_{\nu}}{2} \left[ \frac{1}{2K_{\nu}} (\partial_x \Phi_{\nu}^*)^2 + 2K_{\nu} (\partial_x \Theta_{\nu}^*)^2 \right] \\ & + \int_0^{\infty} dx d_s^{\dagger} \left( \epsilon_s + \frac{\partial_x^2}{2M_s} \right) d_s \\ & + \int_0^{\infty} dx \sum_{\nu} \frac{vf_{\nu}}{\sqrt{\pi}} d_s^{\dagger} d_s \partial_x \Phi_{\nu}^*, \end{aligned} \quad (3.82)$$

### 3. Boundary correlations in 1D

where  $v_{c,s}$  are the charge and spin velocities, respectively,  $K_{c,s}$  are the Luttinger parameters,  $\epsilon_s$  and  $-M_s$  are the energy and effective mass of the high-energy spinon, and  $f_{c,s}$  are impurity-boson coupling constants. At the Luther-Emery point with free holons and spinons [122], we have  $K_c = K_s = 1/2$  and  $f_c = f_s = 0$ . In contrast, SU(2)-symmetric models correspond to strongly interacting spinons.

We decouple the impurity mode by the unitary transformation

$$U = \exp \left\{ -i \sum_{\nu} \frac{K_{\nu} f_{\nu}}{v_{\nu} \sqrt{\pi}} \int_0^{\infty} dx d_s^{\dagger} d_s \Theta_{\nu}^* \right\}. \quad (3.83)$$

We then implement the boundary conditions by the folding trick and diagonalize the low-energy part of the Hamiltonian by a canonical transformation. We define

$$\gamma_{\nu} = \frac{K_{\nu} f_{\nu}}{v_{\nu}}. \quad (3.84)$$

The final expression for the projection of the spinful fermion field operator is

$$\begin{aligned} \Psi_{\uparrow}(x) \sim & \tilde{d}_s^{\dagger}(x) \exp \left\{ \left( -\frac{\sqrt{2K_s}}{4} + \frac{\gamma_s}{\pi\sqrt{2K_s}} \right) \varphi_s(x) \right. \\ & + \left( \frac{\sqrt{2K_s}}{4} + \frac{\gamma_s}{\pi\sqrt{2K_s}} \right) \varphi_s(-x) \\ & + \left( \frac{1}{2\sqrt{2K_c}} + \frac{\sqrt{2K_c}}{4} + \frac{\gamma_c}{\pi\sqrt{2K_c}} \right) \varphi_c(x) \\ & \left. + \left( \frac{1}{2\sqrt{2K_c}} - \frac{\sqrt{2K_c}}{4} + \frac{\gamma_c}{\pi\sqrt{2K_c}} \right) \varphi_c(-x) \right\}. \end{aligned} \quad (3.85)$$

Here  $\varphi_{c,s}(x)$  represent the free low-energy charge and spin modes after decoupling of the impurity and  $\tilde{d}_s^{\dagger}$  creates the decoupled spinon mode.

The exponents for the corresponding oscillating contribution of  $G_{\uparrow}(t, x)$  are easily read off from Eq. (3.85). Let us restrict ourselves to the SU(2) invariant case appropriate for the Hubbard model at zero magnetic field. In this case  $K_s = 1$  and  $\gamma_s = -\pi/2$ . We obtain

$$G(t, x) \sim e^{-i\epsilon_s t - \nu^{(s)} t}, \quad (3.86)$$

with

$$\nu_{\text{bulk}}^{(s)} = 1 + \frac{K_c}{4} + \frac{1}{4K_c} \left( 1 + \frac{2\gamma_c}{\pi} \right)^2, \quad (3.87)$$

$$\nu_{\text{end}}^{(s)} = 2 + \frac{1}{2K_c} \left( 1 + \frac{2\gamma_c}{\pi} \right)^2. \quad (3.88)$$

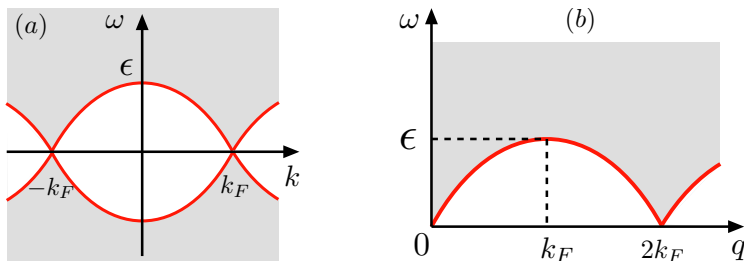


Figure 3.3: (a) Support of the single-fermion spectral function  $A(k, \omega)$  for a generic 1D model of interacting fermions with Fermi momentum  $k_F$ . The solid red line represents the lower threshold  $\omega_-(k)$ , below which  $A(k, \omega)$  vanishes. The band edge frequency can be identified as  $\epsilon = \omega_-(k = 0)$ . (b) Support of the dynamical structure factor  $S(q, \omega)$ .

The singular behavior of the LDOS is obtained by Fourier transformation as before. We also obtain the relation

$$2\nu_{\text{bulk}}^{(s)} - \nu_{\text{end}}^{(s)} = \frac{K_c}{2}, \quad (3.89)$$

which is independent of  $\gamma_c$ . It would be interesting to test this prediction numerically and investigate the relative importance of the spinon and holon impurity configuration for the autocorrelation and LDOS of the Hubbard model.

### 3.5 Role of integrability

Our results predict the exponents of autocorrelation functions at the boundary of critical one-dimensional systems *assuming* that the long-time decay is described by a power law. By Fourier transform, the same theory predicts the exponent of the nonanalyticity at the finite energy  $\omega = \epsilon$  in the frequency domain. We expect this to hold for integrable models, where one can calculate a well-defined band-edge frequency from the renormalized dispersion relation (or dressed energy) for the elementary excitations. Examples of integrable models with open boundary conditions include the open XXZ chain [123, 124] in Eq. (3.55) [or, equivalently, its fermionic version in Eq. (3.7)] and the Hubbard model [125] in Eq. (3.78), on which many of the previous studies of local spectral properties are based.

In generic, nonintegrable models, the persistence of a nonanalyticity inside a multiparticle continuum is questionable. It has been argued that a finite-energy singularity can be protected in 1D systems by conservation of quantum numbers in high-energy bands [49]. However, the high-energy subband in our effective mobile impurity model is defined by a projection of the band edge modes, which carry the same quantum numbers as the low-energy modes. Thus, strictly speaking there is no conservation law associated with the number of  $d$  particles.

### 3. Boundary correlations in 1D

---

Nonetheless, we can argue that the band edge is still well defined for bulk correlations in a semi-infinite system. In the bulk one can measure momentum-resolved response functions, for instance the spectral function

$$A(k, \omega) = \frac{1}{2\pi} \int_{-\infty}^{\infty} dt e^{i\omega t} \sum_y e^{-iky} \times \langle \{\Psi(x+y, t), \Psi^\dagger(x, 0)\} \rangle, \quad (3.90)$$

or the dynamical structure factor

$$S(q, \omega) = \frac{1}{2\pi} \int_{-\infty}^{\infty} dt \sum_y e^{-iqy} \langle n(x+y, t)n(x) \rangle. \quad (3.91)$$

In momentum-resolved dynamical correlations, the spectral weight vanishes identically below a lower threshold [13] [see Fig. 3.3(a)]. This threshold is defined by kinematic constraints and exists even for nonintegrable models. The mobile impurity model in the bulk then predicts a power-law singularity as the frequency approaches the threshold from above. For instance, for the positive-frequency part of the spectral function [15]:

$$A(k, \omega) \sim [\omega - \omega_-(k)]^{-1+2\nu}, \quad (3.92)$$

with  $\nu$  defined in Eq. (3.34). The band edge frequency that governs the oscillations in local correlations can be identified from the spectrum as a local maximum in the lower threshold, about which the threshold is approximately parabolic. For the spectral function this happens for  $k \approx 0$ :

$$\omega_-(k \approx 0) \approx \epsilon - \frac{k^2}{2M}. \quad (3.93)$$

In the dynamical structure factor, the band edge can be read off from the value of the lower threshold at momentum  $q = k_F$ , corresponding to the excitation composed of a hole at  $k = 0$  and a particle at the Fermi point  $k = k_F$  [Fig. 3.3(b)].

The nonanalyticities in the local bulk correlations are related to the threshold singularities of the momentum-resolved correlations by integration over momentum. For instance, integrating the spectral function implies that the LDOS behaves as

$$\begin{aligned} \rho(\omega, x \gg a) &= \int_{-\pi/a}^{\pi/a} dk A(k, \omega) \\ &\sim \int_{-k_0}^{k_0} dk \theta\left(\omega - \epsilon + \frac{k^2}{2M}\right) \\ &\quad \times \left| \omega - \epsilon + \frac{k^2}{2M} \right|^{-1+2\nu} \\ &\sim |\omega - \epsilon|^{-\frac{1}{2}+2\nu}. \end{aligned} \quad (3.94)$$

Since the singularities in the momentum-resolved dynamic response cannot be broadened, the power-law decay of autocorrelations in the bulk is a generic property of critical 1D systems.

However, since momentum is not conserved in the presence of a boundary, the above argument cannot be used to establish power-law decay of autocorrelation functions at the boundary. From the field theory perspective, the difference between bulk and boundary cases can be understood by analyzing the effects of boundary operators that perturb the mobile impurity model in Eq. (3.24). In the following we shall argue that, although formally irrelevant, boundary operators introduce two important effects in nonintegrable models: (i) they may renormalize the frequency of oscillations in the boundary autocorrelation, which will then differ from the frequency in the bulk (only the latter being equal to the band edge frequency  $\epsilon$ ); (ii) boundary operators that do not conserve the number of particles in high-energy subbands may give rise to a decay rate for the mobile impurity, which implies exponential decay of the boundary autocorrelation in time and the associated broadening of the nonanalyticity in the frequency domain.

For discussion purposes we will focus on the regime of weak interactions, which can be analyzed by perturbation theory in the free fermion basis, but the argument can be made more general by bosonizing the low-energy sector and the main points carry through. If we are interested in the impurity decay, we can furthermore safely neglect operators that involve the impurity field but do not couple it to the low-energy modes—these will at most renormalize the impurity dispersion.

As a simple example of a boundary operator respecting the symmetries and boundary conditions, consider the impurity-number-conserving perturbation

$$\partial H = g \partial_x d^\dagger(0) \partial_x d(0) \psi^\dagger(0) \psi(0). \quad (3.95)$$

Here we use  $\psi(x) = \psi_R(x) = -\psi_L(-x)$  to denote the low-energy modes of the fermion field on the unfolded line. We will assume that  $\partial H$  is present in the effective Hamiltonian and analyze its influence on the impurity propagator in perturbation theory.

It is convenient to Fourier transform the time coordinate to make use of energy conservation, but not the space coordinate. We can organize the diagrammatic expansion of the time-ordered impurity propagator

$$G_d(x, x'; t) = \langle T d(x, t) d^\dagger(x', 0) \rangle \quad (3.96)$$

using the Dyson equation

$$G_d(x, x; \omega) = G_d^{(0)}(x, x; \omega) + \int dx_1 \int dx_2 G_d^{(0)}(x, x_2; \omega) \Sigma(x_2, x_1; \omega) G_d(x_1, x; \omega). \quad (3.97)$$

### 3. Boundary correlations in 1D

---

If we take only boundary operators into account, the self-energy  $\Sigma$  is purely local:

$$\Sigma(x_2, x_1; \omega) = \Sigma(\omega)\delta(x_1 - a)\delta(x_2 - a). \quad (3.98)$$

The solution of the Dyson equation for  $x_1 = x_2 = a$  is

$$G_d(a, a; \omega) = \frac{1}{[G_d^{(0)}(a, a; \omega)]^{-1} - \Sigma(\omega)}. \quad (3.99)$$

It follows from Eq. (3.99) that the non-analyticity in the LDOS will be broadened if the local self-energy  $\Sigma(a, a; \omega)$  has a nonzero imaginary part at  $\omega = \epsilon$ .

For the continuation of this calculation, let us use the notation  $G(t) = G(a, a; t)$  for boundary propagators. The free propagator for the  $d$ -particle at the boundary is

$$G_d^{(0)}(t) = \frac{(-iM)^{3/2}}{\sqrt{2\pi}} \frac{\theta(t)e^{-i\epsilon t}}{(t + i\eta/v)^{3/2}}, \quad (3.100)$$

while for the low energy modes we have

$$G_{LL}^{(0)}(t) \equiv \langle T\psi(a, t)\psi^\dagger(a, 0) \rangle = [2\pi i(vt - i\eta \operatorname{sgn} t)]^{-1}, \quad (3.101)$$

where  $\eta$  is a short-distance cutoff and is related to the bandwidth of the impurity and low-energy subbands.

The first order correction in the couplings constant  $g$  corresponds to a tadpole diagram proportional to the density of low-energy modes at the boundary. It will not induce the decay rate that we are after [rather, it is like a nonuniversal renormalization of the coupling constant of the boundary operator  $\partial_x d^\dagger(0)\partial_x d(0)$ , which does not couple the impurity to the low-energy modes]. The second order correction is given by the expression

$$\delta\Sigma^{(2)}(\omega) = -ig^2 \int_{-\infty}^{\infty} dt e^{i\omega t} G_{LL}^{(0)}(t)G_{LL}^{(0)}(-t)G_d^{(0)}(t). \quad (3.102)$$

The imaginary part is then obtained as

$$\operatorname{Im} \delta\Sigma^{(2)} = -\left(\frac{g}{2\pi}\right)^2 \frac{M^{3/2}}{\sqrt{\pi}} \int_{-\infty}^{\infty} dt \frac{e^{i(\omega-\epsilon)t}}{(vt - i\eta)(vt + i\eta)(t + i\eta/v)^{3/2}}. \quad (3.103)$$

By power counting in the integral we see that

$$\delta\Sigma^{(2)}(\omega) \propto |\epsilon - \omega|^{5/2}, \quad (3.104)$$

and hence the self energy vanishes on-shell, when  $\omega = \epsilon$ , so this correction will not induce a finite decay rate

$$\frac{1}{\tau} = -\operatorname{Im} \Sigma(\omega = \epsilon). \quad (3.105)$$

The factor of  $e^{i(\omega-\epsilon)t}$  in Eq. (3.103) is general for self-energy contributions generated by perturbations that conserve the number of  $d$ -particles. Therefore, the decay rate must vanish to all orders if, for some reason, the irrelevant interactions conserve the number of high-energy excitations [49].

To derive a nonzero decay rate, we will have to consider perturbations that do not preserve the number of impurity modes and may contribute to the self-energy for  $\omega = \epsilon$ . As stated before, this is a typical effect of the boundary breaking translational invariance, since in the bulk kinematic constraints associated with momentum and energy conservation prevent the decay of the band-edge mode. Due to the U(1) symmetry (conservation of the total charge), the annihilation (creation) of a high-energy hole entails the annihilation (creation) of a particle in a low-energy state. A family of such boundary operators that are allowed by symmetry and the boundary conditions are for example

$$\partial H_n = g_n \partial_x d(0) [\psi^\dagger(0)\psi(0)]^n \psi(0) + \text{h.c.} \quad (3.106)$$

The first nontrivial correction to the self-energy is of second order in the coupling  $g_n$ . The diagram corresponds to a simple low-energy propagator dressed by  $n$  particle-hole pairs,

$$\delta \Sigma_n^{(2)}(\omega) = -i g_n^2 \int_{-\infty}^{\infty} dt e^{i\omega t} [G_{LL}^{(0)}(t)]^{n+1} [G_{LL}^{(0)}(-t)]^n, \quad (3.107)$$

leading to

$$\text{Im} \delta \Sigma_n^{(2)}(\omega) = -\frac{g_n^2}{(2\pi v)^{2n+1}} \int_{-\infty}^{\infty} dt \frac{t e^{i\omega t}}{i(t^2 + \eta^2/v^2)^{n+1}}. \quad (3.108)$$

Closing the contour in the upper half plane and picking up the pole at  $t = i\eta/v$ , we obtain a cutoff-dependent decay rate

$$\frac{1}{\tau} \propto g_n^2 e^{-\epsilon\eta/v}. \quad (3.109)$$

In contrast to the earlier case, we do find a possibly finite decay rate. We note that  $\epsilon\eta/v \sim \mathcal{O}(1)$  if the short-distance is of the order of the lattice spacing  $a$ , but  $\epsilon\eta/v \gg 1$  if  $\eta \gg a$ .

Boundary operators like  $\partial H_n$  will in principle be generated from lower order processes for a generic model when we integrate out the states outside of our impurity and low-energy subbands in a renormalization group procedure. Physically, we can think of these processes as the result of a cascade, or particle shower [20, 126], involving many intermediate states which are no longer in the description. The number  $n$  of low-energy particle-hole pairs roughly reflects the number of microscopic interaction processes and has to be sizeable (of the order of  $\sim v\eta^{-1}\epsilon^{-1}$ ) to accommodate for the excess energy. The coupling  $g_n$ , therefore, will scale with high powers of the microscopic interaction strength and

thus will be very small for weak interactions leading to a negligible decay rate. Stronger interactions, however, may show sizeable renormalization effects in the decay rate and frequency shift of correlations at the boundary.

Coming back to integrability, we argue that the above corrections do not occur for models with open boundary conditions solvable by Bethe ansatz. The argument relies on the fact that the exact eigenstates of the model still define a conserved impurity state corresponding to a hole in the quantum number configuration of the ground state. This state is parametrized by a rapidity  $\lambda$  and has well-defined energy given by the dressed energy function  $\epsilon(\lambda)$ . One can in fact show, using the thermodynamic Bethe ansatz, that the spectrum is still determined by the bulk dressed energy function by a similar type of folding trick to the one we used for the low-energy theory [127]. Not only does this imply the absence of a decay rate, also the impurity energy does not renormalize and the same frequency should be observed in the autocorrelation in the bulk and at the boundary. The “miracle” of integrability thus manifests itself as a fine tuning of the coupling constants in the effective field theory, in this case the vanishing of the couplings  $g_n$ .

## 3.6 Numerical results for spin chains

In this section, the field theoretical prediction for the asymptotic behavior of the autocorrelations  $C^{\parallel/\perp}(t, j)$  are checked, numerically, for critical spin chains with size  $L = 300$  and open boundary conditions.<sup>1</sup> We use the adaptive tDMRG [114, 128] keeping up to  $m = 300$  ( $m = 450$ ) states per block for the chains with spin  $S = 1/2$  ( $S = 1$  and  $S = 3/2$ ). The time evolution was performed with the second order Suzuki-Trotter decomposition with time step  $0.025 \leq \delta t \leq 0.3$ . The discarded weight was typically about  $10^{-8}$ – $10^{-12}$  during the time evolution. The numerical error sources in the tDMRG have two origins:

1. The Trotter error, which is related with the order ( $n$ ) of the Suzuki-Trotter decomposition. For the order  $n$ , this error is of the order  $(\delta t)^{n+1}$ .
2. The truncation error associated with the number of discard states.

These errors can be controlled by decreasing the time step ( $\delta t$ ) and increasing the number of states kept in the DMRG simulation.

We are interested in the long-time behavior of the longitudinal and transverse spin autocorrelations at the end site,  $C_{\text{end}}^{\parallel/\perp}(t) = C^{\parallel/\perp}(t, 1)$ , and in the bulk,  $C_{\text{bulk}}^{\parallel/\perp}(t) = C^{\parallel/\perp}(t, L/2)$ . As discussed in the Section 3.4.2, these autocorrelations can be described by a combination of universal power laws predicted by the LL theory and oscillating terms predicted by the nLL theory.

---

<sup>1</sup>This work has been performed by F.B. Ramos and J.C. Xavier from Universidade Federal de Uberlândia in Brazil.

### 3.6.1 Integrable spin-1/2 model

First, we consider the integrable spin-1/2 XXZ model in Eq. (3.55). According to Eqs. (3.60), (3.67), and (3.68), the real parts of the autocorrelations behave as

$$\operatorname{Re} [C_{\text{end}}^{\parallel}(t)] = \frac{A_1^{\parallel}}{t^2} + \frac{A_2^{\parallel} \cos(Wt + \varphi)}{t^{\frac{3}{2} + \xi}}, \quad (3.110)$$

$$\begin{aligned} \operatorname{Re} [C_{\text{bulk}}^{\parallel}(t)] &= \frac{B_1^{\parallel}}{t^2} + \frac{B_2^{\parallel}}{t^{2\xi}} + \frac{B_3^{\parallel} \cos(Wt + \varphi)}{t^{\frac{1}{2} + \xi}} \\ &\quad + \frac{B_4^{\parallel} \cos(2Wt + \tilde{\varphi})}{t^{\zeta}}, \end{aligned} \quad (3.111)$$

$$\operatorname{Re} [C_{\text{end}}^{\perp}(t)] = \frac{A_1^{\perp}}{t^{\frac{1}{\xi}}} + \frac{A_2^{\perp} \cos(Wt + \varphi)}{t^{\xi + \frac{1}{\xi} - \frac{1}{2}}}, \quad (3.112)$$

$$\operatorname{Re} [C_{\text{bulk}}^{\perp}(t)] = \frac{B_1^{\perp}}{t^{\frac{1}{2\xi}}} + \frac{B_2^{\perp}}{t^2} + \frac{B_3^{\perp} \cos(Wt + \varphi)}{t^{\xi + \frac{1}{2\xi} - \frac{1}{2}}}. \quad (3.113)$$

Here we have imposed the constraint that for the XXZ model the interaction dependence of all exponents (bulk or boundary, low-energy or high-energy) can be expressed in terms of a single parameter  $\xi$ . The theoretical prediction is  $\xi = K = \frac{\pi}{2(\pi - \arccos \Delta)}$ . The frequency of the oscillating terms is predicted to be the same for bulk and boundary autocorrelations, and is given by  $W = \epsilon = \frac{\pi\sqrt{1-\Delta^2}}{2\arccos \Delta}$ . In Eq. (3.111) we included the oscillating term with frequency  $2W$  which comes from a hole at  $k = 0$  and a particle at  $k = \pi$  [64]. The corresponding exponent is predicted to be  $\zeta = 1$  for  $\Delta = 0$  but  $\zeta = 2$  for  $0 < \Delta < 1$  and  $t \gg 1/\Delta^2$ . In the following we shall test the analytical predictions from the nLL theory by fitting the tDMRG data to the expressions above.

Before presenting the fit results, let us consider the chain with  $\Delta = 0$ . At this point, the autocorrelation  $C^{\parallel}(t, j)$  is equivalent to the density autocorrelation for free spinless fermion (see Section 3.2). It is straightforward to show that for even size  $L$

$$C^{\parallel}(t, j) = \left[ \frac{2}{L+1} \sum_{m=1}^{L/2} \sin^2 \left( \frac{m\pi j}{L+1} \right) e^{i\varepsilon_m t} \right]^2, \quad (3.114)$$

where  $\varepsilon_m = -\cos \left( \frac{\pi m}{L+1} \right)$ . In Fig. 3.4, we present the differences between the exact results of  $C_{\text{end/bulk}}^{\parallel}(t)$  and the tDMRG data obtained considering  $m = 200$  and  $\delta t = 0.1$ . As we can see, the agreement is quite good. It is interesting to note that the errors are of the order  $\sim 10^{-4} - 10^{-6}$ , which are smaller than the errors due to the use of the second order Suzuki-Trotter decomposition, of order  $(\delta t)^3 = 10^{-3}$ .

The results depicted in Fig. 3.4 show that we obtain accurate results for the  $C_{\text{end/bulk}}^{\parallel}(t)$  with the tDMRG by using  $m = 200$  and  $\delta t = 0.1$ . Away from the

### 3. Boundary correlations in 1D

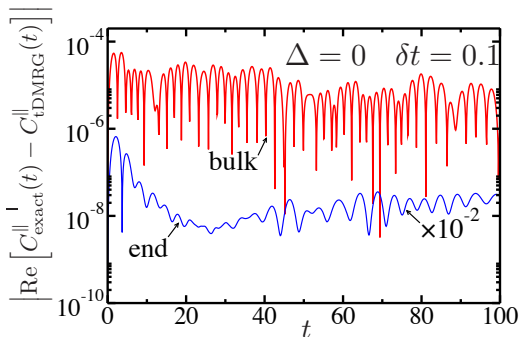


Figure 3.4: The differences between the real parts of the exact results [Eq. (3.114)] and the tDMRG data for the autocorrelations  $C^{\parallel}(t, j)$  for the spin-1/2 XXZ chain with  $L = 300$  and  $\Delta = 0$ . The bulk (end) case corresponds to  $j = L/2$  ( $j = 1$ ). We use  $m = 200$  DMRG states and time step  $\delta t = 0.1$ . We multiply the results of  $C^{\parallel}_{\text{end}}(t)$  by  $10^{-2}$  in order to see both data in the same figure.

point  $\Delta = 0$ , we do not have exact results to compare with. In this case, we compare the autocorrelations  $C^{\parallel/\perp}_{\text{end/bulk}}(t)$  for different values of  $m$  ( $m = 100$ ,  $m = 200$  and  $m = 300$ ) and time step  $\delta t$  ( $\delta t = 0.3$ ,  $\delta t = 0.1$ , and  $\delta t = 0.025$ ), in order to estimate the numerical errors. Overall, we estimate that these errors are at least one order of magnitude smaller than the values of the autocorrelations acquired by tDMRG.

Some typical examples of the numerical data fitted to Eqs. (3.110)-(3.113) are presented in Fig. 3.5 for the spin-1/2 XXZ chain with anisotropy  $\Delta = 0.6$ . The parameters  $\xi$  and  $W$  obtained by this fitting procedure are given in Table 3.1 for some values of the anisotropy  $\Delta$ . Overall, the parameters obtained are in agreement with the theoretical prediction presented in the last column of Table 3.1. In the fitting procedure, the tDMRG data considered were in the range  $15 < t < 80$ . We note that the parameter  $\xi$  changes slightly depending on the time range used in the fit. One of the largest discrepancies found corresponds to the parameter  $\xi$  obtained from  $C^{\parallel}_{\text{end}}(t)$  for  $\Delta = 0.8$  (see Table 3.1). Although this exponent ( $\xi = 0.459$ ) differs slightly from the predicted ( $K = 0.6287$ ), we found a very good agreement of the fit of the tDMRG data to Eq. (3.110) if we consider  $\xi = K$  fixed, as shown in Fig. (3.6). It is also interesting to note that, even though for some values of  $\Delta$  the fitted value of  $\xi$  is not so close to the predicted one, we found that  $|\beta^{\parallel/\perp}_{\text{bulk}} - \beta^{\parallel/\perp}_{\text{end}} - K + 1/2| < 0.06$ , which is close to zero in agreement with the relation predicted in Eq. (3.73).

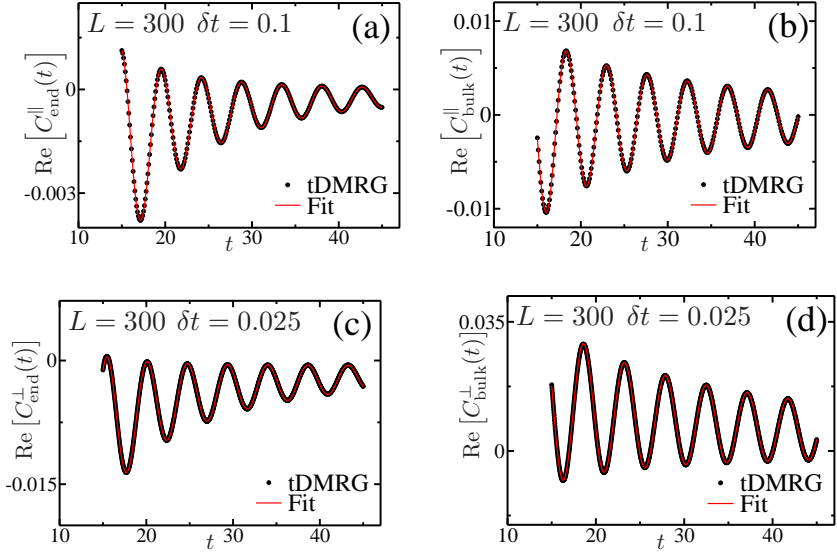


Figure 3.5: Real parts of the autocorrelations  $C_{\text{end/bulk}}^{\parallel/\perp}(t)$  vs.  $t$  for the spin-1/2 XXZ chain for  $\Delta = 0.6$ ,  $L = 300$ , and  $m = 200$ . For the longitudinal [figures (a) and (b)] and transverse [figures (c) and (d)] spin autocorrelations we use  $\delta t = 0.1$  and  $\delta t = 0.025$ , respectively. The symbols are the tDMRG results and the solid lines are fits to our data using Eqs. (3.110)-(3.113) (see text).

Table 3.1: The exponent  $\xi$  and the band edge frequency  $W$  for the autocorrelations  $C_{\text{end/bulk}}^{\parallel/\perp}(t)$  for the spin-1/2 XXZ chain for some values of  $\Delta$ . The parameters  $\xi$  and  $W$  were obtained by fitting the tDMRG data to Eqs. (3.110)-(3.113). The last column are the theoretical predictions for these parameters.

		$C_{\text{end}}^{\parallel}$	$C_{\text{bulk}}^{\parallel}$	$C_{\text{end}}^{\perp}$	$C_{\text{bulk}}^{\perp}$	Exact
$\Delta = 0$	$\xi$	0.992	1.006	0.943	0.981	1
	$W$	1.002	1.000	1.000	1.002	1
$\Delta = 0.3$	$\xi$	0.849	0.829	0.836	0.893	0.8375
	$W$	1.182	1.183	1.184	1.186	1.1835
$\Delta = 0.6$	$\xi$	0.677	0.678	0.711	0.595	0.7093
	$W$	1.355	1.355	1.356	1.358	1.3551
$\Delta = 0.8$	$\xi$	0.459	0.554	0.649	0.585	0.6287
	$W$	1.466	1.465	1.467	1.468	1.4646

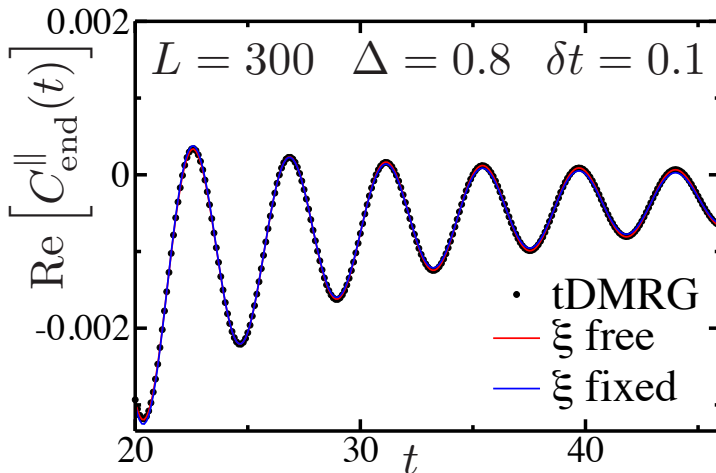


Figure 3.6: Real part of the longitudinal spin autocorrelation  $C_{\text{end}}^{\parallel}(t)$  vs.  $t$  for the spin-1/2 XXZ chain with anisotropy  $\Delta = 0.8$  and system size  $L = 300$ . The data were obtained using  $m = 200$  DMRG states and time step  $\delta t = 0.1$ . We fit the tDMRG data to Eq. (3.110) taking the parameter  $\alpha$  to be either free or fixed as  $\alpha = K$  (see legend).

### 3.6.2 Effects of bound states and nearly flat bands

Before we start analyzing nonintegrable models, let us briefly describe some situations where the predictions of Section 3.4.2 do not hold. As mentioned in Section 3.3, our mobile impurity model assumes that a single type of high-energy excitation (the deep hole) is sufficient to describe the oscillations in the autocorrelation functions. This is equivalent to assuming that in the frequency domain the dominant finite-energy nonanalyticity occurs at the band edge of single-hole excitations. However, more generally dynamical correlation functions may contain additional singularities at frequencies corresponding to bound states which are absent in the noninteracting model. In this case, additional oscillating components in the long-time decay of  $C_{\text{end/bulk}}^{\parallel/\perp}(t)$  can arise and decay more slowly than the contribution considered in Eqs. (3.110)-(3.113). While bound states can be incorporated in a more general mobile impurity model [15], in this work we look for examples where the existence of bound states can be ruled out, so we can test the bulk versus boundary behavior of the band edge contribution.

The signature of bound states can be observed in the longitudinal spin structure factor

$$S^{\parallel}(q, \omega) = \frac{1}{2\pi} \int_{-\infty}^{\infty} dt e^{i\omega t} \sum_j e^{-iqj} C^{\parallel}(t, j). \quad (3.115)$$

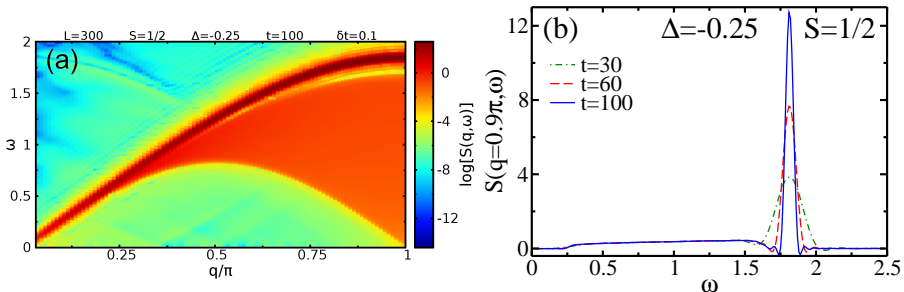


Figure 3.7: (a) Longitudinal spin structure factor for the spin-1/2 XXZ chain with anisotropy  $\Delta = -0.25$  and system size  $L = 300$ . The data were obtained using  $m = 200$  and  $\delta t = 0.1$ . (b) Lines shapes of  $S(q = 0.9\pi, \omega)$  obtained for different maximum times.

It is known [64] that for the spin-1/2 XXZ chain with  $-1 < \Delta < 0$ , which is in the critical regime but is equivalent to spinless fermions with *attractive* interactions,  $S^{\parallel}(q, \omega)$  exhibits a narrow peak above the two-spinon continuum. This peak can be interpreted within the effective field theory as a bound state of a high-energy particle and a high-energy hole. Fig. 3.7 shows  $S^{\parallel}(q, \omega)$  for  $\Delta = -0.25$ . Although this bound state is inside a continuum of multiple particle-hole pairs, we expect that for the integrable model the peak in the longitudinal spin structure factor is not broadened by decay processes and is given by a delta function, *i.e.*,  $S^{\parallel}(q, \omega) \sim \delta(\omega - \Omega_{\text{bs}}(q))$ , where  $\Omega_{\text{bs}}(q)$  is the dispersion relation of the bound state. In our numerical results we observe that the peak has a finite width because the frequency resolution is limited by the finite time in the tDMRG data. However, as shown in Fig. 3.7(b),  $S^{\parallel}(q, \omega)$  becomes narrower as the time increases. This is a strong evidence of the existence of a bound state in the spectrum.

Another situation that limits the applicability of our mobile impurity model is when the excitation spectrum contains particles with a large effective mass  $M$ , *i.e.* in the presence of nearly flat bands. As discussed in Section 3.3, the exponents of the oscillating terms hold for large times compared to the inverse of the band curvature energy scale, in the regime  $t \gg Ma^2$ . If the mass is large, the asymptotic behavior will only be observed after extremely long times, beyond the reach of the tDMRG method.

### 3.6.3 Higher- $S$ spin chains

With the above limitations in mind, we turn to the study of autocorrelations in nonintegrable models. In principle, a simple way to break the integrability of the spin-1/2 XXZ chain (while preserving a gapless spectrum as well as U(1) and discrete symmetries) is to add small next-nearest-neighbor exchange couplings, *e.g.*,  $\delta H \sim \sum_j S_j^z S_{j+2}^z$ . However, it is well known that the adaptive tDMRG only

### 3. Boundary correlations in 1D

---

works efficiently for models with nearest-neighbor exchange couplings [129]. For this reason, we study critical spin- $S$  chains with  $S > 1/2$  [130–133] as examples of nonintegrable models. We consider the Hamiltonian

$$H = \sum_{j=1}^L [S_j^x S_{j+1}^x + S_j^y S_{j+1}^y + \Delta S_j^z S_{j+1}^z + D(S_j^z)^2], \quad (3.116)$$

where  $\mathbf{S}_j$  is the spin- $S$  operators acting on site  $j$ ,  $\Delta$  is the exchange anisotropy and  $D$  is the single-ion anisotropy.

The expressions for spin- $S$  operators within the low-energy effective field theory can be obtained by noting that spin chains with  $S = n/2$  can be represented by  $n$ -leg ladders in the limit where strong rung couplings select the spin- $S$  multiplet of the local spins  $1/2$  [132, 134]. For instance, for  $S = 1$  we can write  $\mathbf{S}_j = \boldsymbol{\sigma}_j + \boldsymbol{\tau}_j$ , where  $\boldsymbol{\sigma}_j$  and  $\boldsymbol{\tau}_j$  are two spin- $1/2$  operators that commute with each other, and use the Jordan-Wigner transformation [essentially two copies of Eqs. (3.58) and (3.59)] to write  $\boldsymbol{\sigma}_j$  and  $\boldsymbol{\tau}_j$  in terms of two fermions, say  $\Psi_\sigma(j)$  and  $\Psi_\tau(j)$ . The resulting fermionic model turns out to be strongly interacting (and contain long-range interactions), but the low-energy sector can be treated by bosonization and a renormalization group analysis [132, 134]. A critical phase with central charge  $c = 1$  (analogous to the spin- $1/2$  XXZ model with  $|\Delta| < 1$ ) can be understood as the result of gapping out all branches of excitations except for one remaining gapless mode.

Here, we go beyond the low-energy regime and apply the nLL theory to investigate spin autocorrelations in the critical phase of model (3.116). Our main goal is to test the predictions of Section 3.5, namely the frequency shift and exponential decay of oscillating terms in the boundary autocorrelation for nonintegrable models. In the bulk case, the mobile impurity model of the nLL theory can be applied phenomenologically [13] after identifying the thresholds of the spectrum in dynamical spin structure factors. Unlike the spin- $1/2$  XXZ model, however, the coupling between the impurity and the low-energy modes is not known exactly and is regarded as a phenomenological parameter.

As our first attempt of studying higher- $S$  spin chains, we calculated the longitudinal spin structure factor for the model above with  $D = 0$  for  $S = 1$  and  $S = 3/2$ . The results for two representative values of  $\Delta$  are shown in Fig. 3.8. For both values of  $S$  we notice a nearly dispersionless threshold in the spectral weight for  $q \approx \pi$ . This behavior is characteristic of finite-energy excitations with a large effective mass, which hinder the direct application of our theory since they introduce a small band curvature energy scale.

Focusing on  $S = 1$  chains, we proceed by modifying the parameters in Eq. (3.116) so as to look for a regime with a larger curvature of the spectrum near  $q = \pi$ . Remarkably, the gap in the spectrum of  $S^\parallel(q \approx \pi, \omega)$  is consistent with the low-energy theory for critical spin-1 chains since the staggered part of the operator  $S_j^z$  excites massive modes [132, 134]. We consider the model with exchange anisotropy  $\Delta = -0.1$  and easy-axis single-ion anisotropy  $D = -1$ ,

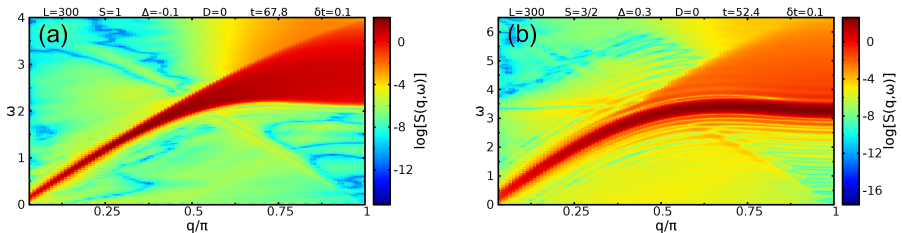


Figure 3.8: (a) The longitudinal spin structure factor of the critical spin- $S$  XXZ chains. (b) Results for  $S = 1$  and  $\Delta = -0.1$  and (b) for  $S = 3/2$  and  $\Delta = 0.3$ .

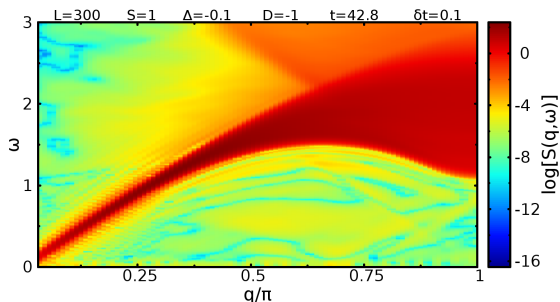


Figure 3.9: The longitudinal spin structure factor of the spin-1 XXZ chain with single-ion anisotropy for  $\Delta = -0.1$  and  $D = -1$ .

which lies in the critical phase [135]. Fig. 3.9 shows that in this case the lower threshold of  $S^{\parallel}(q, \omega)$  has a smaller gap and larger band curvature at  $q = \pi$ . Note also that there is no evidence for bound states in the spectrum of Fig. 3.9.

Next, we investigate the autocorrelation  $C^{\parallel}(t, j)$  for the spin-1 chain with  $\Delta = -0.1$  and  $D = -1$ . As discussed in Section 3.5, the sharp lower threshold of  $S^{\parallel}(q, \omega)$  implies that the bulk autocorrelation exhibits power-law decay of its oscillating components. Note that this argument does not depend on details of the mobile impurity model; the nonanalyticity in  $C_{\text{bulk}}^{\parallel}(t)$  follows from integrating  $S^{\parallel}(q, \omega)$  over momentum in the vicinity of the lower threshold. The frequencies of the oscillations can be read off from the spectrum of  $S^{\parallel}(q, \omega)$  as the values of  $\omega$  about which the lower threshold disperses parabolically. In the examples with spin-1/2 chains, there was only one such frequency corresponding to the band edge of single-hole excitations. By contrast, in Fig. 3.9 we observe two frequencies that can be identified as “edges” of the support:  $W_1 \approx 1.5$  (at  $q \approx 0.65\pi$ ) and  $W_2 \approx 1.1$  (at  $q \approx \pi$ ). Thus, we have fitted the tDMRG data

### 3. Boundary correlations in 1D

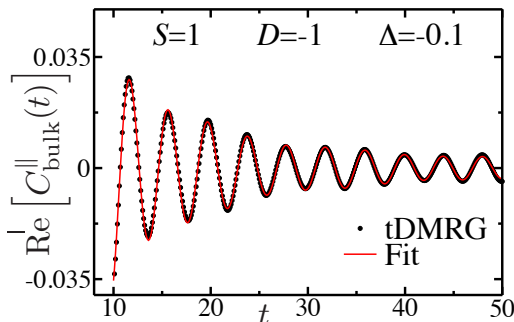


Figure 3.10: Real part of the longitudinal spin autocorrelation  $C_{\text{bulk}}^{\parallel}(t)$  vs.  $t$  for the spin-1 chain with  $\Delta = -0.1$ ,  $D = -1$  and  $L = 300$ . The data were obtained using  $m = 350$  and  $\delta t = 0.1$ . We fit the data to Eq. (3.117) and obtain the frequencies  $W_1 = 1.55$  and  $W_2 = 1.11$  and exponents  $\beta_1 = 1.57$  and  $\beta_2 = 1.76$ .

with the two-frequency formula

$$\begin{aligned} \text{Re} \left[ C_{\text{bulk}}^{\parallel}(t) \right] &= \frac{B_0^{\parallel}}{t^2} + \frac{B_1^{\parallel} \cos(W_1 t + \varphi_1)}{t^{\beta_1}} \\ &+ \frac{B_2^{\parallel} \cos(W_2 t + \varphi_2)}{t^{\beta_2}}. \end{aligned} \quad (3.117)$$

Note that in contrast with Eq. (3.111) here we include the nonoscillating term  $\sim t^{-2}$ , associated with the gapless  $q = 0$  mode, but omit the term  $\sim t^{-2K}$  that in the spin-1/2 case stems from  $q = \pi$  part of the operator  $S_j^z$  in the LL theory. The result of the fit is shown in Fig. 3.10. Note that the frequencies obtained are consistent with the edges of the spectrum observed in Fig. 3.9.

Finally, we analyze the behavior of the boundary autocorrelation  $C_{\text{end}}^{\parallel}(t)$  for the spin-1 chain with  $\Delta = -0.1$  and  $D = -1$ . For nonintegrable models our effective field theory predicts that boundary operators introduce a nonuniversal frequency shift and a decay rate for the high-energy mode. The numerical results indicate that the data can be fitted with a single oscillating component. We have fitted the tDMRG data for  $C_{\text{end}}^{\parallel}(t)$  to two functions:

$$f_1(t) = \frac{A_1}{t^2} + \frac{A_2^{\text{pl}} \cos(W't + \varphi_1)}{t^{\beta}}, \quad (3.118)$$

versus

$$f_2(t) = \frac{A_1'}{t^2} + A_2^{\text{exp}} \cos(W't + \varphi_2) e^{-\gamma t}. \quad (3.119)$$

For both fit functions we find  $W' \approx 1.75$ . This frequency is clearly different from the band edge frequencies  $W_1$  and  $W_2$  obtained from fitting the bulk autocorrelation and lies inside the continuum of  $S^{\parallel}(q, \omega)$  (see Fig. 3.9). This result is

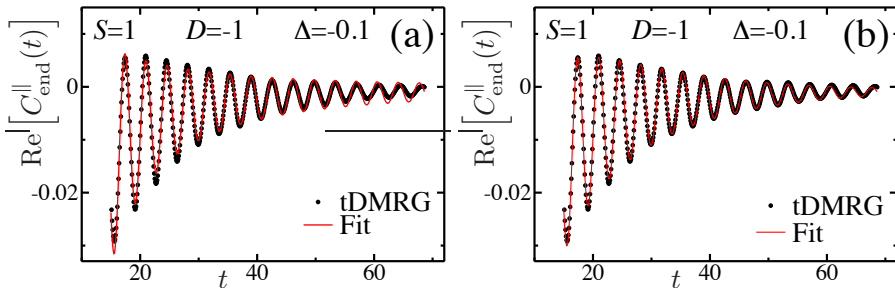


Figure 3.11: Real part of the longitudinal spin autocorrelation  $C_{\text{end}}^{\parallel}(t)$  vs.  $t$  for the spin-1 chain with  $\Delta = -0.1$ ,  $D = -1$  and  $L = 300$ . The symbols are the tDMRG results. The data were obtained using  $m = 350$  and  $\delta t = 0.1$ . (a) Fit to power-law decay in Eq. (3.118). (b) Fit to exponential decay in Eq. (3.119).

consistent with our prediction of a nonuniversal frequency shift for nonintegrable models. Moreover, we can see in Fig. 3.11(a) that the best fit to Eq. (3.118) for  $t > 15$  overestimates the amplitude of the oscillations at larger times  $t \gtrsim 45$ , suggesting that the decay is faster than power law. In fact, the fit to an exponential decay according to Eq. (3.119) with  $\gamma \approx 0.059$  yields better agreement with the numerical data [see Fig. 3.11(b)]. Importantly, the fitted relaxation time  $1/\gamma \approx 17$  is smaller than the time scales reached by the tDMRG.

In order to observe a clear signature of the exponential decay of  $C_{\text{end}}^{\parallel}(t)$ , it is convenient to subtract off the nonoscillating  $t^{-2}$  term in the autocorrelation function. This subtraction is important because the difference between power-law and exponential decay of the oscillating component becomes more pronounced at longer times, after which an exponentially decaying term would become less significant than the  $1/t^2$  or subleading power-law terms. As explained in Sec. 3.7, we can fix the nonuniversal prefactor  $A_1$  in Eq. (3.118) by relating it to the prefactor of the uniform term in the static correlation  $\langle S_1^z S_j^z \rangle \sim 1/j^2$  for  $j \gg 1$ . The numerical result for the boundary autocorrelation after subtracting the nonoscillating term is shown in Fig. 3.12. It is clear that the amplitude of the oscillations decays as a straight line on a log-linear scale. This result indicates an exponential decay of the boundary autocorrelation in the nonintegrable model, in agreement with our prediction.

### 3.7 Boundary-bulk spin correlation

In this section, we relate the prefactors of the nonoscillating terms of the time-dependent boundary autocorrelation and of the static correlation.

Let us first consider the critical spin-1/2 XXZ chain with open boundary

### 3. Boundary correlations in 1D

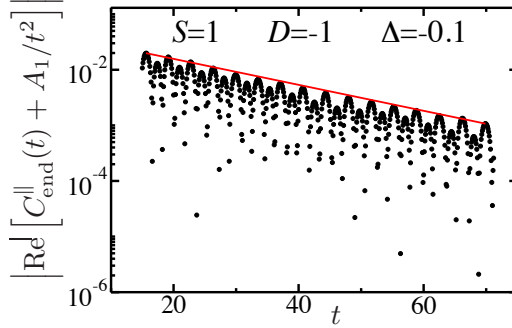


Figure 3.12: (Color online) Same as Fig. 3.11, after subtracting the nonoscillating term  $\sim 1/t^2$ . The prefactor  $A_1 = 2.233$  was obtained independently (see Sec. 3.7). The slope of the red line is  $\approx -0.053$ .

conditions. We are going to show that the static spin correlation is given by

$$\langle S_1^z S_{j=x}^z \rangle \approx -\frac{2\sqrt{K}A}{\pi^2 x^2} + \frac{B(-1)^x}{x^{1+K}}, \quad (3.120)$$

where  $K$  is the Luttinger parameter. The prefactor  $A$  is nonuniversal and also appears in the time-boundary autocorrelation

$$\langle S_1^z(t) S_1^z(0) \rangle \sim -\frac{4A^2}{\pi^2 v^2 t^2} + \text{oscillating terms}. \quad (3.121)$$

Note that if we determine the prefactor  $A$  by fitting the numerical results for the static correlation to Eq. (3.120), we can fix the prefactor of the nonoscillating term in the time-dependent boundary autocorrelation.

We start with the low-energy representation for  $S_j^z$  at the boundary:

$$\begin{aligned} S_1^z &\sim \Psi^\dagger(1)\Psi(1) \\ &\sim : \psi_R^\dagger(1)\psi_R(1) : + : \psi_L^\dagger(1)\psi_L(1) : \\ &\quad + e^{i\pi}[\psi_R^\dagger(1)\psi_L(1) + \text{h.c.}] \\ &= : \psi_R^\dagger(1)\psi_R(1) : + : \psi_R^\dagger(-1)\psi_R(-1) : \\ &\quad + [\psi_R^\dagger(1)\psi_R(-1) + \text{h.c.}] \\ &\sim 4 : \psi_R^\dagger(0)\psi_R(0) : \\ &\sim -\frac{4}{\sqrt{2\pi}}\partial_x\phi_R(0). \end{aligned} \quad (3.122)$$

Next, we need to perform the Bogoliubov transformation:

$$\phi_R(x) = \frac{K^{\frac{1}{2}} + K^{\frac{1}{2}}}{2}\varphi_R(x) - \frac{K^{\frac{1}{2}} - K^{\frac{1}{2}}}{2}\varphi_R(-x). \quad (3.123)$$

In the interacting case, the boundary operator has a nonuniform prefactor because the expression in Eq. (3.122) mixes the staggered part of the density operator  $\psi_R^\dagger \psi_L + \text{h.c.}$  (which has a nonuniversal prefactor when bosonized in the interacting case) with the uniform part  $\psi_R^\dagger \psi_R + \psi_L^\dagger \psi_L$  (which does have a universal prefactor). For this reason, in the general case we must write

$$S_1^z \sim -\frac{4A}{\sqrt{2\pi}} \partial_x \varphi_R(0), \quad (3.124)$$

where  $A = 1$  for free fermions, but  $A$  is nonuniversal in the interacting case. Using Eq. (3.124) together with the bosonic propagator,

$$\langle \partial_x \varphi_R(x, t) \partial_x \varphi_R(0, 0) \rangle = -\frac{1}{2\pi(x - vt)^2}, \quad (3.125)$$

leads to the result in Eq. (3.121).

The spin operator in the bulk is given by

$$\begin{aligned} S_{j=x}^z &\sim \Psi^\dagger(x) \Psi(x) \\ &\sim \psi_R^\dagger(x) \psi_R(x) + \psi_L^\dagger(x) \psi_L(x) \\ &\quad + (-1)^x [\psi_R^\dagger(x) \psi_L(x) + \text{h.c.}] \\ &\sim \sqrt{\frac{K}{2\pi}} [\partial_x \varphi_L(x) - \partial_x \varphi_R(x)] \\ &\quad + \frac{(-1)^x}{2\pi\eta} \left[ e^{i\sqrt{2\pi K}[\varphi_R(x) - \varphi_L(x)]} + \text{h.c.} \right]. \end{aligned} \quad (3.126)$$

Using the folding trick with

$$\partial_x \varphi_L(x) = -\partial_x \varphi_R(-x), \quad (3.127)$$

we obtain

$$\begin{aligned} S_j^z &\sim -\sqrt{\frac{K}{2\pi}} [\partial_x \varphi_R(x) + \partial_x \varphi_R(-x)] \\ &\quad + B' (-1)^x \left[ e^{i\sqrt{2\pi K}[\varphi_R(-x) - \varphi_R(x)]} + \text{h.c.} \right], \end{aligned} \quad (3.128)$$

where  $B'$  is nonuniversal.

Let us first focus on the uniform part in Eq. (3.128). The corresponding term in the static correlation is

$$\begin{aligned} \langle S_1^z S_j^z \rangle &\sim \frac{2\sqrt{K}A}{\pi} [\langle \partial_x \varphi_R(0) \partial_x \varphi_R(x) \rangle + (x \rightarrow -x)] \\ &= -\frac{2\sqrt{K}A}{\pi^2 x^2}, \end{aligned} \quad (3.129)$$

### 3. Boundary correlations in 1D

---

which is the first term on the rhs of Eq. (3.120).

Now consider the staggered part of the operator in Eq. (3.128). Since this term has a nonuniversal prefactor which is independent of  $A$ , we shall focus on deriving the exponent of the large-distance decay. The staggered term in the correlation is

$$\langle S_1^z S_j^z \rangle \sim (-1)^x \langle \partial_x \varphi_R(0) e^{i\sqrt{2\pi K} \varphi_R(-x)} e^{-i\sqrt{2\pi K} \varphi_R(x)} \rangle. \quad (3.130)$$

This is a three-point function involving three primary fields. We use the operator product expansion:

$$\begin{aligned} & : \partial_x \varphi_R(0) : : e^{i\sqrt{2\pi K} \varphi_R(-x)} : \\ &= \sum_{n=0}^{\infty} \frac{(i\sqrt{2\pi K})^n}{n!} : \partial_x \varphi_R(0) : : [\varphi_R(-x)]^n : \\ &\sim \sum_{n=1}^{\infty} \frac{(i\sqrt{2\pi K})^n}{(n-1)!} \langle \partial_x \varphi_R(0) \varphi_R(-x) \rangle : [\varphi_R(-x)]^{n-1} : \\ &= i\sqrt{2\pi K} \langle \partial_x \varphi_R(0) \varphi_R(-x) \rangle : e^{i\sqrt{2\pi K} \varphi_R(-x)} : \\ &= \frac{i\sqrt{K}}{\sqrt{2\pi x}} : e^{i\sqrt{2\pi K} \varphi_R(-x)} : . \end{aligned} \quad (3.131)$$

Thus, in the three-point function we obtain

$$\begin{aligned} & \langle \partial_x \varphi_R(0) e^{i\sqrt{2\pi K} \varphi_R(-x)} e^{-i\sqrt{2\pi K} \varphi_R(x)} \rangle \\ &\sim \frac{1}{x} \langle e^{i\sqrt{2\pi K} \varphi_R(-x)} e^{-i\sqrt{2\pi K} \varphi_R(x)} \rangle \\ &\sim \frac{1}{x} \frac{1}{(2x)^K}. \end{aligned} \quad (3.132)$$

It follows that the staggered term in the spin correlation behaves as

$$\langle S_1^z S_j^z \rangle \sim \frac{(-1)^x}{x^{1+K}}, \quad (3.133)$$

which is the second term in Eq. (3.120).

For the spin-1 chain the uniform part of the spin operator in the bulk becomes

$$S_j^z \sim -\sqrt{\frac{K}{\pi}} [\partial_x \varphi_R(x) + \partial_x \varphi_R(-x)]. \quad (3.134)$$

Note the extra factor of  $\sqrt{2}$  in comparison with Eq. (3.128), which comes from combining the densities of two spinless fermions [132] (more generally, this procedure introduces a factor of  $\sqrt{2S}$  for the spin- $S$  operator). The Luttinger parameter in Eq. (3.134) is defined such that the Kosterlitz-Thouless transition to the

gapped Haldane phase happens at  $K = 1$  and  $K > 1$  in the critical phase [132]. Moreover, for  $S = 1$  the staggered part of  $S_j^z$  couples to gapped modes (recall the spectrum is gapped at  $k = \pi$ ). As a result, the staggered term in the static correlation decays exponentially with the distance from the boundary. The results for the autocorrelation and static correlation for  $S = 1$  are

$$\langle S_1^z(t) S_1^z(0) \rangle \approx -\frac{4C^2}{\pi^2 v^2 t^2}, \quad (3.135)$$

$$\langle S_1^z S_{j=x}^z \rangle \approx -\frac{2\sqrt{2KC}}{\pi^2 x^2}, \quad (3.136)$$

where the coefficient  $C$  is nonuniversal. The LL parameter  $K$  and the spin velocity  $v$  can be determined independently by analyzing the finite-size corrections of the lower energy states together with the machinery of the conformal field theory [136], see for example Ref. [137]. We found for the spin-1 chain with  $\Delta = -0.1$  and  $D = -1$  the following values:  $K = 1.285$  and  $v = 1.211$ . Using these values and fitting the DMRG data of the static correlations to Eq. (3.136), we found that  $C = 2.8423$ .

### 3.8 Conclusion

In conclusion, we have analyzed the effect of reflective boundary conditions in one-dimensional quantum liquids on time-dependent correlations. We have shown that one can generalize the effective impurity model of a high-energy mode interacting with the low-energy subband (nonlinear Luttinger liquid theory) to capture the dominant contributions to late-time asymptotes of autocorrelations and predict the exponents of associated power-law singularities in the frequency domain. This was used to compute, e.g., the autocorrelations in critical spin chains and the local density of states at the band bottom in one-dimensional interacting spinless fermions. The boundary exponents show a characteristic doubling in their dependence on the phase shifts which implies relations between the bulk and boundary exponents depending only on the Luttinger parameter but not on the phase shifts. Generalizations of the method were used to derive similar results for spinful models and different correlation functions.

Our results apply, *mutatis mutandis*, to the class of integrable models, but they need caution when applied to the nonintegrable case. While the impurity mode is effectively protected in the bulk by momentum conservation and power-law behavior of correlations is generic at zero temperature, the breaking of translational invariance at the boundary introduces the possibility of additional renormalization effects. We have discussed two observable consequences: a shift in the impurity energy leading to a shift in the oscillation frequency in the autocorrelation, and the possibility of decay of the impurity leading to exponential damping. These effects can be analysed within the impurity model approach by studying boundary operators as perturbations. Based on the Bethe ansatz solution for models with reflective boundary conditions, we argue that integrable

### 3. Boundary correlations in 1D

---

models should be devoid of such effects and hence identical bulk and boundary frequencies should be observed without exponential decay.

We performed a time-dependent density matrix renormalization group study of both integrable and non-integrable spin chains to verify our predictions. For the integrable case, we studied the XXZ spin-1/2 chain and the numerically obtained correlations agree very well with the effective field theory predictions. For the nonintegrable case we looked at spin chains of higher spin  $S > 1/2$ . We did find evidence for a nonuniversal frequency shift in this case as well as an exponential damping factor of the high-energy contribution to the correlation. Detailed comparison with microscopic models highlights the properties of the spectrum one should consider in formulating the effective impurity model. First of all, one should take into account all contributions from band minima as well as band maxima. Complications may arise when the spectrum features bound states which are a priori not taken into account in the impurity model and lead to additional oscillating contributions, but the impurity model may in principle be adjusted to account for these. Bound-state lifetimes are subject to similar considerations concerning the integrable versus nonintegrable case as the high-energy impurity modes. A second complication comes when one of the high-energy bands becomes nearly flat, resulting in a very large time-scale before the asymptotic behavior of the correlation is reached, which could possibly push it beyond the times for which reliable numerical data can be obtained.

An experimental test of the oscillating, high-energy contribution to correlations in real time would most likely involve the fabrication of an effective spin model using cold atom systems, for which real-space and time-resolved correlations can be imaged by many-body Ramsey interferometry [138]. To test our bulk versus boundary predictions one can resort to an optical box-like potential [139, 140] implementing the appropriate boundary condition.

It would be interesting to extend our results to more general boundary conditions. In particular, in the context of integrable models we may distinguish between integrable and nonintegrable boundary conditions. Moreover, one may differentiate between diagonal and non-diagonal boundary conditions, the latter of which corresponds to boundary conditions that do not conserve particle number in the fermionic picture [124, 141, 142]. The mobile impurity model, viewed as a boundary field theory, in principle provides the flexibility to study all these situations by choosing the appropriate boundary conditions as well as adding boundary operators to account for possibly nontrivial boundary bound states.

# Absence of Luttinger physics in golden chains on germanium

The most pitiful among men is he  
who turns his dreams into silver  
and gold.

---

Khalil Gibran (in *Sand and Foam*)

The search for Luttinger liquids in experiment is an interesting and ongoing pursuit. In this chapter we discuss one of the systems that seemed to be a promising candidate, namely self-organized atomic chains formed when gold is evaporated on a germanium surface: Au/Ge(001).

Surface systems are interesting from an experimental point of view since they are easy to probe and manipulate from the outside. There are powerful techniques, like STM and ARPES, to extract information on the many-body quantum dynamics. Alas, despite earlier findings seemingly establishing Luttinger liquid physics, it appears that the observed behavior of Au/Ge(001) is not due to one-dimensional electron dynamics but is probably an interplay of disorder and strong interactions. The results of this chapter indicate that the coupling between the atomic chains is non negligible, which is likely a generic problem for atomic chains on surfaces for which coupling with the bulk and other chains seems hard to prevent.

This chapter relies heavily on the experimental work in the groups of Harold Zandvliet and Mark Golden in general, and of René Heimbuch and Nick de Jong in particular. It was published in a joined paper *Phys. Rev. B* **93** 235444 (2016) [2]. See for more experimental details the theses [143] and [144].

## 4.1 Introduction

With the tremendous experimental achievements in cold-atoms and nano-technology research nowadays, the systems in the labs of experimentalists and the mathe-

#### 4. Absence of Luttinger physics in golden chains on germanium

---

mathematical models studied by theorists quickly converge. In the context of this thesis, the realization of systems in the Luttinger liquid universality class are of prime interest. Despite the universality of the Tomonaga-Luttinger model, establishing unambiguous realizations of Tomonaga-Luttinger liquid (TLL) physics has proved challenging. In particular, the great desire to ‘see’ Luttinger liquids must be tempered by the hard requirement that simpler explanations do not exist (Occam’s razor). Up to now, carbon nanotubes [145,146], organic crystals with highly anisotropic bulk properties [147–149], and GaAs channels [150] are the most credible examples of classes of materials able to display the exotic effects associated to TLLs. Recently, self-assembled atomic nanowires on semiconductor surfaces have attracted a lot of attention in particular Au-induced nanowires on the Ge(001) surface. In Ref. [113] a compelling case was made for TLL behavior in the Au/Ge(001) system. However, these observations have been challenged immediately in a subsequent remark [151] and the discussion has continued in subsequent publications (see Sec. 4.2). At the time this research was done the situation was not yet settled.

The interpretation of the data on Au/Ge(001) in light of TLL theory is fueled by some promising indications of one-dimensional physics: Upon evaporation of Au on the Ge(001) surface (see experimental details in Sec. 4.3), clear chain-like structures become visible in scanning tunneling microscopy (STM) maps of the surface topography. Scanning tunneling spectroscopy (STS)—probing the local density of states (LDOS)—moreover shows a clear dip at the Fermi level which is a signature of Luttinger liquid, or at least non-Fermi liquid, physics. Angular resolved photo emission spectroscopy (ARPES), probing the hole spectral function, showed electron pockets with a possibly linear Fermi surface and very incoherent behavior near the Fermi level. The decisive argument for the TLL nature of the electronic states of the Au/Ge(001) structures reported in Ref. [113] is the universal scaling of the LDOS with both temperature and energy close to the Fermi level, as predicted from the TL model and a consequence of the conformal invariance of the Luttinger liquid fixed point.

Before we discuss the subsequent experimental findings, it is important to note that from a theory point of view the observation of a TLL in a solid state system like the Au/Ge(001) nanowires raises certain questions concerning instabilities of the Luttinger liquid state. In particular the focus on a small energy window near the Fermi level is likely to be problematic. As is well explained in e.g. [9], one should worry about higher dimensional ordering due to weak residual coupling at such low energies as well as about disorder and localization effects for which one-dimensional systems are particularly susceptible. In Sec. 4.5.1 we present some estimates based on calculations in the literature using renormalization group (RG) arguments.

In the remainder of this chapter we first discuss in more detail the discussion in the literature concerning the Au/Ge(001) system with a focus on the electronic properties. Then, the joined experimental and theoretical effort is presented that uses a combination of LEED, ARPES, STM/STS experiments done at the

University of Amsterdam and the MESA+ institute of the University of Twente augmented with theoretical considerations to provide a detailed picture of the Au-induced electronic states.

## 4.2 The Au/Ge(001) system

The Au/Ge(001) system first appeared in the literature in [152] where it was observed that nanowire-like objects of up to hundreds of nm long appear clearly in STM topographic images with an inter-nanowire separation of 1.6 nm. It has been extensively studied experimentally since. Here we focus on the results obtained for the low temperature phase relevant for the possibility to find Luttinger liquid signatures in the gold induced electronic states that can be observed to appear when the ARPES data is compared to that of the clean Ge(001) surface. (The discussed experimental signatures can be observed in the data presented in Fig. 4.2 or in the cited publications.)

Low-energy electron diffraction (LEED) provides a direct probe of the symmetry of the surface and reveals a basic  $c(8 \times 2)$  periodicity which is in line with STM topography. An additional less pronounced quasi periodicity seen on top of the nanowires—referred to as the VW structure—results in a  $(8 \times 4)$  superstructure [153–155] which is also visible in the LEED images as dimmer spots.

A structure model of the surface was proposed in [152], but this is most likely not correct. The chemical structure of the surface is still under debate [152, 153, 156–161], but one structural model that fits most of the experimental data is the giant missing row model [157]. This picture naturally explains that the depth of the troughs between wires is larger than a single layer of atoms [162], and also rationalizes the difference between the occupied and unoccupied topographic images measured in STM [163]. In addition, the fact that the LDOS observed in the troughs is larger than that on the wires themselves [164], and the increased surface corrugation observed in SPA-LEED measurements [154] could be explained by the giant missing row model, in which the top of the nanowires is formed by Ge-Ge dimers, with the troughs consisting of Ge(111) facets covered in Au trimers [157]. Density-functional theory [165–167] should in the end of the day settle the debate on the structure of the Au/Ge(001) system. The calculations in [163] predict, however, that the most simple version of the giant missing row model is not energetically favorable. In its basic form it also does not contain the VW superstructure [153–155, 168] hence it is likely that the true structure of Au/Ge(001) is a more complicated version of this model for example in which the Au atoms are incorporated into the germanium structure [163].

For the discussion of the electronic states a complete understanding of the atomic structure is not strictly necessary—we can interpret the spectral signatures independently. As mentioned in the introduction, the experimental signatures interpreted as TLL behavior in the Au/Ge(001) system have been subject of controversy in the literature. In STS measurements of the LDOS, a TLL

#### 4. Absence of Luttinger physics in golden chains on germanium

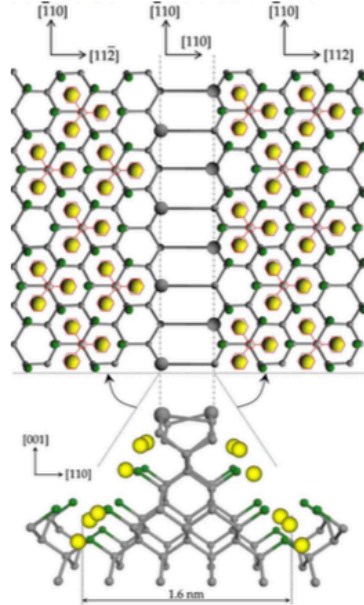


Figure 4.1: Giant missing row model (taken from [157]) for the surface structure of Au/Ge(001). Certain crucial experimental findings are explained by this structure model, but it probably needs refinement in order to faithfully represent the true situation. For the discussion of the electronic properties pursued in the current work, a definitive understanding of the structure model is not necessary.

system should show its face as a dip in the differential conductivity (proportional to the LDOS according to standard STM theory [169]) around zero bias following a characteristic power law [9, 46]. Moreover, this curve should exhibit scaling behavior according to a universal dependence on the temperature and energy away from  $E_F$ . The exponent of the power law,  $\alpha$ , is a measure of the interaction strength between the electrons and should show different values for TLL systems probed in the bulk or at the boundary 1D chains, but the values are universally related through the Luttinger parameter  $K$  (see Ch. 3). On the one hand, the expected power-law form of the measured density of states has indeed been reported in both STS [113] and ARPES data [161, 170]. Furthermore, straight features in constant energy  $E(k_x, k_y)$  maps in ARPES [161, 170] and linear conduction pathways observed in the troughs between the nanowires in STM data [113, 158, 164] also seem to point towards the generation of Au-induced electronic states that show significant dispersion only in one  $k$ -direction, strengthening the case for a TLL state. On the other hand, this conclusion has been disputed based on results of fully analogous experiments carried out

by other groups on the same Au/Ge(001) system [151, 155, 171–174]. These data are argued to be more consistent with the Au-induced surface states being two-dimensional in nature [155, 171] and in fact with the direction of strongest dispersion being perpendicular to the nanowire structures. Thus, experimentally speaking, it is fair to say that the situation appears undecided.

### 4.3 Experiments, data and discussion

This section discusses the experiments done in Amsterdam and Twente on the Au/Ge(001) system. Details on the sample preparation and the execution of the experiments are left out (these can be found in [2] and [143, 144]). Instead we focus on the data from the ARPES, STS/STM and LEED experiments, all performed on consistently obtained samples providing us with a complete characterization of the low-temperature Au-induced electronic states of the Au/Ge(001) nanowires. The main focus will be on the ARPES data—a direct probe of the hole spectral function for the electrons in the system—and what it tells us about the relative orientation of the Fermi surface and the nanowire direction.

In Fig. 4.2 an overview of LEED, STM and ARPES data is presented showing many of the features discussed in the previous section. The STM topography [Fig. 4.2 (b)] shows clear long nanowire structures which occur in two, orthogonally oriented domains. The domain boundaries correspond to step edges in the underlying Ge(001) surface and are a consistent feature of the samples [158]. The appearance of two orientations presents a challenge in interpreting ARPES data since the spot size of the photon beam is much larger than any single domain and the observed signal therefore represents an average of the two types of domains. The LEED patterns also echo the occurrence of the two domains and corresponding reciprocal lattice vectors and Brillouin zones are illustrated in red and blue [Fig. 4.2 (a)]. Also note the dimmer spots highlighted with orange arrows corresponding to the  $(8 \times 4)$  superstructure [153, 154]. The depicted ARPES data shows both constant energy maps at specific energies below the Fermi level as well as fixed momentum cuts. The gold induced states are the four electron pockets highlighted in yellow and these are the most important feature for the lively TLL-inspired discussion of ARPES data on Au/Ge(001) [Fig. 4.2 (c)–(g)] [153, 158, 161, 170, 171, 173]. Note that these Au-induced states appear at a finite momentum offset with wavenumber  $k \approx 0.2 \text{ \AA}^{-1}$  compared to the  $\Gamma$  point  $k_{x,y} = 0$ . As noted, the ARPES signal effectively averages over two domain orientations and the four electron pockets are thus interpreted as consisting of two opposing pairs with each pair corresponding to a different orientation. Pane (c)–(f) also show a different band touching the Fermi level at the  $\Gamma$  point which is referred to as a bulk-derived band and not bulk because this state is present in the clean Ge(001) surface but displays essentially 2D and not 3D dispersion.<sup>1</sup> The current interpretation is that this band correspond to an essentially two-

<sup>1</sup>The  $k_z$ -dispersion direction of this band can be probed by changing the photon energy in the ARPES setup and is shown to be essentially flat in this direction [2, 170].

#### 4. Absence of Luttinger physics in golden chains on germanium

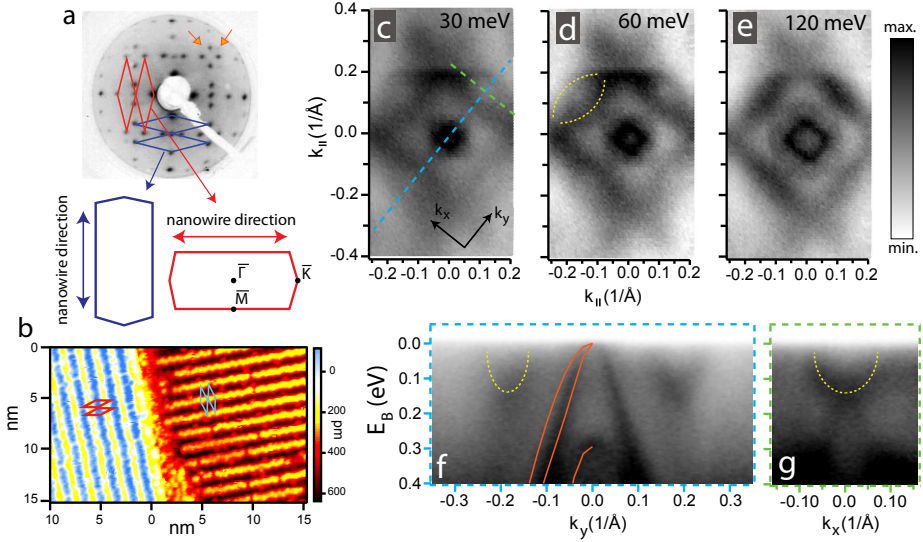


Figure 4.2: (a) Representative LEED image of the nanowire sample, recorded with an electron beam energy of 23 eV, showing a clear, dual-domain  $c(8 \times 2)$  reconstruction. Two reciprocal surface unit cells are shown superimposed in blue and red, and their respective first Brillouin zones are indicated below the LEED image. (b) STM topograph of Au-induced nanowires on Ge(100), recorded at room temperature. The unit cells from LEED data are superimposed in red and light blue. (c-e) Constant energy maps— $I(k_x, k_y)$ —measured using ARPES for binding energies,  $E_B$  of (c) 30 meV, (d) 60 meV and (e) 120 meV. (f)  $I(k_y, E)$  image, which is a cut along the light blue dashed line in panel (c). The orange lines in panel (f) superpose the results of density functional theory calculations for bulk Ge from Ref. [175]. (g)  $I(k_x, E)$  image along the green dashed line in (c). The yellow dotted lines in panels (d), (f) and (g) highlight low-lying Au-induced electronic states. All ARPES data was taken with a photon energy of 21.2 eV at a temperature of 20 K.

dimensional subsurface state occurring for the clean Ge(001) and Au/Ge(001) surface reconstructions alike, but some distance below the surface. This interpretation is also motivated by work on the Ge(111)/metal surfaces [176]. It could be the conduction channel inferred in transport experiments [177]. The presence of this low energy subsurface state may be important for the interpretation of the LDOS measurements later on.

### 4.3.1 The direction of electron dispersion

One of the main topics of debate [151, 178] has been the relative orientation of the nanowire direction and the electron pockets in the ARPES data. As noted, due to domain averaging, this is hard to infer from the ARPES data alone. In [173], Nakatsuji et al. tackle this issue by doing ARPES on samples from Ge wafers with a slight miscut leading to a majority of one of the domains. Their argument was based on an extended Brillouin zone scheme and the signatures of the primary electron pockets in higher Brillouin zones. While the logic is sound (and published before [113]) unfortunately the signal was so weak that the use of second differentials of the data was necessary and the conclusions were still disputed by the authors of [113, 178]. Our main goal is to provide compelling evidence that indeed the direction of strongest dispersion is perpendicular to the wires and to give a physical explanation for the odd shape of the electron pockets from simple band theory.

The constant energy maps displayed in Figs. 4.2 (c)–(e) show that the Au-induced electron pockets are obviously elongated, but there seems to be a deviation from the perfectly straight Fermi surface in one of the  $k$ -directions as expected for an effectively one-dimensional system. A slight curvature in the Fermi surfaces presents a lower bound on the energy scale for which the system behaves one-dimensional [9] and therefore presents a possible tension with the interpretation of the data as a TLL system based on power laws for the LDOS at the Fermi surface. However, by itself it does not disprove the effective 1D nature of the electronic state.

In Fig. 4.3, other constant energy ARPES maps for low-lying electronic states is displayed (15 meV below the Fermi level), measured from the same high-quality Au/Ge(001) nanowire sample as the data shown in Fig. 4.2. Despite the dual-domain nature of the nanowire sample, the different geometry adopted in this experiment (compared to Fig. 4.2) results in a strong asymmetry in the intensity distribution between the two pairs of electron pockets. By a stroke of fortune, this experiment is more sensitive to the domains with nanowires running in one of the two possible orthogonal directions.<sup>2</sup> This intensity asymmetry makes these

---

<sup>2</sup>In the experimental geometry relevant for Fig. 4.3, the  $\Gamma$ - $\bar{K}$  direction of one of the sets of surface nanowire domains is parallel to the entrance slit of the electron analyzer and antiparallel to the majority polarization vector of the partially linearly polarised VUV radiation. This results in favorable photoemission matrix elements for the nanowire states from one domain orientation, while the states from the orthogonal nanowire domains are evidently significantly suppressed.

#### 4. Absence of Luttinger physics in golden chains on germanium

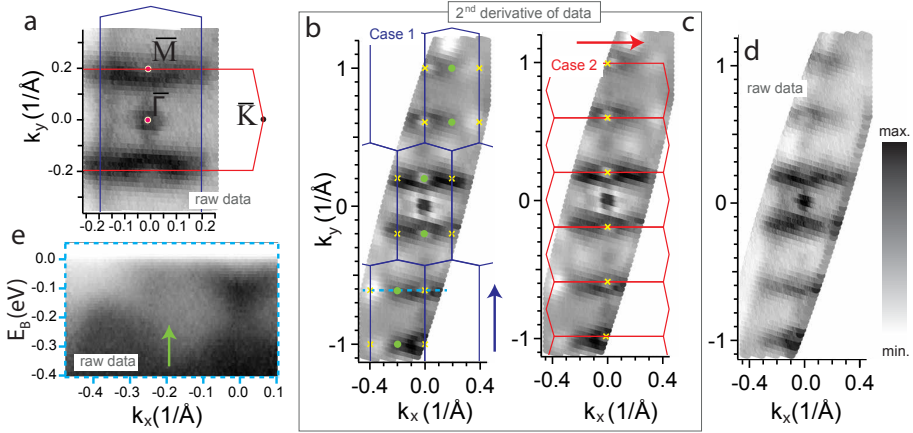


Figure 4.3: (a) ARPES  $I(k_x, k_y)$  map with  $E_B = 15$  meV, recorded in the central portion the first surface Brillouin zone (SBZ). True-to-scale overlays of the expected SBZs from the two orthogonal nanowire domains such as those seen in STM (e.g. Fig. 1(a)) are shown using blue and red solid lines. It is clear that in the experimental geometry used, the ARPES intensity is dominated by one of the two nanowire domains. Panels (b) and (c) show a wide-k-range, constant energy map recorded at a sample temperature of 16K for a binding energy of 30 meV. As the contrast in the experimental data falls off (but remains non-zero) in higher Brillouin zones, the intensity scale shows the second differential (with respect to the binding energy), with the raw data being shown in panel (d). Superimposed on the two sets of identical experimental data in (b) and (c) are SBZs for the two possible nanowire orientations shown in a repeated zone scheme, with the green dots and x's indicating equivalent points in the SBZ. The blue/red arrows indicate the nanowire direction in each case. Panel (e) shows an  $I(k_x, E)$  cut through the raw data at the location in panel (b) indicated by the blue dashed line. All ARPES data were taken with a photon energy of 21.2 eV at a temperature of 20 K.

data a good representation of the electronic structure of a single nanowire surface domain. Of course it is a priori unclear which of the two domains is responsible for the stronger signal. However, as the experiment has recorded data beyond the first Brillouin zone, we can use the observed periodicity to determine the Brillouin zone orientation which corresponds to the  $c(8 \times 2)$  surface symmetry of the nanowire structures. This tells us the relative orientation of the Fermi surface and the nanowires. There are two scenarios:

1. The **blue** version of the Brillouin zone in Figs. 4.2 and 4.3 is correct. In this case, the band bottom of the electron pockets in the first Brillouin zone is not located at a high symmetry  $k$ -point such as the centre of an edge or a corner. This would be unusual, but not impossible. In this scenario, the Au-induced nanowire states would have the greatest velocity for  $k$  along the nanowires. It could correspond to a quasi one-dimensional state if the Fermi surface continues in a rain-gutter-like fashion beyond the first Brillouin zone.
2. The **red** version of the Brillouin zone in Figs. 4.2 and 4.3 is correct. This means that the band-bottom of the electron pocket is centred on the  $\bar{M}$ -point of first Brillouin zone, i.e. the center of the long edge. In this scenario, the Fermi surface of Au-induced bands would form closed contours and the direction of greatest group velocity would be *perpendicular* to the nanowire direction. This situation would lead to the inescapable conclusion that the Au-induced states on Ge(001) are two-dimensional in nature.

Unlike earlier published ARPES data on Au/Ge(001) published [161, 170, 171, 173] Figs. 4.3 (b)–(d) show clear signal beyond the first Brillouin zone (in Fig. 4.3 (d) raw data is shown, while (b) and (c) show second differentials to enhance contrast). The apparent periodicity of the electron pockets—in total, six horizontal streaks of intensity—immediately suggests that the **red** orientation of the Brillouin zone (scenario 2) is correct and the observed electron pockets have a two-dimensional nature. However, from the constant energy maps, which gives an indication of the Fermi surface, this is not beyond doubt. Naively, we could imagine the hole spectral function resemble a modulated rain gutter along the  $k_x$  direction in which the clearly visible band-bottom points [green dots in Fig. 4.3 (b)] and the slightly less clear band bottom like points [yellow crosses in Fig. 4.3 (b)] are equivalent, and the apparent difference in the constant energy maps is due to lack of signal from the continuation of the Fermi surface due to unknown causes. To clarify, Fig. 4.3 (e) shows a constant momentum cut along the line connecting these points in order to display the band bottom energies corresponding to these points. Although the signal at the possible band bottom at  $k_x \approx -0.2 \text{ \AA}^{-1}$  is a little weak, the band bottom at this point seems to be significantly less deep than at  $k_x = 0.0 \text{ \AA}^{-1}$ , which suggests that the points are nonequivalent. Hence, additional evidence for scenario 2 is obtained. Actually, considerations of symmetry really prevent the observed signal from corresponding

#### 4. Absence of Luttinger physics in golden chains on germanium

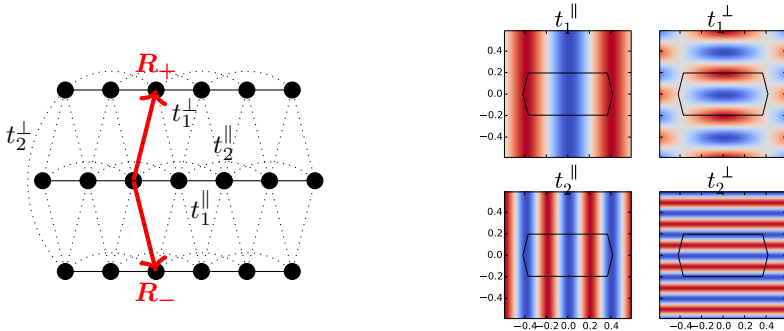


Figure 4.4: Left: Illustration of tight-binding model and hopping parameters. Right: The resulting dispersion relation when only one of the hopping parameters is taken nonzero in arbitrary units. The Brillouin zone is depicted in black. The axes show  $k_{x,y}$  measured in  $\text{\AA}^{-1}$ . Putting  $t_1^\perp > 0$  naturally produces electron pockets comparable to the ARPES data on Au/Ge(001).

to the blue orientation of the Brillouin zone and shows that one of the points should correspond to a local maximum when the other is a local minimum unless additional modulations are present (which do not show up in the data). This is best understood by studying simple tight-binding models, as we shall do next. It leads us to conclude that indeed the red orientation (scenario 2) is correct and the state is unequivocally 2D.<sup>3</sup>

To put the band structure observed in ARPES on a more quantitative footing, we formulate a minimal<sup>4</sup> single-band tight-binding model based on the  $c(8 \times 2)$  surface reconstruction. We start with the idealized lattice that corresponds to the  $c(8 \times 2)$  structure seen in LEED and STM topography. Physically, the shortest-range hoppings should dominate and this is indeed what is found when simulating the data.

We model the nanowire system as a two-dimensional lattice generated by the Bravais lattice vectors  $\mathbf{R}_\pm = (4\mathbf{e}_x \pm 16\mathbf{e}_y)\text{\AA}$ . We will use a pair of integers  $(n, j)$  to label site  $j$  on nanowire  $n$  located at  $\mathbf{R} = n\mathbf{R}_+ + j[\mathbf{R}_- + \mathbf{R}_+]$ . The operators  $c_{\sigma,nj}^\dagger$  ( $c_{\sigma,nj}$ ) create (annihilate) a fermion of spin  $\sigma = \uparrow, \downarrow$  on site  $(n, j)$  and satisfy the canonical anti-commutation relations  $\{c_{\sigma,nj}, c_{\sigma',n'j'}^\dagger\} = \delta_{\sigma\sigma'}\delta_{nn'}\delta_{jj'}$ . The best correspondence with the data is obtained by the model

$$H = \frac{1}{2} \sum_{n,j} t_1^\perp (c_{n,j}^\dagger c_{n+1,j} + c_{n,j}^\dagger c_{n+1,j-1}) + t_1^\parallel c_{n,j}^\dagger c_{n,j+1} + t_2^\parallel c_{n,j}^\dagger c_{n,j+2} + \text{h.c.} \quad (4.1)$$

<sup>3</sup>This conclusion has also been drawn in another synchrotron-based ARPES study of Au/Ge(001) which appeared while we were writing our manuscript [179].

<sup>4</sup>Here, minimal means with the least number of non-zero hopping parameters.

(where h.c. denotes the hermitian conjugate) with the parameters

$$t_1^\perp \approx 130 \text{ meV}, \quad t_1^\parallel \approx 65 \text{ meV}, \quad t_2^\parallel \approx -45 \text{ meV} \quad (4.2)$$

and a chemical potential of  $\mu \approx -134 \text{ meV}$  (see Fig. 4.4 for an illustration of the model). To fix the hopping parameters, we estimated the band bottom to lie around 100–150 meV below  $E_F$  and matched the dispersion relation

$$\varepsilon(k_x, k_y) = -\mu + 2t_1^\perp \cos(4k_x) \cos(16k_y) + t_1^\parallel \cos(8k_x) + t_2^\parallel \cos(16k_x) \quad (4.3)$$

to the data. The corresponding hole part of the dispersion relation is rendered in 3D in Fig. 4.5 and the resulting Fermi surface is compared to the ARPES data. We should note that the tight-binding approximation does not constitute a microscopic model and even as a phenomenological model one knows it misses out on important aspects such as interaction effects, disorder and other couplings. Neglected effects can lead to strong renormalizations of the dispersion relation, loss of coherence and so on, but what is accounted for properly by this model is the surface symmetries which show up consistently in all measurements (LEED, ARPES, STM). This allows one to formulate a family of easily solvable models to explore the ramifications of these symmetries in the shape of the dispersion. Although the true spectral function may be subject to renormalization effects and broadening we argue that—by lack of *ab initio* theory at this point—studying the tight-binding model presents the most effective means to settle the confusion on the direction of the ARPES data compared to the nanowires and to gain a better qualitative understanding of the Au-induced electronic states.

Note that  $t_1^\perp$  is the dominant hopping in Eq. 4.2 with approximately  $t_1^\perp \sim 2t_1^\parallel$ , in line with the conclusion that the direction of highest velocity is perpendicular and not along the wires. This can be considered surprising both because of the apparent conduction channels along the wire direction in STM/STS and because the  $t_1^\perp$ -hoppings correspond to a distance of approximately 1.6 nm in the model while the  $t_1^\parallel$ -hopping corresponds to only  $\sim 0.4 \text{ nm}$ . Another oddity is the positive sign of the dominant hopping parameters as compared to the usual negative sign found from typical *s*-wave overlaps. At the crude level of approximation a tight-binding model offers it is impossible to draw any conclusions from this. It would be interesting to see if a definitive understanding the surface reconstruction [i.e. giant missing row or similar models] in combination with detailed density functional theory calculations support these findings and can lead to a better microscopic understanding in terms of the atom types (Au, Ge or both) and orbitals responsible for the gold induced states.

It is important to note that in arriving at the above results we have considered alternative lattices such as corresponding to the  $8 \times 4$  super structure, and, more importantly, very different values for the hopping parameters. In particular, we have also considered hopping parameters which would be expected for the quasi one-dimensional scenario, i.e. with the dominant hopping in the nanowire direction. The study of the dispersion relations boils down to considering different

#### 4. Absence of Luttinger physics in golden chains on germanium

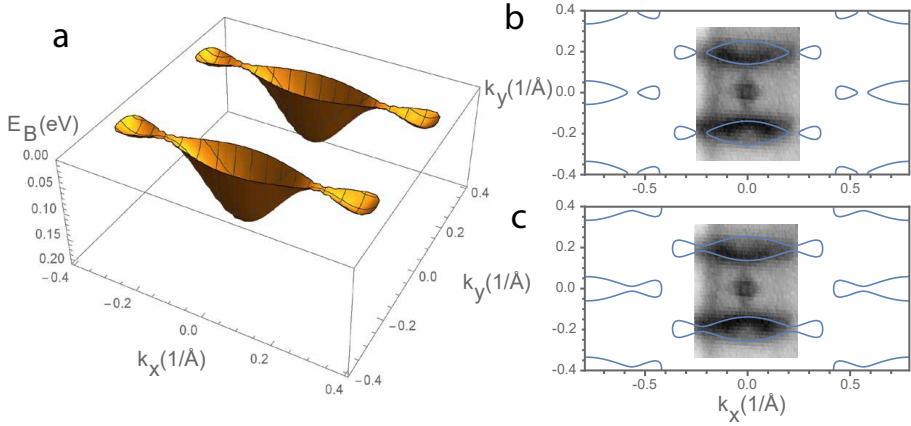


Figure 4.5: (a)  $E(k_x, k_y)$  rendering of the results of the tight-binding model (filled states only) based on Eq. 4.3 with  $\mu = -134$  meV and hopping parameters given in Eq. 4.2. Panels (b) and (c) compare constant energy surfaces in  $k_x, k_y$  taken from the tight binding model at the energies of 0 and -10 meV in (a), with the ARPES data ( $E_B=15$ meV) taken from Fig. 2a.

superpositions of cosine functions in reciprocal space. Easy insight is obtained by examining the allowed terms separately—in particular the ones with the longest wave lengths, corresponding to the shortest range hoppings, as these determine the coarse structure. An example of such explorations is depicted in Fig. 4.5 in the right pane where the different cosines are plotted as height maps when only one of the allowed hoppings is taken to be nonzero. One finds that the  $t_1^\perp$  hopping naturally leads to closed electron pockets in reasonable correspondence with the ARPES data. On the other hand a quasi 1D scenario could be supported by dominant  $t_2^\parallel$  hopping. This reproduces the correct ‘rain gutters’ but it would be physically surprising to have a next-nearest neighbor hopping to be dominant. Finally, there is no term naturally accounting for the additional modulations seen in ARPES in this case.

Two main points thus emerge from the analysis of the tight-binding model, namely that  $t_1^\perp \approx 2t_1^\parallel$ , and that the Fermi surface forms a closed contour along the  $k_x$ -direction, not forming the modulated, yet continuous ‘tramlines’ that would mark a quasi-1D phenomenology of a candidate TLL system. Thus, both the raw ARPES data itself, as well as a simple yet relevant minimal model for the band structure fail to support a 1D scenario for the Au-induced nanowires on Ge(001). In terms of the  $E(k_x, k_y)$  eigenvalues, Occam’s razor points to the two-dimensional character of the Au-induced nanowire states on Ge(001), despite the fact that their topographic signature in STM images looks so one dimensional.

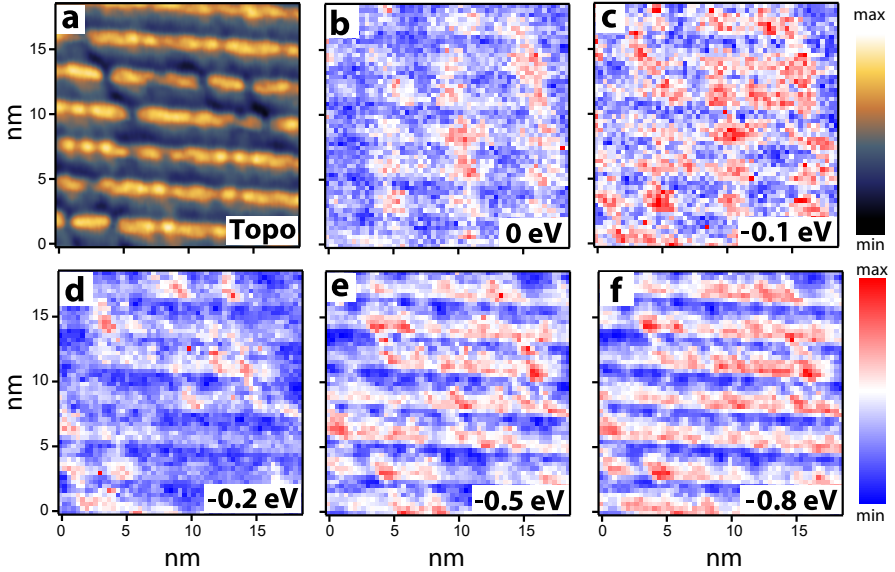


Figure 4.6: (a) Topographic image (bias 1 V, current 0.2 nA) of nanowire sample area for which the LDOS maps shown in (b)–(f) for different bias voltages were measured (set-point 1V and 0.2 nA). On the right the uppermost scale-bar belongs to the topographic image in panel (a), and lower one belongs to the LDOS maps shown in (b)–(f). All data were recorded at a temperature of 4.7 K.

### 4.3.2 Real-space structure of the electronic states

In this section we shift attention from momentum and energy resolved responses by photo-emission of the nanowire system to real-space measurements using an STM. Low temperature STM measurements carried out on identically-prepared Au-induced nanowire samples is shown in Fig. 4.6 (a). In standard STM maps—where bias voltage and target current is held fixed and the height is measured—one should remember that the observed intensity always corresponds to a combination of local electronic density of states and topographic structure of the surface. To probe the density of states more directly, one can fix the height and softly modulate the bias around some set set-point value  $V_{\text{bias}}$  while measuring the current. The recorded  $dI/dV$  is proportional to the electronic LDOS of the surface at  $E = eV_{\text{bias}}$ .

In Fig. 4.6 (b)–(f) the same patch as in pane (a) is imaged using STS at different biases. There are two noteworthy features:

1. At  $V_{\text{bias}} = -0.8$  V we see straight conduction channels running parallel to the wires. However, note that careful inspection shows that the high intensity corresponds to the troughs, not the ridges, as first concluded in

#### 4. Absence of Luttinger physics in golden chains on germanium

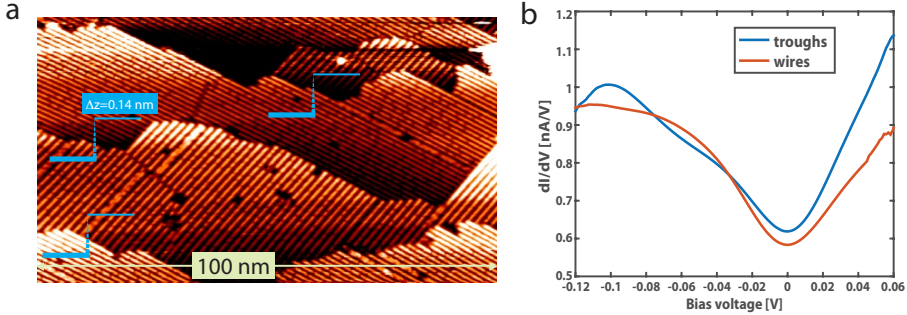


Figure 4.7: (a) Large scale STM topographic image of the Au-induced nanowires on Ge(001) measured at room temperature with a bias voltage of  $-1.5$  V and current set-point of  $0.5$  nA. Indicated in blue are the single-layer steps from one terrace to the next. (b)  $dI/dV$  spectra representative of the nanowires (red curve) and of the troughs between them (blue curve), extracted from a  $20$  nm  $\times$   $20$  nm area in the bulk of a nanowire patch ( $T = 4.7$  K; setpoint current of  $0.2$  nA at a bias of  $-0.1$  V).

Ref. [164].

- At lower biases the  $dI/dV$  maps become more disordered and one could even go as far as arguing that at zero bias a pearl-chain like structure of high intensity spots arises running perpendicular to the wire direction.<sup>5</sup>

The data in Fig. 4.6 are very similar to the data of the detailed STM/STS study in [155], where such features were used to argue against an interpretation of the Au-induced states as one dimensional.

In light of the TLL discussion it is interesting to plot the bias dependence of the  $dI/dV$  as a measure of the behavior of the LDOS close to Fermi level. Curves representative for on-nanowire measurements (red) and for measurements on the troughs between the nanowires (blue), are shown in Fig. 4.7 (b). Both in on-wire and in-trough LDOS curves show a strong asymmetry between negative and positive bias. This asymmetry is robust with respect to the junction resistance and is also independent of the details of any fine structure in individual LDOS curves. In our STS measurements, this asymmetry is always clearly visible, independent of the temperature, location on the surface, and independent of the

<sup>5</sup>The slight angle of the pearl-chain-like structures with respect to the direction normal to the nanowires is comparable to the angle the VW reconstruction has in this direction [155], suggesting a possible relation between this reconstruction and the enhanced LDOS patches. In addition, we note that the so-called bridge atoms, observed in the troughs in topographic images (see Fig. 3b of Ref. [180] for an example in Twente-grown samples), are also possible candidates for the origin of these patches of higher LDOS. When summed over space, these LDOS patches yield the LDOS peak observed at a bias of  $-0.1$  eV in the trough-averaged STS spectra shown in Fig. 4.7(b).

tip condition. Consequently, the STS data shown in Fig. 4.7 (b) are fully representative for tens of regions measured and thousands of individual  $dI/dV$  traces. This asymmetry is relevant, because the TLL prediction is an electron-hole symmetric suppression of the DOS around the Fermi level. Thus, our STS data are incompatible with the  $E/T$  scaling behavior reported in Ref. [113] according to the TLL result

$$\nu(E, T) \propto T^\alpha \cosh\left(\frac{E}{2k_B T}\right) \Gamma\left(\frac{1+\alpha}{2} + i\frac{E}{2\pi k_B T}\right). \quad (4.4)$$

Unfortunately, high-resolution temperature dependent data of a narrow interval around  $E_F$  is not at our disposal. In light of the conclusion that the electronic states represent an inherently two-dimensional system it would be interesting to attempt an exact experimental reproduction of the universal scaling in [113].

The STS data presented here and in Ref. [155] lay bare a discrepancy with those of Ref. [153] in which the straight features in the conductance were linked to the electron pockets seen in ARPES. In past discussions of the dimensionality of the nanowire-related electronic states, differences observed between the energies of the possible 1D states in ARPES and STM data have been suggested to be caused by a shift in the chemical potential, for instance induced by the differences in doping levels of the different substrates used ([181]). However, here we present data taken with ARPES and STM/STS on identically-prepared samples, both using the same batch of substrates from a single Ge(001) wafer. The ARPES data (e.g. Fig. 4.2) enables to easily determine the position of the chemical potential, and no significant shifts are observable between the ARPES data presented here and analogous data reported using differently doped substrates in the literature [161, 170, 171, 173]. Therefore differences in chemical potential or even variation in the details of the sample preparation protocols cannot be used to argue that the electronic states seen within 100 meV of the Fermi level in ARPES are 1D, yet the differential conductance images in STS display essentially 2D patterns when imaged in the same low energy region.

From the above, it is clear that the 1D-like conductance channels observed by STS in the nanowire troughs at higher bias energies [e.g. Fig. 4.6(e,f)] do not come from the low energy electron pockets observed with ARPES. The question is then where do these straight conduction channels come from? Here we propose two alternative explanations:

1. The ARPES data presented here show the presence of both Au-induced surface states, and 2D states derived from the bulk germanium bands. In Ref. [176] it was shown that for interfaces between various metals and Ge(111), surface states and resonances are created with maxima in their charge distributions lying between 5 and 10 layers below the surface. If the situation for Ge(001) were to be similar, sub-surface, 2D Ge states could exist, and, as the tops of the nanowires are at least several germanium layers higher up than troughs between the nanowires [157, 162], the STS

#### 4. Absence of Luttinger physics in golden chains on germanium

---

signal measured in the troughs would be much more likely to pick up a contribution from these germanium subsurface states, thus yielding higher conductance stripes running along the troughs. Put simply: such quasi-2D, Ge subsurface states could ‘shine through’ in the troughs between the nanowires. One can measure photon energy dependent ARPES data from Au/Ge(001) and this shows that the electronic states up to as far as 1.8 eV below  $E_F$  are essentially independent of  $k_z$ , and thus are of 2D character, which would be consistent with the scenario sketched above.

2. Another possible explanation is also closely related to the high degree of corrugation such Au/Ge(001) nanowire surfaces display. A system with spatially inhomogeneous LDOS, but also at the same time strongly varying height profile such as is the case here makes it all but impossible to decouple height and LDOS information in the STS signal. All published work on this system agrees that these samples possess features with a height difference of several atomic layers spatially separated by only 1.6 nm. This is an extremely challenging situation for STM/STS mapping using a real-life tip, the extremity of which may be smaller than, of the same order, or larger than the inter-nanowire trough size. This makes in particular the spatial dependence of STS measurements<sup>6</sup> highly dependent on the sharpness and shape of the tip. Consider setting up an LDOS map with the tip set atop a nanowire—here the choice of set-up bias voltage and current will really set the height difference between the tip and the sample. However, when the tip is set at a trough, the shortest distance from the sample to the tip for a given set-point is less well defined—particularly if the tip apex and the trough profile were to match (like a set of gears). In such a case, it is easy to see how lateral tunnelling could also take place, boosting the final  $dI/dV$  signal for reasons other than an enhanced LDOS at the bottom of the trough itself.

This discussion serves to show that a degree of caution is required in the interpretation of STS data from these systems, a caveat that does not apply to the ‘remote probe’ of the occupied states provided by ARPES experiments.

The data on Au/Ge(001) reveal compelling evidence for a 2D character of the nanowire-induced electron pockets visible in ARPES in par with the bulk-derived Ge(001) states. Forced to consider the system as quasi 2D rather than 1D, we are left with the challenge of explaining the observations that lead to the interpretation of Au/Ge(001) as hosts of a Tomonaga-Luttinger liquid in the first place. In particular the observed power-law dip at the Fermi level of the LDOS and its universal scaling with temperature are tricky to account by another theory. Whether an alternative theory should reproduce the precise predictions for a Luttinger liquid, or whether it should rather have similar features but can

---

<sup>6</sup>Please recall that the electron-hole asymmetry of the top and in-trough DOS curves from STS *was* independent of tip conditions/sharpness.

differ quantitatively depends on the certainty we have about the data being fit precisely by the predicted curves. The asymmetry in the STS data suggests that the correspondence with the TLL predictions is at least lost beyond a certain energy window (as is expected for an effective low-energy theory). A thorough assessment of the theoretical flexibility would benefit from a careful attempt to reproduce the power-law universal scaling and bulk-boundary correspondence for the exponent for the identical window of energies and temperatures used in [113]. Although a complete alternative theoretical characterization of the Au/Ge(001) electronic states is beyond the scope of the present work, we will focus in the next section on what we believe is the most viable explanation for the observed dip in the LDOS and the incoherent signal in the ARPES data at the Fermi level—clear non-Fermi liquid behavior.

## 4.4 Disorder in interacting electron systems

The interplay of disorder and interactions is known to be a general mechanism for non-Fermi liquid behavior in electron systems. Experimentally, an expected signature is an anomalous suppression of the DOS pinned to the Fermi level—either an anomalous (non-Fermi liquid) singular feature in the density of states known as a zero-bias anomaly or a soft (power law) gap. In view of the Au/Ge(001) system, the question is whether the suppression of the LDOS seen at the Fermi level can be due to such an interaction-disorder induced zero-bias anomaly instead of Luttinger liquid physics. Before we turn to this question, let us discuss certain results for interacting disordered systems from the literature.

### 4.4.1 Mechanisms for suppression of the DOS

The underlying mechanism and shape of disorder-interaction induced suppression of the DOS can differ wildly based on dimensionality, amount and type of disorder and the strength and range of interactions. Here we will focus on certain results from the literature for situations without magnetic or spin-orbit effects and the two-dimensional case  $d = 2$ . Note the 2d disordered metals is a wildly debated topic since the scaling theory of disorder predicts universal insulating behavior but metallic behavior is sometimes found. We will focus exclusively on results for the (local) density of states and do not claim to be exclusive in the following. The aim is to provide some intuition and context for the Au/Ge(001) discussion.

For disordered interacting electron systems two classic effects are often discussed:

1. The Efros-Shklovskii Coulomb gap, for systems in the atomic (localized) regime with Coulomb interactions.
2. The Altshuler-Aronov zero-bias anomaly for weak disorder and long-range interactions in the metallic limit.

Before discussing these effects in somewhat greater detail, let us consider a simplified argument useful to gain intuition on how the combination of interactions

#### 4. Absence of Luttinger physics in golden chains on germanium

---

and disorder can lead to a suppression of the DOS.<sup>7</sup>

Consider the atomic limit of a disordered system described as a lattice of localized states with random energies  $\{\epsilon_i\}$ . This description should be valid for states close to the Fermi level when there is Anderson localization. Consider two of those sites with energies  $\epsilon_1, \epsilon_2$  and assume some interaction in the system that couples these states effectively by a potential  $V$ . Then in a mean-field approximation

$$H_{\text{int}} = V c_1^\dagger c_1 c_2^\dagger c_2 \sim V [n_2 c_1^\dagger c_1 + n_1 c_2^\dagger c_2] \quad (4.5)$$

where  $n_{1,2}$  is the occupation of site 1,2 in the ground state. One thus observes that the interaction roughly leads to a renormalization of the energy levels  $\epsilon_{1,2} \rightarrow \epsilon_{1,2} + V n_{2,1}$  hence pushes the energy levels apart but only when one of states was unoccupied and the other occupied, leading to a suppression of the DOS at the Fermi level upon disorder averaging.

Efros and Shklovskii [183] used a more refined argument to show that when we consider the Coulomb interaction  $V(R) = e^2/(\kappa R)$  in a 2D or 3D system, this implies a vanishing of the density of states at the Fermi level by a power law with exponents  $\alpha = d - 1$ . Let us outline their argument: The effective Hamiltonian can be written

$$H = \sum_i \epsilon_i \hat{n}_i + \frac{1}{2} \sum_{i \neq j} V_{ij} \hat{n}_i \hat{n}_j. \quad (4.6)$$

where  $V_{ij} = e^2/(\kappa |\mathbf{r}_i - \mathbf{r}_j|)$ . The spectrum of  $H$  is easily constructed from the single-particle energies  $\epsilon_i$  and occupation numbers  $n_i$  as

$$E_i = \epsilon_i + \sum_j V_{ij} n_j. \quad (4.7)$$

Now imagine taking a particle from an occupied site  $i$  to an unoccupied site  $j$ . The energy difference is

$$\delta E(i \rightarrow j) = E_j - E_i - V_{ij} > 0 \quad (4.8)$$

where the latter term accounts for attractive interaction between the created particle and hole. This leads to the inequality

$$\Delta E = E_j - E_i > V_{ij} \quad (4.9)$$

for all the energies  $E_i, E_j$  where  $E_i$  lies below the Fermi level and  $E_j$  is above the Fermi level. Consider only states in an energy interval of order  $\epsilon$  around the Fermi level. The density of states  $\nu$  is related to the typical distance  $R$  between sites as  $\nu(E_F)\epsilon \sim (L/R)^d$ , since both sides represent the number of states  $N$

---

<sup>7</sup>Adopted from the talk [182].

(where  $\nu(E)$  is the density of states at energy  $E$  and  $L$  is the linear dimension of the system). A typical interaction energy for nearest sites is

$$V_{ij} \sim \frac{e^2}{\kappa R} \quad (4.10)$$

while  $E_j - E_i < 2\epsilon$ . Then, up to unimportant numerical factors, Eq. (4.9) leads to the inequality

$$\epsilon > [\nu(E_F)\epsilon]^{\frac{1}{d-1}}. \quad (4.11)$$

This is inconsistent for a finite  $\nu(E_F)$  when we let  $\epsilon$  go to zero. Hence, argued Efros and Shklovskii, the density of states should vanish at the Fermi level. Assuming that the bound in Eq. (4.11) is saturated and  $\nu E = |E - E_F|^\alpha$  essentially leads to the Efros-Shklovskii prediction

$$\nu(E) \sim |E - E_F|^{d-1}, \quad (4.12)$$

although we must refer to Refs. [183, 184] for a more careful discussion of the argument.

Note that the long range Coulomb interaction plays a crucial role in deriving Eq. (4.12). Hopping is completely neglected in this argument. To see what it does, let us go back to the simple two-site model with localized levels  $\epsilon_{1,2}$ . Hopping introduces an off-diagonal matrix element  $-t$  in the single-particle Hamiltonian such that together with the mean-field interaction we could write something like

$$H_{\text{eff}} = \begin{pmatrix} \epsilon_1 + n_2 V & -t \\ -t & \epsilon_2 + n_1 V \end{pmatrix} \quad (4.13)$$

with energy levels

$$E_{\pm} = \frac{\epsilon_1 + \epsilon_2 + (n_1 + n_2)V \pm \sqrt{[\epsilon_1 - \epsilon_2 + (n_1 - n_2)V]^2 + t^2}}{2}. \quad (4.14)$$

In the absence of interactions,  $t$  leads to simple level separation which parallels the formation of bands in periodic systems when we turn on hopping. Of course, increasing  $t$  leads to delocalization of the states. The mean-field interaction still seems to lead to a suppression of the DOS at the Fermi level, but when the ground state starts consisting of delocalized states, the mean-field treatment would introduce additional terms renormalizing the hopping and the situation becomes much less clear. To handle this limit, i.e. the metallic regime, the model based on localized states is better traded for calculations in the momentum basis. This can be done in a field theoretical framework as first explored by Altshuler and Aranov [185]. Treating the dynamically screened Coulomb interaction in

#### 4. Absence of Luttinger physics in golden chains on germanium

---

disordered perturbation theory, the correction to the DOS was found to have a strong singularity, which for  $d = 2$  reads

$$\delta\nu = -\frac{1}{8\pi^2\hbar D} \ln(|\omega|\tau_0) \ln(|\omega|\tau_1). \quad (4.15)$$

Here,  $D$  is the diffusion constant,  $\tau_0$  is the elastic scattering time and  $\tau_1 = \tau_0(D\kappa^2)^2$ , where  $\kappa = 2\pi e^2 dn/d\mu$  is the inverse screening length.

To establish the small  $\omega$  dependence of the DOS one has to go beyond perturbation theory. A classic result by Finelstein based on renormalization group arguments predicts  $\nu \sim \omega^{1/4}$ . A comprehensive discussion [186] suggests that this may be only accurate in a *perfect metal* state which has vanishing resistivity for which more generally a power law structure  $\nu \sim |\omega|^{\gamma/2}$  can be expected. For a normal metal, with finite resistivity, Ref. [186] predicts a linear Coulomb gap  $\nu \sim |\omega|$  for  $d = 2$ . Finally, for an insulator they find  $\nu \sim |\omega|$ . Note that this corresponds with the Efros-Shklovskii prediction as well as the normal metal prediction, hence for a normal metal this is likely valid throughout the metal-insulator transition. In Ref. [187], a finite temperature result is derived, also under the assumption of finite resistivity. Other approaches, for example based on the Keldysh technique [188] often end up using approximations for which the small  $\omega$  behavior of the DOS becomes unreliable. All treatments seem to agree however on an intermediate frequency result of the form

$$\nu(\omega) \sim \nu_0 \exp\left[-\frac{r_0}{4} \ln(|\omega|\tau_0) \ln(|\omega|\tau_1)\right] \quad (4.16)$$

in line with the perturbative Altshuler-Aronov result (4.15).

Having discussed the Efros-Shklovskii and Altshuler-Aronov effects in some detail, we hope the reader agrees that on the one hand interactions and disorder naturally lead to a suppression of the DOS at the Fermi level, possibly leading to a soft gap or zero-bias anomaly, but on the other hand the theory seems to leave space for the form of this suppression to vary. The assumptions on which the theoretical results are based have to be checked in the situation at hand. For example, both effects rely on the long-range Coulomb interactions. A series of papers based on the Anderson-Hubbard model indicates that short range interactions also lead to a zero-bias anomaly, although the authors claim that the mechanism (driven by kinetic energy) is different [189–191]. Thus strongly correlated materials may show different forms for the suppression of the DOS. Also, anisotropy may lead to different predictions as is illustrated by a theory for multi-wall carbon nanotubes [192] treated as a quasi-2d array of one-dimensional systems finding power-law behavior for the LDOS.

##### 4.4.2 The anomalous LDOS suppression in Au/Ge(001)

Now that we have discussed some background on the interplay of interactions and disorder, we return to the remaining puzzle of the Au/Ge(001) system: the incoherent nature of the electronic states close to the Fermi level seen in ARPES,

and the observation of an anomalous suppression in the density of states at the Fermi level in the STS data (see Fig. 4.7(b)). These observations are consistently found in all published data on Au/Ge(001). On the one hand, the dip in the LDOS at  $E_F$ , and in particular the observation of its universal scaling with both temperature and energy in Ref. [113] has formed the strongest argument in favour of TLL physics in Au/Ge(001) nanowires. On the other hand, the ARPES data presented here rule out TLL-physics for Au-induced nanowires on Ge(001), as their electronic states within 100 meV of the Fermi level are unequivocally shown to be 2D in character. This conclusion is also supported by the STS data from identically-fabricated samples. Therefore, the issue of what else could give rise to the marked departure of the spectral function and (local) density of states from the regular metallic paradigm of the Fermi liquid is one that warrants discussion, which we provide in the following from a theoretical point of view.

In Ref. [113] two other possible explanations are considered for the suppression of the density of states at the Fermi level besides TLL behaviour, namely a Coulomb pseudogap and dynamical Coulomb blockade. The Coulomb blockade is set aside since the experimentally obtained resistance of the tunnelling circuit does not meet the theoretical requirements. We agree that this mechanism for the zero-bias anomaly, which in its standard form relies on the impedance of the tunnelling circuit, would certainly not explain the corresponding ARPES data. We do regard the interplay of disorder and interactions as the most likely cause for the observed data, a conclusion that echoes that made in Ref. [179]. In that case, we should find out which of the mechanisms mentioned above is most likely at play in Au/Ge(001), what discrepancies with the theory remain and how these can be understood and solved.

In Ref. [113] the metallic Altshuler-Aronov anomaly [185] is discussed and dismissed because it predicts exponential behavior close to the Fermi level [187, 193] which did not fit the data of Ref. [113]. The main problem with their conclusion is that they only consider a system in one dimension, but in light of the conclusions of this chapter one should of course use the predictions for a two-dimensional system. For  $d = 2$ , the low-energy dependence of the DOS from the Altshuler-Aronov anomaly has a linear dependence for low energies [186, 187] as discussed in the previous section. This is not really in correspondence with the observed power-law exponent of Ref. [113] which they fit as  $\alpha = 0.61$ . However, as discussed, variations of the theory show that general power-law exponents are also possible [186, 192]. For Au/Ge(001), an interesting approach could be to take the simple band theory described in Sec. 4.3.1 as point of departure and derive the corresponding Altshuler-Aronov result. As the odd shape of the Fermi surface changes the non-interacting propagator, it is a non-trivial question whether the result will be the same or whether power-law behavior will emerge. Moreover, further differences may originate from the details of interaction effects, which may be complicated by nontrivial screening effects.

In  $d = 2$  also the Efros-Shklovskii Coulomb gap has a linear  $\nu \sim |\epsilon|$  prediction and as such seems to deviate from the power-law exponent stated in [113].

#### 4. Absence of Luttinger physics in golden chains on germanium

---

Before dismissing a disordered isolating state in view of tunnelling experiments, however, it is useful to note parallel discussions on universal scaling in transport phenomena in organic conductors [194, 195]. In those systems, the conductance is considered to be caused by hopping between localized states—which corresponds to the conduction mechanism for disordered materials in the Efros-Shklovskii class—and it has been shown that that transport in such systems can give rise to universal scaling with temperature and bias, emulating the TLL predictions [196, 197]. For Au/Ge(001), we regard an Altshuler-Aronov type effect more likely to underlie the suppression of the LDOS than an Efros-Shklovskii type effect because an insulating phase seems harder unite with the ARPES data that shows bands crossing the Fermi level, though be it somewhat incoherent in nature.

A definitive answer on whether a disorder-based theory can predict all the findings for the Au induced states in Au/Ge(001) is still an open question.

#### 4.5 Stability of the Luttinger liquid state

In view of future searches for TLL physics at surfaces of solid-state systems we remark here on the effects of finite chain lengths, higher dimensional coupling and disorder which limit the temperature and energy window in which TLL behavior may be observed. As experimental confirmation of TLL physics often focuses on observations around the Fermi level, this presents a certain tension between theory and experiment. In particular, the low-energy response of quasi one-dimensional systems may be dominated by weak magnetic or charge density order in two or three dimensions, or may become Fermi-liquid-like. Neutron scattering data on materials hosting quasi-1D spin systems are illustrative in this respect. Inelastic neutron scattering experiments on the quantum spin-ladder material  $(\text{C}_5\text{H}_{12}\text{N}_2)\text{CuBr}_4$  [198] and the spin-1/2 Heisenberg chain material  $\text{CuSO}_4\cdot 5\text{D}_2\text{O}$  [199] are well-described in terms of one-dimensional models, which in the pure theory can be shown to be in a spin-Luttinger-liquid phase. While the agreement to the experimental data above a certain threshold energy is remarkable, the correspondence is lost below a threshold energy due to 3D ordering. Another enlightening example comes from the phase diagram of certain transition metal compounds or Bechgaard salts, which show a multitude of ordered phases at low temperatures and even Fermi-liquid-like behavior, while at temperatures above the critical temperature—which can be as high as 100 K—one finds a TLL phase [9]. In fact, also Au/Ge(001) is known to exhibit a high-temperature transition at 585 K. Above this temperature the nanowires display a higher degree of 1D structural order, characterized by simple dimer buckling, while below the STM images indicate a more glassy superstructure with the characteristic VW shapes and the appearance of complex inter-chain correlations [168]. The electronic conduction channels of a surface system like Au/Ge(001) are therefore likely to suffer from similar instabilities towards 2D or 3D ordering or will show a dimensional crossover at some energy scale, even

if they were to host weakly coupled 1D conduction channels. A rough estimate for such a scale may be determined from Renormalization Group arguments, as done below. On a similar note, even in 1D system is the presence of disorder will likely cause deviations from the clean theory below a certain energy scale: one can show quite generally that gaussian disorder is a relevant perturbation leading for repulsive interactions leading to a pinned charge density wave or random antiferromagnetic phase [9, 200] and quasi-periodic disorder can lead to a Mott-like metal-insulator transition, even at incommensurate fillings [201–203].

Assessing at which energy scales ordering effects will dominate is what we will do next.

### 4.5.1 Renormalization Group arguments

Let us ignore for the moment the experimental data we presented in this chapter and entertain the one-dimensional scenario for Au/Ge(001). We imagine that the Fermi surface is approximately straight with the highest velocity of the electronic states parallel to the wires. Our aim here is to estimate the temperature and energy scales for the different transitions expected for a TLL in this case. The temperature scales could be important for systems similar to Au/Ge(001) in relation to higher dimensional coupling, and disorder can be obtained from RG based arguments described in detail Ref. [9] and references therein. We outline this reasoning here applied to the Au/Ge(001) nanowires.

The starting point is an infinite array of one-dimensional wires each described as a TLL with charge and spin velocities  $v_c$  and  $v_s$  and Luttinger parameters  $K_c$  and  $K_s$ . We assume spin-isotropic interactions,  $K_s = 1$ , and adhere to the reported  $K_c \approx 0.26$  [113].

For finite chain length  $L$ , quantization effects may obscure the TLL behavior if the thermal length  $L_T \sim v_c/T$  (in units such that  $\hbar = k_B = 1$ ) becomes comparable to  $L$ . In Au/Ge(001) the maximal nanowire length is approximately  $L \sim 100$  nm. From the maximal  $dE/dk$  at the Fermi level in the ARPES data which is of the order of 1–10 eV Å we obtain a rough estimate for  $v_c$  of the order of  $10^5$ – $10^6$  m/s. This leads to a temperature scale  $T$  of 1–10 meV or 10–100 K. In the conservative estimate of 10 K it is therefore conceivable that finite-size quantization effects pose no limitations on the possible observation of TLL physics in local observables such as the LDOS at the lowest experimentally obtained temperature of order 5K.

Next, let us consider the higher dimensional coupling. As a perturbation to the uncoupled wires, we consider the inter-chain hopping described by the Hamiltonian

$$\delta H = t_{\perp} \sum_{\langle i,j \rangle, \sigma} \int dx \left[ \Psi_{i\sigma}^{\dagger}(x) \Psi_{j\sigma}(x) + \text{h.c.} \right] \quad (4.17)$$

For the repulsive interaction  $K_c \approx 0.26$ , we can neglect superconducting order caused by Cooper-pair hopping. We do need to take density-density interaction and spin-exchange into account which, if not present in the bare Hamiltonian,

#### 4. Absence of Luttinger physics in golden chains on germanium

---

will be generated by second order processes from  $\delta H_{t_\perp}$ . We can compactly write

$$\delta H = J_\alpha \sum_{\langle i,j \rangle, \sigma} \int dx S_i^\alpha(x) S_j^\alpha(x) \quad (4.18)$$

where  $S_i^\alpha(x) = \sum_{\sigma\sigma'} \Psi_{i\sigma}(x) \tau_{\sigma\sigma'}^\alpha \Psi_{\sigma'i}(x)$ . Here  $\tau^0$  denotes the  $2 \times 2$  identity matrix and  $\tau^{1,2,3}$  the Pauli spin-matrices. Assuming spin-rotation invariance, the RG equations to lowest order are [9, 204]

$$\frac{dt_\perp}{dl} = \frac{6 - K_c - K_c^{-1}}{4} \quad (4.19)$$

$$\frac{dJ_\alpha}{dl} = (1 - K_c) J_\alpha + t_\perp^2. \quad (4.20)$$

Starting from small  $t_\perp$  and  $1/3 < K_c < 1$  we find that  $t_\perp$  grows quicker with the RG flow than  $J_\alpha$ , initially, and thus one expects to find the transition temperature  $T_1$  for the dimensional crossover caused by  $\delta H_{t_\perp}$  to occur before the temperature of spin or charge ordering caused by  $\delta H_{J_\alpha}$ . For  $0 < K_c < 1/3$ ,  $\delta H_{J_\alpha}$  always grows faster and hence  $T_2$  is likely to occur first in all cases. An estimate for  $T_1$  may be obtained by neglecting the renormalization for  $K_c$  and  $J_\alpha$ . The dimensional crossover is then expected when the renormalized  $t_\perp$  becomes comparable to the band width  $t_\parallel$ , which based on the band-bottom energy of the Au/Ge(001) ARPES data we take to be of the order of 100 meV for discussion purposes. The crossover energy is estimated as  $T_1 \sim t_\parallel (t_\perp/t_\parallel)^{\nu-1}$ , with  $\nu = (6 - K_c - K_c^{-1})/6$ , which gives  $T_1 \sim t_\perp$  for the non-interacting case  $\nu = 1$ . Setting  $T_1 = 10$  K and  $K_c = 0.26$  we obtain  $t_\perp \sim 10$  meV as the maximal allowable inter-chain hopping, one tenth of the  $t_\parallel$  value.

Similar reasoning can in principle be applied to disorder, and estimates of the localization length  $\xi_{\text{loc}}$  can be obtained [9, 200] from which a temperature follows by setting  $L_T \sim \xi_{\text{loc}}$ . However, since there is no reliable estimate for the disorder strength in Au/Ge(001), no quantitatively meaningful statement can be made here at present.

## 4.6 Conclusions

An extensive experimental study of the Au/Ge(001) system has been performed using LEED, ARPES and STM techniques. Based on these data and theoretical considerations we are led to conclude that a one-dimensional scenario for the Au induced electronic states is unattainable. Our high resolution ARPES data clearly shows a dependence of the low-lying Au-induced electronic states on two orthogonal directions in momentum. The observed  $k$ -space periodicity of the ARPES data fixes irrefutably the orientation of the surface Brillouin zone with respect to the nanowires, showing that the relevant bands have their highest velocity perpendicular to the nanowires. Moreover, the observed periodicity in

$k$ -space cannot be matched with a quasi one-dimensional Fermi surface, and this additionally underpins the form of the ARPES  $I(E, k_x, k_y)$  images which show that this system supports two-dimensional states in which the low-lying electron pockets form closed Fermi surfaces.

Considering a simple tight-binding model based on the  $c(8 \times 2)$  reconstruction as the relevant surface symmetry—consistent with observed LEED pattern, STM data and ARPES data—we find that the qualitative features of the ARPES data are reproduced quite naturally by short-range hoppings. This allowed the hopping to be quantified along and perpendicular to the nanowires, and we found that the latter is the larger, by a factor of two.

In keeping with this, the bias dependence of the spatial maps of the LDOS from STS experiments agrees with a lack of 1D character for the low-lying, Au-induced electron pockets observed in ARPES. The STS spectra measured in the troughs show a broad peak around -0.1 V bias voltage, which we show to be likely to be associated with enhanced LDOS patches observed in the maps. These patches resemble pearl-chain-like structures oriented almost perpendicular to the nanowire direction and are most clearly resolved at the Fermi-level. These observations from STS agree well with the conclusions from ARPES of the dominance of electronic hopping perpendicular to the nanowire direction.

Taken together, all these findings prohibit the observation of one-dimensional physics at low energies in these materials, and thus also exclude the existence of a Tomonaga-Luttinger liquid in the nanowire samples. The density of states close to the Fermi level observed in both tunneling data and the  $k$ -integrated photoemission data is anomalously suppressed. As this cannot be connected to TLL physics, it is most likely an Altshuler-Aronov-like effect, caused by the interplay of disorder and interactions in a two-dimensional metal. Several theoretical studies indicate that the suppression of the tunneling density of states could be explained this way but in fairness it should be stated that a quantitative theoretical underpinning for Au/Ge(001) remains elusive at this point.



# Bragg pulses and Newton's cradles

古池や蛙飛び込む水の音

松尾 芭蕉

This chapter represents the transition in this thesis from equilibrium to non-equilibrium problems. Like in the previous chapter we will deal with modelling aspects of an experimentally relevant situation, although the experiment taking center stage this time is a classic in the literature, namely the famous quantum Newton's cradle experiment performed in the group of David Weiss in 2006 [12]. We pursue a detailed modeling of a Bragg pulse, which was used in this experiment to give a momentum kick to the atoms in opposing directions which initiated long lasting oscillations in the optical trap. The lack of thermalization in this system has been a driver for many theoretical efforts on out-of-equilibrium physics and thermalization in closed quantum systems in recent years. Our focus will be partly on studying microscopic properties of the Bragg pulse which could give insights relevant for experiments and partly on constructing a mathematical testing ground for approximate methods from equilibrium physics to see what happens when they are applied beyond their naively expected domain of applicability. This theme will be continued in the following two chapters of this thesis. The work presented in this chapter is based on Phys. Rev. Lett. **116** 225302 (2016).

## 5.1 Introduction

The study of many-body quantum physics has recently been transformed by progress achieved in experiments on ultracold atoms [11]. The context of one-dimensional (1D) bosonic gases provides a particularly fertile ground for investigating physics beyond traditional paradigms [205], with concepts such as Luttinger liquids and integrability [9] playing a primary role.

One of the main probes of cold gases is Bragg spectroscopy [206–208], which consists in applying a pulsed monochromatic laser grating onto the gas, thereby

creating excitations at (multiples of) the recoil momentum  $q$ . In [209, 210], a two-pulse sequence was optimized to populate the first  $\pm q$  momentum satellites of a Bose-Einstein condensate. The theoretical description of this sequence relied on a two-state model where many-body dynamics were not included. In 1D however, many-body effects are inescapable. One of the fundamental models in this context is the Lieb-Liniger gas [19] of  $\delta$ -interacting bosons. This model is relevant to the description of experiments [16], most prominently the quantum Newton’s cradle experiment [12], in which a Bragg pulse is used to initiate oscillations. Bragg spectroscopy has also recently been used to investigate correlated 1D Bose gases of rubidium [211] and cesium [212], where heating resulting from the Bragg pulse was measured and matched using linear response in the Lieb-Liniger gas [213].

Our main objective is to model the effects of Bragg pulses for strongly correlated 1D Bose gases, from first principles, without approximation (so beyond linear response), for experimentally relevant setups. We study instantaneous pulses of varying amplitude  $A$  and wavevector  $q$  via their effect on physical observables: the time-dependent local density of the gas, and the experimentally more accessible momentum distribution function (MDF). We will first focus on the Tonks-Girardeau limit [214–216] of hard-core bosons both on a periodic interval and in a harmonic trap [217–225], but also discuss certain finite interaction effects.

## 5.2 Theoretical setup

A Bragg pulse is modeled as a one-body potential  $V(x, t) = V_0 \cos(qx - \omega t)$  coupling to the density  $\rho(x) = \Psi^\dagger(x)\Psi(x)$ . Here  $\Psi^\dagger(x), \Psi(x)$  denote bosonic creation and annihilation operators with canonical equal-time commutation relations  $[\Psi(x), \Psi^\dagger(y)] = \delta(x - y)$ . The general case treats traveling waves perturbing the gas for a finite duration  $T_0$ , but we will focus on the limit  $T_0 \rightarrow 0$  and moreover only consider a static grating of the gas by taking  $\omega = 0$ . In this regime the motion of the particles during the pulse can be neglected (the Raman-Nath limit), and the perturbation is also known as a Kapitza-Dirac pulse [226, 227]. Taking the limit  $T_0 \rightarrow 0$  while keeping  $A = V_0 T_0$  finite, the Bragg pulse operator  $\hat{U}_B$  is given by

$$\hat{U}_B(q, A) = \exp\left(-iA \int dx \cos(qx)\rho(x)\right), \quad (5.1)$$

where we have set  $\hbar = 1$  as usual. The action of the instantaneous pulse on the ground state  $|\psi_{\text{GS}}\rangle$  generates the initial state of a quantum quench [228–230]. Typical experimental pulses [12, 211, 212, 231] correspond to Bragg momentum  $q \sim 2\pi\rho_0$  and  $A \sim 1$ , where  $\rho_0$  is the mean density.

For the post-pulse time evolution we use the Lieb-Liniger model

$$H_{\text{LL}} = - \sum_{i=1}^N \frac{1}{2m} \frac{\partial^2}{\partial x_i^2} + 2c \sum_{1 \leq i < j \leq N} \delta(x_i - x_j), \quad (5.2)$$

with periodic boundary conditions (ring) or with an additional one-body potential modelling a harmonic trap,  $V_{\text{trap}}(x) = \frac{1}{2}m\omega^2 x^2$ . Most of the results based on the Lieb-Liniger model which are presented here correspond to the hardcore or Tonks-Girardeau (TG) limit corresponding to infinite interaction  $c \rightarrow \infty$ . We are generally interested in the thermodynamic limit  $N, L \rightarrow \infty$  with  $N/L = \rho_0$  for the ring. For the trap, this implies the scaling  $\omega \rightarrow 0$  with  $\omega N$  fixed. Presented data is produced with  $m = 1$ .

As usual, we can use the a Jordan-Wigner string to map bosonic fields to fermions

$$\Psi(x) = \exp\left(i\pi \int^x dy \rho(y)\right) \Psi_F(x) \quad (5.3)$$

also known as the Fermi-Bose mapping [215]. On the level of the many-body wavefunctions this leads to  $\psi_B(\mathbf{x}; t) = \prod_{1 \leq i < j \leq N} \text{sgn}(x_i - x_j) \psi_F(\mathbf{x}; t)$ , where  $\mathbf{x} = \{x_j\}_{j=1}^N$  and  $\psi_F(\mathbf{x}; t)$  is the usual Slater determinant of the free single-particle wavefunctions,  $\psi_F(\mathbf{x}; t) = \det_N [\psi_j(x_i; t)] / \sqrt{N!}$ . In using the Fermi-Bose mapping when modeling additional perturbations such as the application of the Bragg pulse, note that we must switch to a fermionic representation in the time-evolution operator as well. Since the Bragg pulse only couples to the density, which is insensitive to particle statistics, the bosonic and fermionic representation are identical in form.

Studying the time evolution after a Bragg pulse  $\hat{U}_B(q, A)$  can be considered as a quantum-quench problem [230] with initial state

$$\psi_{q,A} = \hat{U}_B(q, A)|GS\rangle. \quad (5.4)$$

In general, studying post-quench dynamics is a tough problem. In case the initial quenched state can be expanded in the eigenbasis of the final Hamiltonian, i.e. one knows the overlaps, the calculation becomes in principle doable although it might remain intractable in practice. In the case of the Kapitza-Dirac limit the overlaps of the initial state and the eigenstates are readily derived. We will come back to the point of tractability when we discuss results.

The simplest way to find the many-body wavefunctions right after application of the pulse is to consider the single-particle states in the fermionized model, which obtain an additional phase according to

$$\psi_j(x; t = 0) = \frac{1}{\sqrt{L}} e^{-iA \cos(qx)} e^{-i\lambda_j x}, \quad (5.5)$$

## 5. Bragg pulses and Newton's cradles

---

where the rapidities are  $\lambda_j$  correspond to the fermionic momentum. Note that the Bragg momentum is quantized due to the periodic boundary conditions:  $q = \frac{2\pi}{L}n_q$  with  $n_q \in \mathbb{N}$ .

Expanding Eq. (5.5) in plane waves, the time-dependence is easily obtained and gives

$$\psi_j(x; t) = \sum_{\beta=-\infty}^{\infty} \frac{I_{\beta}(-iA)}{\sqrt{L}} e^{-i(\lambda_j+\beta q)x} e^{-i(\lambda_j+\beta q)^2 t/2m}, \quad (5.6)$$

with  $I_{\beta}(z)$  the modified Bessel function of the first kind. This also immediately provides the matrix elements of  $\hat{U}_B(q, A)$  as

$$\langle \boldsymbol{\lambda} | \hat{U}_B(q, A) | \boldsymbol{\mu} \rangle = \det \left[ \left( I_{\frac{\lambda_j - \mu_k}{q}}(-iA) \delta_{\lambda_j, \mu_k}^{(q)} \right)_{j,k} \right], \quad (5.7)$$

where  $\delta_{\mu, \lambda}^{(q)} = \delta_{(\mu - \lambda) \bmod q, 0}$ , as  $\hat{U}_B(q, A)$  is a single-body operator. From here, the overlaps  $\langle \boldsymbol{\lambda} | \hat{U}_B(q, A) | GS \rangle$  important for specifying the post-quench initial state can simply be read off.

A nice derivation of Eq. (5.7) can be performed in standard many-body theory in the bosonic basis as well. By representing the many-particle states

$$|\boldsymbol{\lambda}\rangle = \frac{1}{\sqrt{N!}} \int d^N x \psi_B(\mathbf{x} | \boldsymbol{\lambda}) \Psi^\dagger(x_1) \dots \Psi^\dagger(x_N) |0\rangle, \quad (5.8)$$

with  $\psi_B(\mathbf{x} | \boldsymbol{\lambda}) = \prod_{j < k} \text{sgn}(x_j - x_k) \det[\exp(ix_j \lambda_k)]$ , to write

$$\begin{aligned} \langle \boldsymbol{\lambda} | \hat{U}_B(q, A) | \boldsymbol{\mu} \rangle &= \frac{1}{N!} \int d^N x d^N x' \psi_B^*(\mathbf{x} | \boldsymbol{\lambda}) \psi_B(\mathbf{x}' | \boldsymbol{\mu}) \\ &\times e^{-iA \sum_{j=1}^N \cos(qx_j)} \langle 0 | \Psi^\dagger(x_N) \dots \Psi^\dagger(x_1) \Psi(x'_1) \dots \Psi(x'_N) | 0 \rangle. \end{aligned} \quad (5.9)$$

Although this representation may look overly complicated, in fact one can use that the variables  $x_j, x'_k$  act as dummy variables under the integral sign to reshuffle terms, many of which turn out to be equal. For the TG eigenstates this leads to a determinant of decoupled integrals of the form

$$\frac{1}{L} \int_0^L dx e^{ix(\lambda_j - \mu_k) - iA \cos(qx)} = I_{\frac{\lambda_j - \mu_k}{q}}(-iA) \delta_{\lambda_j, \mu_k}^{(q)} \quad (5.10)$$

and hence to Eq. (5.7).

The important ingredient used in this derivation is that the commutation of the density operator with the field operator can be done according to

$$\Psi(y) F[\rho(x)] = F[\rho(y) + \delta(x - y)] \Psi(y) \quad (5.11)$$

for any function  $F$ , which in the end also underlies the single-particle equation Eq. (5.5). The benefit of this latter derivation is that one could easily use the full wavefunctions for Lieb-Liniger in the case  $c \neq 0$  and find a representation for the matrix elements of  $\hat{U}_B(q, A)$  which looks a bit simpler than the ones obtained when sticking to purely first quantized language. However, we still have not been able to evaluate the expression for general  $c$ .

## 5.3 Results

In relation to the quantum Newton's cradle experiment, the momentum distribution function is the most physically interesting result we have obtained from a detailed modelling of the Bragg pulse, including a comparison of the trapped and the periodic system. From a theoretical point of view, it is also interesting to look at the steady state and results concerning the density profile in time and density fluctuations in particular as they will serve as a test bed to compare approximate theoretical approaches.

### 5.3.1 Steady state

States of the Lieb-Liniger model in the thermodynamic limit are best described in terms of a density of rapidities  $\rho(\lambda)$ . One way of fixing the density describing the state in the late-time limit is by a generalized thermodynamic Bethe ansatz procedure based on the expectation values of conserved quantities, or via the quench action approach working directly with the thermodynamic limit of the overlap coefficients [3, 232–234]. In both cases, one ends up extremizing a free energy or action functional. The saddle point gives the desired density, which in our case reads

$$\rho_{q,A}^{\text{sp}}(\lambda) = \frac{1}{2\pi} \sum_{\alpha} |J_{\alpha}(A)|^2 [\theta(\lambda - \alpha q + \lambda_F) - \theta(\lambda - \alpha q - \lambda_F)]. \quad (5.12)$$

Note that this is a sum of copies of the ground state distribution  $\rho_{\text{GS}}(\lambda) = (1/2\pi)[\theta(\lambda + \lambda_F) - \theta(\lambda - \lambda_F)]$  displaced by multiples of the Bragg momentum  $q$  (see Fig. 5.1).

### 5.3.2 Density profile

The expectation value of the density operator after the Bragg pulse in the thermodynamic limit is defined as

$$\langle \hat{\rho}(x, t) \rangle = \langle \psi_{q,A} | \Psi^{\dagger}(x, t) \Psi(x, t) | \psi_{q,A} \rangle. \quad (5.13)$$

We can compute this function in the TG limit in three equivalent ways: (i) using the saddle point state and the Quench Action approach it is possible to perform the full calculation in the bosonic basis; (ii) since the Fermi-Bose mapping leaves the density  $\Psi^{\dagger}(x)\Psi(x)$  invariant, we can also work in the fermionic basis for which the combined effects of the Bragg pulse and time-evolution are easily accounted for; (iii) finally, we can treat the same problem in the Tomonaga-Luttinger model

## 5. Bragg pulses and Newton's cradles

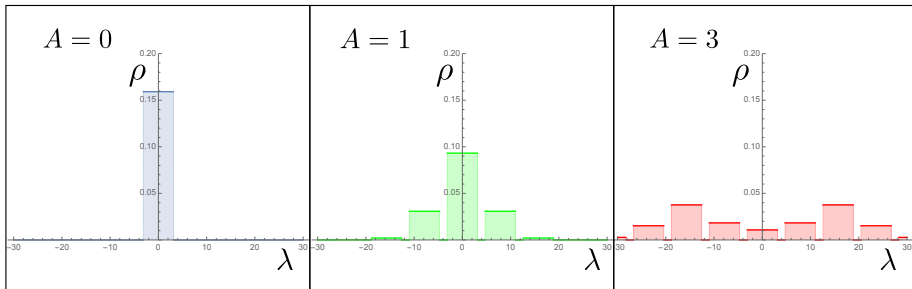


Figure 5.1: The saddle-point root density  $\rho = \rho_{q,A}^{\text{sp}}(\lambda)$  for different values of  $A$  describing the steady state after the Bragg pulse in the TG limit. We used  $q = 5\pi/2$  and unit density.

by including a quadratic band curvature term. The nonlinear Luttinger liquid (nLL) Hamiltonian is then given by

$$H_{\text{nLL}}^{(0)} = \int dx \sum_{\alpha} \Psi_{\alpha}^{\dagger} \left[ -i\alpha v_F \partial_x - \frac{1}{2m} \partial_x^2 \right] \Psi_{\alpha} \quad (5.14)$$

where  $\alpha = R, L = +, -$ ,  $v_F = \lambda_F/m = \pi\rho_0/m$  and  $\Psi_{R,L}$  denotes the annihilation operator of fermionic right- or left-mover fields.

The Hamiltonian in (5.14) can be obtained from the fermionic dual of the Lieb-Liniger model in the TG limit by expanding the dispersion relation around the Fermi points. The left and right movers simply correspond to positive and negative momenta, but with momenta shifted by  $\mp k_F$ . The ground state corresponds to all  $k < 0$  modes of  $\Psi_R$  occupied and all  $k > 0$  modes of  $\Psi_L$ .

The interesting aspect of using the model in terms of left and right movers is that there is a straightforward way to generalize to an interacting model. A number of recent advances in the equilibrium theory for one-dimensional systems show that the most relevant terms of a short range interaction can be accounted for in a fashion similar to Fermi liquid theory by going to a quasi-particle basis. The corresponding fermions  $\tilde{\Psi}_{R,L}$  remain weakly interacting, and can to first approximation be considered free with dynamics governed by the Hamiltonian [58]

$$H_{\text{nLL}}^{(0)} = \int dx \sum_{\alpha} \tilde{\Psi}_{\alpha}^{\dagger} \left[ -i\alpha v_s \partial_x - \frac{1}{2m^*} \partial_x^2 \right] \tilde{\Psi}_{\alpha}. \quad (5.15)$$

Here  $v_s$  and  $m^*$  correspond to the renormalized dispersion (dressed energy) of excitations at the Fermi point in the equilibrium Lieb-Liniger model. The relation

between the fermionic quasi-particles and the bare fermions is given by

$$\begin{aligned}\Psi_\alpha(x) &= F_\alpha(x)\tilde{\Psi}_\alpha, \\ F_\alpha(x) &= e^{-2\pi i \int^x dy \left\{ \left[1 - \frac{1}{2\sqrt{K}} - \frac{\sqrt{K}}{2}\right] \tilde{\rho}_\alpha(y) + \left[\frac{1}{2\sqrt{K}} - \frac{\sqrt{K}}{2}\right] \tilde{\rho}_{-\alpha}(y) \right\}}.\end{aligned}\tag{5.16}$$

Together, Eq. (5.15) and (5.16) can be used to compute dynamical correlations at zero temperature in the vicinity of the Fermi points for general gapless one-dimensional systems which is one of the successes of the past years in the study of one-dimensional systems beyond the Luttinger liquid paradigm.

All three computations of  $\langle \hat{\rho}(x, t) \rangle$  (bosonic, fermionic and nonlinear Luttinger liquid) are instructive, but we will focus on the nLL result as it is by far the most surprising in the present out-of-equilibrium context of the Bragg pulse. On the technical level, the calculations using the Fermi-Bose mapping or the Quench Action approach are similar and can be used to verify the result in the TG limit.

In the nLL theory, the slowly fluctuating components of the density operator can be expressed as [235]

$$\begin{aligned}\Psi^\dagger \Psi &\sim \rho_0 + [\rho_R + \rho_L] \\ &\sim \rho_0 + \sqrt{K}[\tilde{\rho}_R + \tilde{\rho}_L].\end{aligned}\tag{5.17}$$

We will use this as an identity both in the unitary operator implementing the Bragg pulse as in the density as observable for which we want to compute the expectation value. The computation splits into separate contributions from the right and the left movers. Let us focus on the right movers.

One has the following behavior for the modes

$$\hat{U}_B^\dagger \tilde{\Psi}_{R,k} \hat{U}_B = \sum_\beta I_\beta (-i\sqrt{K}A) \tilde{\Psi}_{R,k-\beta q}\tag{5.18}$$

This leads in the thermodynamic limit to

$$\langle 0 | \hat{U}_B^\dagger \tilde{\Psi}_R^\dagger(x, t) \tilde{\Psi}_R(x, t) \hat{U}_B | 0 \rangle = \sum_{\beta \neq 0} J_\beta \left( -2\sqrt{K}A \sin \frac{\beta q^2 t}{2m^*} \right) \frac{e^{-i\beta q[x-v_s t]}}{2\pi i \beta q t / m^*}\tag{5.19}$$

where we used the quasi-particle dispersion for the right movers

$$\tilde{\xi}_{R,k} = vk + \frac{k^2}{2m^*}\tag{5.20}$$

and Graf's summation formula [236]. Here  $|0\rangle$  denotes the ground state in the appropriate model. Combining Eq. (5.19) with a similar expression for left movers in the thermodynamic limit we arrive at

$$\langle \hat{\rho}(x, t) \rangle_{nLL} = \rho_0 + \sqrt{K} \sum_{\beta \neq 0} J_\beta \left( -2\sqrt{K}A \sin \frac{\beta q^2 t}{2m^*} \right) \cos(\beta q x) \frac{\sin(\beta q v_s t)}{\pi \beta q t / m^*}.\tag{5.21}$$

## 5. Bragg pulses and Newton's cradles

In the equilibrium case and the computation of dynamical correlations, the use of Eq. (5.15) is justified by Renormalization Group arguments. Here, there is no such justification. It is all the more surprising that the exact result is recovered in the TG limit. Because of this and since Eq. (5.15) does include the most relevant terms of a general interacting model, we expect that there will be a range of  $q$  and  $A$  for which Eq. (5.21) is a good approximation. The importance here is that this would hold beyond the Lieb-Liniger model. A more detailed discussion will feature in future work. Notice that the result in a linear Luttinger liquid calculation  $\langle \hat{\rho}(x, t) \rangle_{\text{LuttLi}} = \rho_0 - K A q \cos(qx) \sin(qv_s t)/\pi$ , which can be obtained by taking the limit  $1/m^* = 0$  in Eq. (5.21), only captures the behavior for very short times and gives unphysical results for intermediate to late times.

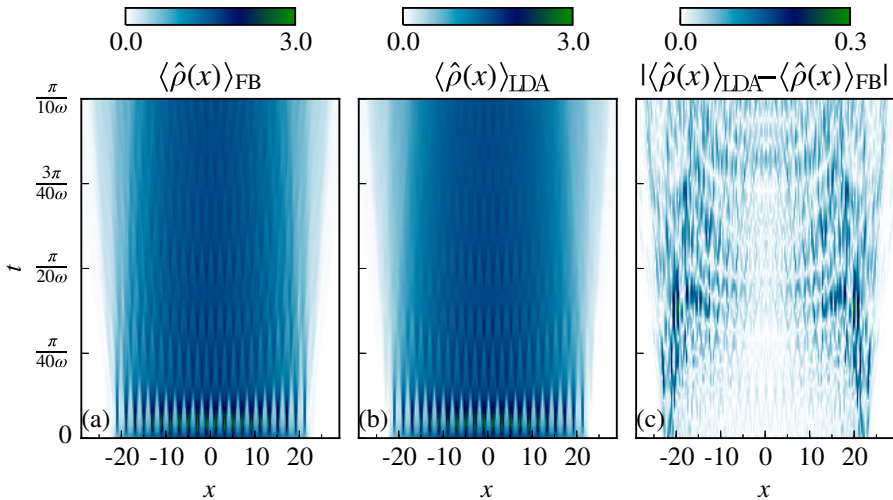


Figure 5.2: Time evolution of the density in a trap, computed with: the FB mapping for  $N = 50$  particles (a), the exact result on a ring with an LDA accounting for the trap (b). The difference between the two results is shown in panel (c). The Bragg pulse parameters are set to  $A = 1.5$  and  $q = \pi$  with  $\omega = 10/N$ .

Let us shift attention to another approximate method often employed in equilibrium physics, namely the local density approximation (LDA) which, for the gas in a parabolic trap, amounts to replacing the value for the mean density by a space dependent value corresponding to the ground-state density profile in the trap. In the present case, we can use a similar approach out of equilibrium and replace the mean density in the result (5.21) exact in the TG limit by the space dependent density in the trap. It turns out that this approximation is considerably improved when one introduces the classical harmonic motion of the density profile in accordance with the exact  $t = 0$  MDF Eq. (5.33) and in fact

leads to a surprisingly accurate reproduction of finite-size in-trap simulations obtained using the Fermi-Bose mapping, as we discuss next.

In the thermodynamic limit the ground state density profile in a harmonic trap is given by

$$\rho_{\text{GS}}(x) = \langle \hat{\rho}(x) \rangle_{\text{GS}} = \frac{1}{\pi} \sqrt{mN\omega - m^2\omega^2 x^2}. \quad (5.22)$$

Writing  $\rho(x, t; \rho_0)$  for the function in Eq. (5.21) for a gas with mean density  $\rho_0$  in the TG limit  $K = 1$ ,  $v_s = \pi n/m$ ,  $m^* = m$ , our result for the improved LDA in the trap reads

$$\rho_{\text{LDA}}(x, t) = \sum_l J_l(A)^2 \rho \left( x - \frac{lq}{\omega m} \sin(\omega t), t; \rho_{\text{GS}} \left( x - \frac{lq}{\omega m} \sin(\omega t) \right) \right). \quad (5.23)$$

Fig. 5.2 shows this function compared to the FB mapping results. It appears that this way of applying the LDA leads to pretty accurate predictions in this case, in particular for the region where the density is large which has the smallest gradients. The discrepancy of the LDA with the exact simulation is initially largest at the edges of the cloud of atoms which has diverging gradient, as expected, and then propagates inwards towards the center of the cloud.

### 5.3.3 Momentum distribution function

The momentum distribution function (MDF)  $\langle \hat{n}(k, t) \rangle$  after the Bragg pulse can be defined as the Fourier transform of the one-body density matrix, which due to the breaking of translational invariance by the pulse, leads to the expression

$$\langle \hat{n}(k, t) \rangle = \int dx dy e^{i(x-y)k} \langle \psi_{q,A} | \Psi^\dagger(x, t) \Psi(y, t) | \psi_{q,A} \rangle \quad (5.24)$$

Thanks to Eq. (5.11), the one-body density matrix at  $t = 0$  (after the Bragg pulse) is readily computed as

$$\langle \hat{U}_B^\dagger(q, A) \Psi^\dagger(x) \Psi(y) \hat{U}_B(q, A) \rangle = \langle \Psi^\dagger(x) \Psi(y) \rangle e^{-i2A \sin(q \frac{x-y}{2}) \sin(q \frac{x+y}{2})}. \quad (5.25)$$

Since the latter equality follows strictly from the commutation relations of the Bose fields with the density it holds irrespective of interaction or geometry. For the case of the ring geometry, the associated MDF is

$$\langle \hat{n}(k, t = 0) \rangle = \frac{1}{L} \int_0^L d\xi e^{ik\xi} I_0(i2A \sin(q\xi/2)) \langle \Psi^\dagger(\xi) \Psi(0) \rangle \quad (5.26)$$

where we defined  $\xi = x - y$  and used the integral

$$\frac{1}{L} \int_0^L dy e^{-i2A \sin(q\xi/2) \sin(qy+q\xi/2)} = I_0(i2A \sin(q\xi/2)) \quad (5.27)$$

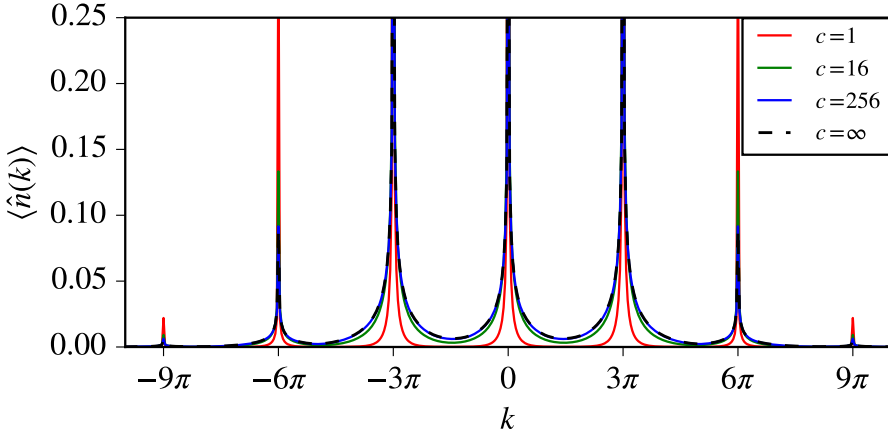


Figure 5.3: The initial MDF ( $t = 0$ ) for  $A = 1.5$ ,  $q = 3\pi$  and different values of the interaction strength  $c$ . The finite- $c$  interactions cause a decrease of the width of the satellites but do not influence their relative heights.

under the assumption that  $qL/2\pi$  is integer. Using the convolution theorem we obtain

$$\langle \hat{n}(k, t = 0) \rangle = \sum_{k'} f(k') \langle \hat{n}(k - k') \rangle_{\text{GS}} \quad (5.28)$$

where

$$f(k) = \frac{1}{L} \int_0^L dx e^{ikx} I_0(i2A \sin(qx/2)) \quad (5.29)$$

and  $\langle \hat{n}(k) \rangle_{\text{GS}}$  is the MDF of the ground state.

Using the expansion  $I_0(z) = \sum_{n=0}^{\infty} (\frac{1}{4}z^2)^n / (n!)^2$  one finds

$$\begin{aligned} I_0(i2A \sin(qx/2)) &= \sum_{n=0}^{\infty} \frac{(-1)^n}{(n!)^2} A^{2n} \sin^{2n}(qx/2) \\ &= \sum_{n=0}^{\infty} \sum_{l=-n}^n \frac{(-1)^{n+l} (2n)!}{(n!)^2 (n-l)! (n+l)!} \left(\frac{A}{2}\right)^{2n} e^{ilqx} \end{aligned} \quad (5.30)$$

where we used the binomium to expand in plane waves.

The order of the sums can now be interchanged. Defining the coefficients

$$c_l(A) = \sum_{n=|l|}^{\infty} \frac{(-1)^{n+l} (2n)!}{(n!)^2 (n-l)! (n+l)!} \left(\frac{A}{2}\right)^{2n} \quad (5.31)$$

we obtain  $f(k) = \sum_l c_l \delta_{k,lq}$ . The coefficients  $c_l(A)$  can in fact be resummed and expressed in terms of a Besselfunction

$$c_l(A) = J_l(A)^2. \quad (5.32)$$

The  $t = 0$  post-pulse MDF can therefore be exactly expressed in terms of the MDF before the pulse  $\langle \hat{n}(k) \rangle_{\text{GS}}$  as

$$\langle \hat{n}(k, t = 0) \rangle = \sum_{l=-\infty}^{\infty} J_l(A)^2 \langle \hat{n}(k + lq) \rangle_{\text{GS}}. \quad (5.33)$$

Note that this result holds for arbitrary interaction strength  $c$  with  $\langle \hat{n}(k) \rangle_{\text{GS}}$  the appropriate ground state MDF. The result is plotted in Fig. 5.3 for different values of  $c$ . The influence of the finite interactions resides solely in the groundstate MDF  $\langle \hat{n}(k + ql) \rangle_{\text{GS}}$ , leading to a decreasing width of the peaks as one goes from the hard-core limit ( $c \rightarrow \infty$ ) to the BEC limit ( $c \rightarrow 0$ ). In contrast, Eq. (5.33) shows that their relative heights are completely determined by the value of  $A$ .

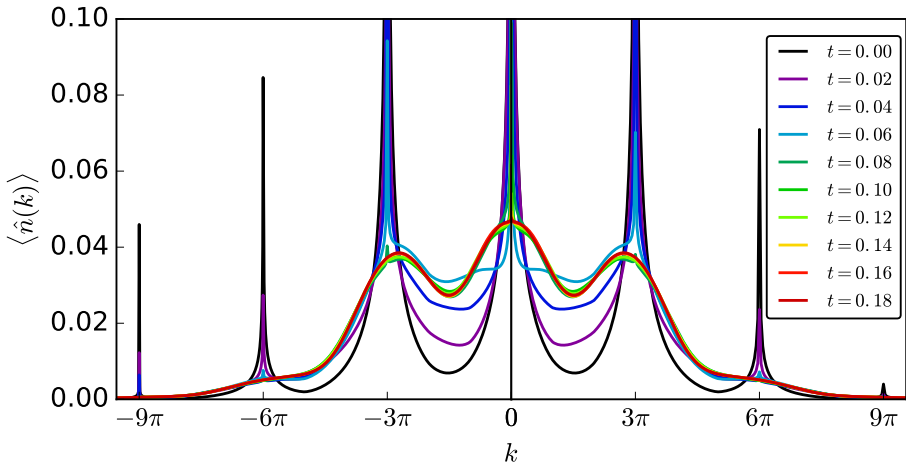


Figure 5.4: Time evolution of the MDF after a Bragg pulse with  $q = 3\pi$  and  $A = 1.4$ , computed with the QA approach (left half) and the FB mapping (right half). Because the FB mapping treats a finite system ( $N = 50$ ) the momenta are quantized, causing less pronounced peaks for short times. All other results are in excellent agreement with the QA computations.

The full time evolution of the MDF can also be studied using the quench action approach or the FB mapping [3, 237]. The relaxation of the sharp  $t = 0$  peaks to the ghost shaped features well known from the Newton's cradle experiment on very short time scales is probably the most relevant relation between

the experimental setup of David Weiss and the present theoretical investigations. The excellent correspondence of quench action and FB results is an indication of the quality of the finite size results using the FB mapping endowing trust in the conclusions reached which are particularly relevant for the case with an harmonic trap which at present is beyond reach for the quench action approach.

In Fig. 5.5 the result for the in-trap dynamics of both the MDF and the density is presented computed with the FB mapping. The perfect recurrences are an artifact of expected to diminish for finite interactions. The most remarkable aspect is the large difference of the relaxation time-scale due to dephasing, which is very short, as compared to the essentially classical oscillatory dynamics of the gas due to the harmonic trap, which is given by much larger period determined by the trapping frequency  $\omega$ .

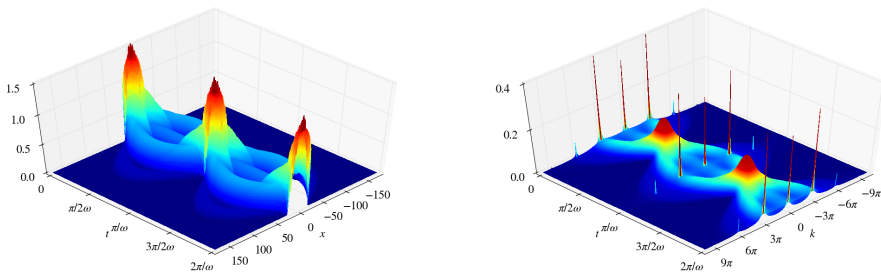


Figure 5.5: The time evolution of the density (left) and MDF (right) in the trap, computed with the FB mapping for  $N = 50$ ,  $\omega = 10/N$ ,  $A = 1.5$  and  $q = 3\pi$ .

## 5.4 Conclusion

We provide detailed modeling of the Bragg pulse used in quantum Newton's cradle-like settings or in Bragg spectroscopy experiments for strongly repulsive bosons in one dimension. We reconstruct the post-pulse time evolution and study the time-dependent local density profile and momentum distribution by a combination of exact and approximate techniques. Our results display a clear separation of timescales between rapid and trap-insensitive relaxation immediately after the pulse, followed by slow in-trap periodic behaviour. The time evolution of the density profile in the TG limit on the ring can be exactly reproduced by a computation based on nonlinear Luttinger liquid theory while when supplemented with an appropriate local density approximation this leads to quite accurate predictions for this function in the trap.

# On the Moses sea

The waters were divided.

---

Exodus 14:21

In the last chapter we have discussed a Bragg pulse in the Lieb-Liniger model, mimicking as close as possible an experimental situation. The steady state in the long-time limit was shown to correspond to a distribution of particle rapidities similar to several copies of Fermi seas separated by multiples of the Bragg momentum  $q$ . A microscopic picture of this state would however reveal that, different from a true Fermi sea, the filling of the quantum numbers does not correspond to completely filled blocks. Instead, the Bragg pulse generates a huge superposition in which a representative state would feature filled and empty quantum number slots in some ratio set by the coefficients  $J_\beta(A)^2$  with a lot of ‘room’ to microscopically reorder the quantum numbers, and hence a huge entropy.

Here we consider an artificial set of states corresponding to a scenario where the copies of the Fermi seas could somehow be cooled separately in which case we would arrive at a zero-entropy version of the Bragg pulsed steady state described in the last chapter. These states can be constructed in terms of the Bethe ansatz solution of the model as consecutive intervals of filled and empty quantum numbers. They resemble the ground-state Fermi sea in having sharply defined Fermi momenta and vanishing thermodynamic entropy.

The material in this chapter represents the work published in Phys. Rev. A **89**, 033637 (2014) and SciPost Physics **1** (1), 008 (2016).

## 6.1 Introduction

Much of our understanding of 1d systems stems from the existence of robust non-perturbative methods developed over the last decades. First and foremost, the concept of the Tomonaga-Luttinger liquid [30,31] and the technique of bosonization [9, 36, 238, 239] have provided the consistent framework for describing the

universal low-energy physics of these systems. On the other hand, the existence of isolated examples of exactly-solvable 1d models [24] whose wavefunctions can be obtained from Bethe Ansatz [240] has opened up the door to many nonperturbative computations of physical properties of representative systems.

One seldom-exploited characteristic of the Bethe Ansatz is that, in marked contrast to bosonization, it provides exact wavefunctions for *any* state in the Hilbert space, irrespective of its energy. Besides allowing to consider e.g. finite-temperature thermodynamics of exactly-solvable models, this fact also opens the door to the investigation of many more general issues going beyond conventional equilibrium physics.

Our aim here is to consider a relatively simple class of states in two integrable models—namely in a gas of repulsive bosons described by the Lieb-Liniger model and in the XXZ spin chain—which, while being highly excited, share many properties with the ground state: They have vanishing thermodynamic entropy and show quantum critical correlations that can be studied by adjusting effective-field-theory methods to this situation [4, 5, 241]. The same holds for the entanglement entropy [242].

The theoretical construction of the states we want to consider is easy: split the ground-state Fermi sea into separate blocks and translate each block’s quantum numbers by some number of slots. In view of this ‘splitting’ of the Fermi sea, and in analogy with Dirac and Fermi seas, we will refer to such states as a *Moses sea*.

The experimental fabrication of a Moses sea could well be excruciatingly difficult. It is intriguing in this light that experiments in cold atoms have shown that domain-wall melting of a one-dimensional Mott insulator leads to sharp quasi-condensate peaks in the momentum distribution at finite momenta in the late-time limit [243] similar to what we find for a Moses sea (see Sec. 6.5.4). The initial state studied in the experiment also has zero entropy but the relation to Moses seas of the late-time steady state has yet to be established.

If a Moses sea is created in out-of-equilibrium settings one would expect it to be ultimately unstable against external perturbations, but, being eigenstates of a physically meaningful Hamiltonian, their lifetimes can in principle be extremely large if perturbations are weak. They therefore realize another instance of ‘metastable criticality’ [244] in interacting gases.

The persistence of ground-state properties in the class of Moses sea states can be regarded in the light of generalized Gibbs ensembles (GGEs), as these states can alternatively be viewed as the zero temperature limit of a GGE and thus a ground state of the generalized Hamiltonian constructed as some superposition of additional local conserved charges. It is not clear however to which extend such generalized Hamiltonians describe physical systems. In Lieb-Liniger for instance, expressing the conserved charges in terms of physical operators is highly nontrivial and leads to expressions which cannot be written as simple integrals of Hamiltonian densities [245]. On the other hand, one can obtain certain physically sensible models for integrable spin ladders which have Moses seas as ground state [246, 247].

We will henceforth not be bothered by questions related to the physical realization of these states but consider them purely as a theoretically interesting class generalizing the ground state. Still, it is important to note that we will adhere to the physical Lieb-Liniger or XXZ Hamiltonian to define time-evolution, which makes the study of dynamical correlations qualitatively different from cases where these states would appear as the ground state of some more general Hamiltonian.

## 6.2 Definitions

To introduce our definitions and notations we give a coarse review of the two models under consideration followed by the construction of Moses seas. See [4, 5, 24] for further details.

## 6.3 Models

To start, consider the Lieb-Liniger Hamiltonian [19, 248] (with  $\hbar = 2m = 1$ )

$$H = \int_0^L dx [\partial_x \Psi^\dagger(x) \partial_x \Psi(x) + c \Psi^\dagger(x) \Psi^\dagger(x) \Psi(x) \Psi(x)]. \quad (6.1)$$

Eigenstates are completely characterized by the two-particle scattering phase  $\theta(\lambda) = 2 \arctan(\lambda/c)$ , thanks to the magic of diffractionless scattering in quantum integrable models [21]. Similarly, the XXZ model

$$H = J \sum_{j=1}^L \left[ S_j^x S_{j+1}^x + S_j^y S_{j+1}^y + \Delta \left( S_j^z S_{j+1}^z - \frac{1}{4} \right) - h S_j^z \right], \quad (6.2)$$

which we will consider in the critical regime  $0 \leq \Delta \leq 1$ , allows for a construction of the complete set of wave functions in terms of  $\theta(\lambda) = 2 \arctan[\tanh(\lambda)/\tan(\zeta)]$  for  $\Delta = \cos(\zeta) \in (0, 1)$  or  $\theta(\lambda) = 2 \arctan(\lambda)$  for  $\Delta = 1$ . We put  $J = 1$  such that the ground state has anti-ferromagnetic correlations.

Let us agree to label the lattice indices  $j$  in XXZ with a continuum variable  $x$  to align the notations for the Lieb-Liniger and XXZ models. In terms of the appropriate phase shift and appropriate parametrization of the single-particle momenta in terms of rapidities, the full  $N$  body wave functions can be written as

$$\begin{aligned} \chi_N(\{x_j\}_{j=1}^N | \{\lambda_j\}_{j=1}^N) &\propto \prod_{j>k}^N \text{sgn}(x_j - x_k) \\ &\times \sum_{P \in \mathcal{S}_N} (-1)^{[P]} e^{\frac{i}{2} \sum_{j>k} \text{sgn}(x_j - x_k) \theta(\lambda_{P_j} - \lambda_{P_k})} e^{i \sum_j p_0(\lambda_{P_j}) x_j}, \end{aligned} \quad (6.3)$$

where  $p_0(\lambda) = \lambda$  for Lieb-Liniger and  $p_0(\lambda) = 2 \arctan[\tanh(\lambda)/\tan(\zeta/2)]$  or  $p_0(\lambda) = 2 \arctan(2\lambda)$  for XXZ with  $0 < \Delta < 1$  and  $\Delta = 1$  respectively. Here

## 6. On the Moses sea

---

$P \in \mathcal{S}_N$  denotes a permutation on  $N$  symbols and  $(-1)^{|P|}$  is its sign. Note that all momenta are measured mod  $2\pi$  on the lattice.

In Lieb-Liniger there is a natural choice of vacuum state  $|0\rangle$  which is used to construct the  $N$  particle sectors according to

$$|\{\lambda_j\}_{j=1}^N\rangle = \int \prod_{j=1}^N dx_j \chi_N(\{x_j\}_{j=1}^N | \{\lambda_j\}_{j=1}^N) \prod_{j=1}^N \Psi^\dagger(x_j) |0\rangle. \quad (6.4)$$

In  $XXZ$  we choose the fully polarized state  $|\Downarrow\rangle = \otimes_{x=1}^L |\downarrow\rangle_x$  as pseudo vacuum and we identify the  $N$  particle states with the sector of magnetization  $M = N - L/2$  constructed according to [249, 250]

$$|\{\lambda_j\}_{j=1}^N\rangle = \int \prod_{j=1}^N dx_j \chi_N(\{x_j\}_{j=1}^N | \{\lambda_j\}_{j=1}^N) \prod_{j=1}^N S_{x_j}^+ |\Downarrow\rangle. \quad (6.5)$$

Imposing (anti-)periodic boundary conditions depending on whether  $N$  is even (odd) leads to consistency conditions on the rapidities known as the Bethe equations:

$$p_0(\lambda_j)L = 2\pi I_j - \sum_{l=1}^N \theta(\lambda_j - \lambda_l) \quad (6.6)$$

where  $I_j$  are integers or half-odd integers depending on whether  $N$  is odd or even.

The construction of Bethe states (6.3) and the Bethe equations (6.6) in principle represent the full information needed to solve the model, either Lieb-Liniger or  $XXZ$ , exactly: use the Bethe equations to find the set of rapidities and then construct the full wave functions that in principle contain the information to any physical question one may ask. Yet, the road to computing for example physical correlation functions is far from paved from here on but still has many practical and fundamental hurdles awaiting.

First, let us quickly comment on the differences between solutions to the Bethe equations in  $XXZ$  and Lieb-Liniger. While for Lieb-Liniger with  $c > 0$  all solutions to the Bethe to the Bethe equations are real and a state can be declared uniquely by specifying  $N$  of the allowed quantum numbers  $I_j$ , in  $XXZ$  the rapidities  $\lambda_j$  may take on complex values and can organize in so called string solutions [23]. We will restrict our focus to states with only real rapidities for the construction of Moses seas, but string states may appear in the computation of correlations as intermediate states of the matrix element summations. In  $XXZ$  the allowed set of quantum numbers that may lead to real rapidities is constrained to lie within a finite symmetric interval  $|I_j| < I_\infty$  bounded by the value  $I_\infty = (L - N)/2 - \zeta(L/2 - N)/\pi$  for  $0 < \Delta < 1$  and  $I_\infty(L - N + 1)/2$  for  $\Delta = 1$ . The ground state for  $XXZ$  still has only real rapidities and corresponds

to choosing a symmetric configuration of quantum numbers,

$$I_j^{GS} = (1 - N)/2 + j, \quad j = 1, \dots, N \quad (6.7)$$

as it does for Lieb-Liniger.

The energy and momentum of eigenstates are simply sums of single-particle contributions

$$P = \sum_{j=1}^N p_0(\lambda_j) \quad E = \sum_{j=1}^N \epsilon_0(\lambda_j) \quad (6.8)$$

where the bare energy function is  $\epsilon_0(\lambda) = \lambda^2$  for Lieb-Liniger and  $\epsilon_0(\lambda) = -2 \sin^2(\zeta)/[\cosh(2\lambda) - \cos(\zeta)]$  for  $0 < \Delta < 1$  and  $\epsilon_0(\lambda) = -2/(1 + 4\lambda^2)$ .

In Lieb-Liniger, the so-called Tonks-Girardeau limit  $c \rightarrow \infty$  [215, 251] simplifies the system considerably, reducing it to a gas of impenetrable bosons which is equivalent to free fermions up to particle statistics. Similarly,  $\Delta \rightarrow 0$  in XXZ makes the spin chain equivalent to free lattice fermions. The effect of particle statistics can be formally accounted for by employing a Jordan-Wigner string to map between the corresponding bosonic and fermionic creation and annihilation operators. We will use these limit later on as a separate check of our results as well as to construct an appropriate effective field theory.

### 6.3.1 Moses sea

Both in the XXZ model and in Lieb-Liniger, a Moses sea is defined by declaring intervals of occupied quantum numbers (no holes) and leaving all other quantum numbers unoccupied. The simplest non-groundstate case has two intervals  $[I_{1L}, I_{1R}]$  and  $[I_{2L}, I_{2R}]$ , which is the case we will put most emphasis on, while in general we can consider  $n$  intervals  $[I_{1L}, I_{1R}], \dots, [I_{nL}, I_{nR}]$ . In the case of XXZ we will assume that there is enough ‘room’ in the available slots for the quantum numbers corresponding to real rapidities.

Let us establish some notations. We will use indices  $i, j, k, \dots = 1, 2, \dots, n$  to denote the  $n$  ‘seas’ (usually  $n = 2$ ) and indices  $a, b, c, \dots = L, R$  to denote the left or right edge of a sea. The declaration of the numbers  $\{I_{ia}\}$  or, rather yet, the associated ‘Fermi momenta’  $\{k_{iaL}\}$  with  $k_{ia} = (2\pi/L)I_{ia}$  will be used to specify the state. The Fermi momenta will be kept fixed when taking the thermodynamic limit  $N, L \rightarrow \infty, N/L = \rho_0$ . The  $I_{ia}$  are taken half-way between occupied and empty slots such that the filled quantum numbers of sea  $j$  are  $\{I_{jL} + 1/2, \dots, I_{jR} - 1/2\}$ . The extremal quantum numbers  $I_{ia}$  are mapped by the Bethe equations to the quasi-momenta  $\lambda_{ia}$  which, for Lieb-Liniger, become equal to  $k_{ia}$  in the Tonks-Girardeau limit. It is useful to define  $k_F = \sum_{ia} s_a k_{ia} = \pi \rho_0$  with  $s_{R/L} = \pm 1$ . Fig. 6.1 illustrates the construction.

Some immediate facts concerning Moses seas are that their energy is thermodynamically large above that of the ground state, and their momentum distribution will be peaked around nonzero momenta (namely at momenta dictated

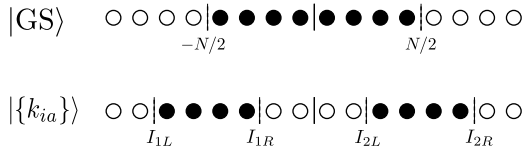


Figure 6.1: Illustration of quantum number configuration for the ground state Fermi sea (top) and Moses sea (bottom).

by the size of and distance between the Fermi pockets), unlike the ground state case. Moreover, the fact that these states have zero entropy maximizes quantum effects in observables such as correlation functions.

Such Moses seas were previously considered in [252] for mean field studies and in [241] where their local two and three body correlations were calculated (similar correlations were computed in [253, 254] using the method of [255]). As argued in [241], the momentum kick caricatures the effects of the Bragg pulse performed in [12], but in view of our findings in Ch. 5 we know that the zero entropy nature is markedly different.

## 6.4 Correlations from integrability

The structure of dynamic correlations in one dimensional systems display sharp thresholds closely related to the excitation spectrum of particle, hole or particle-hole excitations. The splitting of the Fermi sea is clearly visible in the structure of the excitation spectrum.

Let us consider Lieb-Liniger for illustration. As compared to the ground state, there are now more branches of particle (Type I) and hole (Type II) excitations leading to a very characteristic single particle-hole continuum. Due to the vacancies for quantum numbers in between the seas, part of the spectrum is shifted to the negative energy domain, leaving an excluded area for a range of positive energy and momentum values as compared to the ground-state case. This is illustrated for the Tonks-Girardeau case in Fig. 6.11, where the types of excitations that correspond to the different parts of the spectrum are also indicated. When more than a single particle-hole are considered, another difference shows up as compared to the ground state, namely that because of the negative energy branch the spectrum will become completely gapless.

Table 6.1: Levels of saturation of the f-sum rule for the DSF computations presented in Fig. 6.2.

	$c = 1$	$c = 4$	$c = 16$	$c = 64$
$k = \pi$	99.3%	99.2%	99.6%	99.7%
$k = 2\pi$	98.1%	97.0%	98.6%	98.9%

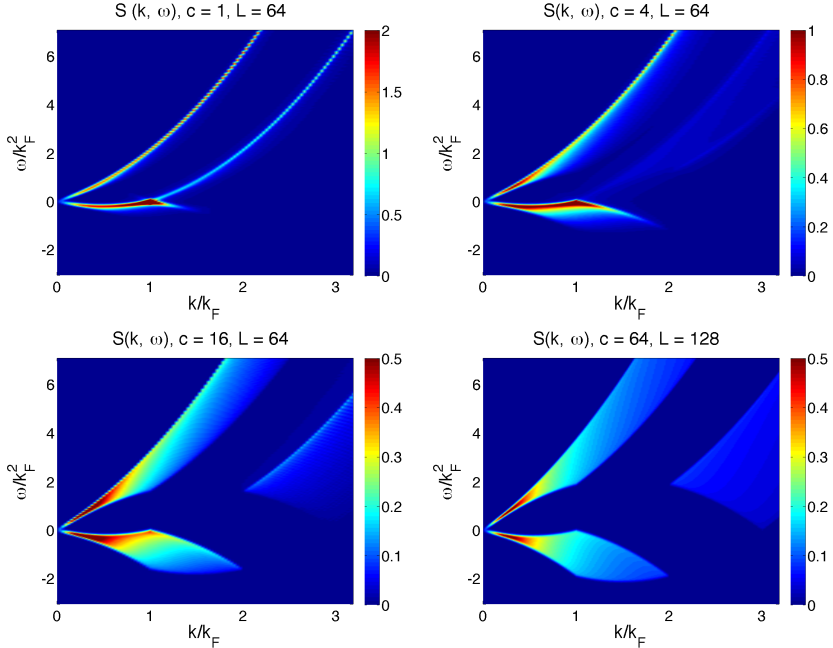


Figure 6.2: The dynamical structure factor  $S(k, \omega)$  in Lieb-Liniger for Moses sea with  $c = 1, 4, 16, 64$  computed using ABACUS.

The particle-hole continuum dictates the outlines of the dynamical structure factor (DSF), defined as

$$\begin{aligned}
 S(k, \omega) &= \int_{-\infty}^{\infty} dt \int_0^L dx e^{i\omega t - ikx} \langle \rho(x, t) \rho(0, 0) \rangle \\
 &= \frac{2\pi}{L} \sum_{\alpha} |\langle \{k_{ia}\} | \rho_k | \alpha \rangle|^2 \delta(\omega - E_{\alpha} + E_0),
 \end{aligned} \tag{6.9}$$

where  $|\{k_{ia}\}\rangle$  symbolizes the Moses sea,  $\alpha$  labels a complete set of eigenstates with energies  $E_{\alpha}$ , and  $\rho(x) = \Psi^{\dagger}(x)\Psi(x)$  is the density operator. We have used the ABACUS routine [26] to evaluate the DSF numerically (see Fig. 6.2), generalizing the ground state computations in [256]. Just like in the case of the ground state, the single particle-hole continuum is visible in the DSF marked by thresholds and displaying the dominant correlation weight.

For small interactions the system becomes more and more like two coupled BECs as can also be seen from the solution of the extremal rapidities that collapse onto each other when  $c \rightarrow 0$ . The DSF is then extremely sharply peaked at low energy and at a momentum corresponding to the distance between the internal

## 6. On the Moses sea

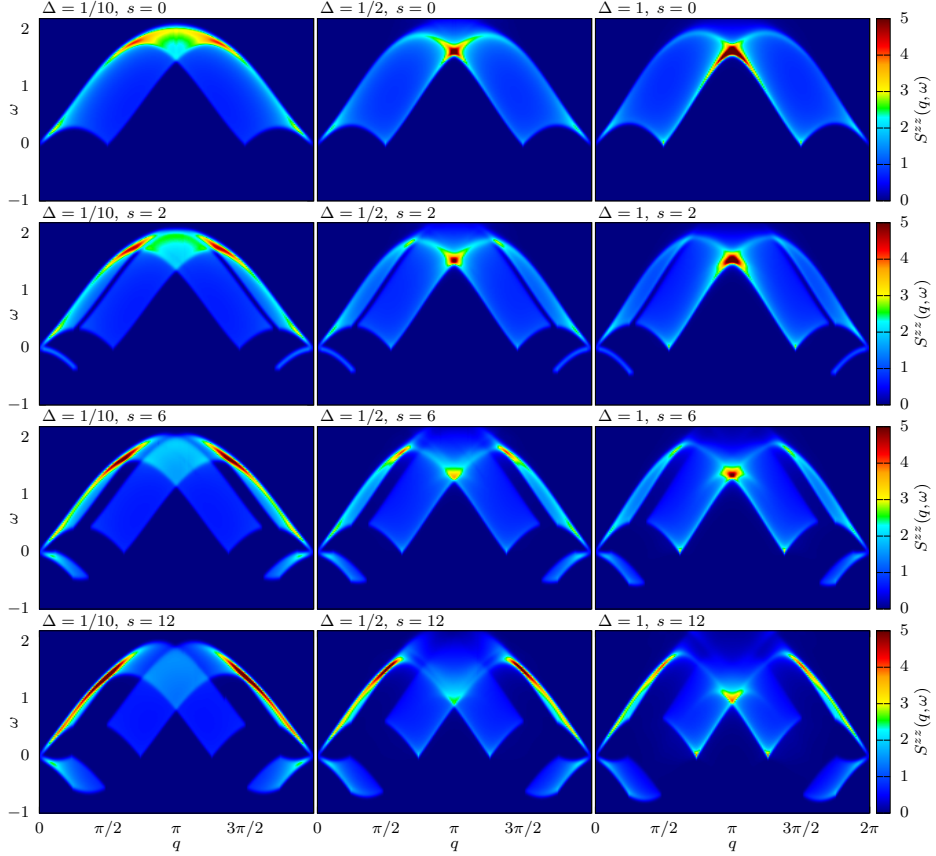


Figure 6.3: Longitudinal structure factor  $S^{zz}(q, \omega)$  in XXZ for  $N = 200$  and  $M = 50$  computed by summing matrix elements obtained from algebraic Bethe Ansatz for  $\Delta = 1/10, 1/2, 1$ . The parameter  $s = 0, 2, 6, 12$  the shift of the quantum numbers such that the separation between seas is  $2s$  slots.

edges of the two seas. On the other hand, for very large interactions, the DSF becomes essentially energy-independent.

For XXZ, the quantity corresponding to the boson DSF is the longitudinal structure factor defined as

$$S^{zz}(q, \omega) = \frac{1}{L} \sum_{x,y}^L e^{-iq(x-y)} \int_{-\infty}^{\infty} dt e^{i\omega t} \langle S^z(x, t) S^z(y, 0) \rangle, \quad (6.10)$$

In Fig. 6.9 results for an asymmetric configuration are shown. The effects of ‘unbalancing’ the Fermi pockets is quite easily visualized by following the

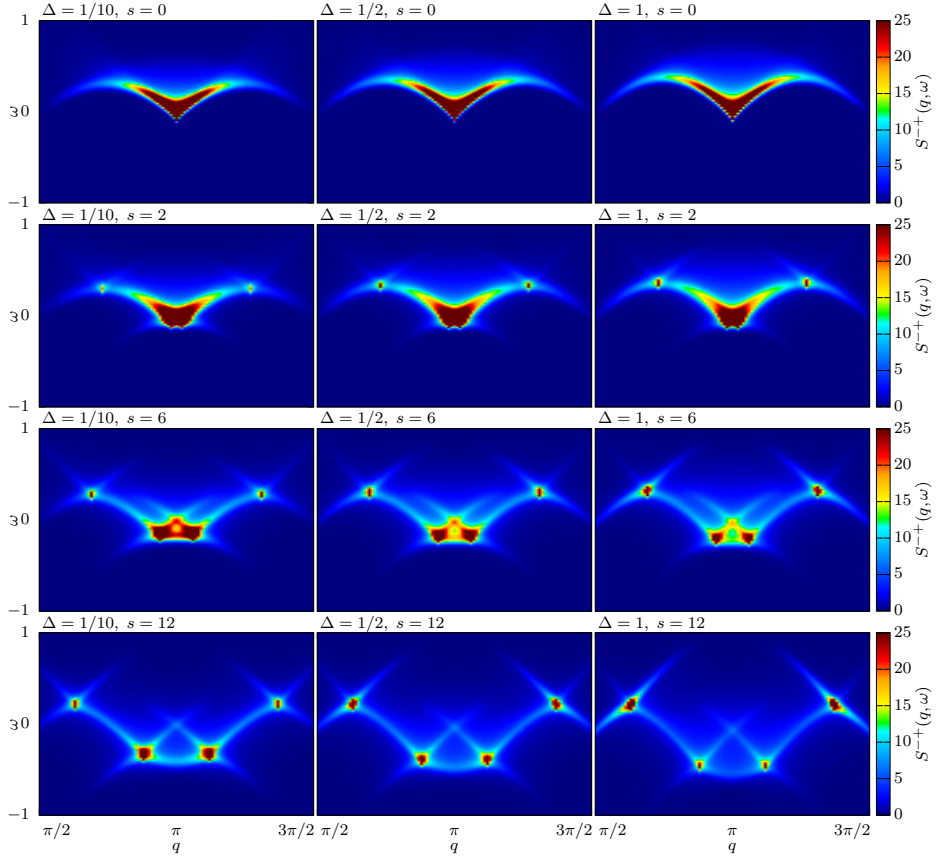


Figure 6.4: Transverse dynamical structure factor  $S^{-+}(q, \omega)$  at  $N = 200$ ,  $M = 50$ ,  $\Delta = 1$  computed from summations of matrix elements obtained from algebraic Bethe ansatz. From left to right, the momentum shifts in the quantum numbers are  $s = 0, 2, 6, 12$ . The corresponding sum rule saturations of the data are listed in Tab. 6.2.

changes in the dispersion lines. All features of the DSF mentioned above survive imposing such an asymmetry with minimal change.

The quality of the computations is evaluated with sumrules. For the DSF, the f-sumrule  $\int_{-\infty}^{\infty} \omega S(k, \omega) \frac{d\omega}{2\pi} = \frac{N}{L} k^2$  was used. Saturation levels at two representative momenta for all data sets presented in Fig. 6.2 are given in Tab. 6.1. Lower momenta are saturated better than the percentages given. For XXZ sumrule saturation values are given in Tab. 6.2.

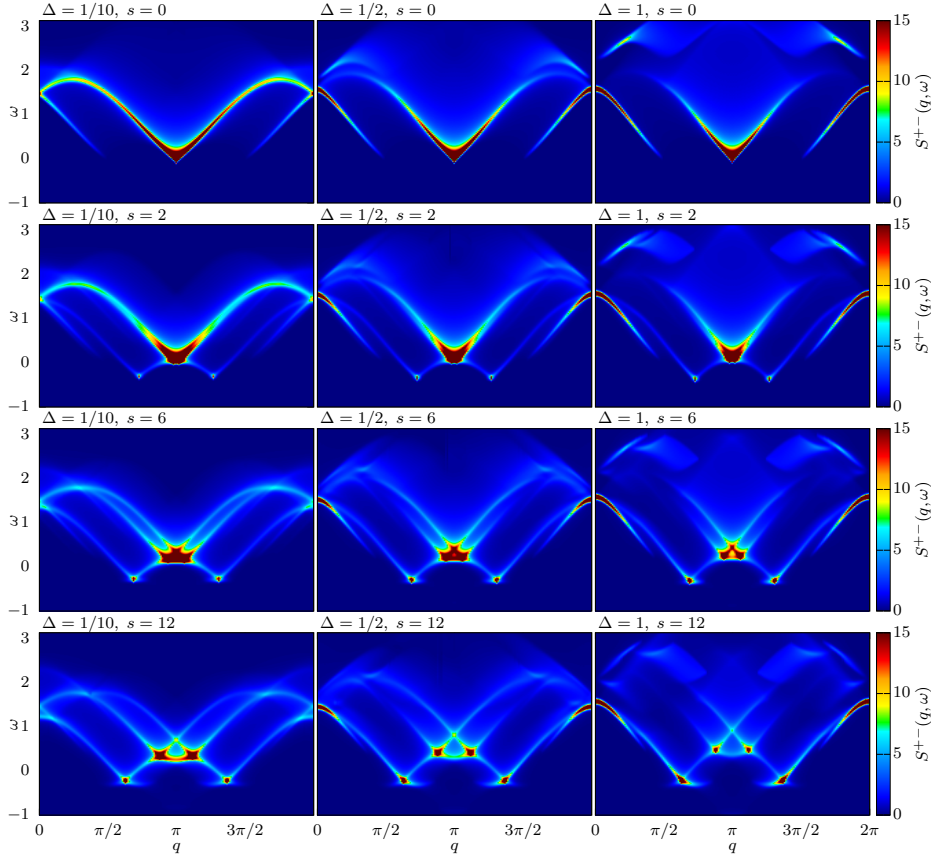


Figure 6.5: Transverse dynamical structure factor  $S^{+-}(q, \omega)$  at  $N = 200$ ,  $M = 50$ ,  $\Delta = \frac{1}{10}$  computed from summations of matrix elements obtained from algebraic Bethe ansatz. From left to right, the momentum shifts in the quantum numbers are  $s = 0, 2, 6, 12$ . The corresponding sum rule saturations of the data are listed in Tab. 6.2.

## 6.5 Effective field theory for static correlations

The construction of an effective field theory (a multi-component Tomonaga-Luttinger model) for Moses seas in Lieb-Liniger and XXZ proceeds by representing the model in terms of fermions by a Jordan-Wigner transformation and taking the continuum limit if need be.

	$s$	$S^{zz}$	$S^{-+}$	$S^{+-}$
$\Delta = \frac{1}{10}$	0	99.50%	99.50%	98.74%
	2	99.50%	98.52%	91.49%
	6	99.50%	97.73%	89.18%
	12	99.16%	95.27%	85.47%
$\Delta = \frac{1}{2}$	0	99.50%	99.50%	98.97%
	2	98.73%	99.49%	94.42%
	6	98.05%	99.90%	90.85%
	12	98.00%	98.16%	88.61%
$\Delta = 1$	0	99.38%	99.50%	94.40%
	2	98.04%	99.50%	89.45%
	6	98.00%	99.12%	87.57%
	12	97.80%	98.80%	86.55%
$\Delta = 1$	$6_l, 18_r$	95.67%	98.01%	

Table 6.2: Sum rule saturations for all data obtained from the ABACUS algorithm at  $N = 200$  and  $M = 50$  for various values of the anisotropy and the momentum shift in the Fermi seas. The bottom row shows the saturations for an asymmetric shift of the quantum numbers.

### 6.5.1 Multi-component Tomonaga-Luttinger model

For Lieb-Liniger, we use the Jordan-Wigner transformation

$$\Psi(x) = \cos\left(i\pi \int^x dy \rho(y)\right) \Psi_F(x) \quad (6.11)$$

representing the Bose field in terms of fermions  $\Psi_F(x)$  in the continuum. The use of the cosine rather than an exponential for the Jordan-Wigner string conveniently implements the correct symmetry properties upon bosonization. This fermionization of the Lieb-Liniger model leads to the dual Cheon-Shigehara model [257,258] wavefunctions of which can be obtained by an anti-symmetrization procedure. The interaction potential characterizing this model can be thought of as  $V(x) = -\delta''(x)/(m^2c)$ . The TG limit  $c \rightarrow \infty$  corresponding to free fermions will be the starting point of the construction.

For XXZ, one first maps the model to spinless fermions on a lattice by the Jordan-Wigner transformation

$$S_j^- \rightarrow (-1)^j \cos\left(\pi \sum_{l < j} n_l\right) c_j^\dagger, \quad S_j^z \rightarrow \frac{1}{2} - n_j \quad (6.12)$$

with  $n_j = c_j^\dagger c_j$ . The Hamiltonian then reads (neglecting chemical potential terms

and with  $J = 1$ )

$$H = \sum_{j=1}^N \left[ -\frac{1}{2} \left( c_j^\dagger c_{j+1} + c_{j+1}^\dagger c_j \right) + \Delta n_j n_{j+1} \right]. \quad (6.13)$$

To arrive at the same starting point as in the case of Lieb-Liniger, we will take the continuum limit in writing  $\Psi_F(x) = c_x$  and base the construction on the XX point  $\Delta = 0$  corresponding to free fermions. The fermionized XXZ Hamiltonian is then diagonal in momentum space with a dispersion relation  $\varepsilon^0(k) = -J \cos(k)$  while Lieb-Liniger has  $\varepsilon^0(k) = k^2/2m$ . If we agree to measure distances in units of the inverse mean density  $\rho_0^{-1}$  in Lieb-Liniger and the lattice spacing  $a$  (so far taken to be unity) in XXZ, subsequent steps in the construction and the results become identical in form for the two models.

To construct a Moses sea we must specify Fermi points  $k_{ia}$  which we identify with the fermionic momenta. We then introduce a branch of chiral fermions  $\psi_{ia}$  for each  $i = 1, \dots, n$ ,  $a = L, R$  and obtain an effective model at the free fermion point by expanding the dispersion relation for  $\Psi_F(x)$  around the points  $k_{ia}$  and taking this as the dispersion  $\varepsilon_{ia}(k)$  for  $\psi_{ia}$ . In computations we identify

$$\Psi_F(x) \sim \sum_{ia} e^{ik_{ia}x} \psi_{ia}. \quad (6.14)$$

This is essentially a mode expansion and the fields  $\psi_{ia}$  can be considered slowly varying and represent the modes of  $\Psi_F(x)$  close to the momenta  $k_{ia}$  which will be most important for correlations. In the next step we switch on interactions but we linearize the dispersion relation such that the effective Hamiltonian can be written

$$H_{\text{TL}} = \int dx \left[ \sum_{ia} s_a v_{ia}^0 \psi_{ia}^\dagger (-i\partial_x) \psi_{ia} + \sum_{ia,jb} g_{ia,jb} \rho_{ia} \rho_{jb} \right] \quad (6.15)$$

where  $\rho_{ia} = \psi_{ia}^\dagger \psi_{ia}$  is the density of species  $ia$ ,  $g_{ia,jb}$  are effective  $g$ -ology-like interaction parameters,  $v_{ia}^0 = \partial_k \varepsilon^0(k_{ia})$  are the ‘Fermi velocities’ corresponding to the bare, cosine dispersion of the XX model. Here and throughout the chapter normal ordering is left implicit. The Hamiltonian (6.15) constitutes a multi-component Tomonaga-Luttinger model [46, 259, 260]. Note that we define the velocity by taking the derivative of the dispersion to the right, also at left Fermi points. The combination  $s_a v_{ia}^0$  would be positive in equilibrium and corresponding to the Fermi velocity, however, it may be negative in our out-of-equilibrium context. For Moses seas, the validity of Hamiltonian (6.15) beyond weak interactions cannot be justified by renormalization group arguments in the usual sense since we are describing a high-energy state. Still, the approximations here made rely on the idea that we keep the most important terms for the long range physics determined by the modes that are ‘close’ to the Fermi points  $k_{ia}$ ,

which is done by keeping operators of scaling dimension  $\leq 2$ . We will adhere to the equilibrium terminology and call these marginal while terms of higher scaling dimension are called irrelevant.

Note that when we fix the quantum number configuration but vary the interaction  $c$  or  $\Delta$ , the  $k_{ia}$  remain fixed. This is most easily seen by realizing that the momentum of an excitations can always be obtained from adding the filled quantum numbers the momentum of adding removing a particle at the  $I_{ia}$  point therefore always leads to a momentum difference of  $k_{ia}$  when starting from a Moses sea. We thus observe that a kind of generalized Luttinger's theorem fixes the  $k_{ia}$  independent of interactions. Note that this conservation is a many-body effect away from the free fermion limit: it results of the backflow of the rapidities in the Moses sea upon creating the excitation. The individual rapidities vary when we change the interaction, generally making the edges a Fermi sea coming closer together when we increase fermionic attraction. For  $c \rightarrow 0$  in Lieb-Liniger for example, two seas will have their left and right fermi points resulting in a BEC-like quasi-condensate with but at condensed around two momenta. See Fig. 6.6 for an illustration of the Tomonaga-Luttinger construction and this effect.

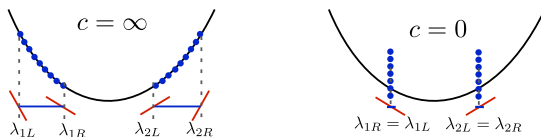


Figure 6.6: The multi-component Tomonaga-Luttinger liquid construction for Moses seas (here in Lieb-Liniger). The  $c = \infty$  limit corresponding to free fermions is the starting point (left). Tuning to the free boson limit  $c = 0$  the system becomes more BEC-like (right). The right and left velocities of the two seas will converge but each sea will maintain a definite mean momentum.

In order to compute correlations, we bosonize the chiral fermions according to

$$\psi_{ia} \sim \frac{1}{\sqrt{2\pi}} e^{-i\sqrt{2\pi}\phi_{ia}}, \quad \rho_{ia} = -\frac{s_a}{\sqrt{2\pi}} \partial_x \phi_{ia} \quad (6.16)$$

(where  $s_{R,L} = \pm 1$ ). The Hamiltonian then becomes quadratic in terms of the bosonic fields and can be diagonalized by a Bogoliubov transformation:

$$\phi_{ia} = \sum_{jb} U_{ia,jb} \varphi_{jb}. \quad (6.17)$$

This results in the diagonal form of the effective Hamiltonian

$$H_{\text{TL}} = \sum_{ia} \frac{s_a v_{ia}}{2\pi} \int dx (\partial_x \varphi_{ia})^2 \quad (6.18)$$

## 6. On the Moses sea

---

where the velocities  $v_{ia}$  are now related to the dressed dispersion of the XXZ model with  $\Delta \neq 0$  of Lieb-Liniger with  $c \neq \infty$ . While the interaction parameters  $g_{ia,jb}$  cannot be reliably obtained, the Bogoliubov parameters  $U_{ia,jb}$ —which also determine the exponents of physical correlation functions—are related to finite-size energy contributions when we extend the filled quantum number blocks by  $N_{ia}$  particles at Fermi point  $k_{ia}$ . The correction  $\delta E = E[\{N_{ia}\}] - E[\{0\}]$  is then to order  $1/N$  given by

$$\delta E = \sum_{ia} \epsilon_{ia} N_{ia} + \sum_{ia,jb,kc} \frac{\pi}{L} s_c v_{kc} U_{ia,kc} U_{jb,kc} N_{ia} N_{jb}. \quad (6.19)$$

Here  $N_{ia}$  is the number of added (or removed when  $N_{ia} < 0$ ) particles corresponding to chiral species  $\psi_{ia}$  and  $\epsilon_{ia} = \varepsilon(k_{ia})$  is the energy associated to Fermi point  $k_{ia}$ . Eq. (6.19) gives a relation between the  $U_{ia,jb}$  and the finite-size energy differences upon addition or removal of a particle at the Fermi points  $k_{ia}, k_{jb}$ . Thanks to the properties of the matrix  $U_{ia,jb}$ , this relation can in fact be inverted and leads to a way to determine  $U_{ia,jb}$  and  $v_{ia}$  directly from these finite-size corrections. The  $U_{ia,jb}$  generalizes the universal compressibility parameter  $K$  used in equilibrium situations, in which case we have

$$U_{ab} = \begin{pmatrix} \frac{1}{2\sqrt{K}} + \frac{1}{2}\sqrt{K} & \frac{1}{2\sqrt{K}} - \frac{1}{2}\sqrt{K} \\ \frac{1}{2\sqrt{K}} - \frac{1}{2}\sqrt{K} & \frac{1}{2\sqrt{K}} + \frac{1}{2}\sqrt{K} \end{pmatrix} \quad (6.20)$$

We have tossed the index for the seas in this case and  $a, b = R, L$  denote the Fermi points  $k_{R,L} = \pm k_F$ . Note that there is only one effective parameter in stead of two—which would be expected for a  $2 \times 2$  matrix with the quasi-unitarity condition. In general, a symmetric combination of seas as one would obtain for any parity invariant state leads to such a reduction of the number of parameters determining the Bogoliubov transformation as detailed in Sec. 6.5.2.

The Bogoliubov parameters  $U_{ia,jb}$  have a beautiful interpretation in terms of the phase shifts of the modes at Fermi point  $k_{ia}$  upon addition of a particle at Fermi point  $k_{jb}$ . This can be argued upon refermionization of the effective Tomonaga-Luttinger theory and can be made precise in terms of the shift function  $F(\lambda|\lambda')$  describing the change of the rapidities when the system is excited. In the thermodynamic limit the shift function is determined by the integral equation

$$F(\lambda|\lambda') - \sum_j \int_{\lambda_{j1}}^{\lambda_{j2}} \frac{d\mu}{2\pi} K(\lambda - \mu) F(\mu|\lambda') = \frac{\theta(\lambda - \lambda')}{2\pi} \quad (6.21)$$

with  $K(\lambda) = \theta'(\lambda)$ . The relation to the Bogoliubov parameters is then

$$U_{ia,jb} = \delta_{ia,jb} - s_b F(\lambda_{jb}|\lambda_{ia}), \quad (6.22)$$

which can be shown by comparing the finite size corrections to the energy. A derivation of this relation will be presented in Ch. 7. In equilibrium it is known

[261] and the shift function plays an important role in going beyond the Luttinger liquid approximation in computing dynamic correlation functions [65, 118].

### 6.5.2 Parity symmetric case

In the case of a symmetric configuration of  $n$  seas corresponding to parity invariant states, we can reduce the number of independent Bogoliubov parameters by a factor two. In this case, we have  $-k_{iL} = k_{n+1-iR}$  and  $-v_{iL} = v_{n+1-iR}$  and in general that the system is symmetric under simultaneously exchanging  $i \leftrightarrow n+1-i$  and  $L \leftrightarrow R$ . It is then convenient to combine the fields at Fermi points at opposite momenta and define

$$\phi_i = \frac{1}{\sqrt{2}}(\phi_{iL} - \phi_{n+1-iR}), \quad \theta_i = \frac{1}{\sqrt{2}}(\phi_{iL} + \phi_{n+1-iR}). \quad (6.23)$$

with inverse transformation

$$\phi_{iL} = \frac{1}{\sqrt{2}}(\theta_i + \phi_i), \quad \phi_{n+1-iR} = \frac{1}{\sqrt{2}}(\theta_i - \phi_i). \quad (6.24)$$

The Hamiltonian for the multi-component TL model can then be written as

$$H_{\text{TL}} = \sum_i \frac{v_i^0}{2} \int dx [(\partial_x \phi_i)^2 + (\partial_x \theta_i)^2] + \sum_{ij} \int dx \frac{1}{2\pi} [g_{ij}^+ \partial_x \phi_i \partial_x \phi_j + g_{ij}^- \partial_x \theta_i \partial_x \theta_j] \quad (6.25)$$

with  $v_i^0 = v_{n+1-iR}^0$  and  $g_{ij}^\pm = g_{iLjL} \pm g_{n+1-iRjL}$ .

In order to respect the canonical commutation relations and diagonalize  $H_{\text{TL}}$  we introduce new fields according to

$$\phi_i = \sum_j U_{ij} \varphi_j, \quad \theta_i = \sum_j [U^{-1}]_{ji} \vartheta_j \quad (6.26)$$

where the  $U_{ij}$  are related to the Bogoliubov parameters  $U_{ia,jb}$  as

$$U_{ij} = U_{iLjL} - U_{iLn+1-jR} \quad (6.27)$$

by virtue of the symmetry  $U_{ia,jb} = U_{n+1-i\bar{a},n+1-j\bar{b}}$ . The effective Hamiltonian takes the familiar diagonal form

$$H_{\text{TL}} = \sum_i \frac{v_i}{2} \int dx [(\partial_x \varphi_i)^2 + (\partial_x \vartheta_i)^2]. \quad (6.28)$$

The matrix  $U_{ij}$  is straightforwardly obtained from calculations in finite size and finite particle number from corrections to the energy upon creating particle-number or current excitations

$$\delta E = \sum_i \frac{\pi v_i}{2L} \left[ \left( \sum_j [U^{-1}]_{ij} \Delta N_j \right)^2 + \left( \sum_j U_{ji} \Delta J_j \right)^2 \right]. \quad (6.29)$$

Here

$$\Delta N_i = N_{n+1-iR} + N_{iL}, \quad \Delta J_i = N_{n+1-iR} - N_{iL} \quad (6.30)$$

in terms of the numbers  $N_{ia}$  of particles added at Fermi point  $k_{ia}$ .

### 6.5.3 Asymptotes of correlations

Physical correlations generally translate into (products of) two-point functions of vertex operators in bosonized language, which in our conventions are evaluated according to

$$\langle e^{i\alpha\sqrt{2\pi}\varphi_{ia}(x)} e^{-i\alpha\sqrt{2\pi}\varphi_{ia}(0)} \rangle = (s_a i/x)^{\alpha^2}. \quad (6.31)$$

Here,  $x$  is measured in units of the lattice spacing in XXZ or the inverse density  $\rho_0^{-1}$  in Lieb-Liniger.

Asymptotes of correlation functions are now obtained by applying the appropriate Jordan-Wigner transformation and, in XXZ, the continuum limit to translate the correlation we want to compute to an expression in terms of the fermionic field  $\Psi_F$ . We then use the mode expansion to write it in terms of the chiral fermions  $\psi_{ia}$  after which we can use the bosonization identities to express the physical operators in terms of the bosonic fields  $\phi_{ia}$ , or better yet, in terms of the free fields  $\varphi_{ia}$  by using the Bogoliubov transformation. This leads to expressions for correlations of the form (6.31) with the  $U_{ia,jb}$  determining the exponents—or derivations of it.

For example, the density operator in Lieb-Liniger is

$$\rho(x) = \rho_0 + \sum_{ia} \rho_{ia}(x) + \sum_{ia \neq jb} e^{-i(k_{ia} - k_{jb})x} \psi_{ia}^\dagger(x) \psi_{jb}(x). \quad (6.32)$$

The density-density correlation function

$$S(x) = \frac{\langle \rho(x) \rho(0) \rangle}{\rho_0^2} \quad (6.33)$$

can easily be obtained from the multicomponent Tomonaga-Luttinger model as

$$S(x) = 1 - \frac{\sum_{ia,jb,kc} s_a s_b U_{ia,kc} U_{jb,kc}}{4\pi^2(\rho_0 x)^2} + \sum_{ia \neq jb} \frac{A_{ia,jb}}{4\pi^2} (-1)^{\delta_{ab}(1-\delta_{ij})} \cos((k_{ia} - k_{jb})x) \left( \frac{1}{\rho_0 x} \right)^{\mu_{ia,jb}} \quad (6.34)$$

with

$$\mu_{ia,jb} = \sum_{kc} (U_{ia,kc} - U_{jb,kc})^2. \quad (6.35)$$

In the Tonks-Girardeau limit,  $U_{ia,jb} = \delta_{ia,jb}$  and  $A_{ia,jb} = 1$ , the above expression reduces to the exact result for any configuration of the Fermi seas with edges  $\{k_{1L}, k_{1R}, k_{2L}, k_{2R}\}$  as can be confirmed by an exact calculation.

The  $A_{ia,jb}$  are nonuniversal prefactors, giving the amplitude of the fluctuating terms (corresponding to Umklapp-like excitations). It was recently shown that the nonuniversal prefactors in Luttinger liquid correlations can be obtained from the finite size scaling of matrix elements [40, 41]. This logic can be carried over to the present context. In leading order, the matrix elements satisfy the scaling relation

$$\frac{|\langle ia, jb | \rho | \{k_{ia}\} \rangle|^2}{\rho_0^2} = \frac{A_{ia,jb}}{4\pi^2} \left( \frac{2\pi}{\rho_0 L} \right)^{\mu_{ia,jb}} \quad (6.36)$$

where  $|\{k_{ia}\}\rangle$  denotes the Moses sea and  $|ia, jb\rangle$  the state obtained after creating an ‘Umklapp’ excitation transferring a particle from the  $ia$  to the  $jb$  branch or *vice versa* (see [40, 41] for the detailed explanations).

By the same logic as used above, the prediction for the real space longitudinal correlation from the multi-component Tomonaga-Luttinger model is

$$\begin{aligned} \langle S^z(x) S^z(0) \rangle_{\text{TL}} &= s_z^2 - \frac{\sum_{ia,jb,kc} s_a s_b U_{ia,kc} U_{jb,kc}}{4\pi^2 x^2} \\ &+ \sum_{ia \neq jb} \frac{A_{ia,jb}}{4\pi^2} (-1)^{\delta_{ab}(1-\delta_{ij})} \cos[(k_{ia} - k_{jb})x] \left( \frac{1}{x} \right)^{\mu_{ia,jb}} \end{aligned} \quad (6.37)$$

The non-universal prefactors  $A_{ia,jb}$  behave as  $1 + \mathcal{O}(\Delta)$  in this case.

The comparison of these results with the data obtained from ABACUS is presented in Fig 6.7. To fix the prefactors  $A_{ia,jb}$  we obtained the scaling numerically by explicitly evaluating the relevant matrix elements for increasing system size (see Fig. 6.8). The Tomonaga-Luttinger result with independently obtained prefactors yields a completely parameter-free fit for the correlations away from the Tonks-Girardeau or  $\Delta = 0$  regime. In addition, the exponents are obtained efficiently from the scaling of the prefactors, providing an independent check on the parameters determined from finite size corrections to the spectrum or a different route to obtaining the correlation exponents. To fit the finite size data, we make the substitution  $x \rightarrow \frac{L}{\pi} \sin(\pi x/L)$ . There is excellent agreement for all distances larger than a fraction of the system length (Fig. 6.7).

For the computation of one-body correlations, such as the spectral function in Lieb-Liniger or transversal spin correlations, one should be careful to take particle statistics into account. To illustrate, let us study the one-body reduced density matrix in Lieb-Liniger

$$g_1(x) = \frac{\langle \Psi^\dagger(x) \Psi(0) \rangle}{\rho_0} \quad (6.38)$$

which is related to the hole spectral function and is the Fourier transform of the momentum distribution functions.

## 6. On the Moses sea

---

In order to obtain  $g_1(x)$  we bosonize the fermions and neglect the fast fluctuating terms of the density operator under the integral in the Jordan-Wigner string.

$$\Psi(x) \sim \frac{1}{\sqrt{8\pi}} \sum_{ia} \sum_{\epsilon=\pm 1} e^{i(k_{ia} + \epsilon k_F)x} e^{-i\sqrt{2\pi} \sum_{kc} (\epsilon s_c/2 + \delta_{ia,kc}) \phi_{kc}(x)}. \quad (6.39)$$

which leads to the one-body function

$$g_1(x) = \sum_{ia,\epsilon} \frac{B_{ia,\epsilon}}{2\pi} (-1)^{\delta_{s_a,\epsilon}} e^{-ik_{ia,\epsilon}x} \left( \frac{1}{\rho_0 x} \right)^{\mu_{ia,\epsilon}}. \quad (6.40)$$

with

$$\mu_{ia,\epsilon} = \sum_{kc} \left[ \sum_{jb} (\epsilon/2 + s_a \delta_{ia,kc}) U_{jb,kc} \right]^2. \quad (6.41)$$

with the notation  $k_{ia,\epsilon} \equiv k_{ia} + \epsilon k_F$ .

Similar reasoning gives asymptotes for the transversal spin correlations in XXZ as

$$\langle S^\mp(x) S^\pm(0) \rangle_{\text{TL}} = \sum_{ia} \sum_{\epsilon=\pm 1} \frac{B_{ia,\epsilon}}{2\pi} (-1)^{\delta_{s_a,\epsilon}} e^{-ik_{ia,\epsilon}x} \left( \frac{1}{x} \right)^{\mu_{ia,\epsilon}} \quad (6.42)$$

where  $k_{ia,\epsilon} = k_{ia} + \epsilon\pi M/N$ . The non-universal prefactors  $B_{ia,\epsilon}$  in Eq. (6.40) have to be obtained independently from

$$\frac{|\langle ia, \epsilon | \Psi | M \rangle|^2}{\rho_0} = \frac{B_{ia,\epsilon}}{2\pi} \left( \frac{2\pi}{\rho_0 L} \right)^{\mu_{ia,\epsilon}}, \quad (6.43)$$

according to a procedure similar to that described above for the DSF (see also Fig. 6.8).

### 6.5.4 Momentum distribution function

The momentum distribution function (MDF) is defined as the Fourier transform of the static one-body function:

$$n(k) = \int_0^L dx e^{ikx} \langle \Psi^\dagger(x) \Psi(0) \rangle. \quad (6.44)$$

Let us begin by discussing the impenetrable limit, which illustrates some generic features and can be treated analytically following the work of Lenard [262]. This calculation can also be done for states different from the ground state and we used the result in the form given in [25]. In Fig. 6.10, the momentum distribution for different configurations of the Fermi seas is given in the Tonks-Girardeau

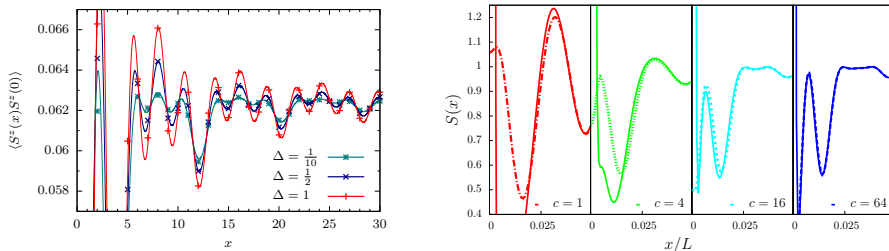


Figure 6.7: Comparison of effective Tomonaga-Luttinger (TL) theory and integrability result for  $\langle S^z(x)S^z(0) \rangle$  in XXZ (left) and  $S(x) = \langle \rho(x)\rho(0) \rangle$  in Lieb-Liniger (right). Solid lines are TL result. The correspondence is accurate even for small differences: Note that for Lieb-Liniger only a fraction of the system size is displayed from whereon the correspondence is essentially perfect.

limit. In this limit we see four peaks in the momentum distribution. If the Fermi momenta are given by  $\{k_{1L}, k_{1R}, k_{2L}, k_{2R}\}$  then the peaks are located at  $\{k_{1L} + k_F, k_{1R} - k_F, k_{2L} + k_F, k_{2R} - k_F\}$ , where  $k_F = \sum_{ia} s_a k_{ia} = \pi \rho_0$ . The outer Fermi edges thus give rise to the inner peaks in the momentum distribution, and inner Fermi edges to the outer peaks. Moving the two seas closer to each other, we see that the outer peak becomes smaller and the inner peak becomes larger and closer to zero. If the Fermi seas are far away from each other the peaks become equally large. The limit of the two Fermi seas far away from each other is thus completely different from two non-interacting Fermi seas. In the latter case one would just have two peaks and not four.

The MDF for generic values of the interaction parameter  $c$  is computed using ABACUS again using an adaptation of the ground state algorithm used in [263]. For finite values of  $c$ , the outer peak of the momentum distribution becomes smaller and the inner peak larger, since reducing the repulsive interactions makes the system more like a decoupled BEC, whose MDF would have two isolated delta peaks. Already for  $c \lesssim 10$ , the momentum distribution shows only two distinguishable momentum peaks instead of four. One can thus view the internal peaks as ‘BEC’-driven, and the outer ones as ‘interaction’-driven. It is an interesting challenge for experiments to try to create a state sufficiently similar to a Moses state in a tight toroidal trap [264] such that the interaction-driven peaks in the MDF are visible, thereby demonstrating that the system is in a highly correlated quantum state, similar to the phase correlations in spatially split one-dimensional Bose gases [265].

Results for  $n(k)$  in Lieb-Liniger can be derived from the expression for  $g_1(x)$  in Eq. (6.40), which are valid momenta in a small interval around  $k_{ia,\epsilon}$ . The result reads

$$n(k - k_{ia,\epsilon}) \sim |k - k_{ia,\epsilon}|^{\mu_{ia,\epsilon} - 1}. \quad (6.45)$$

## 6. On the Moses sea

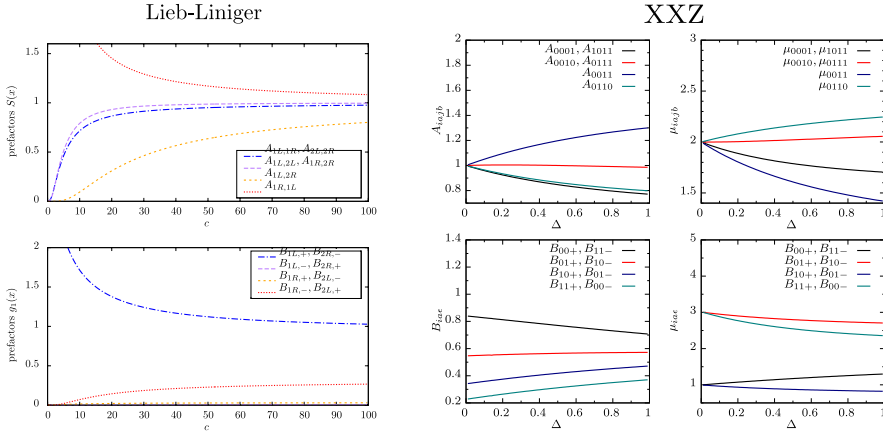


Figure 6.8: Prefactors for static correlation functions for a Moses sea state in Lieb-Liniger (left) and XXZ (right).

In the limit of infinite repulsion this becomes

$$\mu_{ia,\epsilon}^{c=\infty} = 1 + \frac{n}{2} + \epsilon s_a, \quad (6.46)$$

where  $n$  is the total number of seas.

Note that we can understand the position of the peaks at  $k_{ia,\epsilon}$  from the Tomonaga-Luttinger model and the Jordan-Wigner transformation: The sign  $\epsilon$  in the Jordan-Wigner string shifts the momenta  $k_{ia}$  by  $k_F$  to either the left or right. It absorbs the mismatch of the quantum number lattices in the Bethe Ansatz solution for even and odd numbers of particles—it corresponds to the choice of moving all occupied quantum numbers by a half to the left or to the right after removing a single particle from the system.

The prefactors (see Fig. 6.8) and the exponents both show the relative importance of the contributions with  $\epsilon s_a = -1$ : these have a much larger contribution and decay more slowly. Indeed, this clarifies appearance of four peaks at  $\{k_{1L} + k_F, k_{1R} - k_F, k_{2L} + k_F, k_{2R} - k_F\}$  (in stead of eight) in the momentum distribution function that were mentioned above. The power law at zero momentum for a gas of bosons in the ground state is obtained from reduction to the conventional Tomonaga-Luttinger liquid, i.e. with  $U_{a,b}$  given by Eq. (6.20). This leads to the well-known result [266]

$$n(k) \sim k^{\mu_0-1} \quad \text{with} \quad \mu_0 = \frac{1}{2K}. \quad (6.47)$$

Choosing  $s_{ia} = 1$ ,  $\epsilon = -1$  in Eq. (6.46) indeed gives the correct result  $\mu_0^{c=\infty} = 1/2$  for the Tonks-Girardeau ground state ( $K = 1$ ).

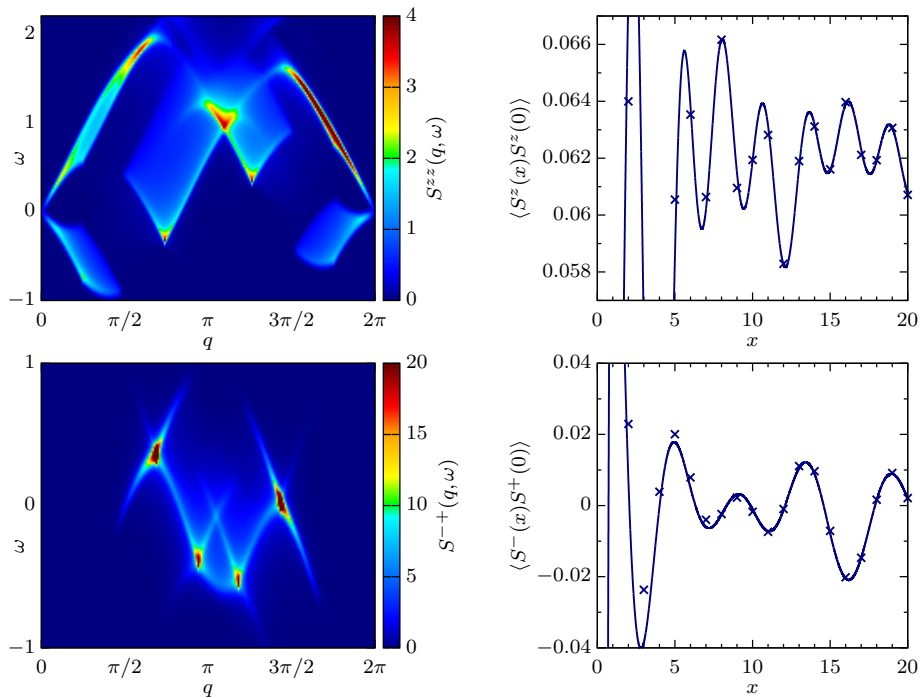


Figure 6.9: Correlations for an asymmetric, non-parity invariant Moses sea. Dynamic correlations (left) are obtained with ABACUS. Static correlations (right) are obtained by Fourier transform and integration and show comparable accuracy to the Tomonaga-Luttinger predictions as the symmetric case. Sum rule saturation of the ABACUS data is given in Tab. 6.2.

At large momenta, the MDF decays as  $1/k^4$  as expected from the logic of Tan’s contact [267]. We have also directly verified this from the small- $x$  expansion of  $g_1(x)$  in the Tonks-Girardeau limit.

## 6.6 Effective field theory for dynamic correlations

The fact that the zero-entropy states we are considering are far from equilibrium is not visible when we restrict attention to the static correlations, which would be the same if this state was obtained as the ground state of a different Hamiltonian. In order to make the out-of-equilibrium nature apparent we have to probe the energies of ‘excitations’, i.e. modifications of the Moses sea by creating additional particles and holes which may now have both positive and negative energy differences with respect to the reference state. A physically meaningful way to probe the energy landscape is by computing time-dependent correlations which

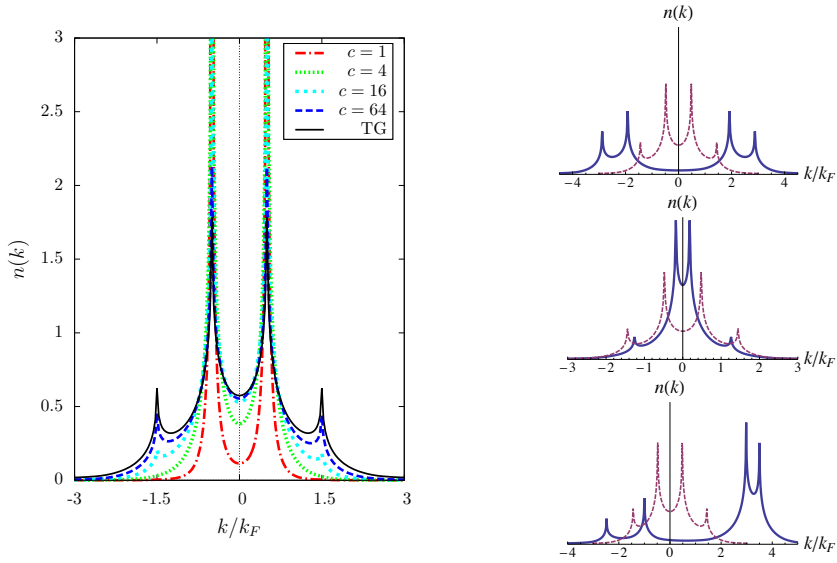


Figure 6.10: Momentum distribution function (MDF)  $n(k)$  for Moses sea in Lieb-Liniger. Left: MDF for symmetric configuration of Fermi seas for different interactions. Right: The effect of changing the configuration of the Moses sea for  $c = \infty$  (TG limit). Peaks correspond to  $k = k_{ia} \pm s_a k_F$  which can be understood from bosonization and the Jordan-Wigner transformation.

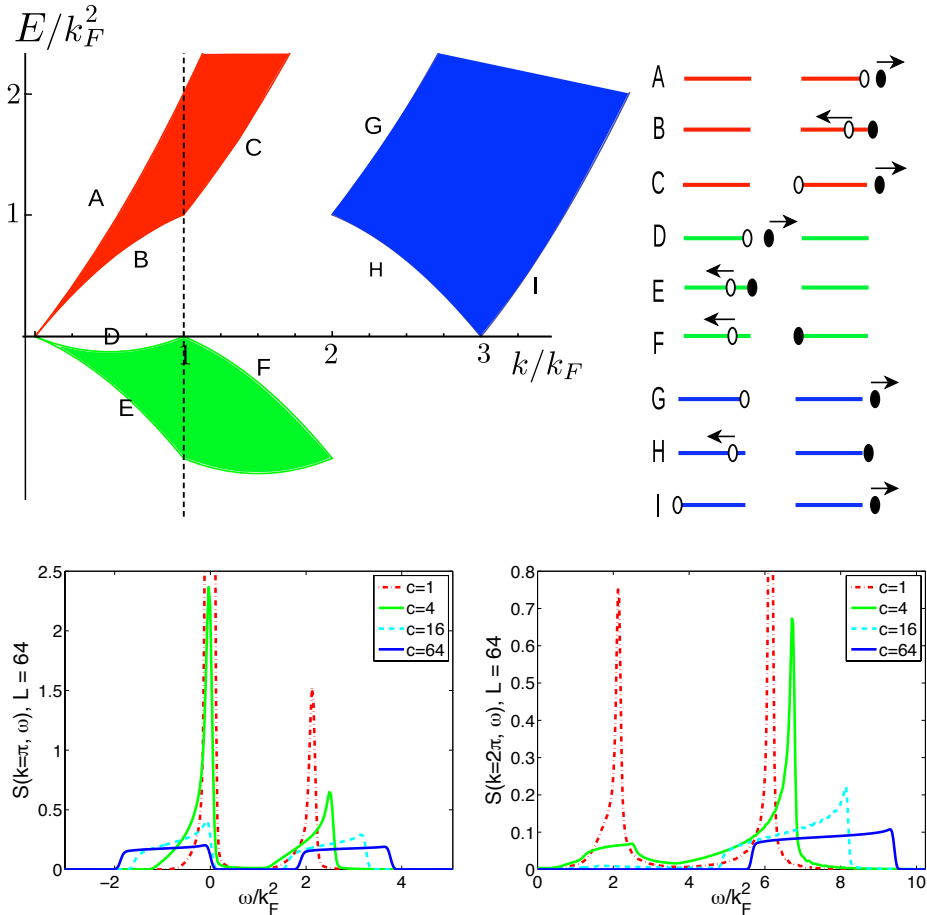


Figure 6.11: Top: Illustration of the single particle-hole spectrum for a Moses sea in Lieb-Liniger with illustration of the excitations tracing out the edges of the support. Bottom: Fixed momentum cut at  $k = k_F$  of the dynamic structure factor showing the threshold behavior at the edge of support of the particle-hole spectrum for different interaction strengths.

can in principle be related to observable quantities. These are already encoded in the dynamical structure factors computed with ABACUS and can be obtained by Fourier transformation.

Recent years have witnessed a revolutionary advancements in understanding of dynamical correlations in critical one-dimensional systems from the perspective of both effective field theory methods and integrability [1, 13, 15, 47, 56–58, 60–70, 84–86, 122, 268–273]. The threshold behavior of many dynamical correlations in energy and momentum space can be understood in terms of specific configurations of particle and hole excitations. These lead to a scattering phase shift of the modes close to the Fermi energy which is identified as the cause of the characteristic power-law singularities by means of Anderson’s orthogonality catastrophe. This threshold behavior, which also determines the asymptotic behavior of the correlations in real space and time, is then described by an effective model in which the high energy particle or hole excitation is treated as a mobile impurity interacting with the low-energy modes.

We generalize this mobile impurity approach to the present out-of-equilibrium context by extending our multi-component Tomonaga-Luttinger model to include the appropriate impurity configurations and interactions. To be specific, we will compute the spin autocorrelation

$$C(t) = \langle S_j^z(t) S_j^z(0) \rangle = \langle \Psi^\dagger(t) \Psi(t) \Psi^\dagger(0) \Psi(0) \rangle, \quad (6.48)$$

where  $\Psi(t) = \Psi(x=0, t)$  denotes the Jordan-Wigner fermion and we used translational invariance. By imagining to obtain  $C(t)$  as a Fourier transform in  $(k, \omega)$ -space taking the  $k$ -integral first, one can argue that as a function of  $\omega$  singular behavior stems from the ‘Fermi points’ and points where the edge of support has a tangent with vanishing velocity. This identifies the important impurity configurations for this function as corresponding to a particle or hole with vanishing velocity, i.e. either at the bottom or the top of the band. Let us assume that the Moses state leaves the corresponding quantum numbers unoccupied, which is valid for a symmetric configuration with an even number of seas. This means that there are only high-energy particle impurities. We will use an index  $\gamma = 0, 1$  to label the particle at the bottom/top of the band respectively. The mobile impurity model becomes

$$H_{\text{MIM}} = \int dx \left[ \sum_{ia} \frac{s_a v_{ia}}{2} (\partial_x \varphi_{ia})^2 + \sum_{\gamma} d_{\gamma}^{\dagger} \left( \epsilon_{\gamma} - \frac{\partial_x^2}{2m_{\gamma}} \right) d_{\gamma} - \sum_{ia, \gamma} \frac{s_a \kappa_{ia, \gamma}}{\sqrt{2\pi}} d_{\gamma}^{\dagger} d_{\gamma} \partial_x \varphi_{ia} \right]. \quad (6.49)$$

Note that the last term is just a density-density interaction between the impurity modes and the chiral fermions parametrized by the coupling constants  $\kappa_{ia, \gamma}$ , while the first two terms correspond to the impurity dispersions and the TL

modes. In the small  $\Delta$  limit all parameters in  $H_{\text{MIM}}$  can be obtained from  $H$  in Eq. (6.13) as in Sec. 6.6.1. In general they can be obtained from integrability.

The impurity modes are decoupled from the Tomonaga-Luttinger model up to irrelevant operators by the unitary transformation

$$U = \exp \left\{ i \int dx \sum_{ia,\gamma} \frac{\kappa_{ia,\gamma}}{s_a v_{ia} \sqrt{2\pi}} d_\gamma^\dagger d_\gamma \varphi_{ia} \right\}. \quad (6.50)$$

The effect is that correlators of the TL model are still computed in the same way, but the impurity operator obtains an extra vertex operator in terms of the bosonic modes

$$d \rightarrow d \exp \left\{ -i \sum_{ia} \frac{\kappa_{\gamma,ia}}{s_a v_{ia} \sqrt{2\pi}} \varphi_{ia} \right\}. \quad (6.51)$$

The logic is identical to the ground state case, and this also suggests that we can identify the parameter  $\kappa_{ia,\gamma}/v_{ia}$  as the phase shift at the Fermi points upon creating the impurity according to [65, 118]

$$\frac{\kappa_{ia,\gamma}}{v_{ia}} = -2\pi F(\lambda_{ia}|\lambda_\gamma). \quad (6.52)$$

For the computation of the autocorrelation  $C(t)$ , the crucial observation is now that the asymptotic behavior, determined by the behavior around a few singular points of the longitudinal structure factor, is well captured by certain correlations computable using the Hamiltonian  $H_{\text{MIM}}$ . In marked contrast to the equilibrium case, the TL model does not account for zero-energy states only, and therefore even the contributions to Eq. (6.48) that do not involve the impurity will display the energy difference of the Fermi points leading to fluctuating terms

$$e^{i(\epsilon_{ia} - \epsilon_{jb})t} \langle \psi_{ia}^\dagger(t) \psi_{jb}(t) \psi_{jb}^\dagger(0) \psi_{ia}(0) \rangle \quad (6.53)$$

where  $\epsilon_{ia}$  is the energy associated to Fermi point  $k_{ia}$ . The TL contributions sum up to an expression similar to the static correlation in Eq. (6.37). The impurity contributions are of the form

$$e^{i(\epsilon_{ia} - \epsilon_\gamma)t} \langle \psi_{ia}^\dagger(t) d_\gamma(t) d_\gamma^\dagger(0) \psi_{ia}(0) \rangle. \quad (6.54)$$

Using the impurity correlator

$$\langle d_\gamma(t) d_\gamma^\dagger(0) \rangle = \int \frac{dk}{2\pi} e^{-i \frac{k^2}{2m_\gamma} t} = \sqrt{\frac{m_\gamma}{2\pi i t}} \quad (6.55)$$

we find the result

$$\begin{aligned}
 C(t) \sim & s_0^2 - \sum_{ia,jb,kc} \frac{s_a s_b U_{ia,kc} U_{jb,kc}}{4\pi v_{kc}^2 t^2} \\
 & + \sum_{ia,jb} \frac{A_{ia,jb} \cos(\epsilon_{ia} - \epsilon_{jb})}{4\pi^2} \prod_{kc} \left( \frac{1}{i s_c v_{kc} t} \right)^{[U_{ia,kc} - U_{jb,kc}]^2} \\
 & + \sum_{ia,\gamma} \frac{A'_{ia,\gamma} e^{i(\epsilon_{ia} - \epsilon_\gamma)t}}{2\pi} \sqrt{\frac{m_\gamma}{2\pi i t}} \prod_{kc} \left( \frac{1}{i s_c v_{kc} t} \right)^{[U_{ia,kc} + \frac{\kappa_{ia,\gamma}}{2\pi s_c v_{kc}}]^2}. \quad (6.56)
 \end{aligned}$$

The prefactor  $A'_{ia,\gamma} = 1 + \mathcal{O}(\Delta)$  can in principle be obtained from finite-size scaling of matrix elements similar to  $A_{ia,jb}$  but with the Umklapp state replaced by the appropriate impurity state [41]. We have checked this expression for the autocorrelation against Fourier transformed ABACUS data for small values of  $\Delta$ , and find that it converges to the exact result on quite short time scales for a configuration when the Fermi points  $k_{ia}$  are well away from the band top and bottom at  $k_\gamma = 0, \pi$  (Fig. 6.12), but the correspondence for short to moderate times becomes noticeably worse when we decrease the separation between the two seas. This could be a finite size effect since the number of states in between the impurity mode and the Fermi edges becomes small, but rather we believe that the correlation is not well-captured by the impurity model in that case as a clear separation in sub-bands becomes questionable.

When the current mobile-impurity approach works well, this tells us that the time-dependent correlation is determined by the modes very close to the Fermi points  $k_{ia}$  which correspond to particle-hole excitations involving only the quantum numbers close to the edges of the two Fermi seas. The role of the spectrum at the Fermi points and of the impurity is two-fold: (i) The energy differences determine the frequencies of fluctuations. (ii) The Fermi velocities  $v_{ia}$  and impurity mass  $m_\gamma$  change the prefactor of the separate terms. Note that the decay of the correlation on the other hand is determined by energy independent data, namely by the appropriate phase shifts and Anderson's orthogonality catastrophe, very similar to the equilibrium case.

### 6.6.1 Perturbative expressions for parameters in XXZ

We conclude this section by a discussion of perturbative results for the effective field theory parameters for XXZ. These are conveniently obtained by deriving the effective Hamiltonian to first order in the interaction in taking the continuum limit and are often useful as a check on numeric results.

Starting from the Hamiltonian of spinless fermions Eq. (6.13) on the lattice we use the mode expansion

$$\Psi(x) \sim \sum_{ia} e^{ik_{ia}x} \psi_{ia}(x) + \sum_{\gamma} e^{ik_{\gamma}x} d_{\gamma}(x) \quad (6.57)$$

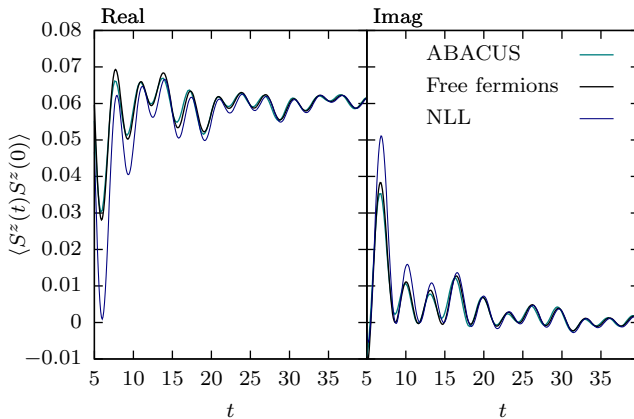


Figure 6.12: Comparison of computations for the autocorrelations  $\langle S^z(t)S^z(0) \rangle$ , from ABACUS at  $N = 200$ ,  $M = 50$ ,  $\Delta = \frac{1}{100}$ ,  $s = 12$ , from free fermions ( $\Delta = 0$ ), and from non-linear Luttinger (NLL) theory with effective field parameters taken for free fermions.

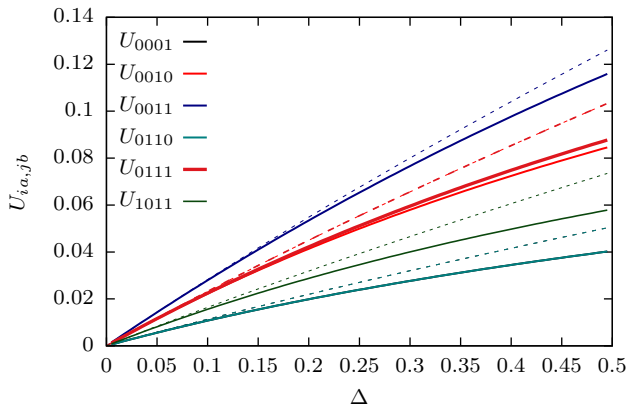


Figure 6.13: Bogoliubov parameters as a function of anisotropy for the static real space  $\langle S^z(x)S^z(0) \rangle$  correlations of the multicomponent Tomonaga-Luttinger model. The figure shows a comparison between the expansion in small anisotropy (dashed lines) and the parameters computed from integrability (solid lines) for a state with a double Fermi sea at  $N = 200$ ,  $M = 50$  and momentum shift  $s = 12$ .

and bosonize the chiral fermions. The kinetic term leads to the velocities for the chiral fermions  $v_{ia}^0 = J \sin(k_{ia})$  and the impurity parameters in the noninteract-

## 6. On the Moses sea

---

ing limit  $\epsilon_\gamma^0 = \mp J$  and  $m_\gamma^0 = \pm J$ . The interaction term

$$H_{\text{int}} = \sum_x J\Delta n(x)n(x+1) \quad (6.58)$$

renormalizes these values. By plugging in the bosonization identities, normal ordering and neglecting irrelevant terms we get the first order in  $\Delta$  expressions

$$g_{ia,jb} = J\Delta \begin{cases} \sum_{ld} \cos(k_{ia} - k_{ld}), & (ia = jb) \\ 1 - \cos(k_{ia} - k_{jb}), & (ia \neq jb). \end{cases} \quad (6.59)$$

These give

$$U_{ia,jb} = \delta_{ia,jb} - [1 - \delta_{ia,jb}] \frac{J\Delta s_b [1 - \cos(k_{ia} - k_{jb})]}{\pi (v_{ia}^0 - v_{jb}^0)}. \quad (6.60)$$

Next, we focus on the terms from the interaction involving the impurity. This leads to a density-density interaction of the impurity modes with the chiral fermions with parameters

$$\kappa_{ia,\gamma} = 2J\Delta [1 - \cos(k_{ia} - k_\gamma)]. \quad (6.61)$$

There is also a first order correction to the impurity energy appearing from Eq. (6.58) from the terms proportional to  $d^\dagger d$  (after normal ordering), which is

$$\epsilon_{\gamma=0,1} = \mp J \left( 1 \mp 2n_0\Delta + \sum_{ia} \frac{\Delta}{\pi} s_a \sin(k_{ia}) \right). \quad (6.62)$$

This corresponds to the Hartree-Fock correction

$$\delta\epsilon_\gamma = \sum_i \int_{k_{iL}}^{k_{iR}} \frac{dk}{2\pi} [V(0) - V(k_\gamma - k)] \quad (6.63)$$

with  $V(q) = 2J\Delta \cos(q)$ , which corresponds to the interaction potential in Eq. (6.58):  $H_{\text{int}} = \frac{1}{2L} \sum_q V(q)n_q n_{-q}$ .

The non-universal prefactors can also be obtained perturbatively using the methods discussed in Ref. [40], but we have not done this calculation.

## 6.7 Conclusion

In conclusion, we have presented results on correlations Moses seas in two integrable models, namely the Lieb-Liniger model of interacting bosons and the XXZ spin chain. Moses seas are zero-entropy states generalizing the ground state. These could show up as ground states of generalized Hamiltonians, however, in our investigations we take the well-known physical Hamiltonians to determine time evolution and thus consider Moses seas as an interesting class of

out-of-equilibrium states. The distinctive features, which may serve for identification in experiment, can be understood by adapting the familiar ground state reasoning. By making the appropriate adjustments to equilibrium techniques based on the Tomonaga-Luttinger model many aspects can furthermore be understood in great detail and with quantitative agreement once a handful of parameters is fixed from integrability. Static correlations cannot tell whether we consider Moses seas as ground states of generalized Hamiltonians or as sincere out-of-equilibrium states. This difference is noticeable in the time-dependence of correlation functions, and we made the initial steps towards studying such correlations by techniques from nonlinear Luttinger liquid theory. It appears that the mobile impurity model is able of reproducing asymptotes of time-dependent correlations in a similar fashion to the equilibrium case but a more careful check of interaction effects should be performed. Nevertheless, it is quite enlightening to put the equilibrium techniques often associated to renormalization group arguments to the test in this setting extending their application.

Although we have focused on purely vanishing entropy density, we may consider thermal-like dressings to the split seas. In the Tomonaga-Luttinger description, finite temperatures are treated by a simple functional replacement for the fundamental correlators. On the side of integrability, recent work has shown that finite temperature correlators are also numerically accessible, at least for the Lieb-Liniger model [213]. How the correspondence between integrability results and the field theory works out in split-sea configurations at finite temperature remains to be investigated.



# General finite-size effects

We must accept finite  
disappointment, but never lose  
infinite hope.

---

Martin Luther King, Jr.

We present a general derivation of the spectrum of excitations for gapless states of zero entropy density in Bethe ansatz solvable models. Our formalism is valid for an arbitrary choice of bare energy function which is relevant to situations where the Hamiltonian for time evolution differs from the Hamiltonian in a (generalized) Gibbs ensemble, i.e. out of equilibrium. The energy of particle and hole excitations, as measured with the time-evolution Hamiltonian, is shown to include additional contributions stemming from the shifts of the Fermi points that may now have finite energy. The finite-size effects are also derived and the connection with conformal field theory discussed. The critical exponents can still be obtained from the finite-size spectrum, however the velocity occurring here differs from the one in the constant Casimir term. The derivation highlights the importance of the phase shifts at the Fermi points for the critical exponents of asymptotes of correlations. We generalize certain results known for the ground state and discuss the relation to the dressed charge (matrix). Finally, we discuss the finite-size corrections in the presence of an additional particle or hole which are important for dynamical correlation functions.

## 7.1 Introduction

The combination of Bethe ansatz (BA) and conformal field theory (CFT) is a strong set of tools in the study of quantum mechanical systems in one space dimension. To get insight into the correlations, a routinely employed technique is to compute general expressions for correlation asymptotes from CFT, fixing the critical exponents from the finite size spectrum compared to the BA solution. This works well for static correlations by taking the ground state as a reference state [24, 39], while for time-dependent correlations also contributions from

## 7. General finite-size effects

---

certain impurity configurations should be included [13, 15, 274]. This set of approaches thus provide a rather complete picture of (asymptotics of) equilibrium correlations in one-dimensional systems.

One of the outstanding benefits of the BA solution is the description it provides of the full Hilbert space and the possibility to study out-of-equilibrium states. The exact solvability can be attributed to the existence of an infinite collection of local charges  $\hat{Q}_n$  commuting with the Hamiltonian  $H$ ,

$$[H, \hat{Q}_n] = 0, \quad n \in \mathbb{N}. \quad (7.1)$$

Out-of-equilibrium problems have attracted a lot of attention recently regarding the question when and how unitary quantum systems do or do not thermalize. Important in this respect is the idea that correlations at late times can be computed in a generalized Gibbs ensemble (GGE) [229, 275] defined not just by the Hamiltonian, but rather by all [276, 277] conserved (quasi) local quantities

$$\hat{\rho}_{\text{GGE}} = Z_{\text{GGE}}^{-1} \exp\left\{-\sum_n \beta_n \hat{Q}_n\right\}. \quad (7.2)$$

Equivalently, correlations can be computed on a single representative eigenstate which can be determined by reasonings paralleling (generalizing) the thermodynamic Bethe ansatz (gTBA) or by the Quench Action (QA) method [232–234, 276–292]. In the latter, one constructs a free-energy functional straight from the overlaps of the initial state with the eigenstates of the time evolution Hamiltonian  $H$  [232, 234]. The GGE reasoning underscores the double role the Hamiltonian has in equilibrium quantum mechanics in determining both the statistical ensemble as well as the time evolution. Out of equilibrium, these two roles are separated, at least in the presence of nontrivial local conserved quantities.

A simple class of out-of-equilibrium states in BA solvable models corresponds to the zero-temperature equivalent of a GGE with nonmonotonic effective bare free energy (in gTBA language: driving function). Such states can be specified by consecutive blocks of filled quantum numbers in the Bethe ansatz solution, and in many ways resemble the ground-state Fermi sea or a simple boosted version of it, although now it combines several of such Fermi-sea blocks with different mean momentum. It has been shown that even in such cases, the description of correlation asymptotics is provided by multiple CFTs and that the finite-size corrections to the spectrum can again be used to obtain the critical exponents provided that the appropriate GGE energy function  $\epsilon_{\text{GGE}}(\lambda)$  is used [293].

The point here is to draw attention to a slightly uncanny feature of the standard derivation of the finite-size spectrum from Bethe ansatz [24, 39, 293], namely that it requires the dressed energy function to vanish for excitations at the Fermi points. This is done in equilibrium by subtracting the appropriate chemical potential. In other words, this requirement naturally follows when we use the Hamiltonian that defines the statistical ensemble in a grand canonical or GGE sense to measure energies, but out of equilibrium, one may question

the naturalness of this assumption. In particular, when discussing dynamical correlations it is important to use the time-evolution Hamiltonian to measure energies. This suggests that one should be able to derive the relation between critical exponents and the finite-size spectrum for states of zero entropy density using  $H$ —or any combination of the conserved quantities for that matter—and the corresponding energy function, also when this is not in line with the statistical ensemble. This has indeed been verified numerically in studies of dynamical correlations in out-of-equilibrium zero entropy states in the Lieb-Liniger and XXZ models [4, 5].

We therefore revisit the derivation of the energy of zero-entropy states and excitations in the limit of large system size and show that many of the well known relations between the spectrum and CFT hold for arbitrary energy functions, but with essential modifications. In terms of applications, the simplest example of such a situation occurs when we choose to measure energies with respect to a different chemical potential while still fixing a certain filling in a microcanonical sense. This would of course change the energy of excitations, but should not change the physics in an essential way. Another simple application is that of a boosted state observed in the lab frame. We however here present a general treatment, applicable to any (multiply) split Fermi sea in an integrable model.

## 7.2 Bethe ansatz and finite-size corrections

To be specific, consider the repulsive Lieb-Liniger model defined by the Hamiltonian

$$H = \int dx [\partial_x \Psi^\dagger(x) \partial_x \Psi(x) + c \Psi^\dagger(x) \Psi^\dagger(x) \Psi(x) \Psi(x)], \quad c > 0. \quad (7.3)$$

The coordinate Bethe ansatz provides exact expressions for all eigenstates  $|\{\lambda_j\}\rangle$  of the system with  $N$  particles in a box of size  $L$  in terms of the rapidities  $\lambda_j$  satisfying the Bethe equations [24]

$$L p_0(\lambda_j) + \sum_{k=1}^N \theta(\lambda_j - \lambda_k) = 2\pi I_j. \quad (7.4)$$

Here  $p_0(\lambda) = \lambda$  is the bare momentum of particles and  $\theta(\lambda) = 2 \arctan(\lambda/c)$  is the two-particle scattering phase and  $I_j$  are (half-odd) integers depending on whether  $N$  is (even) odd. All states are classified by specifying  $N$  filled quantum numbers  $I_j$ . The momentum and energy of a state are

$$P = \sum_j \frac{2\pi}{L} I_j = \sum_j p_0(\lambda_j), \quad E = \sum_j \epsilon_0(\lambda_j) \quad (7.5)$$

with  $\epsilon_0(\lambda) = \lambda^2$ . Note that the energy does not include a chemical potential term and is really the eigenvalue of the operator  $H$ . The conserved charges  $\hat{Q}_n$

## 7. General finite-size effects

---

of the Lieb-Liniger model can be taken to represent the monomials in the Bethe basis

$$\tilde{Q}|\{\lambda_j\}\rangle = Q_n|\{\lambda_j\}\rangle, \quad Q_n = \sum_j \lambda_j^2 \quad (7.6)$$

such that  $Q_0 = N$ ,  $Q_1 = P$  and  $Q_2 = E$ . Using the conserved charges we can in principle construct a Hamiltonian for any bare energy function  $\epsilon_0(\lambda) = \sum_n \beta_n \lambda^n$  by matching the  $\beta_n$  in the GGE.

Let us now consider a state  $|\{k_{ia}\}\rangle$  which corresponds to  $n$  disjoint Fermi seas specified by left and right Fermi momenta,

$$k_{ia}, \quad a = R, L, \quad i = 1, \dots, n. \quad (7.7)$$

These determine intervals of filled quantum numbers between extrema  $I_{ia} = (2\pi)^{-1} L k_{ia}$ . We take the  $I_{ia}$  to lie halfway between allowed quantum-number slots such that the filled quantum numbers correspond to

$$\{I_j\} = \bigcup_{i=1}^n \{I_{iL} + 1/2, I_{iL} + 3/2, \dots, I_{iR} - 1/2\}. \quad (7.8)$$

To take the thermodynamic limit  $N, L \rightarrow \infty$  with  $N/L$  fixed, we introduce the rapidity density

$$\rho(\lambda_j) = \frac{1}{L(\lambda_{j+1} - \lambda_j)}. \quad (7.9)$$

Using the Euler-Maclaurin formula, one can show that to order  $1/L$  the density satisfies

$$\rho(\lambda) = \frac{p'_0(\lambda)}{2\pi} + \sum_i \int_{\lambda_{iL}}^{\lambda_{iR}} \frac{d\nu}{2\pi} K(\lambda - \nu) \rho(\nu) + \frac{1}{24L^2} \sum_{ia} \frac{s_a K'(\lambda - \lambda_{ia})}{2\pi \rho(\lambda_{ia})} \quad (7.10)$$

where  $K(\lambda) = \theta'(\lambda)$  and we introduced  $s_{R,L} = \pm 1$ , and  $\lambda_{ia}$  as the image of  $I_{ia}$  in rapidity space under the Bethe equations. The energy similarly becomes (to order  $1/L$ )

$$E = L \sum_i \int_{\lambda_{iL}}^{\lambda_{iR}} d\lambda \epsilon_0(\lambda) \rho(\lambda) - \frac{1}{24L} \sum_{ia} \frac{s_a \epsilon'_0(\lambda)}{\rho(\lambda_{ia})}. \quad (7.11)$$

The remainder of this chapter is largely concerned with the analysis of these expressions.

We note that the solutions to other integrable models follow similar lines with appropriate definitions of the functions  $\theta(\lambda)$ ,  $p_0(\lambda)$  and  $\epsilon_0(\lambda)$ . For the XXZ model for instance,

$$H = \sum_{j=1}^L [S_j^x S_{j+1}^x + S_j^y S_{j+1}^y + \Delta(S_j^z S_{j+1}^z - 1/4)] \quad (7.12)$$

with  $\Delta = \cos \zeta \in (-1, 1)$ , we have

$$p_0(\lambda) = 2 \arctan \left[ \frac{\tanh(\lambda)}{\tan(\zeta/2)} \right], \quad \theta(\lambda) = 2 \arctan \left[ \frac{\tanh(\lambda)}{\tan(\zeta)} \right] \quad (7.13)$$

and

$$\epsilon_0(\lambda) = \frac{-2 \sin^2 \zeta}{\cosh(2\lambda) - \cos \zeta}. \quad (7.14)$$

A complicating factor in XXZ is that solutions to the Bethe equations can be complex. Using the string hypothesis the reasoning can easily be generalized to these string states, but for simplicity we will assume that quantum numbers and parameters are chosen such that we deal with real rapidities. As is often the case in BA solvable models, the specific definitions do not matter much in the later derivations, but the relations between the functions do. This also means that  $\epsilon_0(\lambda)$  can be chosen essentially at will.

### 7.3 The energy of zero-entropy states

Our first task is the evaluation of Eqs. (7.10) and (7.11). This follows standard practice [24, 293], but we include it for completeness. We expand the solution to Eq. (7.10) in powers of  $1/L$  as

$$\rho(\lambda) = \rho_\infty(\lambda) + \sum_{ia} \frac{s_a \rho_{ia}(\lambda)}{24L^2 \rho_\infty(\lambda_{ia})} \quad (7.15)$$

which results in the defining integral equations

$$\rho_\infty(\lambda) = \frac{p'_0(\lambda)}{2\pi} + \sum_i \int_{\lambda_{iL}}^{\lambda_{iR}} \frac{d\nu}{2\pi} K(\lambda - \nu) \rho_\infty(\nu), \quad (7.16)$$

$$\rho_{ia}(\lambda) = \frac{K'(\lambda - \lambda_{ia})}{2\pi} + \sum_i \int_{\lambda_{iL}}^{\lambda_{iR}} \frac{d\nu}{2\pi} K(\lambda - \nu) \rho_{ia}(\nu). \quad (7.17)$$

The equation for  $\rho(\lambda)$  is the straightforward generalization of the standard Lieb equation [19]. The second equation shows that  $\rho_{ia}(\lambda)$  is related to the two-parameter function  $L(\lambda|\lambda')$  defined by

$$L(\lambda|\lambda') = \frac{K(\lambda - \lambda')}{2\pi} + \sum_i \int_{\lambda_{iL}}^{\lambda_{iR}} \frac{d\nu}{2\pi} K(\lambda - \nu) L(\nu|\lambda'). \quad (7.18)$$

Eq. (7.18) shows that, considered as integration kernels on the domain specified by the Fermi rapidities  $\lambda_{ia}$ , the operator  $(1 + L)$  is the inverse of  $(1 - \widehat{\frac{K}{2\pi}})$ . Using this fact we obtain

$$E = L \sum_i \int_{\lambda_{iL}}^{\lambda_{iR}} d\lambda \epsilon_0(\lambda) \rho_\infty(\lambda) - \sum_{ia} \frac{s_a \epsilon'(\lambda_{ia})}{24L \rho_\infty(\lambda_{ia})} \quad (7.19)$$

## 7. General finite-size effects

---

to order  $1/L$ , where the function  $\epsilon(\lambda)$  is defined by the integral equation

$$\epsilon(\lambda) = \epsilon_0(\lambda) + \sum_i \int_{\lambda_{iL}}^{\lambda_{iR}} \frac{d\nu}{2\pi} K(\lambda - \nu) \epsilon(\nu). \quad (7.20)$$

This definition is the direct analogue of the dressed energy function in equilibrium settings which specifies the energy of the single particle and hole excitations on the ground state, but, as we will see later, this is not the case anymore. The true single particle dispersion, which we will denote by  $\tilde{\epsilon}(\lambda)$ , will in fact pick up additional contributions from the Fermi points  $\lambda_{ia}$  due to their nonzero energy.

CFT predicts a universal  $1/L$  energy correction in terms of the velocities of right and left moving modes of the form in Eq. (7.19). However, here the velocity

$$v_{ia} = \frac{\epsilon'(\lambda_{ia})}{2\pi\rho_\infty(\lambda_{ia})} \quad (7.21)$$

differs from the dynamic velocity  $\tilde{v}_{ia}$  from the dispersion  $\tilde{\epsilon}(\lambda)$  which governs the propagation of correlations.

From here on we will drop the subscript  $\infty$  and denote by  $\rho(\lambda)$  the density in the thermodynamic limit.

### 7.4 The shift function

As it turns out, the shift function  $F(\lambda|\lambda')$  determined by the integral equation

$$F(\lambda|\lambda') = \frac{\theta(\lambda - \lambda')}{2\pi} + \sum_i \int_{\lambda_{iL}}^{\lambda_{iR}} \frac{d\nu}{2\pi} K(\lambda - \nu) F(\nu|\lambda') \quad (7.22)$$

plays an important role. Its definition can be obtained by considering a particle-hole excitation with rapidity  $\lambda_p$  for the particle and  $\lambda_h$  for the hole, as is discussed in standard textbooks [24]. Denoting  $\lambda_j$  for the solution of the Bethe equations for the state  $|\{k_{ia}\}\rangle$  and  $\tilde{\lambda}_j$  for the excited state, we can define the shift function for the particle-hole excitation as

$$F(\lambda_j|\lambda_p, \lambda_h) = \frac{\lambda_j - \tilde{\lambda}_j}{\lambda_{j+1} - \lambda_j}. \quad (7.23)$$

From the Bethe equations one can show that  $F(\lambda|\lambda_p, \lambda_h) = F(\lambda|\lambda_p) - F(\lambda|\lambda_h)$  with definitions according to (7.22).

In this section we collect various results on the shift function for zero entropy states which are quite useful. Especially for the case of the ground state this is all known, but a discussion of the generality seems unavailable in the literature or is at least hard to find.

Since  $\partial_{\lambda'} \theta(\lambda - \lambda') = -K(\lambda - \lambda')$  we easily see that

$$\partial_{\lambda'} F(\lambda|\lambda') = -L(\lambda|\lambda'). \quad (7.24)$$

It is worth noting that  $L(\lambda|\lambda') = L(\lambda'|\lambda)$ , but

$$\partial_\lambda F(\lambda|\lambda') = L(\lambda|\lambda') - \sum_{ia} s_a L(\lambda|\lambda_{ia}) F(\lambda_{ia}|\lambda') \quad (7.25)$$

which follows from Eq. (7.22) by using a partial integration. Another, very useful, relation is

$$F(\lambda|\lambda') + F(\lambda'|\lambda) = \sum_{ia} s_a F(\lambda_{ia}|\lambda) F(\lambda_{ia}|\lambda'). \quad (7.26)$$

This in particular implies

$$\sum_{kc} [\delta_{ia,kc} - s_c F(\lambda_{kc}|\lambda_{ia})] [\delta_{jb,kc} - s_b F(\lambda_{kc}|\lambda_{jb})] = \delta_{ia,jb} \quad (7.27)$$

hence we have found a matrix-inverse pair

$$U_{ia,jb} = \delta_{ia,jb} - s_b F(\lambda_{jb}|\lambda_{ia}), \quad [U^{-1}]_{ia,jb} = \delta_{ia,jb} - s_b F(\lambda_{ia}|\lambda_{jb}). \quad (7.28)$$

Finally,

$$\sum_{ia} s_a F(\lambda|\lambda_{ia}) F(\lambda'|\lambda_{ia}) = \sum_{ia} s_a F(\lambda_{ia}|\lambda) F(\lambda_{ia}|\lambda'). \quad (7.29)$$

Strictly speaking, the function  $F(\lambda|\lambda')$  does not encode the shift of rapidities when a single particle or hole is created in bosonic models such as Lieb-Liniger and XXZ due to the  $1/2$  shift in the quantum number lattice when we change particle-number parity. Rather,  $F(\lambda|\lambda')$  represents the phase shifts in the fermionic dual which is the Cheon-Shigehara model [257,258] for Lieb-Liniger and spinless lattice fermions for XXZ.

Using the conventions that adding a particle shifts the occupied quantum numbers to the left while adding a hole shifts them to the right, we can define the bosonic shift function

$$F_B(\lambda|\lambda') = \frac{\theta(\lambda - \lambda') - \pi}{2\pi} + \sum_i \int_{\lambda_{iL}}^{\lambda_{iR}} \frac{d\nu}{2\pi} K(\lambda - \nu) F_B(\nu|\lambda'). \quad (7.30)$$

The relation between  $F(\lambda|\lambda')$  and  $F_B(\lambda|\lambda')$  may be expressed as

$$F_B(\lambda|\lambda') = F(\lambda|\lambda') - \frac{1}{2} Z(\lambda) \quad (7.31)$$

where  $Z(\lambda)$  is the analogue of the dressed charge

$$Z(\lambda) = 1 + \sum_i \int_{\lambda_{iL}}^{\lambda_{iR}} \frac{d\nu}{2\pi} K(\lambda - \nu) Z(\nu) \quad (7.32)$$

which is related to critical exponents in the case of the ground state, but a similar interpretation is not present in the general case. Note that derivatives with respect to  $\lambda$  or  $\lambda'$  of  $F(\lambda|\lambda')$  and  $F_B(\lambda|\lambda')$  coincide.

From hereon we will implicitly assume that we deal with the fermionic version of the models. This makes the connection with the (fermionic) effective field theory most transparent. The difference is only important for single particle or hole excitations.

## 7.5 Energy and momentum of excitations

In order to determine the single-particle dispersion function, let us consider again a particle-hole excitation on top of the state  $|\{k_{ia}\}\rangle$  with particle rapidity  $\lambda_p$  and hole rapidity  $\lambda_h$ . Let  $\lambda_j$  and  $\tilde{\lambda}_j$  again denote the solution to the Bethe equations before and after excitation. The energy difference

$$\Delta E(\lambda_p, \lambda_h) = \epsilon_0(\lambda_p) - \epsilon_0(\lambda_h) + \sum_j [\epsilon_0(\tilde{\lambda}_j) - \epsilon_0(\lambda_j)] \quad (7.33)$$

can be expressed in the thermodynamic limit as

$$\Delta E(\lambda_p, \lambda_h) = \tilde{\epsilon}(\lambda_p) - \tilde{\epsilon}(\lambda_h) \quad (7.34)$$

with

$$\tilde{\epsilon}(\lambda) = \epsilon_0(\lambda) - \sum_i \int_{\lambda_{iL}}^{\lambda_{iR}} d\nu \epsilon'_0(\nu) F(\nu|\lambda). \quad (7.35)$$

By a partial integration we obtain

$$\tilde{\epsilon}(\lambda) = \epsilon_0(\lambda) - \sum_{ia} s_a \epsilon_0(\lambda_{ia}) F(\lambda_{ia}|\lambda) + \sum_i \int_{\lambda_{iL}}^{\lambda_{iR}} d\nu \epsilon_0(\nu) \partial_\nu F(\nu|\lambda) \quad (7.36)$$

from where Eq. (7.25) expresses the actual single-particle dispersion as

$$\tilde{\epsilon}(\lambda) = \epsilon(\lambda) - \sum_{ia} s_a \epsilon(\lambda_{ia}) F(\lambda_{ia}|\lambda). \quad (7.37)$$

Note that this indeed differs from  $\epsilon(\lambda)$  when  $\epsilon(\lambda_{ia}) \neq 0$  and we have nontrivial backflow  $F(\lambda_{ia}|\lambda) \neq 0$ .

The momentum of a particle is defined by the equation

$$k(\lambda) = p_0(\lambda) - \sum_i \int_{\lambda_{iL}}^{\lambda_{iR}} d\nu p'_0(\nu) F(\nu|\lambda) \quad (7.38)$$

from which it is easy to see that  $k'(\lambda) = 2\pi\rho(\lambda)$  as in the equilibrium case.

Of particular interest is the energy and velocity of particles close to the Fermi points  $k_{ia}$ . We note that Eqs. (7.37) and (7.27) imply

$$\tilde{\epsilon}(\lambda_{ia}) = \sum_{jb} [\delta_{ia,jb} - s_b F(\lambda_{jb}|\lambda_{ia})] \epsilon(\lambda_{jb}), \quad (7.39)$$

$$\epsilon(\lambda_{ia}) = \sum_{jb} [\delta_{ia,jb} - s_b F(\lambda_{ia}|\lambda_{jb})] \tilde{\epsilon}(\lambda_{jb}). \quad (7.40)$$

The Fermi velocity for the Fermi point  $k_{ia}$  is defined as

$$\tilde{v}_{ia} = \left. \frac{\partial \epsilon}{\partial k} \right|_{k=k_{ia}} = \frac{\tilde{\epsilon}'(\lambda_{ia})}{2\pi\rho(\lambda_{ia})}. \quad (7.41)$$

The relation between  $\epsilon(\lambda)$  and  $\tilde{\epsilon}(\lambda)$  can also be expressed as

$$\epsilon(\lambda) = \tilde{\epsilon}(\lambda) - \sum_{ia} s_a \tilde{\epsilon}(\lambda_{ia}) F(\lambda|\lambda_{ia}). \quad (7.42)$$

## 7.6 Finite-size spectrum and critical exponents

Now that we have established the energy of zero-entropy states to order  $1/L$  [Eq. (7.11)] and the energy of particle and hole excitations in the thermodynamic limit [Eq. (7.37)] we will ask the usual question: what is the change in energy upon adding or removing particles very close to the Fermi points  $I_{ia}$ ? Let us consider a state defined by  $I_{ia} \rightarrow I_{ia} + s_a N_{ia}$ , i.e.  $N_{ia}$  denotes the number of particles added or removed at the Fermi point  $k_{ia}$ .

In terms of the quantum numbers

$$N_i = L \int_{\lambda_{iL}}^{\lambda_{iR}} d\lambda \rho(\lambda), \quad D_i = L \left\{ \int_{-\infty}^{\lambda_{iL}} - \int_{\lambda_{iR}}^{\infty} \right\} d\lambda \rho(\lambda) \quad (7.43)$$

we have

$$N_{ia} = \frac{\Delta N_i + s_a \Delta D_i}{2} \quad (7.44)$$

where  $\Delta N_i$ ,  $\Delta D_i$  denotes the change in  $N_i$ ,  $D_i$ . We can also express the variation of the state in terms of the change in the Fermi rapidities  $\lambda_{jb} \rightarrow \lambda_{jb} + \delta\lambda_{jb}$ . The definitions in Eq. (7.43) allow us to compute the Jacobian

$$\frac{\partial N_{ia}}{\partial \lambda_{jb}} = s_a L \left\{ \rho(\lambda_{ia}) \delta_{ia,jb} + \frac{1}{2} \int_{-\infty}^{\infty} d\lambda s_a \operatorname{sgn}(\lambda_{ia} - \lambda) \frac{d\rho}{d\lambda_{jb}}(\lambda) \right\}. \quad (7.45)$$

Using that

$$\frac{\partial \rho}{\partial \lambda_{jb}}(\lambda) = s_b \rho(\lambda_{jb}) L(\lambda_{jb}|\lambda) = -s_b \rho(\lambda_{jb}) \partial_\lambda F(\lambda_{jb}|\lambda) \quad (7.46)$$

## 7. General finite-size effects

---

and a partial integration one finds

$$\frac{\partial N_{ia}}{\partial \lambda_{jb}} = L s_b \rho(\lambda_{jb}) [\delta_{ia,jb} - s_a F(\lambda_{jb} | \lambda_{ia})]. \quad (7.47)$$

We recognize the matrix  $[U^{-1}]_{jb,ia}$  from Eq. (7.28), which immediately gives

$$\frac{\partial \lambda_{ia}}{\partial N_{jb}} = \frac{1}{L s_a \rho(\lambda_{ia})} [\delta_{ia,jb} - s_a F(\lambda_{ia} | \lambda_{jb})] \quad (7.48)$$

and therefore we can express

$$\delta \lambda_{ia} = \sum_{jb} \frac{\delta_{ia,jb} - s_a F(\lambda_{ia} | \lambda_{jb})}{L s_a \rho(\lambda_{ia})} N_{jb}. \quad (7.49)$$

Since the Fermi momenta are directly related to the numbers  $I_{ia}$ , the change in Fermi momentum is

$$\delta k_{ia} = \frac{L s_a N_{ia}}{2\pi} \quad (7.50)$$

which can also be obtained from the definition of  $k(\lambda)$  in Eq. (7.38). Hence also the relations

$$\frac{\partial k_{ia}}{\partial \lambda_{jb}} = [\delta_{ia,jb} - s_b F(\lambda_{jb} | \lambda_{ia})] 2\pi \rho(\lambda_{jb}), \quad (7.51)$$

$$\frac{\partial \lambda_{ia}}{\partial k_{jb}} = \frac{1}{2\pi \rho(\lambda_{ia})} [\delta_{ia,jb} - s_b F(\lambda_{ia} | \lambda_{jb})] \quad (7.52)$$

are valid.

Let us consider corrections to the energy  $E$  in Eq. (7.11) to order  $1/L$  when  $k_{ia} \rightarrow k_{ia} + \delta k_{ia}$ . We express

$$\delta E = \sum_{ia} \frac{\partial E}{\partial \lambda_{ia}} \delta \lambda_{ia} + \frac{1}{2} \sum_{ia,jb} \frac{\partial^2 E}{\partial \lambda_{ia} \partial \lambda_{jb}} \delta \lambda_{ia} \delta \lambda_{jb} \quad (7.53)$$

or equivalently

$$\delta E = \sum_{ia} \frac{\partial E}{\partial k_{ia}} \delta k_{ia} + \frac{1}{2} \sum_{ia,jb} \frac{\partial^2 E}{\partial k_{ia} \partial k_{jb}} \delta k_{ia} \delta k_{jb}. \quad (7.54)$$

Note that these corrections can only come from the extensive contribution to  $E$  since  $\delta \lambda_{ia}$  and  $\delta k_{ia}$  are of order  $1/L$ .

From Eq. (7.11) and (7.40) we obtain

$$\frac{\partial E}{\partial \lambda_{ia}} = L s_a \rho(\lambda_{ia}) \epsilon(\lambda_{ia}) = \sum_{jb} L s_a \rho(\lambda_{ia}) [\delta_{ia,jb} - s_b F(\lambda_{ia} | \lambda_{jb})] \tilde{\epsilon}(\lambda_{jb}) \quad (7.55)$$

which together with Eqs. (7.52) shows

$$\frac{\partial E}{\partial k_{ia}} = \frac{s_a L}{2\pi} \tilde{\epsilon}(\lambda_{ia}) \quad (7.56)$$

so that

$$\delta E^{(1)} = \sum_{ia} \frac{\partial E}{\partial k_{ia}} \delta k_{ia} = \sum_{ia} \tilde{\epsilon}(\lambda_{ia}) N_{ia} \quad (7.57)$$

(where we have introduced the notation  $\delta E^{(n)}$  for the order  $L^{-n}$  term in  $\delta E$ ).

Next, consider the second order correction

$$\delta E^{(2)} = \frac{1}{2} \sum_{ia,jb} \frac{\partial E}{\partial k_{ia} \partial k_{jb}} \delta k_{ia} \delta k_{jb}. \quad (7.58)$$

From Eq. (7.35) we find that

$$\frac{\partial \tilde{\epsilon}}{\partial \lambda_{jb}}(\lambda) = -s_b \epsilon'_0(\lambda_{jb}) F(\lambda_{jb}|\lambda) - \sum_i \int_{\lambda_{iL}}^{\lambda_{iR}} d\nu \epsilon'_0(\nu) \frac{\partial F}{\partial \lambda_{jb}}(\nu|\lambda), \quad (7.59)$$

which together with

$$\frac{\partial F}{\partial \lambda_{jb}}(\lambda|\lambda') = s_b L(\lambda|\lambda_{jb}) F(\lambda_{jb}|\lambda') \quad (7.60)$$

can be used to show that

$$\frac{\partial \tilde{\epsilon}}{\partial \lambda_{jb}}(\lambda) = -s_b \tilde{\epsilon}'(\lambda_{jb}) F(\lambda_{jb}|\lambda). \quad (7.61)$$

For the derivation it is useful to note

$$\epsilon'(\lambda) = \epsilon'_0(\lambda) + \sum_i \int_{\lambda_{iL}}^{\lambda_{iR}} d\nu \partial_\lambda L(\lambda|\nu) \epsilon_0(\nu), \quad (7.62)$$

$$\tilde{\epsilon}'(\lambda) = \epsilon'(\lambda) + \sum_{ia} s_a \epsilon(\lambda_{ia}) L(\lambda_{ia}|\lambda). \quad (7.63)$$

Computing

$$\frac{\partial}{\partial \lambda_{jb}} \left( \frac{\partial E}{\partial k_{ia}} \right) = \frac{s_a L}{2\pi} [\delta_{ia,jb} - s_b F(\lambda_{jb}|\lambda_{ia})] \tilde{\epsilon}'(\lambda_{jb}) \quad (7.64)$$

we thus find

$$\delta E^{(2)} = \frac{1}{2} \sum_{ia,jb,kc} \frac{\partial \lambda_{kc}}{\partial k_{jb}} \frac{\partial}{\partial \lambda_{kc}} \left( \frac{\partial E}{\partial k_{ia}} \right) \quad (7.65)$$

$$\begin{aligned} &= \frac{1}{L} \sum_{ia,jb,kc} \frac{\tilde{\epsilon}'(\lambda_{kc})}{2\rho(\lambda_{kc})} [\delta_{ia,kc} - s_c F(\lambda_{kc}|\lambda_{ia})] \\ &\quad \times [\delta_{jb,kc} - s_c F(\lambda_{kc}|\lambda_{jb})] N_{ia} N_{jb}. \end{aligned} \quad (7.66)$$

## 7. General finite-size effects

Now, it is easy to also incorporate the number of particle-hole excitations corresponding to a total number of momentum quanta  $n_{ia}$  close to the Fermi point  $k_{ia}$  and arrive at the general result for the spectrum

$$\delta E = \sum_{ia} \tilde{\epsilon}(\lambda_{ia}) N_{ia} + \frac{2\pi}{L} \sum_{ia} s_a \tilde{v}_{ia} \left[ n_{ia} + \frac{1}{2} \left( \sum_{jb} U_{jb,ia} N_{jb} \right)^2 \right] \quad (7.67)$$

This is valid for general zero-entropy states  $|\{k_{ia}\}\rangle$  and general energy functions  $\epsilon_0(\lambda)$  with

$$U_{ia,jb} = \delta_{ia,jb} - s_b F(\lambda_{ia}|\lambda_{jb}), \quad [U^{-1}]_{ia,jb} = s_a s_b U_{jb,ia}. \quad (7.68)$$

Note that the velocity  $s_a \tilde{v}_{ia}$  can be negative in the current setup.

The matrix  $U_{ia,jb}$  is identified with the matrix of the Bogoliubov transformation diagonalizing the multi-component Tomonaga-Luttinger Hamiltonian describing the state [5] (see Ch. 6). These parameters determine the exponents of critical correlations, i.e. the conformal dimensions of scaling fields in the language of CFT.

### 7.7 The symmetric case

In the case of a symmetric quantum number configuration,  $I_{iL} = -I_{n+1-iR}$ , we have the equalities

$$\tilde{v}_{iL} = -\tilde{v}_{n+1-iR} \quad \text{and} \quad U_{ia,jb} = U_{n+1-i\bar{a},n+1-j\bar{b}} \quad (7.69)$$

(with  $\bar{L} = R$  and  $\bar{R} = L$ ). Define the matrices

$$Z_{ij} = U_{iR,jR} - U_{n+1-iL,jR} = \delta_{ij} - F(\lambda_{jR}|\lambda_{iR}) + F(\lambda_{jR}|\lambda_{n+1-iL}), \quad (7.70)$$

$$Y_{ij} = U_{iR,jR} + U_{n+1-iL,jR} = \delta_{ij} - F(\lambda_{jR}|\lambda_{iR}) - F(\lambda_{jR}|\lambda_{n+1-iL}). \quad (7.71)$$

Using that in the symmetric case  $F(-\lambda|-\lambda') = -F(\lambda|\lambda')$  and  $\lambda_{iL} = -\lambda_{n+1-iR}$ , Eq. (7.26) gives

$$\sum_k Z_{ik} Y_{jk} = \delta_{ij} \quad (7.72)$$

and so  $Z^{-1} = Y^T$  which is closely related to the general relation  $[U^{-1}]_{ia,jb} = s_a s_b U_{jb,ia}$ .

The finite-size correction to the energy can then be written as

$$\delta E = \sum_i \tilde{\epsilon}_i \tilde{N}_i + \frac{2\pi}{L} \sum_i \frac{\tilde{v}_i}{2} \left[ \left( \sum_j [Z^{-1}]_{ij} \tilde{N}_j \right)^2 + \left( \sum_j Z_{ji} \tilde{D}_j \right)^2 \right] \quad (7.73)$$

where  $\tilde{\epsilon}_i = \tilde{\epsilon}(\lambda_{iR})$ ,  $\tilde{v}_i = \tilde{v}_{iR}$  and

$$\tilde{N}_i = N_{iR} + N_{n+1-iL}, \quad \tilde{D}_i = N_{iR} - N_{n+1-iL}. \quad (7.74)$$

We can write

$$Z_{ij} = \delta_{ij} + \int_{\lambda_{n+1-iL}}^{\lambda_{iR}} d\nu F(\lambda_{jR}|\nu). \quad (7.75)$$

We can also obtain this matrix from as  $Z_{ij} = \xi_{ij}(\lambda_{jR})$  where  $\xi_{ij}(\lambda)$  is defined by

$$\xi_{ij}(\lambda) = \delta_{ij} + \sum_k \int_{\lambda_{n+1-iL}}^{\lambda_{iR}} \frac{d\nu}{2\pi} K(\lambda - \nu) \xi_{kj}(\nu) \quad (7.76)$$

which is straightforward to derive using the relation  $\partial_{\lambda'} F(\lambda|\lambda') = -L(\lambda|\lambda')$  from Eq. (7.75). Hence, in the symmetric case we reach the same conclusion as Ref. [293], namely that the critical exponents can equivalently be expressed in terms of a dressed charge matrix  $\xi_{ij}(\lambda)$  similar to models solvable by nested Bethe ansatz [28, 247, 294–302].

## 7.8 Impurity configurations

Let us consider an impurity configuration defined by one hole with  $\lambda_h$  in, or one particle with  $\lambda_p$  outside of one of the Fermi-sea blocks and ask again what the spectrum of excitations at the Fermi points is to order  $1/L$ . Here, the energy of the state  $\{|k_{ia}\rangle\}$  still serves as the reference. We restrict the analysis to the particle case, as the case of a hole just introduces appropriate minus signs. Note that we assume to work in the fermionic dual here such that  $F(\lambda|\lambda')$  encodes the shift of rapidities for a single-particle excitation.

In the case of an impurity we have to go back to the derivation of for the root density in Sec. 7.3 to order  $1/L^2$ . From the Bethe equations we find

$$\rho(\lambda) = \frac{\rho'_0(\lambda)}{2\pi} + \sum_i \int_{\lambda_{iL}}^{\lambda_{iR}} \frac{d\nu}{2\pi} K(\lambda - \nu) \rho(\nu) + \frac{K(\lambda - \lambda_p)}{2\pi L} + \frac{1}{24L^2} \sum_{ia} \frac{s_a K'(\lambda - \lambda_{ia})}{2\pi \rho(\lambda_{ia})} \quad (7.77)$$

in this case. The solution for  $\rho(\lambda)$  thus has an extra contribution due to the impurity

$$\rho(\lambda) = \rho_\infty(\lambda) + \frac{\rho_{\text{imp}}(\lambda|\lambda_p)}{L} + \sum_{ia} \frac{\rho_{ia}(\lambda)}{24L^2 \rho_\infty(\lambda_{ia})} \quad (7.78)$$

where clearly

$$\rho_{\text{imp}}(\lambda|\lambda_p) = L(\lambda|\lambda_p). \quad (7.79)$$

## 7. General finite-size effects

---

Going back to the definitions of  $N_i$  and  $D_i$ , we find that

$$N_i = n_i^{\text{imp}} + L \int_{\lambda_{iL}}^{\lambda_{iR}} d\lambda \rho_\infty(\lambda), \quad D_i = d_i^{\text{imp}} + L \left\{ \int_{-\infty}^{\lambda_{iL}} - \int_{\lambda_{iR}}^{\infty} \right\} d\lambda \rho_\infty(\lambda) \quad (7.80)$$

with

$$n_i^{\text{imp}} = \int_{\lambda_{iL}}^{\lambda_{iR}} d\lambda L(\lambda|\lambda_p) = -F(\lambda_{iR}|\lambda_p) + F(\lambda_{iL}|\lambda_p), \quad (7.81)$$

$$d_i^{\text{imp}} = \left\{ \int_{-\infty}^{\lambda_{iL}} - \int_{\lambda_{iR}}^{\infty} \right\} d\lambda L(\lambda|\lambda_p) = -F(\lambda_{iR}|\lambda_p) - F(\lambda_{iL}|\lambda_p). \quad (7.82)$$

Considering the energy difference of the state  $|\{k_{ia}\}\rangle$  and the state defined by the addition of particles at the Fermi points according to the numbers  $\{N_{ia}\}$  and the additional particle impurity with quantum number  $I_p$  leads to

$$\begin{aligned} \delta E = \tilde{\epsilon}(\lambda_p) + \sum_{ia} \tilde{\epsilon}(\lambda_{ia}) [N_{ia} - n_{ia}^{\text{imp}}] \\ + \frac{2\pi}{L} \sum_{ia} s_a \tilde{v}_{ia} \left[ n_{ia} + \frac{1}{2} \left( \sum_{jb} U_{jb,ia} [N_{jb} - n_{jb}^{\text{imp}}] \right)^2 \right] \end{aligned} \quad (7.83)$$

with

$$n_{ia}^{\text{imp}} = \frac{n_i^{\text{imp}} + s_a d_i^{\text{imp}}}{2} = -s_a F(\lambda_{ia}|\lambda_p) \quad (7.84)$$

which follows by the same reasoning as leading up to Eq. (7.67) but using Eq. (7.80).

A hole impurity just replaces  $F(\lambda_{ia}|\lambda_p) \rightarrow -F(\lambda_{ia}|\lambda_h)$ . The generalization to multiple impurities is straightforward.

## 7.9 Conclusion

We have considered the energy of excitations on states of zero entropy density in the Lieb-Liniger and other Bethe ansatz solvable models. These states can be considered as the zero-temperature limit of a statistical ensemble defined by a generalized Hamiltonian in the spirit of the GGE. We explicitly allowed the energies to be measured with a different Hamiltonian which generically would correspond to the physical Hamiltonian of the model. We have shown that the dispersion function is not necessarily determined by a single integral equation, but includes contributions from the generalized Fermi points that may have finite energy in the situation under consideration. We derived a generalization of the expression for finite-size corrections to the spectrum. This derivation is valid

for arbitrary bare energy functions  $\epsilon_0(\lambda)$  constructed from the eigenvalues of local charges on the Bethe basis and also for arbitrary configurations of Fermi seas. The energy corrections related to addition or subtraction of particles at the generalized Fermi points, which are directly related to critical exponents, are expressed in terms of the shift function and only for a symmetric configuration can this be expressed in terms of a dressed charge matrix. Similar expressions are derived in the presence of an additional particle and hole impurity.

Our results are interesting in the light of recent developments in the correspondence between Bethe ansatz solvable models and effective field theory methods. The characteristic power-law behavior of correlations well known from the correspondence with CFT can be interpreted in terms of the Anderson orthogonality catastrophe due to the phase shift of the modes at the Fermi points. While for static correlations one only considers Umklapp-like configurations, time dependent correlations include additional contributions from certain impurity configurations, but the logic in both cases is remarkably similar. The point is that the power law exponents are completely determined by the phase shifts (static data) while the characteristic frequencies of oscillations in space and time are determined by the momentum and energy differences of the reference state with the Umklapp or impurity excitation respectively. Our work suggests that this decomposition of effects can be extended to out-of-equilibrium correlations of zero-entropy states and the power-law exponents depend only on the scattering data of the theory and are Hamiltonian independent.



# Conclusion

We have discussed the time-dependence of correlations of one-dimensional systems with a boundary, the absence of Luttinger liquid physics in the Au/Ge(001) atomic chains, Bragg pulses in atomic systems and the class of Moses sea states in Bethe ansatz solvable models. The underlying questions were sometimes fueled directly by experimental results, other times the motivation was purely theoretical, but for each topic it was a combination of insights from different models and techniques that allowed us to gain an understanding of the physics at play. The interplay of integrability and effective-field-theory methods in particular provides a rich and effective set of tools to address a variety of questions. Undoubtedly, these will reveal more surprising features of one-dimensional physics in times to come.

To conclude, let us speculate on some of the future directions of this research. First of all, not all questions in nonlinear Luttinger liquid theory are completely settled. We have barely touched upon the universal predictions based on refermionizing the most important dimension-three operators leading to an effective theory of free quasi-particles with quadratic dispersion. This has led to a universal expression of the spectral function  $A(k, \epsilon)$  beyond the Luttinger liquid approximation valid in the limit  $k \rightarrow k_F$  [58] which can be related to the Painlevé IV differential equation [303]. One can show that the dimension-three interaction term that is neglected in the quasi-particle Hamiltonian contributes to the phase shifts at higher order in  $k - k_F$ , hence these, and terms of higher dimension, can be neglected to first approximation for generic systems with nonlinear dispersions. This is however no longer valid once the quadratic dispersion term vanishes as is the case for systems with particle-hole symmetry. In this case one has to take into account dimension-four operators as lowest non-trivial order. It is not yet clear whether universal results for the spectral function or dynamic structure factor can be derived using this theory. It would however be interesting to do so as these would be directly applicable to spin systems in zero field and to the spin sector of electronic systems.

The last few years have seen huge progress in understanding quantum systems out of equilibrium and the mechanisms and properties of equilibration. Tradi-

## 8. Conclusion

---

tionally, effective-field-theory methods are thought to be applicable mainly to describe the low-energy limit of equilibrium systems. Nonlinear Luttinger liquid theory highlights the subtleties that may arise in naively applying field-theory methods but also how field theory can be amazingly effective even beyond the low-energy domain. In the final chapters we have even explored applications of field-theory methods to genuine out-of-equilibrium states. We expect more results to be possible to obtain. In particular, the identification saddle-point contributions in the computations of certain correlations seems to align well with the method of the quench action.

In the experimental search for Luttinger liquid systems it seems to us that atomic chains on surfaces are likely to suffer from difficulties exhibiting Luttinger liquid physics as the Au/Ge(001). The problem of isolating the interesting electronic states from the substrate is likely to be a tough challenge. Whether this can ever be at all in surface systems (either in Au/Ge or using altogether other substances) remains an open question. The outlook is perhaps somewhat pessimistic: as we have seen, in order for the most interesting effects of one-dimensional physics to emerge, it is necessary to have a clear separation of various energy scales which represents a prohibitively difficult challenge for these setups.

Lastly, one can address the question whether the insights gained in 1d could be transported to higher dimensions. One possibility might be to look at extending the ideas associated to impurity Hamiltonians to these more generic situations—the origin of impurity problems such as the the X-ray edge singularity and Kondo effects in fact already illustrates this. Although none of the nonperturbative 1d results could be directly translated to these cases, one might nonetheless find inspiration from the idea of using high-energy/momentum impurities to formulate new forms of perturbative expansions.

# Bibliography

- [1] I. S. Eliëns, F. B. Ramos, J. C. Xavier, and R. G. Pereira. Boundary versus bulk behavior of time-dependent correlation functions in one-dimensional quantum systems. *Phys. Rev. B*, 93:195129, May 2016.
- [2] N. de Jong, R. Heimbuch, S. Eliëns, S. Smit, E. Frantzeskakis, J.-S. Caux, H. J. W. Zandvliet, and M. S. Golden. Gold-induced nanowires on the  $ge(100)$  surface yield a 2d and not a 1d electronic structure. *Phys. Rev. B*, 93:235444, Jun 2016.
- [3] R. van den Berg, B. Wouters, S. Eliëns, J. De Nardis, R. M. Konik, and J.-S. Caux. Separation of time scales in a quantum newton’s cradle. *Phys. Rev. Lett.*, 116:225302, Jun 2016.
- [4] T. Fokkema, I. S. Eliëns, and J.-S. Caux. Split fermi seas in one-dimensional bose fluids. *Phys. Rev. A*, 89:033637, Mar 2014.
- [5] R. Vlijm, I. S. Eliëns, and J. S. Caux. Correlations of zero-entropy critical states in the XXZ model: integrability and Luttinger theory far from the ground state. *SciPost Phys.*, 1:008, 2016.
- [6] Sebas Eliëns and Jean-Sébastien Caux. General finite-size effects for zero-entropy states in one-dimensional quantum integrable models. *Journal of Physics A: Mathematical and Theoretical*, 49(49):495203, 2016.
- [7] R. Toskovic, R. van den Berg, A. Spinelli, I.S. Eliëns, B. van den Toorn, B. Bryant, J.-S. Caux, and F.A. Otte. Atomic spin chain realization of a model of quantum criticality. *Nat. Physics*, 12:656–660, 2016.
- [8] I. S. Eliëns, J. C. Romers, and F. A. Bais. Diagrammatics for bose condensation in anyon theories. *Phys. Rev. B*, 90:195130, Nov 2014.
- [9] T. Giamarchi. *Quantum Physics in One Dimension*. Oxford University Press, 2004.
- [10] John Von Neumann. Method in the physical sciences. *Collected Works*, 6:491–498, 1955.
- [11] I. Bloch, J. Dalibard, and W. Zwerger. Many-body physics with ultracold gases. *Rev. Mod. Phys.*, 80(3):885–964, 2008.

## 8. BIBLIOGRAPHY

---

- [12] Toshiya Kinoshita, Trevor Wenger, and David S. Weiss. A quantum Newton's cradle. *Nature*, 440:900–903, April 2006.
- [13] Adilet Imambekov, Thomas L. Schmidt, and Leonid I. Glazman. One-dimensional quantum liquids: Beyond the luttinger liquid paradigm. *Rev. Mod. Phys.*, 84:1253–1306, Sep 2012.
- [14] R G Pereira, J Sirker, J-S Caux, R Hagemans, J M Maillet, S R White, and I Affleck. Dynamical structure factor at small  $q$  for the xxz spin-1/2 chain. *Journal of Statistical Mechanics: Theory and Experiment*, 2007(08):P08022, 2007.
- [15] Rodrigo G. Pereira, Steven R. White, and Ian Affleck. Spectral function of spinless fermions on a one-dimensional lattice. *Phys. Rev. B*, 79:165113, Apr 2009.
- [16] M. Olshanii. Atomic Scattering in the Presence of an External Confinement and a Gas of Impenetrable Bosons. *Phys. Rev. Lett.*, 81(5):938–941, 1998.
- [17] Elliott H. Lieb, Robert Seiringer, and Jakob Yngvason. One-dimensional bosons in three-dimensional traps. *Phys. Rev. Lett.*, 91:150401, Oct 2003.
- [18] Robert Seiringer and Jun Yin. The lieb-liniger model as a limit of dilute bosons in three dimensions. *Communications in Mathematical Physics*, 284(2):459–479, 2008.
- [19] E. H. Lieb and W. Liniger. Exact Analysis of an Interacting Bose Gas. I. The General Solution and the Ground State. *Phys. Rev.*, 130(4):1605–1616, 1963.
- [20] H. Bethe and W. Heitler. On the stopping of fast particles and on the creation of positive electrons. *Proc. R. Soc. Lond. A*, 146(856):83–112, 1934.
- [21] B. Sutherland. *Beautiful Models*. World Scientific, 2004.
- [22] Jean-Sébastien Caux and Jorn Mossel. Remarks on the notion of quantum integrability. *Journal of Statistical Mechanics: Theory and Experiment*, 2011(02):P02023, 2011.
- [23] M. Takahashi. *Thermodynamics of one-dimensional solvable models*. Cambridge University Press, Cambridge, 1999.
- [24] V. E. Korepin, N. M. Bogoliubov, and A. G. Izergin. *Quantum Inverse Scattering Method and Correlation Functions*. Cambridge Univ. Press, 1993.
- [25] Mikhail Zvonarev. *Correlations in 1D boson and fermion systems: exact results*. PhD thesis, Copenhagen University, 2005.

- [26] J.-S. Caux. Correlation functions of integrable models: a description of the ABACUS algorithm. *J. Math. Phys.*, 50(9):095214, 2009.
- [27] M. Gaudin. *La fonction d'onde de Bethe*. Masson, Paris, 1983.
- [28] F. H. L. Essler, H. Frahm, F. Göhmann, A. Klümper, and V. E. Korepin. *The One-Dimensional Hubbard Model*. Cambridge University Press, 2005.
- [29] L. D. Landau. Theory of fermi-liquids. *Sov. Phys. JETP*, 3(920), 1957.
- [30] F. D. M. Haldane. ‘Luttinger liquid theory’ of one-dimensional quantum fluids. I. Properties of the Luttinger model and their extension to the general 1D interacting spinless Fermi gas. *J. Phys C: Sol. St. Phys.*, 14(19):2585, 1981.
- [31] F. D. M. Haldane. Effective Harmonic-Fluid Approach to Low-Energy Properties of One-Dimensional Quantum Fluids. *Phys. Rev. Lett.*, 47(25):1840–1843, 1981.
- [32] S.-I. Tomonaga. Remarks on Bloch’s Method of Sound Waves applied to Many-Fermion Problems. *Prog. Theor. Phys.*, 5(4):544–569, 1950.
- [33] J. M. Luttinger. Fermi Surface and Some Simple Equilibrium Properties of a System of Interacting Fermions. *Phys. Rev.*, 119:1153–1163, Aug 1960.
- [34] C. Karrasch, J. Rentrop, D. Schuricht, and V. Meden. Luttinger-liquid universality in the time evolution after an interaction quench. *Phys. Rev. Lett.*, 109:126406, Sep 2012.
- [35] J Rentrop, D Schuricht, and V Meden. Quench dynamics of the tomonaga-luttinger model with momentum-dependent interaction. *New Journal of Physics*, 14(7):075001, 2012.
- [36] E. Miranda. Introduction to bosonization. *Braz. Jour. of Phys.*, 33(1), March 2003.
- [37] F. Bloch. Bemerkung zur Elektronentheorie des Ferromagnetismus und der elektrischen Leitfähigkeit. *Z. Phys.*, 57:545, 1929.
- [38] Kurt Schönhammer. Luttinger liquids: the basic concepts. In *Strong interactions in low dimensions*, pages 93–136. Springer, 2004.
- [39] N M Bogoliubov, A G Izergin, and N Y Reshetikhin. Finite-size effects and infrared asymptotics of the correlation functions in two dimensions. *Journal of Physics A: Mathematical and General*, 20(15):5361, 1987.
- [40] Aditya Shashi, Leonid I. Glazman, Jean-Sébastien Caux, and Adilet Imambekov. Nonuniversal prefactors in the correlation functions of one-dimensional quantum liquids. *Phys. Rev. B*, 84:045408, Jul 2011.

## 8. BIBLIOGRAPHY

---

- [41] Aditya Shashi, Miłosz Panfil, Jean-Sébastien Caux, and Adilet Imam-bekov. Exact prefactors in static and dynamic correlation functions of one-dimensional quantum integrable models: Applications to the calogero-sutherland, lieb-liniger, and  $xxz$  models. *Phys. Rev. B*, 85:155136, Apr 2012.
- [42] A. Luther and I. Peschel. Single-particle states, Kohn anomaly, and pairing fluctuations in one dimension. *Phys. Rev. B*, 9(7):2911–2919, 1974.
- [43] V. Meden and K. Schönhammer. Spectral functions for the tomonaga-luttinger model. *Phys. Rev. B*, 46:15753–15760, Dec 1992.
- [44] J Voit. Charge-spin separation and the spectral properties of luttinger liquids. *Journal of Physics: Condensed Matter*, 5(44):8305, 1993.
- [45] Johannes Voit. Charge-spin separation and the spectral properties of Luttinger liquids. *Phys. Rev. B*, 47:6740–6743, Mar 1993.
- [46] J. Voit. One-dimensional fermi liquids. *Rep. Prog. Phys.*, 58(9):977–1116, 1995.
- [47] M. Khodas, M. Pustilnik, A. Kamenev, and L. I. Glazman. Fermi-luttinger liquid: Spectral function of interacting one-dimensional fermions. *Phys. Rev. B*, 76(15):155402, 2007.
- [48] K. D. Schotte and U. Schotte. Tomonaga’s Model and the Threshold Singularity of X-Ray Spectra of Metals. *Phys. Rev.*, 182(2):479–482, 1969.
- [49] Leon Balents. X-ray-edge singularities in nanotubes and quantum wires with multiple subbands. *Phys. Rev. B*, 61:4429–4432, Feb 2000.
- [50] A. Theumann. Single-Particle Green’s Function for a One-Dimensional Many-Fermion System. *J. Math. Phys.*, 8(12):2460–2467, 1967.
- [51] J. M. Luttinger. An Exactly Soluble Model of a Many-Fermion System. *Journal of Mathematical Physics*, 4(9):1154–1162, 1963.
- [52] K. V. Samokhin. Lifetime of excitations in a clean luttinger liquid. *J. Phys. Condens. Matter*, 10(31):L533, 1998.
- [53] D. N. Aristov. Luttinger liquids with curvature: Density correlations and coulomb drag effect. *Phys. Rev. B*, 76:085327, Aug 2007.
- [54] Sofian Teber. Bosonization approach to charge and spin dynamics of one-dimensional spin- $\frac{1}{2}$  fermions with band curvature in a clean quantum wire. *Phys. Rev. B*, 76:045309, Jul 2007.
- [55] S. Teber. Tails of the dynamical structure factor of 1d spinless fermions beyond the tomonaga approximation. *The European Physical Journal B - Condensed Matter and Complex Systems*, 52(2):233–244, 2006.

- [56] Tom Price and Austen Lamacraft. Fine structure of the phonon in one dimension from quantum hydrodynamics. *Phys. Rev. B*, 90:241415, Dec 2014.
- [57] A. V. Rozhkov. Fermionic quasiparticle representation of tomonaga-luttinger hamiltonian. *Eur. Phys. J. B*, 47(2):193–206, 2005.
- [58] Adilet Imambekov and Leonid I. Glazman. Universal theory of nonlinear luttinger liquids. *Science*, 323(5911):228–231, 2009.
- [59] P. W. Anderson. Infrared Catastrophe in Fermi Gases with Local Scattering Potentials. *Phys. Rev. Lett.*, 18:1049–1051, Jun 1967.
- [60] J. M. P. Carmelo and P. D. Sacramento. Finite-energy landau liquid theory for the one-dimensional hubbard model: Pseudoparticle energy bands and degree of localization/delocalization. *Phys. Rev. B*, 68:085104, Aug 2003.
- [61] R. G. Pereira, J. Sirker, J.-S. Caux, R. Hagemans, J. M. Maillet, S. R. White, and I. Affleck. Dynamical spin structure factor for the anisotropic spin-1/2 heisenberg chain. *Phys. Rev. Lett.*, 96:257202, Jun 2006.
- [62] M. Pustilnik, M. Khodas, A. Kamenev, and L. I. Glazman. Dynamic response of one-dimensional interacting fermions. *Phys. Rev. Lett.*, 96:196405, May 2006.
- [63] M. Khodas, M. Pustilnik, A. Kamenev, and L. I. Glazman. Dynamics of excitations in a one-dimensional bose liquid. *Phys. Rev. Lett.*, 99:110405, Sep 2007.
- [64] Rodrigo G. Pereira, Steven R. White, and Ian Affleck. Exact edge singularities and dynamical correlations in spin-1/2 chains. *Phys. Rev. Lett.*, 100:027206, Jan 2008.
- [65] Vadim V. Cheianov and Michael Pustilnik. Threshold singularities in the dynamic response of gapless integrable models. *Phys. Rev. Lett.*, 100:126403, Mar 2008.
- [66] Adilet Imambekov and Leonid I. Glazman. Phenomenology of one-dimensional quantum liquids beyond the low-energy limit. *Phys. Rev. Lett.*, 102:126405, Mar 2009.
- [67] Fabian H. L. Essler. Threshold singularities in the one-dimensional hubbard model. *Phys. Rev. B*, 81:205120, May 2010.
- [68] Thomas L. Schmidt, Adilet Imambekov, and Leonid I. Glazman. Spin-charge separation in one-dimensional fermion systems beyond luttinger liquid theory. *Phys. Rev. B*, 82:245104, Dec 2010.

## 8. BIBLIOGRAPHY

---

- [69] Thomas L. Schmidt, Adilet Imambekov, and Leonid I. Glazman. Fate of 1d spin-charge separation away from fermi points. *Phys. Rev. Lett.*, 104:116403, Mar 2010.
- [70] R. G. Pereira, K. Penc, S. R. White, P. D. Sacramento, and J. M. P. Carmelo. Charge dynamics in half-filled hubbard chains with finite on-site interaction. *Phys. Rev. B*, 85:165132, Apr 2012.
- [71] P Debray, V N Zverev, V Gurevich, R Klesse, and R S Newrock. Coulomb drag between ballistic one-dimensional electron systems. *Semiconductor Science and Technology*, 17(11):R21, 2002.
- [72] M. Yamamoto, M. Stopa, Y. Tokura, Y. Hirayama, and S. Tarucha. Coulomb drag between quantum wires: magnetic field effects and negative anomaly. *Physica E: Low-dimensional Systems and Nanostructures*, 12(1–4):726 – 729, 2002. Proceedings of the Fourteenth International Conference on the Electronic Properties of Two-Dimensional Systems.
- [73] M. Pustilnik, E. G. Mishchenko, L. I. Glazman, and A. V. Andreev. Coulomb drag by small momentum transfer between quantum wires. *Phys. Rev. Lett.*, 91:126805, Sep 2003.
- [74] Laroche D., Gervais G., Lilly M. P., and Reno J. L. Positive and negative Coulomb drag in vertically integrated one-dimensional quantum wires. *Nat Nano*, 6:793–797, 2011.
- [75] Rodrigo G. Pereira and Eran Sela. Spin-charge coupling in quantum wires at zero magnetic field. *Phys. Rev. B*, 82:115324, Sep 2010.
- [76] K. A. Matveev and A. Furusaki. Decay of fermionic quasiparticles in one-dimensional quantum liquids. *Phys. Rev. Lett.*, 111:256401, Dec 2013.
- [77] I. V. Protopopov, D. B. Gutman, and A. D. Mirlin. Relaxation in luttinger liquids: Bose-fermi duality. *Phys. Rev. B*, 90:125113, Sep 2014.
- [78] I. V. Protopopov, D. B. Gutman, M. Oldenburg, and A. D. Mirlin. Dissipationless kinetics of one-dimensional interacting fermions. *Phys. Rev. B*, 89:161104, Apr 2014.
- [79] Jie Lin, K. A. Matveev, and M. Pustilnik. Thermalization of acoustic excitations in a strongly interacting one-dimensional quantum liquid. *Phys. Rev. Lett.*, 110:016401, Jan 2013.
- [80] Gilad Barak, Hadar Steinberg, Loren N. Pfeiffer, Ken W. West, Leonid Glazman, Felix von Oppen, and Amir Yacoby. Interacting electrons in one dimension beyond the luttinger-liquid limit. *Nat. Phys.*, 6:489 – 493, 2010.

- [81] Eldad Bettelheim and Leonid Glazman. Quantum ripples over a semiclassical shock. *Phys. Rev. Lett.*, 109:260602, Dec 2012.
- [82] E. Bettelheim, A. G. Abanov, and P. Wiegmann. Orthogonality catastrophe and shock waves in a nonequilibrium fermi gas. *Phys. Rev. Lett.*, 97:246402, Dec 2006.
- [83] I. V. Protopopov, D. B. Gutman, P. Schmitteckert, and A. D. Mirlin. Dynamics of waves in one-dimensional electron systems: Density oscillations driven by population inversion. *Phys. Rev. B*, 87:045112, Jan 2013.
- [84] Rodrigo G. Pereira. Long time correlations of nonlinear luttinger liquids. *International Journal of Modern Physics B*, 26(22):1244008, 2012.
- [85] C. Karrasch, R. G. Pereira, and J. Sirker. Low temperature dynamics of nonlinear luttinger liquids. *New Journal of Physics*, 17(10):103003, 2015.
- [86] Luis Seabra, Fabian H. L. Essler, Frank Pollmann, Imke Schneider, and Thomas Veness. Real-time dynamics in the one-dimensional hubbard model. *Phys. Rev. B*, 90:245127, Dec 2014.
- [87] John L. Cardy. Boundary conditions, fusion rules and the verlinde formula. *Nucl. Phys. B*, 324(3):581 – 596, 1989.
- [88] I Affleck and A W W Ludwig. The fermi edge singularity and boundary condition changing operators. *Journal of Physics A: Mathematical and General*, 27(16):5375, 1994.
- [89] P. Fendley, F. Lesage, and H. Saleur. A unified framework for the kondo problem and for an impurity in a luttinger liquid. *Journal of Statistical Physics*, 85(1-2):211–249, 1996.
- [90] C. L. Kane and Matthew P. A. Fisher. Transmission through barriers and resonant tunneling in an interacting one-dimensional electron gas. *Phys. Rev. B*, 46:15233–15262, Dec 1992.
- [91] Eugene Wong and Ian Affleck. Tunneling in quantum wires: A boundary conformal field theory approach. *Nucl. Phys. B*, 417(3):403 – 438, 1994.
- [92] M. Fabrizio and Alexander O. Gogolin. Interacting one-dimensional electron gas with open boundaries. *Phys. Rev. B*, 51:17827–17841, Jun 1995.
- [93] Sebastian Eggert and Ian Affleck. Magnetic impurities in half-integer-spin heisenberg antiferromagnetic chains. *Phys. Rev. B*, 46:10866–10883, Nov 1992.
- [94] Reinhold Egger and Hermann Grabert. Friedel oscillations for interacting fermions in one dimension. *Phys. Rev. Lett.*, 75:3505–3508, Nov 1995.

## 8. BIBLIOGRAPHY

---

- [95] A. Leclair, F. Lesage, and H. Saleur. Exact friedel oscillations in the  $g = 1/2$  luttinger liquid. *Phys. Rev. B*, 54:13597–13603, Nov 1996.
- [96] Stefan Rommer and Sebastian Eggert. Spin- and charge-density oscillations in spin chains and quantum wires. *Phys. Rev. B*, 62:4370–4382, Aug 2000.
- [97] Nicolas Laflorencie, Erik S. Sørensen, Ming-Shyang Chang, and Ian Affleck. Boundary effects in the critical scaling of entanglement entropy in 1d systems. *Phys. Rev. Lett.*, 96:100603, Mar 2006.
- [98] L. Taddia, J. C. Xavier, F. C. Alcaraz, and G. Sierra. Entanglement entropies in conformal systems with boundaries. *Phys. Rev. B*, 88:075112, Aug 2013.
- [99] K. Schönhammer, V. Meden, W. Metzner, U. Schollwöck, and O. Gunnarsson. Boundary effects on one-particle spectra of luttinger liquids. *Phys. Rev. B*, 61:4393–4396, Feb 2000.
- [100] V. Meden, W. Metzner, U. Schollwöck, O. Schneider, T. Stauber, and K. Schönhammer. Luttinger liquids with boundaries: Power-laws and energy scales. *The European Physical Journal B - Condensed Matter and Complex Systems*, 16(4):631–646, 2000.
- [101] U. Schollwöck, V. Meden, W. Metzner, and K. Schönhammer. Dmrg studies of impurities in luttinger liquids. *Progress of Theoretical Physics Supplement*, 145:312–319, 2002.
- [102] V. Meden, W. Metzner, U. Schollwöck, and K. Schönhammer. Scaling behavior of impurities in mesoscopic luttinger liquids. *Phys. Rev. B*, 65:045318, Jan 2002.
- [103] S. Andergassen, T. Enss, V. Meden, W. Metzner, U. Schollwöck, and K. Schönhammer. Functional renormalization group for luttinger liquids with impurities. *Phys. Rev. B*, 70:075102, Aug 2004.
- [104] S. Andergassen, T. Enss, V. Meden, W. Metzner, U. Schollwöck, and K. Schönhammer. Renormalization-group analysis of the one-dimensional extended hubbard model with a single impurity. *Phys. Rev. B*, 73:045125, Jan 2006.
- [105] Imke Schneider, Alexander Struck, Michael Bortz, and Sebastian Eggert. Local density of states for individual energy levels in finite quantum wires. *Phys. Rev. Lett.*, 101:206401, Nov 2008.
- [106] D. Schuricht, S. Andergassen, and V. Meden. Local spectral properties of luttinger liquids: scaling versus nonuniversal energy scales. *Journal of Physics: Condensed Matter*, 25(1):014003, 2013.

- [107] Stefan A. Söffing, Imke Schneider, and Sebastian Eggert. Low-energy local density of states of the 1d hubbard model. *EPL (Europhysics Letters)*, 101(5):56006, 2013.
- [108] E Jeckelmann. Local density of states of the one-dimensional spinless fermion model. *Journal of Physics: Condensed Matter*, 25(1):014002, 2013.
- [109] Sebastian Eggert, Henrik Johannesson, and Ann Mattsson. Boundary effects on spectral properties of interacting electrons in one dimension. *Phys. Rev. Lett.*, 76:1505–1508, Feb 1996.
- [110] Ann E. Mattsson, Sebastian Eggert, and Henrik Johannesson. Properties of a luttinger liquid with boundaries at finite temperature and size. *Phys. Rev. B*, 56:15615–15628, Dec 1997.
- [111] Y. Wang, J. Voit, and Fu-Cho Pu. Exact boundary critical exponents and tunneling effects in integrable models for quantum wires. *Phys. Rev. B*, 54:8491–8500, Sep 1996.
- [112] Marc Bockrath, David H. Cobden, Jia Lu, Andrew G. Rinzler, Richard E. Smalley, Leon Balents, and Paul L. McEuen. Luttinger-liquid behaviour in carbon nanotubes. *Nature*, 397:598–601, 1999.
- [113] C. Blumenstein, J. Schäfer, S. Mietke, S. Meyer, A. Dollinger, M. Lochner, X. Y. Cui, L. Patthey, R. Matzdorf, and R. Claessen. Atomically controlled quantum chains hosting a tomonaga-luttinger liquid. *Nat Phys*, 7:776 – 780, 2011.
- [114] Steven R. White and Adrian E. Feiguin. Real-time evolution using the density matrix renormalization group. *Phys. Rev. Lett.*, 93:076401, Aug 2004.
- [115] Ulrich Schollwöck. The density-matrix renormalization group in the age of matrix product states. *Ann. Phys.*, 326(1):96 – 192, 2011.
- [116] Elliott H. Lieb and Derek W. Robinson. The finite group velocity of quantum spin systems. *Comm. Math. Phys.*, 28(3):251–257, 1972.
- [117] C. Karrasch, J. E. Moore, and F. Heidrich-Meisner. Real-time and real-space spin and energy dynamics in one-dimensional spin- $\frac{1}{2}$  systems induced by local quantum quenches at finite temperatures. *Phys. Rev. B*, 89:075139, Feb 2014.
- [118] Adilet Imambekov and Leonid I. Glazman. Exact exponents of edge singularities in dynamic correlation functions of 1d bose gas. *Phys. Rev. Lett.*, 100:206805, May 2008.
- [119] S. Katsura, T. Horiguchi, and M. Suzuki. Dynamical properties of the isotropic {XY} model. *Physica*, 46(1):67 – 86, 1970.

## 8. BIBLIOGRAPHY

---

- [120] Joachim Stolze, Angela Nöppert, and Gerhard Müller. Gaussian, exponential, and power-law decay of time-dependent correlation functions in quantum spin chains. *Phys. Rev. B*, 52:4319–4326, Aug 1995.
- [121] Hamed Karimi and Ian Affleck. Transverse spectral functions and dzyaloshinskii-moriya interactions in  $xxz$  spin chains. *Phys. Rev. B*, 84:174420, Nov 2011.
- [122] F. H. L. Essler, R. G. Pereira, and I. Schneider. Spin-charge-separated quasiparticles in one-dimensional quantum fluids. *Phys. Rev. B*, 91:245150, Jun 2015.
- [123] F. C. Alcaraz, M. N. Barber, M. T. Batchelor, R. J. Baxter, and G. R. W. Quispel. Surface exponents of the quantum  $xxz$ , ashkin-teller and potts models. *J. Phys. A: Math. Gen.*, 20(18):6397, 1987.
- [124] E K Sklyanin. Boundary conditions for integrable quantum systems. *J. Phys. A: Math. Gen.*, 21(10):2375, 1988.
- [125] H Schulz. Hubbard chain with reflecting ends. *J. Phys C: Solid State Phys.*, 18(3):581, 1985.
- [126] L. Landau and G. Rumer. The cascade theory of electronic showers. *Proc. R. Soc. Lond. A*, 166(925):213–228, 1938.
- [127] A.A. Zvyagin. *Finite Size Effects in Correlated Electron Models: Exact Results*. World Scientific, 2005.
- [128] A J Daley, C Kollath, U Schollwöck, and G Vidal. Time-dependent density-matrix renormalization-group using adaptive effective hilbert spaces. *J. Stat. Mech.: Theory Exp.*, (04):P04005, 2004.
- [129] Adrian E. Feiguin and Steven R. White. Time-step targeting methods for real-time dynamics using the density matrix renormalization group. *Phys. Rev. B*, 72:020404, Jul 2005.
- [130] F.D.M. Haldane. Continuum dynamics of the 1-d heisenberg antiferromagnet: Identification with the  $o(3)$  nonlinear sigma model. *Phys. Lett. A*, 93(9):464 – 468, 1983.
- [131] F. D. M. Haldane. Nonlinear field theory of large-spin heisenberg antiferromagnets: Semiclassically quantized solitons of the one-dimensional easy-axis néel state. *Phys. Rev. Lett.*, 50:1153–1156, Apr 1983.
- [132] H. J. Schulz. Phase diagrams and correlation exponents for quantum spin chains of arbitrary spin quantum number. *Phys. Rev. B*, 34:6372–6385, Nov 1986.

- [133] F. C. Alcaraz and A. Moreo. Critical behavior of anisotropic spin- $S$  heisenberg chains. *Phys. Rev. B*, 46:2896–2907, Aug 1992.
- [134] J. Timonen and A. Luther. Continuum-limit correlation functions for the spin-one anisotropic heisenberg chain. *J. Phys. C*, 18(7):1439, 1985.
- [135] Wei Chen, Kazuo Hida, and B. C. Sanctuary. Ground-state phase diagram of  $s = 1$  XXZ chains with uniaxial single-ion-type anisotropy. *Phys. Rev. B*, 67:104401, Mar 2003.
- [136] P. DiFrancesco, P. Mathieu, and D. Sénéchal. *Conformal Field Theory*. Springer, 1997.
- [137] J. C. Xavier. Entanglement entropy, conformal invariance, and the critical behavior of the anisotropic spin- $s$  heisenberg chains: Dmrg study. *Phys. Rev. B*, 81:224404, Jun 2010.
- [138] Michael Knap, Adrian Kantian, Thierry Giamarchi, Immanuel Bloch, Mikhail D. Lukin, and Eugene Demler. Probing real-space and time-resolved correlation functions with many-body ramsey interferometry. *Phys. Rev. Lett.*, 111:147205, Oct 2013.
- [139] Alexander L. Gaunt, Tobias F. Schmidutz, Igor Gotlibovych, Robert P. Smith, and Zoran Hadzibabic. Bose-einstein condensation of atoms in a uniform potential. *Phys. Rev. Lett.*, 110:200406, May 2013.
- [140] L. Chomaz, L. Corman, T. Bienaimé, C. Weitenberg, S. Nascimbène, and J. Dalibard. Emergence of coherence via transverse condensation on a uniform quasi-two-dimensional bose gas. *Nat. Comm.*, 6(6162), 2015.
- [141] S. Ghoshal and A. Zamolodchikov. Boundary S matrix and boundary state in two-dimensional integrable quantum field theory. *Int. J. Mod. Phys. A*, 09(21):3841–3885, 1994.
- [142] Xin Zhang, Yuan-Yuan Li, Junpeng Cao, Wen-Li Yang, Kangjie Shi, and Yupeng Wang. Bethe states of the XXZ spin-chain with arbitrary boundary fields. *Nucl. Phys. B*, 893:70 – 88, 2015.
- [143] R.U. Heimbuch. *The Quantum Highway: electronic properties of metal-induced nanowires on semiconductor surfaces*. PhD thesis, University of Twente, Enschede, 2015.
- [144] N. de Jong. *To be published*. PhD thesis, University of Amsterdam, 2016.
- [145] H. Ishii, H. Kataura, H. Shiozawa, H. Yoshioka, H. Otsubo, Y. Takayawa, T. Miyahara, S. Suzuki, Y. Achiba, M. Nakatake, T. Narimura, M. Higashiguchi, K. Shimada, H. Namatame, and M. Taniguchi. Direct observation of tomonaga-luttinger-liquid state in carbon nanotubes at low temperatures. *Nature*, 426(6966):540–544, 2003.

## 8. BIBLIOGRAPHY

---

- [146] Jinhwan Lee, S. Eggert, H. Kim, S.-J. Kahng, H. Shinohara, and Y. Kuk. Real space imaging of one-dimensional standing waves: Direct evidence for a luttinger liquid. *Phys. Rev. Lett.*, 93:166403, Oct 2004.
- [147] J. D. Denlinger, G.-H. Gweon, J. W. Allen, C. G. Olson, J. Marcus, C. Schlenker, and L.-S. Hsu. Non-fermi-liquid single particle line shape of the quasi-one-dimensional non-cdw metal  $\text{Li}_0.9\text{Mo}_6\text{O}_{17}$ : Comparison to the luttinger liquid. *Phys. Rev. Lett.*, 82(12):2540–2543, 1999.
- [148] J. Hager, R. Matzdorf, J. He, R. Jin, D. Mandrus, M. A. Cazalilla, and E. W. Plummer. Non-fermi-liquid behavior in quasi-one-dimensional  $\text{Li}_{0.9}\text{Mo}_6\text{O}_{17}$ . *Phys. Rev. Lett.*, 95:186402, Oct 2005.
- [149] R. Claessen, M. Sing, U. Schwingenschlögl, P. Blaha, M. Dressel, and C. S. Jacobsen. Spectroscopic signatures of spin-charge separation in the quasi-one-dimensional organic conductor ttf-tcnq. *Phys. Rev. Lett.*, 88:096402, Feb 2002.
- [150] O. M. Auslaender, A. Yacoby, R. de Picciotto, K. W. Baldwin, L. N. Pfeiffer, and K. W. West. Tunneling spectroscopy of the elementary excitations in a one-dimensional wire. *Science*, 295(5556):825–828, 2002.
- [151] K. Nakatsuji and F. Komori. Debate over dispersion direction in a tomonaga-luttinger-liquid system. *Nat. Phys.*, 8(3):174, 2012.
- [152] J. Wang, M. Li, and E. I. Altman. Scanning tunneling microscopy study of self-organized au atomic chain growth on  $\text{ge}(001)$ . *Phys. Rev. B*, 70(23):1–4, 2004.
- [153] C Blumenstein, S Meyer, S Mietke, J Schäfer, A Bostwick, E Rotenberg, R Matzdorf, and R Claessen. Au-induced quantum chains on  $\text{ge}(001)$ —symmetries, long-range order and the conduction path. *Journal of Physics: Condensed Matter*, 25(1):014015, 2013.
- [154] T. Lichtenstein, H. Teiken, H. Pfnür, J. Wollschläger, and C. Tegenkamp. Au-chains grown on  $\text{ge}(100)$ : A detailed spa-leed study. *Surface Science*, 632(0):64 – 70, 2015.
- [155] Jewook Park, Kan Nakatsuji, Tae-Hwan Kim, Sun Kyu Song, Fumio Komori, and Han Woong Yeom. Absence of luttinger liquid behavior in au-ge wires: A high-resolution scanning tunneling microscopy and spectroscopy study. *Phys. Rev. B*, 90:165410, Oct 2014.
- [156] J. Wang, M. Li, and E. I. Altman. Scanning tunneling microscopy study of au growth on  $\text{ge}(0\ 0\ 1)$ : Bulk migration, self-organization, and clustering. *Surf. Sci.*, 596(1-3):126–143, 2005.

- [157] Arie van Houselt, Marinus Fischer, Bene Poelsema, and Harold J. W. Zandvliet. Giant missing row reconstruction of au on ge(001). *Phys. Rev. B*, 78:233410, 2008.
- [158] J. Schäfer, C. Blumenstein, S. Meyer, M. Wisniewski, and R. Claessen. New model system for a one-dimensional electron liquid: Self-organized atomic gold chains on ge(001). *Phys. Rev. Lett.*, 101:236802, 2008.
- [159] Tijs F. Mocking, Daan Stam, Bene Poelsema, and Harold J.W. Zandvliet. Dynamics of au-induced nanowires on ge(001). *Surf. Sci.*, 604(21-22):2021–2023, 2010.
- [160] S. López-Moreno, A. H. Romero, A. Muñoz, and U. Schwingenschlögl. First-principles description of atomic gold chains on ge(001). *Phys. Rev. B*, 81:041415, Jan 2010.
- [161] S. Meyer, J. Schäfer, C. Blumenstein, P. Höpfner, A. Bostwick, J. L. McChesney, E. Rotenberg, and R. Claessen. Strictly one-dimensional electron system in au chains on ge(001) revealed by photoelectron  $k$ -space mapping. *Phys. Rev. B*, 83:121411, Mar 2011.
- [162] Daan Kockmann, Tijs F. Mocking, Arie van Houselt, Bene Poelsema, and Harold J. W. Zandvliet. Structural and electronic properties of au induced nanowires on ge(001). *J. Phys. Chem. C*, 113(39):17156–17159, 2009.
- [163] S. Sauer, F. Fuchs, F. Bechstedt, C. Blumenstein, and J. Schäfer. First-principles studies of au-induced nanowires on ge(001). *Phys. Rev. B*, 81:075412, Feb 2010.
- [164] R. Heimbuch, M. Kuzmin, and H. J. W. Zandvliet. Origin of the Au/Ge(001) metallic state. *Nat Phys*, 8:697–698, 2012.
- [165] R. O. Jones. Density functional theory: Its origins, rise to prominence, and future. *Rev. Mod. Phys.*, 87:897–923, Aug 2015.
- [166] W. Kohn. Nobel lecture: Electronic structure of matter—wave functions and density functionals. *Rev. Mod. Phys.*, 71:1253–1266, Oct 1999.
- [167] R.G. Parr and Y. Weitao. *Density-Functional Theory of Atoms and Molecules*. International Series of Monographs on Chemistry. Oxford University Press, 1994.
- [168] C. Blumenstein, J. Schäfer, M. Morresi, S. Mietke, R. Matzdorf, and R. Claessen. Symmetry-breaking phase transition without a peierls instability in conducting monoatomic chains. *Phys. Rev. Lett.*, 107:165702, Oct 2011.
- [169] J. Tersoff and D. R. Hamann. Theory of the scanning tunneling microscope. *Phys. Rev. B*, 31:805–813, Jan 1985.

## 8. BIBLIOGRAPHY

---

- [170] S. Meyer, L. Dudy, J. Schäfer, C. Blumenstein, P. Höpfner, T. E. Umbach, A. Dollinger, X. Y. Cui, L. Patthey, and R. Claessen. Valence band and core-level photoemission of au/ge(001): Band mapping and bonding sites. *Phys. Rev. B*, 90:125409, Sep 2014.
- [171] Kan Nakatsuji, Ryota Niikura, Yuki Shibata, Masamichi Yamada, Takushi Iimori, and Fumio Komori. Anisotropic two-dimensional metallic state of Ge(001)c(8×2)-Au surfaces: An angle-resolved photoelectron spectroscopy. *Phys. Rev. B*, 80:081406, Aug 2009.
- [172] Arie van Houselt, Daan Kockmann, Tijs F. Mocking, Bene Poelsema, and Harold J. W. Zandvliet. Comment on “new model system for a one-dimensional electron liquid: Self-organized atomic gold chains on ge(001)”. *Phys. Rev. Lett.*, 103:209701, Nov 2009.
- [173] Kan Nakatsuji, Ryota Niikura, Yuki Shibata, Masamichi Yamada, Takushi Iimori, Fumio Komori, Yasuhiro Oda, and Akira Ishii. Anisotropic splitting and spin polarization of metallic bands due to spin-orbit interaction at the ge(111)( $\sqrt{3} \times \sqrt{3}$ )r30°-au surface. *Phys. Rev. B*, 84:035436, Jul 2011.
- [174] Ryota Niikura, Kan Nakatsuji, and Fumio Komori. Local atomic and electronic structure of au-adsorbed ge(001) surfaces: Scanning tunneling microscopy and x-ray photoemission spectroscopy. *Phys. Rev. B*, 83:035311, Jan 2011.
- [175] Jean-Marc Jancu, Reinhard Scholz, Fabio Beltram, and Franco Bassani. Empirical spds\* tight-binding calculation for cubic semiconductors: General method and material parameters. *Phys. Rev. B*, 57:6493–6507, Mar 1998.
- [176] Yoshiyuki Ohtsubo, Koichiro Yaji, Shinichiro Hatta, Hiroshi Okuyama, and Tetsuya Aruga. Two-dimensional states localized in subsurface layers of ge(111). *Phys. Rev. B*, 88:245310, Dec 2013.
- [177] Franciszek Krok, Mark R. Kaspers, Alexander M. Bernhart, Marek Nikiel, Benedykt R. Jany, Paulina Indyka, Mateusz Wojtaszek, Rolf Möller, and Christian A. Bobisch. Probing the electronic transport on the reconstructed au/ge(001) surface. *Beilstein Journal of Nanotechnology*, 5:1463–1471, 2014.
- [178] C. Blumenstein, J. Schäfer, S. Mietke, S. Meyer, A. Dollinger, M. Lochner, X. Y. Cui, L. Patthey, R. Matzdorf, and R. Claessen. Reply to ”debate over dispersion direction in a tomonaga-luttinger-liquid system”. *Nat. Phys.*, 8(3):174, 2012.

- [179] K. Yaji, R. Yukawa, S. Kim, Y. Ohtsubo, P. Le Fèvre, F. Bertran, A. Taleb-Ibrahimi, I. Matsuda, K. Nakatsuji, and F. Komori. Deviation from Fermi-liquid behavior in two-dimensional surface states of Au-induced nanowires on Ge(001) by correlation and localization. *ArXiv e-prints*, February 2016.
- [180] A. Safaei, A. van Houselt, B. Poelsema, H. J. W. Zandvliet, and R. van Gastel. Dynamics of the wetting-induced nanowire reconstruction of au/ge(001). *Phys. Rev. B*, 88:085415, Aug 2013.
- [181] J Schäfer, C Blumenstein, S Meyer, M Wisniewski, and R Claessen. Schäfer et al. reply. *Physical Review Letters*, 103(20):209702, 2009.
- [182] Rachel Wortis. Disorder-induced zero bias anomalies in strongly correlated systems. 4 Corner Southwest Ontario Condensed Matter Physics Symposium, 2011.
- [183] A L Efros and B I Shklovskii. Coulomb gap and low temperature conductivity of disordered systems. *Journal of Physics C: Solid State Physics*, 8(4):L49, 1975.
- [184] A L Efros. Coulomb gap in disordered systems. *Journal of Physics C: Solid State Physics*, 9(11):2021, 1976.
- [185] B.L. Altshuler and A.G. Aronov. Zero bias anomaly in tunnel resistance and electron-electron interaction. *Solid State Communications*, 30(3):115 – 117, 1979.
- [186] Peter Kopietz. Coulomb gap in the density of states of disordered metals in two dimensions. *Phys. Rev. Lett.*, 81:2120–2123, Sep 1998.
- [187] L. Bartosch and P. Kopietz. Zero bias anomaly in the density of states of low-dimensional metals. *The European Physical Journal B - Condensed Matter and Complex Systems*, 28(1):29–36, 2002.
- [188] Alex Kamenev and Anton Andreev. Electron-electron interactions in disordered metals: Keldysh formalism. *Phys. Rev. B*, 60:2218–2238, Jul 1999.
- [189] Yun Song, R. Wortis, and W. A. Atkinson. Dynamical mean field study of the two-dimensional disordered hubbard model. *Phys. Rev. B*, 77:054202, Feb 2008.
- [190] R. Wortis and W. A. Atkinson. Physical mechanism for a kinetic energy driven zero-bias anomaly in the anderson-hubbard model. *Phys. Rev. B*, 82:073107, Aug 2010.
- [191] J. Perera and R. Wortis. Energy dependence of localization with interactions and disorder: The generalized inverse participation ratio of an ensemble of two-site anderson-hubbard systems. *Phys. Rev. B*, 92:085110, Aug 2015.

## 8. BIBLIOGRAPHY

---

- [192] R. Egger and A. O. Gogolin. Bulk and boundary zero-bias anomaly in multiwall carbon nanotubes. *Phys. Rev. Lett.*, 87:066401, Jul 2001.
- [193] E. G. Mishchenko, A. V. Andreev, and L. I. Glazman. Zero-bias anomaly in disordered wires. *Phys. Rev. Lett.*, 87:246801, Nov 2001.
- [194] A. J. Kronemeijer, E. H. Huisman, I. Katsouras, P. A. van Hal, T. C. T. Geuns, P. W. M. Blom, S. J. van der Molen, and D. M. de Leeuw. Universal scaling in highly doped conducting polymer films. *Phys. Rev. Lett.*, 105:156604, Oct 2010.
- [195] Hassan Abdalla, Kevin van de Ruit, and Martijn Kemerink. Effective temperature and universal conductivity scaling in organic semiconductors. *Scientific reports*, 5, 2015.
- [196] A. S. Rodin and M. M. Fogler. Apparent power-law behavior of conductance in disordered quasi-one-dimensional systems. *Phys. Rev. Lett.*, 105:106801, Sep 2010.
- [197] Kamal Asadi, Auke J Kronemeijer, Tobias Cramer, L Jan Anton Koster, Paul WM Blom, and Dago M de Leeuw. Polaron hopping mediated by nuclear tunnelling in semiconducting polymers at high carrier density. *Nature communications*, 4:1710, 2013.
- [198] B. Thielemann, Ch. Rüegg, H. M. Rønnow, A. M. Läuchli, J.-S. Caux, B. Normand, D. Biner, K. W. Krämer, H.-U. GÜdel, J. Stahn, K. Habicht, K. Kiefer, M. Boehm, D. F. McMorrow, and J. Mesot. Direct observation of magnon fractionalization in the quantum spin ladder. *Phys. Rev. Lett.*, 102:107204, Mar 2009.
- [199] Martin Mourigal, Mechthild Enderle, Axel Klopfferpieper, Jean-Sébastien Caux, Anne Stunault, Rønnow, and Henrik M. Fractional spinon excitations in the quantum heisenberg antiferromagnetic chain. *Nat Phys*, 9, 2013.
- [200] T. Giamarchi and H. J. Schulz. Anderson localization and interactions in one-dimensional metals. *Phys. Rev. B*, 37(325), 1988.
- [201] Eugene B. Kolomeisky. Universal jumps of conductance at the metal-insulator transition in one dimension. *Phys. Rev. B*, 47:6193–6196, Mar 1993.
- [202] Julien Vidal, Dominique Mouhanna, and Thierry Giamarchi. Correlated fermions in a one-dimensional quasiperiodic potential. *Phys. Rev. Lett.*, 83:3908–3911, Nov 1999.
- [203] Kazuo Hida. Quasiperiodic hubbard chains. *Phys. Rev. Lett.*, 86:1331–1334, Feb 2001.

- [204] Daniel Boies, C. Bourbonnais, and A. M. S. Tremblay. One-particle and two-particle instability of coupled luttinger liquids. *Phys. Rev. Lett.*, 74:968–971, Feb 1995.
- [205] M. A. Cazalilla, R. Citro, T. Giamarchi, E. Orignac, and M. Rigol. One dimensional bosons: From condensed matter systems to ultracold gases. *Rev. Mod. Phys.*, 83:1405–1466, Dec 2011.
- [206] Peter J. Martin, Bruce G. Oldaker, Andrew H. Miklich, and David E. Pritchard. Bragg scattering of atoms from a standing light wave. *Phys. Rev. Lett.*, 60:515–518, Feb 1988.
- [207] J. Stenger, S. Inouye, A. P. Chikkatur, D. M. Stamper-Kurn, D. E. Pritchard, and W. Ketterle. Bragg spectroscopy of a bose-einstein condensate. *Phys. Rev. Lett.*, 82:4569–4573, Jun 1999.
- [208] R. Ozeri, N. Katz, J. Steinhauer, and N. Davidson. *Colloquium* : Bulk Bogoliubov excitations in a Bose-Einstein condensate. *Rev. Mod. Phys.*, 77:187–205, Apr 2005.
- [209] Ying-Ju Wang, Dana Z. Anderson, Victor M. Bright, Eric A. Cornell, Quentin Diot, Tetsuo Kishimoto, Mara Prentiss, R. A. Saravanan, Stephen R. Segal, and Saijun Wu. Atom Michelson Interferometer on a Chip Using a Bose-Einstein Condensate. *Phys. Rev. Lett.*, 94:090405, Mar 2005.
- [210] Saijun Wu, Ying-Ju Wang, Quentin Diot, and Mara Prentiss. Splitting matter waves using an optimized standing-wave light-pulse sequence. *Phys. Rev. A*, 71:043602, Apr 2005.
- [211] N. Fabbri, M. Panfil, D. Clément, L. Fallani, M. Inguscio, C. Fort, and J.-S. Caux. Dynamical structure factor of one-dimensional bose gases: Experimental signatures of beyond-luttinger-liquid physics. *Phys. Rev. A*, 91:043617, Apr 2015.
- [212] F. Meinert, M. Panfil, M. J. Mark, K. Lauber, J.-S. Caux, and H.-C. Nägerl. Probing the excitations of a lieb-liniger gas from weak to strong coupling. *Phys. Rev. Lett.*, 115:085301, Aug 2015.
- [213] Miłosz Panfil and Jean-Sébastien Caux. Finite-temperature correlations in the lieb-liniger one-dimensional bose gas. *Phys. Rev. A*, 89:033605, Mar 2014.
- [214] L. Tonks. The complete equation of state of one, two and three-dimensional gases of hard elastic spheres. *Phys. Rev.*, 50(10):955–963, 1936.
- [215] M. Girardeau. Relationship between Systems of Impenetrable Bosons and Fermions in One Dimension. *J. Math. Phys.*, 1(6):516–523, 1960.

## 8. BIBLIOGRAPHY

---

- [216] Elmar Haller, Mattias Gustavsson, Manfred J. Mark, Johann G. Danzl, Russell Hart, Guido Pupillo, and Hanns-Christoph Nägerl. Realization of an excited, strongly correlated quantum gas phase. *Science*, 325(5945):1224–1227, 2009.
- [217] A. Minguzzi and D. M. Gangardt. Exact coherent states of a harmonically confined tonks-girardeau gas. *Phys. Rev. Lett.*, 94(24):240404, 2005.
- [218] R. Pezer and H. Buljan. Momentum Distribution Dynamics of a Tonks-Girardeau Gas: Bragg Reflections of a Quantum Many-Body Wave Packet. *Phys. Rev. Lett.*, 98:240403, Jun 2007.
- [219] D. M. Gangardt and M. Pustilnik. Correlations in an expanding gas of hard-core bosons. *Phys. Rev. A*, 77:041604, Apr 2008.
- [220] Dominik Muth, Bernd Schmidt, and Michael Fleischhauer. Fermionization dynamics of a strongly interacting one-dimensional bose gas after an interaction quench. *New Journal of Physics*, 12(8):083065, 2010.
- [221] C. Schenke, A. Minguzzi, and F. W. J. Hekking. Nonadiabatic creation of macroscopic superpositions with strongly correlated one-dimensional bosons in a ring trap. *Phys. Rev. A*, 84:053636, 2011.
- [222] G. E. Astrakharchik and L. P. Pitaevskii. Lieb’s soliton-like excitations in harmonic traps. *Europhys. Lett.*, 102(3):30004, 2013.
- [223] Mario Collura, Spyros Sotiriadis, and Pasquale Calabrese. Equilibration of a Tonks-Girardeau Gas Following a Trap Release. *Phys. Rev. Lett.*, 110:245301, Jun 2013.
- [224] E. Quinn and M. Haque. Modulated trapping of interacting bosons in one dimension. *Phys. Rev. A*, 90:053609, 2014.
- [225] Florian Cartarius, Eiji Kawasaki, and Anna Minguzzi. Dynamical depinning of a Tonks Girardeau gas. May.
- [226] P. L. Kapitza and P. A. M. Dirac. The reflection of electrons from standing light waves. *Proceedings of the Cambridge Philosophical Society*, 29:297, 1933.
- [227] Daniel L Freimund, Kayvan Aflatooni, and Herman Batelaan. Observation of the kapitza-dirac effect. *Nature*, 413:142–143, Sept 2001.
- [228] P. Calabrese and J. Cardy. Time Dependence of Correlation Functions Following a Quantum Quench. *Phys. Rev. Lett.*, 96:136801, 2006.
- [229] M. Rigol, V. Dunjko, V. Yurovsky, and M. Olshanii. Relaxation in a Completely Integrable Many-Body Quantum System: An Ab Initio Study of the Dynamics of the Highly Excited States of 1D Lattice Hard-Core Bosons. *Phys. Rev. Lett.*, 98:050405, 2007.

- [230] Anatoli Polkovnikov, Krishnendu Sengupta, Alessandro Silva, and Mukund Vengalattore. *Colloquium* : Nonequilibrium dynamics of closed interacting quantum systems. *Rev. Mod. Phys.*, 83:863–883, Aug 2011.
- [231] R. E. Sapiro, R. Zhang, and G. Raithel. Atom interferometry using kapitzadirac scattering in a magnetic trap. *Phys. Rev. A*, 79:043630, Apr 2009.
- [232] J.-S. Caux and F. H. L. Essler. Time Evolution of Local Observables After Quenching to an Integrable Model. *Phys. Rev. Lett.*, 110:257203, 2013.
- [233] Jorn Mossel and Jean-Sébastien Caux. Generalized tba and generalized gibbs. *Journal of Physics A: Mathematical and Theoretical*, 45(25):255001, 2012.
- [234] Jean-Sébastien Caux. The quench action. *Journal of Statistical Mechanics: Theory and Experiment*, 2016(6):064006, 2016.
- [235] A. V. Rozhkov. Density-density propagator for one-dimensional interacting spinless fermions with nonlinear dispersion and calculation of the coulomb drag resistivity. *Phys. Rev. B*, 77:125109, Mar 2008.
- [236] George Neville Watson. *A treatise on the theory of Bessel functions*. Cambridge university press, 1995.
- [237] J. De Nardis and J.-S. Caux. Analytical expression for a post-quench time evolution of the one-body density matrix of one-dimensional hard-core bosons. *J. Stat. Mech.: Th. Exp.*, 2014(12):P12012, 2014.
- [238] A. O. Gogolin, A. A. Nersesyan, and A. M. Tsvelik. *Bosonization and Strongly Correlated Systems*. Cambridge University Press, 1998.
- [239] J. von Delft and H. Schoeller. Bosonization for Beginners - Refermionization for Experts. *Ann. Phys. (Leipzig)*, 7(4):225–306, 1998.
- [240] H. Bethe. Zur Theorie der Metalle. i. Eigenwerte und Eigenfunktionen der linearen Atomkette. *Zeit. für Physik*, 71:205, 1931.
- [241] Márton Kormos, Yang-Zhi Chou, and Adilet Imambekov. Exact three-body local correlations for excited states of the 1d bose gas. *Phys. Rev. Lett.*, 107:230405, Dec 2011.
- [242] Vincenzo Alba, Maurizio Fagotti, and Pasquale Calabrese. Entanglement entropy of excited states. *Journal of Statistical Mechanics: Theory and Experiment*, 2009(10):P10020, 2009.
- [243] L. Vidmar, J. P. Ronzheimer, M. Schreiber, S. Braun, S. S. Hodgman, S. Langer, F. Heidrich-Meisner, I. Bloch, and U. Schneider. Dynamical quasicondensation of hard-core bosons at finite momenta. *Phys. Rev. Lett.*, 115:175301, Oct 2015.

## 8. BIBLIOGRAPHY

---

- [244] Miłosz Panfil, Jacopo De Nardis, and Jean-Sébastien Caux. Metastable criticality and the super tonks-girardeau gas. *Phys. Rev. Lett.*, 110:125302, Mar 2013.
- [245] B. Davies. Higher conservation laws for the quantum non-linear schrödinger equation. *Physica A: Statistical Mechanics and its Applications*, 167(2):433 – 456, 1990.
- [246] H. Frahm and C. Rödenbeck. A generalized spin ladder in a magnetic field. *Eur. Phys. J. B*, 10(3):409–414, 1999.
- [247] AA Zvyagin, A Klümper, and J Zittartz. Integrable correlated electron model with next-nearest-neighbour interactions. *The European Physical Journal B-Condensed Matter and Complex Systems*, 19(1):25–36, 2001.
- [248] E. H. Lieb. Exact Analysis of an Interacting Bose Gas. II. The Excitation Spectrum. *Phys. Rev.*, 130(4):1616–1624, 1963.
- [249] W. Heisenberg. Zur Theorie des Ferromagnetismus. *Z. Phys.*, 49:619, 1928.
- [250] R. Orbach. Linear antiferromagnetic chain with anisotropic coupling. *Phys. Rev.*, 112(2):309–316, 1958.
- [251] Belén Paredes, Artur Widera, Valentin Murg, Olaf Mandel, Simon Fölling, Ignacio Cirac, Gora V Shlyapnikov, Theodor W Hänsch, and Immanuel Bloch. Tonks–girardeau gas of ultracold atoms in an optical lattice. *Nature*, 429(6989):277–281, 2004.
- [252] M. de Llano and J. P. Vary. Generalized fermi sea for plane-wave hartree-fock theory: One dimensional model calculation. *Phys. Rev. C*, 19:1083–1088, Mar 1979.
- [253] B. Pozsgay. Mean values of local operators in highly excited Bethe states. *J. Stat. Mech.: Th. Exp.*, 2011(01):P01011, 2011.
- [254] M. Kormos, G. Mussardo, and A. Trombettoni. Local correlations in the super-Tonks-Girardeau gas. *Phys. Rev. A*, 83:013617, 2011.
- [255] M. Kormos, G. Mussardo, and A. Trombettoni. Expectation Values in the Lieb-Liniger Bose Gas. *Phys. Rev. Lett.*, 103(21):210404, 2009.
- [256] J.-S. Caux and P. Calabrese. Dynamical density-density correlations in the one-dimensional Bose gas. *Phys. Rev. A*, 74(3):031605, Sep 2006.
- [257] Taksu Cheon and T Shigehara. Realizing discontinuous wave functions with renormalized short-range potentials. *Physics Letters A*, 243(3):111 – 116, 1998.

- [258] Taksu Cheon and T. Shigehara. Fermion-boson duality of one-dimensional quantum particles with generalized contact interactions. *Phys. Rev. Lett.*, 82:2536–2539, Mar 1999.
- [259] K. Penc and J. Sólyom. One-dimensional hubbard model in a magnetic field and the multicomponent tomonaga-luttinger model. *Phys. Rev. B*, 47:6273–6292, Mar 1993.
- [260] M. Pletyukhov and V. Gritsev. Persistent currents in a multicomponent Tomonaga-Luttinger liquid: Application to a mesoscopic semiconductor ring with spin-orbit interaction. *Phys. Rev. B*, 70:165316, 2004.
- [261] V. Korepin and N. Slavnov. The new identity for the scattering matrix of exactly solvable models. *The European Physical Journal B - Condensed Matter and Complex Systems*, 5(3):555–557, 1998.
- [262] A. Lenard. Momentum Distribution in the Ground State of the One-Dimensional System of Impenetrable Bosons. *J. Math. Phys.*, 5(7):930–943, 1964.
- [263] J.-S. Caux, P. Calabrese, and N. A. Slavnov. One-particle dynamical correlations in the one-dimensional Bose gas. *J. Stat. Mech.: Th. Exp.*, page P01008, 2007.
- [264] C. Ryu, M. F. Andersen, P. Cladé, Vasant Natarajan, K. Helmerson, and W. D. Phillips. Observation of persistent flow of a bose-einstein condensate in a toroidal trap. *Phys. Rev. Lett.*, 99:260401, Dec 2007.
- [265] M. Gring, M. Kuhnert, T. Langen, T. Kitagawa, B. Rauer, M. Schreitl, I. Mazets, D. Adu Smith, E. Demler, and J. Schmiedmayer. Relaxation and prethermalization in an isolated quantum system. *Science*, 337(6100):1318–1322, 2012.
- [266] M A Cazalilla. Bosonizing one-dimensional cold atomic gases. *Journal of Physics B: Atomic, Molecular and Optical Physics*, 37(7):S1, 2004.
- [267] S. Tan. Energetics of a strongly correlated Fermi gas. *Ann. Phys.*, 323(12):2952 – 2970, 2008.
- [268] N Kitanine, K K Kozłowski, J M Maillet, N A Slavnov, and V Terras. A form factor approach to the asymptotic behavior of correlation functions in critical models. *Journal of Statistical Mechanics: Theory and Experiment*, 2011(12):P12010, 2011.
- [269] K K Kozłowski, J M Maillet, and N A Slavnov. Correlation functions for one-dimensional bosons at low temperature. *Journal of Statistical Mechanics: Theory and Experiment*, 2011(03):P03019, 2011.

## 8. BIBLIOGRAPHY

---

- [270] Suhas Gangadharaiah, Thomas L. Schmidt, and Daniel Loss. Structure factor of interacting one-dimensional helical systems. *Phys. Rev. B*, 89:035131, Jan 2014.
- [271] Karol K Kozłowski and Jean Michel Maillet. Microscopic approach to a class of 1d quantum critical models. *Journal of Physics A: Mathematical and Theoretical*, 48(48):484004, 2015.
- [272] Karol Kajetan Kozłowski. Large-distance and long-time asymptotic behavior of the reduced density matrix in the non-linear schrödinger model. *Annales Henri Poincaré*, 16(2):437–534, 2015.
- [273] Thomas Veness and Fabian H. L. Essler. Mobile impurity approach to the optical conductivity in the hubbard chain. *Phys. Rev. B*, 93:205101, May 2016.
- [274] K K Kozłowski, J M Maillet, and N A Slavnov. Long-distance behavior of temperature correlation functions in the one-dimensional bose gas. *Journal of Statistical Mechanics: Theory and Experiment*, 2011(03):P03018, 2011.
- [275] M. Rigol, V. Dunjko, and M. Olshanii. Thermalization and its mechanism for generic isolated quantum systems. *Nature*, 452:854–858, 2008.
- [276] E. Ilievski, J. De Nardis, B. Wouters, J.-S. Caux, F. H. L. Essler, and T. Prosen. Complete generalized gibbs ensembles in an interacting theory. *Phys. Rev. Lett.*, 115:157201, Oct 2015.
- [277] F. H. L. Essler, G. Mussardo, and M. Panfil. Generalized gibbs ensembles for quantum field theories. *Phys. Rev. A*, 91:051602, May 2015.
- [278] Maurizio Fagotti and Fabian H. L. Essler. Reduced density matrix after a quantum quench. *Phys. Rev. B*, 87:245107, Jun 2013.
- [279] Jean-Sébastien Caux and Robert M. Konik. Constructing the generalized gibbs ensemble after a quantum quench. *Phys. Rev. Lett.*, 109:175301, Oct 2012.
- [280] Fabian H. L. Essler, Stefano Evangelisti, and Maurizio Fagotti. Dynamical correlations after a quantum quench. *Phys. Rev. Lett.*, 109:247206, Dec 2012.
- [281] Amy C. Cassidy, Charles W. Clark, and Marcos Rigol. Generalized thermalization in an integrable lattice system. *Phys. Rev. Lett.*, 106:140405, Apr 2011.
- [282] G. Mussardo. Infinite-time average of local fields in an integrable quantum field theory after a quantum quench. *Phys. Rev. Lett.*, 111:100401, Sep 2013.

- [283] Balázs Pozsgay. The generalized gibbs ensemble for heisenberg spin chains. *Journal of Statistical Mechanics: Theory and Experiment*, 2013(07):P07003, 2013.
- [284] Vincenzo Alba and Pasquale Calabrese. The quench action approach in finite integrable spin chains. *Journal of Statistical Mechanics: Theory and Experiment*, 2016(4):043105, 2016.
- [285] Márton Kormos, Aditya Shashi, Yang-Zhi Chou, Jean-Sébastien Caux, and Adilet Imambekov. Interaction quenches in the one-dimensional bose gas. *Phys. Rev. B*, 88:205131, Nov 2013.
- [286] Maurizio Fagotti, Mario Collura, Fabian H. L. Essler, and Pasquale Calabrese. Relaxation after quantum quenches in the spin- $\frac{1}{2}$  heisenberg xxz chain. *Phys. Rev. B*, 89:125101, Mar 2014.
- [287] B. Wouters, J. De Nardis, M. Brockmann, D. Fioretto, M. Rigol, and J.-S. Caux. Quenching the anisotropic heisenberg chain: Exact solution and generalized gibbs ensemble predictions. *Phys. Rev. Lett.*, 113:117202, Sep 2014.
- [288] B. Pozsgay, M. Mestyán, M. A. Werner, M. Kormos, G. Zaránd, and G. Takács. Correlations after quantum quenches in the *xxz* spin chain: Failure of the generalized gibbs ensemble. *Phys. Rev. Lett.*, 113:117203, Sep 2014.
- [289] Márton Kormos, Mario Collura, and Pasquale Calabrese. Analytic results for a quantum quench from free to hard-core one-dimensional bosons. *Phys. Rev. A*, 89:013609, Jan 2014.
- [290] J. De Nardis, B. Wouters, M. Brockmann, and J.-S. Caux. Solution for an interaction quench in the Lieb-Liniger Bose gas. *Phys. Rev. A*, 89:033601, 2014.
- [291] Spyros Sotiriadis and Pasquale Calabrese. Validity of the gge for quantum quenches from interacting to noninteracting models. *Journal of Statistical Mechanics: Theory and Experiment*, 2014(7):P07024, 2014.
- [292] Márton Mestyán and Balázs Pozsgay. Short distance correlators in the xxz spin chain for arbitrary string distributions. *Journal of Statistical Mechanics: Theory and Experiment*, 2014(9):P09020, 2014.
- [293] Erik Eriksson and Vladimir Korepin. Finite-size effects from higher conservation laws for the one-dimensional bose gas. *Journal of Physics A: Mathematical and Theoretical*, 46(23):235002, 2013.
- [294] A G Izergin, V E Korepin, and N Y Reshetikhin. Conformal dimensions in bethe ansatz solvable models. *Journal of Physics A: Mathematical and General*, 22(13):2615, 1989.

## 8. BIBLIOGRAPHY

---

- [295] A. M. Tsvelik. Incommensurate phases of quantum one-dimensional magnetics. *Phys. Rev. B*, 42:779–785, Jul 1990.
- [296] H Frahm. Integrable spin-1/2 xxz heisenberg chain with competing interactions. *Journal of Physics A: Mathematical and General*, 25(6):1417, 1992.
- [297] SV Pokrovsky and AM Tsvelik. Spectrum of conformal dimensions of lattice integrable models of magnets. *Zh. Eksp.Theor. Fiz.*, 93(6):2232–2246, 1987.
- [298] Holger Frahm and Claus Rödenbeck. Properties of the chiral spin liquid state in generalized spin ladders. *Journal of Physics A: Mathematical and General*, 30(13):4467, 1997.
- [299] H Frahm and Nai-C Yu. Finite-size effects in the integrable xxz heisenberg model with arbitrary spin. *Journal of Physics A: Mathematical and General*, 23(11):2115, 1990.
- [300] A. A. Zvyagin. Commensurate–incommensurate phase transitions for multichain quantum spin models: exact results. *Low Temperature Physics*, 26(2):134–146, 2000.
- [301] A. A. Zvyagin and A. Klümper. Quantum phase transitions and thermodynamics of quantum antiferromagnets with next-nearest-neighbor couplings. *Phys. Rev. B*, 68:144426, Oct 2003.
- [302] Holger Frahm and V. E. Korepin. Critical exponents for the one-dimensional hubbard model. *Phys. Rev. B*, 42:10553–10565, Dec 1990.
- [303] T. Price, D. L. Kovrizhin, and A. Lamacraft. Nonlinear Luttinger Liquid from Painlevé IV. *ArXiv e-prints*, June 2016.